UNIVERSIDAD MICHOACANA
DE SAN NICOLÁS DE HIDALGO

Facultad de Ingeniería Eléctrica
División de Estudios de Posgrado

# A Generalized Static and Dynamic State Estimation of Electric Power Systems

by
Omar Yamil VIDAL LEÓN ROMAY

*A thesis presented in compliance with the requirements*
*for the degree of Doctor of Science in Electrical Engineering*

Advisor: Claudio Rubén FUERTE ESQUIVEL, Ph.D.

Morelia, Michoacán
February 2021

# A GENERALIZED STATIC AND DYNAMIC STATE ESTIMATION OF ELECTRIC POWER SYSTEMS

Los Miembros del Jurado de Examen de Grado aprueban la **Tesis de Doctorado en Ciencias en Ingeniería Eléctrica, Opción en Sistemas Eléctricos** de ***Omar Yamil Vidal León Romay.***

Dr. Fernando Ornelas Téllez
*Presidente del Jurado*

Dr. Claudio Rubén Fuerte Esquivel
*Director de Tesis*

Dr. Antonio Ramos Paz
*Vocal*
Antonio Ramos Paz

Dr. J. Aurelio Medina Rios
*Vocal*

Dr. Boris Adrián Alcaide Moreno
*Revisor Externo* (CENACE)

Dr. Roberto Tapia Sánchez
*Jefe de la División de Estudios de Posgrado*
*de la Facultad de Ingeniería Eléctrica. UMSNH*
*(Por reconocimiento de firmas)*
Roberto

UNIVERSIDAD MICHOACANA DE SAN NICOLÁS DE HIDALGO
Febrero 2021

# *Abstract*

The higher levels of uncertainties in power systems operation because of the increasing penetration of converter-based generators and controllers are a new challenge faced by system operators. Under these operating scenarios, new state estimation methods are crucial for monitoring, operating and controlling power systems in a real-time and reliable fashion.

Based on the information mentioned above, general frameworks for formulating and solving the static and dynamic state estimation problems are proposed in this thesis. To fulfill these goals, this dissertation focuses on the following three areas. First, the static co-estimation of nodal voltages together with system parameters and unknown statuses of circuit breakers, respectively, in a single frame of reference without modifying the general formulation of the equality-constrained static state estimator. Secondly, the development of a new way for including hard limits associated with control devices in the formulation of the transient stability problem. This set of constraints is added to the rest of the equations representing the dynamics of an electric power system for a unified framework of analysis, where hard limits are simultaneously and automatically handled during the numerical solution of the transient stability problem. Lastly, a wide area dynamic state estimator is proposed for the simultaneous estimation of nodal voltages and dynamic states associated with synchronous machines and their controller units. This approach is formulated in a structure-preserving framework of analysis, performing the automatic check of the non-windup and windup controllers operating limits and, when applicable, the automatic enforcement of these limits during the iterative solution process of the state estimation.

***Keywords:*** Complementarity constraints, generalized state estimation, hard limits, optimization, transient stability.

# *Resumen*

Los mayores niveles de incertidumbre en la operación de los sistemas de potencia debido a la creciente penetración de generadores y controladores basados en convertidores es un nuevo reto al que se enfrentan los operadores del sistema. En estos escenarios operativos, las nuevas metodologías de estimación de estado son cruciales para supervisar, operar y controlar los sistemas de potencia de forma confiable y en tiempo real.

A partir de la información anteriormente mencionada, en esta tesis se proponen marcos generales para formular y resolver los problemas de estimación de estado estático y dinámico. Para cumplir estos objetivos, esta tesis se centra en las tres áreas siguientes. En primer lugar, la co-estimación estática de los voltajes nodales junto con los parámetros del sistema y los estados desconocidos de interruptores de potencia, respectivamente, en un mismo marco de referencia sin modificar la formulación general del estimador de estado estático con restricciones de igualdad. En segundo lugar, el desarrollo de una nueva forma de incluir los límites asociados a los dispositivos de control en la formulación del problema de estabilidad transitoria. Este conjunto de restricciones se añade al resto de las ecuaciones que representan la dinámica de un sistema eléctrico para obtener un marco de análisis unificado, en el que los límites se manejan simultánea y automáticamente durante la solución numérica del problema de estabilidad transitoria. Por último, se propone un estimador de estado dinámico de área amplia para la estimación simultánea de los voltajes nodales y los estados dinámicos asociados a las máquinas síncronas y sus controladores. Este enfoque se formula en un marco de análisis que preserva la estructura, realizando la comprobación automática de los límites operativos de los controladores non-windup y windup y, cuando es aplicable, la aplicación automática de estos límites durante el proceso de solución iterativa de la estimación de estado.

***Palabras clave:*** Restricciones de complementariedad, estimación de estado generalizada, límites restrictivos, optimización, estabilidad transitoria.

# *Acknowledgements*

I would like to express my sincerely gratitude to Claudio Rubén Fuerte Esquivel because under his guidance, his teachings and his valuable mentoring during these years of study, I have been able to accomplish this work. Professor Claudio taught me the main courses on power systems so that I was able to develop this thesis and I am grateful for all the time he invested in my education. I also appreciate his friendship, patience and confidence during the development of this work.

To my family for giving me their unconditional support.

To Enrique Arnoldo Zamora Cárdenas and Víctor Javier Gutiérrez Martínez for their valuable support and for sharing with me their knowledge in state estimation studies that helped me to publish a conference paper. I also appreciate your friendship.

To Ricardo Martínez Parrales for his valuable assistance and for sharing with me his knowledge in state estimation studies with complementarity constraints which served me for the publication of a journal article. Thank you for your friendship.

To José Luis Sánchez Garduño for his valuable support and for sharing with me his knowledge in multi-energy systems that helped me to publish a conference paper. I am grateful for your friendship.

To Jorge Uriel Sevilla Romero, Iván Isidro García and Laura Jaqueline Santander Hernández for sharing this trip with me and for all the moments of happiness we enjoyed.

To my friends and colleagues from División de Estudios de Posgrado-Facultad de Ingeniería Eléctrica with whom I interacted with and shared great experiences during my doctoral studies. I appreciate the time we spent together and I wish you all a lot of success.

To my reviewers who helped me to improve this thesis.

To Universidad Michoacana de San Nicolás de Hidalgo for giving me the opportunity to belong to its doctoral program and all the facilities they gave me during my stage in this institution.

To CONACyt for the financial support I received through the scholarship 592310. This work was also supported by the Fondo de Sustentabilidad Energética SENER-Conacyt, México, under grants 246949 and 249795.

# *Contents*

# *List of Figures*

# *List of Tables*

# *Abbreviations*

| | |
|---|---|
| AUKF-UI | Adaptative unscented Kalman filter for systems with unknown inputs |
| CB | Circuit breaker |
| CRUKF | Constrained robust unscented Kalman filter |
| CKF | Cubature Kalman filter |
| DAE | Differential-algebraic equation |
| DSIC | Double-sided inequality constraint |
| DSE | Dynamic state estimation |
| EKF | Extended Kalman filter |
| EPS | Electric power system |
| ECC | Energy control center |
| EnKF | Ensemble Kalman filter |
| GPS | Global positioning system |
| HIEKF | H-Infinite extended Kalman filter |
| HIUKF | H-Infinite unscented Kalman filter |
| IEEE | Institute of electrical and electronics engineers |
| LNER | Largest normalized estimated residual |
| LAV | Least absolute value |
| MAPE | Mean absolute percentage error |
| MVA | Megavolt ampere |
| MIPS | Mexican interconnected power system |
| NR | Newton-Raphson |
| PKF | Particle Kalman filter |
| PMU | Phasor measurement unit |
| RIEKF | Robust iterated extended Kalman filter |
| RUKF | Robust unscented Kalman filter |
| SE | State estimator |
| SSE | Static state estimation |
| SCADA | Supervisory control and data acquisition |
| TD | Time-domain |
| UKF | Unscented Kalman filter |
| WLS | Weighted least squares |
| WLS-EC | Weighted least squares with equality constraints |
| WLAV | Weighted least absolute value |
| WADSE | Wide area dynamic state estimation |

# *Nomenclature*

| | |
|---|---|
| $\mathcal{N}_e$ | Set of buses in the system. |
| $\mathcal{T}_e$ | Set of transmission elements. |
| $\boldsymbol{V}$ | Vector of nodal voltage magnitudes. |
| $\boldsymbol{\theta}$ | Vector of nodal phase angles. |
| $\mathcal{N}_{oe}$ | Subset of observable buses. |
| $\mathcal{T}_{oe}$ | Subset of observable transmission elements. |
| $M_e^{SCADA}$ | Number of SCADA measurements. |
| $M_e^{PMU}$ | Number of PMU measurements. |
| $M$ | Number of SCADA and PMU measurements. |
| $\boldsymbol{V_k^{SCADA}}$ | SCADA nodal voltage magnitudes’ measurements. |
| $\boldsymbol{P_k^{SCADA}}$ | SCADA nodal injections’ measurements of the active powers. |
| $\boldsymbol{Q_k^{SCADA}}$ | SCADA nodal injections’measurements of the reactive powers. |
| $\boldsymbol{P_{km}^{SCADA}}$ | SCADA branch active power flows’ measurements. |
| $\boldsymbol{Q_{km}^{SCADA}}$ | SCADA branch reactive power flows’ measurements. |
| $\boldsymbol{z_e^{SCADA}}$ | Vector of SCADA measurements. |
| $\boldsymbol{V_k^{PMU}}$ | PMU nodal voltage magnitudes’ measutrements. |
| $\boldsymbol{\theta_k^{PMU}}$ | PMU nodal phase angles’ measurements. |
| $\boldsymbol{I_{km}^{PMU}}$ | PMU branch current magnitudes’ measurements. |
| $\boldsymbol{\theta_{I_{km}}^{PMU}}$ | PMU phase angles of branch currents’ measurements. |
| $\boldsymbol{z_e^{PMU}}$ | Vector of PMU measurements. |
| $\boldsymbol{z}$ | Vector of measurements. |
| $\hat{\boldsymbol{z}}(.)$ | Vector of estimated measurements. |
| $\boldsymbol{x_e}$ | Vector of system algebraic variables. |
| $\boldsymbol{J}(.)$ | Objective function. |
| $\boldsymbol{r}$ | Vector of measurements’ residuals. |
| $\boldsymbol{W}$ | Weighting matrix. |
| $\ni$ | Such that. |
| $\mathcal{N}_{tbe}$ | Subset of transition buses in the transmission system. |
| $\boldsymbol{c}(.)$ | Vector of zero injection measurements. |
| $\perp$ | Complement operator. |
| $\mathcal{T}_{eb}$ | Set of transmission lines with doubtful parameters. |
| $\boldsymbol{g_{sekm}}$ | Vector of series conductances. |

| | |
|---|---|
| $\boldsymbol{b}_{sekm}$ | Vector of series susceptances. |
| $\boldsymbol{b}_{shkm}$ | Vector of shunt susceptances. |
| $\boldsymbol{L}_{N}$ | Vector of normalized lengths. |
| $\boldsymbol{P}_{st}$ | Vector of active power flow from internal node *s* to internal node *t*. |
| $\boldsymbol{Q}_{st}$ | Vector of reactive power flow from internal node *s* to internal node *t*. |
| $\boldsymbol{P}_{ss}$ | Vector of active power flow through the shunt branch connected at the internal node *s*. |
| $\boldsymbol{Q}_{ss}$ | Vector of reactive power flow through the shunt branch connected at the internal node *s*. |
| $\boldsymbol{P}_{ts}$ | Vector of active power flow from internal node *t* to internal node *s*. |
| $\boldsymbol{Q}_{ts}$ | Vector of reactive power flow from internal node *t* to internal node *s*. |
| $\boldsymbol{P}_{tt}$ | Vector of active power flow through the shunt branch connected at the internal node *t*. |
| $\boldsymbol{Q}_{tt}$ | Vector of reactive power flow through the shunt branch connected at the internal node *t*. |
| $\boldsymbol{I}_{st}(.)$ | Vector of the complex current from internal node *s* to internal node *t*. |
| $\boldsymbol{I}_{ts}(.)$ | Vector of the complex current from internal node *t* to internal node *s*. |
| $\boldsymbol{y}_{shkm}(.)$ | Vector of the complex admittance connected to internal bus *s*. |
| $\boldsymbol{y}_{shmk}(.)$ | Vector of the complex admittance connected to internal bus *t*. |
| $\boldsymbol{x}_{e\text{-}eb}$ | Vector of system algebraic variables and transmission line parameters. |
| $\mathcal{N}_{se}$ | Set of buses at power substations. |
| $\mathcal{T}_{cb}$ | Set of circuit breakers. |
| $\boldsymbol{P}_{cb}$ | Vector of active power flows of circuit breakers. |
| $\boldsymbol{Q}_{cb}$ | Vector of reactive power flows of circuit breakers. |
| $\boldsymbol{x}_{e\text{-}cb}$ | Vector of system algebraic variables and power flows of circuit breakers. |
| $\mathcal{T}_{ccb}$ | Subset of closed circuit breakers. |
| $\mathcal{T}_{ocb}$ | Subset of open circuit breakers. |
| $\mathcal{N}_{ccb}$ | Subset of buses for closed circuit breakers. |
| $\mathcal{N}_{ocb}$ | Subset of buses for open circuit breakers. |
| $\mathbf{OC}_{ccb}(.)$ | Closed breaker's operating conditions. |
| $\mathbf{OC}_{ocb}(.)$ | Open breaker's operating conditions. |
| $\mathcal{T}_{ucb}$ | Subset of unknown circuit breakers. |
| $\mathcal{N}_{ucb}$ | Subset of buses for unknown circuit breakers |
| $\boldsymbol{\Phi}_{ucb}(.)$ | Open status constraints vector for unknown breakers. |

| | |
|---|---|
| $\boldsymbol{\Gamma}_{\boldsymbol{ucb}}(.)$ | Closed status constraints vector for unknown breakers |
| $\mathbf{OC}_{\boldsymbol{ucb}}(.)$ | Vector of nonlinear complementarity constraints for unknown circuit breakers. |
| $\boldsymbol{c}_{\boldsymbol{te}}(.)$ | Vector of zero injection measurements at the transitions' buses located in the transmission system and explicitly modeled substations. |
| $\mathcal{T}_{tdb}$ | Set of transmission lines with temperature dependent parameters. |
| $r_{sekm,i}(T_{km,i})$ | Temperature dependent series resistivity of the *i*-th transmission line connected from bus *k* to bus *m*. |
| $g_{sekm,i}(T_{km,i})$ | Series conductance of the *i*-th transmission line as a function of conductor temperature. |
| $b_{sekm,i}(T_{km,i})$ | Series susceptance of the *i*-th transmission line as a function of conductor temperature. |
| $P_{Losstb,i}$ | Active power loss of the *i*-th transmission line with temperature dependent parameters. |
| $P_{RatedLosstb,i}$ | Nominal active power loss of the *i*-th transmission line with temperature dependent parameters. |
| $R_{\theta,i}$ | Thermal resistance of the *i*-th transmission line with temperature dependent parameters. |
| $\boldsymbol{T}_{\boldsymbol{km}}$ | Vector of transmission line temperatures. |
| $\boldsymbol{x}_{\boldsymbol{e\text{-}tdb}}$ | Vector of system algebraic variables and temperatures of transmission lines with temperature dependent parameters. |
| $\boldsymbol{T}(.)$ | Vector of constraints imposed by temperatures of transmission lines. |
| $\boldsymbol{x}$ | Vector of dynamic states related to both generators and all controllers without non-windup and windup limiters. |
| $\boldsymbol{\psi}$ | Controllers outputs with non-windup limiters. |
| $\boldsymbol{\tau}$ | Controllers outputs with windup limiters. |
| $\boldsymbol{\mu}$ | Dummy variables' vector located at windup limiters outputs. |
| $\boldsymbol{y}$ | Vector of network's algebraic variables. |
| $\boldsymbol{\beta}$ | Vector of time-invariant parameters. |
| $\dot{\boldsymbol{\gamma}}$ | Differential equations vector of $\boldsymbol{x}$, $\boldsymbol{\tau}$ and $\boldsymbol{\mu}$. |
| $\dot{\boldsymbol{\psi}}_{\boldsymbol{nwl}}$ | Differential equations vector of $\boldsymbol{\psi}$. |
| $\boldsymbol{g}(\cdot)$ | Vector of algebraic equations. |
| $\boldsymbol{\psi}^{\mathbf{min}}$ | Vector of lower limits for non-windup limiters. |
| $\boldsymbol{\psi}^{\mathbf{max}}$ | Vector of upper limits for non-windup limiters |
| $\boldsymbol{\mu}^{\mathbf{min}}$ | Vector of lower limits for windup limiters. |
| $\boldsymbol{\mu}^{\mathbf{max}}$ | Vector of upper limits for windup limiters |
| $\boldsymbol{\upsilon}^{\mathbf{min}}$ | Vector of complementarity variables at the lower limit for non-windup limiters. |
| $\boldsymbol{\upsilon}^{\mathbf{max}}$ | Vector of complementarity variables at the upper limit for non-windup limiters. |

| | |
|---|---|
| $\boldsymbol{\rho}^{\min}$ | Vector of complementarity variables at the lower limit for windup limiters. |
| $\boldsymbol{\rho}^{\max}$ | Vector of complementarity variables at the upper limit for windup limiters. |
| $\boldsymbol{\varphi}_{nwl}$ | Vector of complementarity constraints for non-windup limiters. |
| $\boldsymbol{\phi}_{wl}$ | Vector of complementarity constraints for windup limiters. |
| $\boldsymbol{\upsilon}$ | Vector of complementarity variables for non-windup limiters. |
| $\boldsymbol{\rho}$ | Vector of complementarity variables for windup limiters. |
| $\boldsymbol{\eta}_{wl}$ | Vector that gathers the guiding equations of windup limiters. |
| $\boldsymbol{x}_{tsa}$ | Vector of dynamic and algebraic state variables for the transient stability assesment. |
| $\boldsymbol{\Gamma}(\cdot)$ | Vector of difference equations. |
| $\boldsymbol{\Phi}(\cdot)$ | Vector of algebraic equations that are associated with hard limits. |
| $\boldsymbol{G}(\cdot)$ | Vector of algebraic nodal power mismatch equations and the power exchanged between synchronous machines and the transmission system. |
| $\boldsymbol{F}(.)$ | Right vector of the Newton-Raphson method. |
| $\boldsymbol{J}$ | Jacobian matrix of the Newton-Raphson method. |
| $\Delta\boldsymbol{x}_{tsa}$ | Vector of increments in dynamic and algebraic variables of the Newton-Raphson method. |
| $a$ | Number of synchronous machine dynamic states. |
| $b$ | Number of synchronous machine inputs. |
| $p$ | Number of synchronous machine parameters. |
| $\boldsymbol{\lambda}$ | Vector of synchronous machine dynamic states. |
| $\varsigma$ | Vector of known input variables to the synchronous machine. |
| $\dot{\boldsymbol{\lambda}}$ | Vector of differential equations associated with a synchronous machine. |
| $\boldsymbol{\varpi}$ | Noise vector associated with the dynamic model of the synchronous machine. |
| $\boldsymbol{Q}$ | Covariance matrix of $\boldsymbol{\varpi}$. |
| $\boldsymbol{\varepsilon}$ | Noise vector associated with the available measurements. |
| $\boldsymbol{R}$ | Covariance matrix of $\boldsymbol{\varepsilon}$. |
| $\Delta t$ | Time step of integration. |
| $\hat{\boldsymbol{S}}_k$ | Matrix that contains a set of sigma point vectors in $t_k$. |
| $\hat{\boldsymbol{\lambda}}_k^+$ | Vector of *a posteriori* dynamic variables in $t_k$. |
| $\boldsymbol{P}_k^+$ | *A posteriori* covariance matrix in $t_k$. |
| $\hat{\boldsymbol{\chi}}_{k+1}$ | Matrix that contains a modified set of sigma point vectors in $t_{k+1}$. |
| $\hat{\boldsymbol{\lambda}}_{k+1}^-$ | *A priori* state estimation vector in $t_{k+1}$. |
| $\boldsymbol{P}_{k+1}^-$ | *A priori* covariance matrix in $t_{k+1}$. |
| $\boldsymbol{\vartheta}_{k+1}$ | Matrix that contains a new set of sigma point vectors in $t_{k+1}$. |
| $\boldsymbol{P}_{k+1}^{zz}$ | Predicted measurement covariance matrix. |
| $\boldsymbol{P}_{k+1}^{\lambda z}$ | Cross-covariance matrix. |

| | |
|---|---|
| $\boldsymbol{K}_{k+1}$ | Kalman gain matrix. |
| $\hat{\boldsymbol{\lambda}}_{k+1}^{+}$ | Corrected state estimation vector in $t_{k+1}$ . |
| $\boldsymbol{P}_{k+1}^{+}$ | Corrected covariance matrix in $t_{k+1}$ . |
| $\mathcal{N}$ | Set of buses in the transmission system. |
| $\mathcal{T}$ | Set of transmission elements. |
| $\boldsymbol{y}_{\boldsymbol{dq}}$ | Vector of algebraic variables associated with the synchronous machines. |
| $\boldsymbol{y}_{\boldsymbol{DQ}}$ | Vector of algebraic variables associated with the transmission network. |
| $\boldsymbol{I}_{\boldsymbol{dq}}^{\boldsymbol{DQ}}(\cdot)$ | Vector of stator algebraic equations. |
| $\boldsymbol{x}_{\boldsymbol{dav}}$ | Vector of dynamic and algebraic state variables for wide area dynamic state estimation. |
| $\Re\left(\vec{\boldsymbol{I}}^{\boldsymbol{PMU}}\right)$ | PMU measurement vector of real parts of the branch complex current of transmission elements. |
| $\Im\left(\vec{\boldsymbol{I}}^{\boldsymbol{PMU}}\right)$ | PMU measurement vector of imaginary parts of the branch complex current of transmission elements. |
| $\boldsymbol{f}^{\boldsymbol{PMU}}$ | PMU measurement vector of nodal frequencies. |
| $\mathcal{SBD}_1$ | Set of suspected erroneous measurements. |
| $\mathcal{SBD}_2$ | Reduced set of suspected erroneous measurements. |
| $A_{inc}$ | Incidence matrix for the correlation between measurements. |
| $\mathcal{IBD}$ | Set of identified bad data. |

# *List of Publications*

**Published papers in Journals:**

- **O. Romay**, R. Martínez-Parrales and C. R. Fuerte-Esquivel, "Transient Stability Assessment Considering Hard Limits on Dynamic States", ***IEEE Transactions on Power Systems***, vol. 36, no. 1, pp. 533-536, DOI: 10.1109/TPWRS.2020.3025430, 2021.

**Cited by:**

- R. T. Elliott, P. Arabshahi and D. S. Kirschen, "Stabilizing Transient Disturbances With Utility-Scale Inverter-Based Resources", IET Generation, Transmission, & Distribution, 2020.

**Published papers in Conferences:**

- **O. Romay**, J. L. Sánchez-Garduño and C. R. Fuerte-Esquivel, "A unified state estimation in integrated natural gas and electricity networks", ***2020 IEEE International Autumn Meeting on Power, Electronics and Computing (ROPEC)***, DOI: 10.1109/ROPEC50909.2020.9258722, November 4-6, 2020.
- **O. Romay**, C. R. Fuerte-Esquivel, E. A. Zamora-Cárdenas and V. J. Gutiérrez-Martínez, "Methodologies for parameter and state estimation in electric power systems: A comparative analysis", ***2019 IEEE International Autumn Meeting on Power, Electronics and Computing (ROPEC)***, DOI: 10.1109/ROPEC48299.2019.9057032, November 13-15, 2019.

**Papers under review in Journals:**

- **O. Romay**, E. A. Zamora-Cárdenas, C. R. Fuerte-Esquivel and V. J. Gutiérrez-Martínez, "A PMU-Based Ultra Fast Linear State Estimator for Real-Time Applications", submitted to ***IEEE Power Engineering Letters***, December 1, 2020.

**Papers to be submitted in Journals:**

- **O. Romay**, R. Martínez-Parrales, C. R. Fuerte-Esquivel, E. Acha Daza and E. A. Zamora-Cárdenas, “A generalized estimation of dynamic and algebraic state variables in power systems”, in the process to be submitted to ***IEEE Trans. on Power Systems***.
- **O. Romay** C. R. Fuerte-Esquivel and A. Medina, “A complementarity approach for state and topology estimation in power systems”, in the process to be submitted to ***Electric Power Systems Research***.
- **O. Romay** and C. R. Fuerte-Esquivel, “A conductor temperature estimation study applied to the Mexican interconnected system”, in the process to be submitted to ***IEEE Power Engineering Letters***.

# Chapter

# 1 Introduction

## 1.1 Introduction

From the smart grid initiative viewpoint, applying advanced sensing, measurement and intelligent control devices to existing electric power systems will be necessary for supporting decisions in energy control centers (ECCs) concerned with increasing the utilization, efficiency, quality and security of the power systems. These advanced applications will transform the way in which most electric power systems (EPSs) have been operating. The estimation of the electric power network's states constitutes the main core of the on-line security analysis and other energy management system applications. Power systems state estimation is the process carried out in ECC to provide the best estimate of what is happening in the system based on real-time system measurements and a predetermined system model. A redundant set of real-time measurements are collected from the entire network through the supervisory control and data acquisition (SCADA) system and phasor measurement units (PMUs). These measurements are transmitted to the ECC and subjected to a statistical analysis in order to assess the system state. Since transmitted measurements are usually corrupted by errors, this erroneous data should be filtered to eliminate bad measurements and minimize the effect of random measurement noise. This is accomplished with the help of a supplementary function called bad data processing. If after this analysis all state variables can be estimated using the available measurements, a system is said to be observable. Once an accurate estimation has been performed, the entire system's quantities, such as branch power flows, line current magnitudes and nodal power injections, can be calculated. Even though the number of PMUs installed in practical systems has gradually increased, the transition for transforming the present transmission networks and control centers into smart infrastructures will require many years to be completed and must be carefully planned and executed. An important step forward, however, can be done in this long awaited transition if the state estimators (SEs) used to operate electric power systems are upgraded by considering the operation characteristics of the existing PMUs already installed in the network. Hence, the development of suitable strategies for upgrade state estimators is the main objective of this work to help in the transition towards smart control centers and transmission networks.

## 1.2 State of the art

### 1.2.1 Static state and parameter co-estimation

The state estimator correctness depends on the accuracy with which the transmission grid parameters are known. In this context, if the database of transmission line parameters contains erroneous values, the static state estimation (SSE) is biased from the real operation state. A critical consequence of this biased estimation is that erroneous control actions can be taken by the system operators or automatic controllers, which could jeopardize the correct operation of the power system.

Different methodologies for performing parameter estimation in EPS have been proposed in the literature, from which the simultaneous estimation of nodal voltages and network's parameters by using the weighted least squares (WLS) formulation is distinguished [Abur & Gómez Expósito, 2004; Larson, *et al*., 1970; Liu & Lim, 1995; Alsac, *et al*., 1998; London, *et al*., 2004; Zhu & Abur, 2006; Olarte & Diaz, 2008]. Alternative proposals to this approach focus on estimating the system operating state and network parameters using the sequential processing of several sets of measurements [Castillo, *et al*., 2009; Castillo, *et al*., 2011; Castillo, *et al*., 2012]. This method uses the WLS approach in which for each set of measurements nodal voltages are estimated by using a fixed set of values for transmission line parameters. A subproblem is then formulated to update the parameters of transmission lines at the end of the conventional estimation process. This sequential iterative solution approach is repeated until the difference of updated values of the estimated variables in two sequential solutions is below a specified tolerance. The main disadvantage of this sequential methodology, however, is the large number of sets of measurements required to obtain good results. Another variant of this approach is to use the Kalman filter theory, which is a minimum variance estimator that processes several sets of measurements [Debs, 1974; Slutsker, *et al*., 1996; Zhang & Larsson, 2010; Mishra, *et al*., 2015]. This approach first predicts nodal voltages and some parameters of the EPS, then the resulting values are corrected by processing each set of measurements for a sampling time in a finite period of time. A drawback of this approach is associated with the right initialization of the covariance matrix of parameter errors in order to achieve a good performance from the Kalman filter. Other methodologies focus on estimating transmission line parameters at the local level by simultaneously processing several sets of measurements [Liao, 2009; Liao & Kezunovic, 2009; Du & Liao, 2012; Davis, *et al*., 2013]. The main drawback of this formulation, however, is that only the parameters of transmission elements connected between two buses of the system can be determined. Similarly, other methodologies focus on estimating conductor temperatures, based on environmental data to which transmission lines are exposed [Bockarjova & Andersson, 2007; Rakpenthai & Uatrongjit, 2017]. Note that these methodologies require additional data that are not completely available in the current databases of control centers. Finally, there are robust methodologies that use the minimum absolute value criteria in which the estimator is not only able to reject erroneous measurements but can also estimate some network parameters [Ozdemir & Gol, 2015; Lin & Abur, 2017; Lin & Abur, 2018]. These types of methodologies, however, demand a long computing time for converging to an optimal solution, so they are not used in current control centers. Even though this drawback can be overcome by using parallel processing techniques [Donmez & Abur, 2020] and gradient-based approaches [Venkatraman, *et al*., 2019], this topic is out of the scope of this thesis.

Considering that the WLS-based SSE is the formulation currently used in energy control centers, the most convenient methodology for static state and parameter co-estimation is the simultaneous approach [Abur & Gómez Expósito, 2004; Larson, *et al*., 1970; Liu & Lim, 1995; Alsac, *et al*., 1998; London, *et al*., 2004; Zhu & Abur, 2006; Olarte & Diaz, 2008] under the on-line processing of a single set of measurements [Abur & Gómez Expósito, 2004; Larson, *et al*., 1970; Liu & Lim, 1995; Alsac, *et al*., 1998; Zhu & Abur, 2006], unlike those simultaneous approaches reported in [London, *et al*., 2004; Olarte & Diaz, 2008] that require different sets of measurements and must be applied off-line. The most important difference between different approaches for the on-line estimation of parameters and state variables consists of the type of parameters added to the original vector of state variables to be estimated. For instance, in [Larson, *et al*., 1970] and [Zhu & Abur, 2006], the admittances of transmission elements are directly used as state variables to be estimated. The normalized lengths of transmission lines are used in [Abur & Gómez Expósito, 2004] to estimate transmission lines parameters considering a π circuit model. Changes in the branch power flows associated with parameter errors are used in [Liu & Lim, 1995] to correct the series impedance value of a transmission line, but no other parameter of the π model is estimated. On the other hand, in [Alsac, *et al*., 1998] power flows of transmission lines are used as variables to be estimated in such a way that the impedances of the π circuit could be determined. Apart from the theoretical differences between the different methodologies for simultaneously estimating parameters and state variables reported above, there is a need to perform a comparative numerical study among these methods to assess which one provides the best estimates of transmission line parameters.

### 1.2.2 Static state and topology co-estimation

Static state estimation (SSE) is a fundamental tool for power system static security assessment, which is applied to a bus level network model under the assumption that the network topology provided by a network configurator is known and without any uncertainty associated with circuit breaker (CB) statuses in power substations. An incorrect network topology provokes inaccurate state estimation results due to an erroneous bus-branch model, which does not correctly represent the current connectivity of transmission elements in the grid [Abur & Gómez Expósito, 2004]. These connectivity failures are known as topology errors and can be classified as branch status errors and substation configuration errors. The second ones are associated with switching devices arrays in power substations and can be further subdivided into split and merging errors. The first occurs when two connected electric buses are modeled as two independent buses, while the second corresponds to the opposite modeling scenario. All these errors produce large deviations of estimated values of magnitudes and phase angles of nodal voltages and control actions being taken by system operators that may compromise the static security of the EPS. To overcome this problem, the SSE formulation must be enhanced to correct substations configuration errors.

Different methodologies have been proposed to cope with substation configuration errors, which are described below. Monticelli [Monticelli, 1993] extended the nonlinear WLS-based SSE to consider the status of circuit breakers (CBs). All CBs with known statuses are modeled by operational constraints and included in the SSE problem as pseudo-measurements with assigned high weights. An open breaker is represented by setting the active and reactive power flows through it to 0. In contrast, the voltage phase angle difference and the voltage drop at both ends of a circuit breaker are set to 0 to represent its closed operating condition. No operating constraints are proposed, however, for handling CBs with unknown statuses. In this case, the breaker is modeled by considering the active and reactive powers that flow through it as state variables to be estimated. A methodology to determine the unknown operating status of a CB is proposed in [Monticelli, 2000] that is based on a hypothesis testing procedure applied to a linear equality constraint. Since this constraint is not included in the formulation of the state estimation problem, the proposed testing approach is applied after estimating the operating state. A process to identify topology errors in substations is proposed in [Clements & Costa, 1998] based on a constrained WLS formulation of the state estimation problem. All CBs are assumed to have known statuses such that the pseudo-measurements proposed in [Monticelli, 1993] are incorporated into the state estimator through operational equality constraints. Once the state estimation has been obtained, the topology error identification is performed by comparing the normalized Lagrange multipliers' values associated with those constraints with respect to a proposed statistical threshold. If the assumed known status of a single circuit breaker is identified as being incorrectly reported to the state estimator, this status is changed at this post-processing stage, and the state estimation is again performed. Hence, the Lagrange multipliers's values associated with these constraints are statistically tested to determine which statuses have been incorrectly reported to the state estimator.

In [Abur, *et al*., 1995], a two-stage approach based on the minimum least absolute value (LAV) state estimation method is proposed to identify errors in CBs with assumed known statuses. In the first stage, the nodal voltages and power flows associated with CBs are estimated using a bus-level system model. The normalized residual test is then applied to all inconsistent measurements rejected by the estimator to identify suspected measurements. In the second stage, the substation associated with the bus in which the highest number of suspected measurements are incident is modeled in detail and added to the system model. Based on this updated network, a new state estimation study is performed to assess the substation topology based on the power flows through the CBs. Note that this proposal avoids modeling the entire system at the substation level.

[de la Villa Jaen & Exposito, 2001] demonstrated that considering only the power flows through CBs with unknown statuses is not a sufficient condition for estimating their correct operating statuses. The possible inaccuracy in the results is prevented by adding two equality constraints to the state estimation problem for every CB with unknown status [de la Villa Jaen & Exposito, 2001]. One of the constraints is given by the product of the active power flow and the difference of voltage phase angles at both ends of the CB, while the other is stated by the reactive power flow times the voltage drop in the CB. The enforcement of both constraints determines the operating status of the CB: closed or open. Two different approaches for identifying topological errors are reported in [Pereira, *et al*., 2001]. The method proposed in [Clements & Costa, 1998] is also used in [Pereira, *et al*., 2001], but it uses a hypothesis testing to identify topology errors based on Bayes' theorem. The other method relies on representing the unknown status of CBs by topology variables, which are added to the state estimation problem's state vector. For each topology variable, a quadratic constraint is also included in the problem formulation to ensure that its estimated value is 0 for an open CB and 1 when it is closed.

Based on the work reported in [Abur, *et al*., 1995], a LAV-based method is proposed in [Donmez, *et al*., 2019] to estimate nodal voltages and statuses of CBs simultaneously. The estimation is achieved by considering the power system bus-branch model and a detailed model of all substations making up the network. A linear estimation approach in rectangular coordinates is formulated to reduce the problem dimension of incorporating detailed substation models under the assumption that the node-breaker model is entirely observable by phasor measurement units (PMUs). The states of CBs are defined by their current flows, while the operating constraints of closed and open breakers are given by zero voltage drops and zero current flows, respectively. Even though the LAV-based estimation rejects bad data and topology errors, a statistical analysis of all CBs states is performed after the estimation process to identify which CBs had erroneous statuses.

To avoid the use of hypothesis testing for determining topology errors [Clements & Costa, 1998], a methodology relying on the application of collinearity tests between the vector of Lagrange multipliers and the covariance matrix is proposed in [Lourenco, *et al*., 2006]. This permits the identification of all CBs with an incorrectly assumed operating status from a set of CBs with a suspected operating status. The latter is obtained based on the normalized Lagrange multiplier test [Clements & Costa, 1998] considering that analog measurements are free of gross errors. In this case, all CBs are assumed to have a known status, and a state estimation is performed based on a node-breaker model. All those CBs with normalized Lagrange multiplier values larger than a specified threshold are assumed to be suspicious with an incorrect operating status. The collinearity test is then applied in two stages. The first stage ensures that all CBs with an incorrectly assumed known status are already included in the set of suspicious CBs. In the second stage, all CBs incorrectly identified with an erroneous status are removed from the suspect set to only have breakers with a wrongly assumed status. Lastly, all these statuses are changed at this post-processing stage, and the state estimation is newly performed.

The proposal of [Lourenco, *et al*., 2006] is extended in [Lourenco, *et al*., 2015] to consider the simultaneous presence of topological and multiple bad data errors in a reduced network model, which is referred to as an anomaly zone model. In this case, the suspected set of bad data and erroneous statuses of circuit breakers is obtained by sequentially applying the normalized Lagrange multiplier test and geometric test. This iterative identification process continues until the geometric test is satisfied in terms of the collinearity concept. A debugging process is applied to detect and identify each topology error from the resulting suspected set by using the geometric test. Once the erroneous statuses of circuit breakers are corrected, the state estimation is again performed, and another suspected set of errors is obtained. This sequential process is repeated until the suspected set is only composed of measurements with gross errors. At this stage of the solution process, any bad data analysis can be applied to identify erroneous measurements in order to estimate the correct operating state of the reduced network model. The main disadvantages are that the statuses' identification process is subsequently performed to the state estimation and requires several state estimation processes to identify several errors of switching devices.

An alternative approach [Vosgerau, *et al*., 2010; da Silva, *et al*., 2016] formulates a bi-objective optimization problem that merges the WLS approach and the weighted least absolute value (WLAV) criterion. The former is associated with analog measurements, while the latter reflects the statuses of circuit breakers. The proposal is applied to a detailed model of the anomaly zone: the network region where the existence of topology errors are identified. In this case, the few substations of the anomaly zone are modeled in detail; furthermore, other parts of the network could be included using the conventional bus-branch level. A DC model of the network is employed in [Vosgerau, *et al*., 2010] to reduce the computational burden, while the full nonlinear approach is adopted in [da Silva, *et al*., 2016]. These approaches require an appropriate specification of the objective function weighting parameters to achieve convergence towards the solution. The WLS residual terms are weighted in the usual manner, while the LAV terms are weighted by a scalar value heuristically obtained. The power flow through circuit breakers is added to the set of state variables to be estimated, and it is also used to determine the circuit breaker statuses through a hypothesis testing procedure reported in [Clements & Costa, 1998]. Unlike [Clements & Costa, 1998], the tests are applied to the power flow through the circuit breakers. If the absolute value of the power is greater than a threshold, the breaker is closed; otherwise, the breaker is considered open. The identifications of topology errors and bad data analysis are performed in two nested loops: inner and outer loops. The former consists of solving two mutually related problems: the state and topology co-estimation as well as the detection and correction of topology errors, respectively. These two problems are sequentially solved until correcting all topology errors. A bad data analysis of analog measurements is then performed, and the inner loop is newly executed after removing measurements with gross errors. The correct estimation of state variables and network topology is achieved when all topology errors and bad data have been properly identified.

Lastly, the co-estimation of network states and substation topology reported in [da Silva, *et al*., 2016] is performed in [Meneghetti, *et al*., 2020] by using the maximum correntropy criterion, which robustly estimates nodal voltages and power flows of circuit breakers by using a single objective function. Similar to other works, the operational constraints are related to the assumed statuses of circuit breakers, while structural conditions enforce the Kirchhoff laws in the detailed representation of circuit breakers and bus sections. All these constraints are treated as pseudo-measurements. The solution process relies on two stages: inner and outer loops. In the former, the state variables are estimated considering fixed values of variances. In the outer loop, the value or width of the kernel variance is adjusted to ensure the automatic rejection of outliers. Suppose the residual of the $k$-th operational constraint, which is considered as a pseudo-measurement, is greater than the corresponding kernel variance. In that case, the measurement is tagged as a potential outlier, and the kernel variance value is reduced to eliminate the effect of this measurement on the objective function. Once all suspected measurements are obtained, a hypothesis testing procedure similar to the one reported in [da Silva, *et al.*, 2016] is performed to assess the correct statuses of circuit breakers associated with those suspected measurements. Lastly, before applying the procedure mentioned above, referred to as the information theoretic generalized state estimation, a conventional state estimation is performed in which all bad data associated with analog measurements are eliminated by using the LNR test.

Keeping in mind that the WLS-based state estimation formulation is the one currently used in control centers, this work proposes a new, different and general approach to simultaneously estimate nodal voltages and the current statuses of all circuit breakers at power substations explicitly incorporated in the electric power system.

### 1.2.3 Static state and temperature co-estimation

One important source of errors during the state estimation process is associated with the database of network parameters, which is one of the most challenging problems to be identified because those parameters are supposed to be known and error-free. In this context, as shown in [Bockarjova & Andersson, 2007], the series resistance parameter of overhead transmission lines is dependent on conductive material properties, the current flow through the line, the surface conditions, and the environmental conditions to which the lines are exposed. These factors can affect the series resistance found in electric companies databases, which in turn biases the state estimation results and degrades the reliability and accuracy of all analyses and applications by conducting at a post-estimation stage. This problem can be overcome by estimating nodal voltages and some network parameters, for instance, the series resistance of transmission lines. In [Rakpenthai & Uatrongjit, 2017], it is proposed to estimate the overhead line conductors temperature using a three-phase estimator and environmental data to which the system lines are exposed. On the other hand, a formulation of the temperature-dependent power flow of overhead conductors is proposed in [Frank, *et al.*, 2013], based on the information of transmission line ratings and data about the material of lines, which is available information in control centers. Therefore, the temperature-dependent equations of [Frank, *et al*., 2013] can be used in the SSE formulation to estimate transmission lines temperatures and correct series resistance parameter values of transmission lines. This novel idea is mathematically developed and implemented for the first time to formulate the static state estimation problem.

### 1.2.4 Transient stability considering hard limits in dynamic states

Currently EPSs operate under more stressful conditions because of the need to increase the power transfer capability of existing transmission lines at the lowest possible cost. These operating conditions make a power system more vulnerable to large disturbances because of the likelihood of losing stability increases, making the transient stability problem a major concern for system operators. In this situation, the modeling of hard limits of control devices is of the utmost importance because a constrained state variable may reach one of its limits during the system transient evolution, which can have a significant influence on the overall system behavior.

The inclusion of hard limits of control devices in a transient stability program is generally performed by using conditional tests, which are the guiding principle for conducting limit revisions [Milano, 2010]. This approach has been recently applied for incorporating VSC-based energy storage systems [Ortega & Milano, 2016] and multi-terminal high-voltage direct current converters [Moawwad, *et al*., 2018] in transient stability studies. In this method, the hard limits are checked at each time step of the time-domain simulation, and if one limit of a non-windup controller is reached at a given time step, the controller's differential equation is replaced by an algebraic equation to maintain the state variable at the limit value. In this case, the solution process must be reinitialized from that time step because of the change in the system dynamic structure. The hard limits have also been represented by using saturation functions [Pico, *et al*., 2017], where some parameters of these functions must have to be adjusted to properly approximate the limiters. A different approach to directly include hard limits of controllers in transient stability studies is proposed in this research based on complementarity constraints. Note that this approach has not been previously proposed.

### 1.2.5 Dynamic state estimation

The control and operation of power systems are experiencing an increasing complexity because of the high penetration of converter-based nonsynchronous generation and controllers, which results in stochastic behaviors and nonlinear dynamics for which the power system did not plan [Zhao, *et al*., 2019; Zhao, *et al*., 2020]. Within this context, accurate real-time estimates of nodal voltages and dynamic state variables are essential for the reliable operation of electric power systems, which must tend to a foresighted operation instead of the current reacting operation.

Using SCADA, measurements with sampling rates and communication delays in the order of seconds have been employed to track the quasi-state evolution of nodal voltages in power systems [Chen, *et al*., 2014]. A tracking state estimator suitable for assessing how the nodal voltages evolve in time based on the processing of both synchronized phasor and SCADA measurements according to as and when they are received in the control center is also proposed in [Alcaide-Moreno, *et al*., 2018].

The continuous capture of the system dynamic responses at fast sampling rates under normal and abnormal operating conditions has been possible through the availability of PMUs and advanced computing technologies. This has allowed the development of several types of dynamic state estimation (DSE) methods to estimate and continuously track dynamic state variables associated with synchronous machines and their corresponding controller units using PMUs' measurements and the dynamic models of those devices.

Several methodologies have been proposed for DSE in which the predominant formulation is the nonlinear Kalman filter theory. The Kalman-based estimator is a minimal variance estimator that estimates dynamic variables from PMU measurements [Singh & Pal, 2019]. Initially, the filter performs a prediction stage in which state variables are predicted from a mathematical model that describes the components involved in the dynamic process. A correction stage is then conducted in which the processing of PMU measurements improves the predicted values of state variables. There are different variants of the nonlinear Kalman filter to perform DSE, which are outlined and compared in [Zhou, *et al*., 2015; Liu, *et al*., 2020]. The extended Kalman filter (EKF) linearizes the dynamic process nonlinear functions and measurement equations for performing the prediction and correction stages. The unscented Kalman filter (UKF) seeks to approximate the assumed Gaussian probability density functions of the prediction and correction stages from a small set of samples called sigma points obtained in a deterministic manner. The ensemble Kalman filter (EnKF) also approximates Gaussian probability density functions from many samples called ensembles; it is calculated with a Monte Carlo approach. The cubature Kalman filter (CKF) matches Gaussian probability density functions from a set of cubature points. This set of points is obtained from a spherical-radial rule approach. Finally, the particle Kalman filter (PKF) seeks to approximate the probability density functions of the prediction and correction stages that do not follow a Gaussian distribution. Robust versions of the Kalman filter have also been proposed in which the following are outstanding: Robust iterated extended Kalman filter (RIEKF) [Zhao, *et al*., 2017; Zhao, *et al*., 2017], robust unscented Kalman filter (RUKF) [Zhao & Mili, 2019], h-infinite extended Kalman filter (HIEKF) [Zhao J. , 2018], h-infinite unscented Kalman filter (HIUKF) [Zhao & Mili, 2019], constrained robust unscented Kalman filter (CRUKF) [Zhao, *et al*., 2019] and adaptative unscented Kalman filter for systems with unknown inputs (AUKF-UI) [Zhao, *et al*., 2020]. The RIEKF and RUKF are robust against outliers present in the process and measurements. Furthermore, these estimators simultaneously process both predictions and observations from a generalized maximum probability estimator in which outliers are attenuated from a process called statistical projection. The HIEKF and HIUKF are robust against outliers present in the process, measurements and dynamic model parameters. The main difference between these estimators relies on the manner of making the prediction stage: while RIEKF and HIEKF use the EKF prediction stage, RUKF and HIUKF perform the prediction stage from sigma points. The CRUKF extends the capabilities of the RUKF and addresses inequality constraints on dynamic states, control inputs and parameters from a proposed project operator, which brings the sigma points that exceed their specified limits to the boundaries of the feasible region. By the same line of reasoning, AUKF-UI is robust because it handles bad data in the process, measurements and unknown inputs to synchronous machines by applying the statistical projection process to a generalized maximum probability estimator. This approach additionally includes cross-correlations between unknown inputs and dynamic states. Recently, the p-norm square root unscented Kalman filter was proposed in [Wang, *et al*., 2020], which adds a p-norm term to the UKF's objective function. Sigma points are generated by using the square root of the estimation error covariance to handle outliers in measurements. Lastly, the artificial neural networks theory is applied in [Tian, *et al*., 2020] to estimate rotor angles and angular speeds of synchronous machines from phasor measurements of nodal voltages.

Despite the appropriate performance of all DSE formulations mentioned above, their most significant drawback is that all of them estimate dynamic variables locally in generation buses, disregarding algebraic variables associated with the transmission system. The local estimation of dynamic variables provides a tool to supervise rotor angle instabilities of synchronous machines. Note, however, that it is impossible to know if nodal voltages are within operational limits or if power flows in transmission lines do not exceed their nominal ratings. Another open area of research is the treatment of inequality constraints in dynamic states. Even though [Zhao, *et al*., 2019] applies constraints to dynamic variables of synchronous machines in the RUKF approach, it does not present cases when non-windup and windup limiters set dynamic variables in their physical limits from the state estimation framework. Consequently, it is essential to develop a new generalized formulation that incorporates both the transmission system algebraic variables and the treatment of controller's limiters. Note that such an estimator has not been previously proposed.

## 1.3 Justification

Power system state estimation plays a core part in the operation and control of electric power systems in terms of providing accurate information of the power system operation state, which is used to perform security assessment studies in a reliable way.

Currently, electric power systems are experiencing unprecedented operational complexity because of the increasing use of nonsynchronous generators with random natural behavior, the necessity of performing wide area monitoring and control, the integration of synchronized measurement units with SCADA systems, and the aging of electric components forming the transmission grid.

Based on the information mentioned above, the state estimators on which power engineers rely to make real-time operation and control decisions must be upgraded to fit the actual and future operating scenarios of power systems. Hence, new proposals to formulate static and dynamic state estimators are presented in this thesis, which are expected to help in the transition from a reacting system operation to a farsighted system operation.

## 1.4 Objective

The main objective of this thesis is to develop innovative formulations for the static co-estimation of nodal voltages, parameters of transmission lines, statuses of circuit breakers and operating temperatures of transmission lines as well as for the dynamic co-estimation of nodal voltages and dynamic states of synchronous machines and their controllers.

To achieve this objective, the following goals must be achieved:

- To develop a new set of operating constraints to simultaneously estimate nodal voltages and unknown operating statuses of circuit breakers in a unified framework of analysis.
- To include the temperature dependence of transmission lines' parameters in the static state estimation formulation through a set of equality constraints that relates the temperature at which a transmission line is exposed with its corresponding active power losses.
- To apply the complementarity theory for directly including the inequality constraints of non-windup and windup limiters in the transient stability problem's formulation and solution.
- To formulate and implement a wide area dynamic state estimator to track the system's dynamic and algebraic states in a structure-preserving framework of analysis.

## 1.5 Main contributions

The main contributions of this thesis are listed as follows.

- A new and general methodology that simultaneously estimates the system operating state and the current statuses of all circuit breakers at power substations is proposed.
- A new state estimation methodology capable of estimating transmission line temperatures from a hybrid set of SCADA and PMU measurements is proposed.

- A fundamentally different, comprehensive and general approach for directly including hard limits of controllers in the formulation and solution of the transient stability problem is proposed.
- A new wide area dynamic state estimation (WADSE) methodology that is capable of simultaneously estimating algebraic variables of system nodal voltages, as well as dynamic variables of synchronous machines and their controls, is proposed.

## 1.6 Methodology

The methodology that has been adopted in this thesis is described as:

- A full review of previous works in the co-estimation of static nodal voltages and transmission line parameters, operating status of circuit breakers, and temperatures at which transmission lines are subjected. A survey is also done to study transient stability considering hard limits on dynamic states and dynamic state estimation.
- The implementation of the following power flow programs: conventional power flows, power flows that includes explicitly modeled power substations [Lourenco, *et al*., 2010], temperature-dependent power flows [Frank, *et al*., 2013] and transient stability considering hard limits on dynamic states [Romay, *et al*., 2021]. These programs are used to build ideal measurement sets to which random noise is added to perform static and dynamic state estimation studies.
- To perform a comparative study of state and parameter co-estimation methodologies already proposed in the literature to assess the proposal that provides the best parameter estimations of transmission lines from a hybrid set SCADA and PMU measurements.
- To develop a new complementarity-based operational constraint for unknown statuses of circuit breakers. This constraint is incorporated in the formulation of the WLS-based static state estimation problem for the co-estimation of nodal voltages and the unknown statuses of switching devices.
- To add temperature-dependent constraints associated with active power flow losses in the static state estimation formulation to estimate series resistance values of transmission lines.

- To develop a complementarity-based unified framework of analysis for the transient stability problem, where hard limits of controllers are simultaneously and automatically checked and, when applicable, enforced during the transient stability solution process.
- To formulate a new complementarity-based wide area dynamic state estimation by including the set of differential-algebraic equations associated with synchronous machines and their controllers in the tracking state estimation problem.
- To test the proposed approaches considering electric power systems of different sizes and topological structures.

## 1.7 Thesis outline

This thesis is organized as follows.

**Chapter 2** presents a generalized static state estimation methodology to determine the system operating state and identify the parameters and operating statuses of electrical components. First, a comparative study of three state and parameter co-estimation methods based on a hybrid set of SCADA and PMU measurements is presented. Next, a new complementarity approach is proposed for co-estimating nodal voltages and unknown statuses of circuit breakers using a set of measurements provided by a SCADA system. The proposal effectiveness is numerically demonstrated considering different substations' configurations and several unknown switching devices' statuses. Lastly, a new methodology for state and temperature co-estimation based on a hybrid set of SCADA and PMU measurements is detailed.

**Chapter 3** presents a new way of including hard limits associated with control devices in the formulation of the transient stability problem. First, the dynamic modeling of power systems with constrained states is described, and the operation of non-windup and windup limiters is explained through *if*-based conditional tests. Secondly, the new representation of hard limits based on the complementarity theory is detailed. Subsequently, a complementarity-based formulation of the transient stability problem is proposed to treat hard limits in dynamic states. Finally, the effectiveness of the proposal for preventing the controllers' dynamic states from exceeding specified limits is numerically demonstrated.

**Chapter 4** presents a new generalized approach for the wide area dynamic state estimation of power systems by only processing PMU measurements. Firstly, the conventional formulation of dynamic state estimation from the unscented Kalman filter is described. Secondly, the modeling of a synchronous machine and its controls are presented. Thirdly, the tracking state estimation problem is detailed and extended by including the constraint-based dynamic equations associated with synchronous machines and their controllers, which results in the WADSE approach. Finally, the effectiveness of the WADSE approach is numerically demonstrated and validated.

**Chapter 5** reports the general conclusions of the research topics presented in previous chapters and recommendations for future research work are given.

# Chapter

# 2 Generalized static state estimation

## 2.1 Introduction

This chapter focuses on presenting a generalized formulation of the static state estimation problem at the transmission level based on the weighted least squares approach with equality constraints. This generalized approach is capable of estimating nodal algebraic state variables together with other quantities of interest such as parameters of transmission lines, circuit breaker statuses and conductor temperatures of transmission lines. Within this context, three main specific contributions are presented as follows. Firstly, a comparative study of three methodologies for estimating transmission lines parameters together with nodal voltage state variables at the system level is reported. Secondly, two new operational constraints are proposed to model circuit breakers with unknown statuses in electric substations. These new constraints are included in the static state estimation optimization problem by using complementarity constraints. Lastly, a set of equality constraints that relate line temperatures with active power losses is added to the static state estimation problem to estimate operating temperatures of transmission lines.

## 2.2 Conventional formulation of the static estimation problem

The process of determining the value of a set of algebraic state variables of an electric power system from a given set of physical measurements in a given time instant is referred to as static state estimation [Abur & Gómez Expósito, 2004]. The conventional formulation of this problem considers that an electric power system is composed of a set of buses $\mathcal{N}_e := \{1, 2, \ldots, N_e\}$ interconnected through a set of transmission elements $\mathcal{T}_e := \left\{1, 2, \ldots, N_{\mathcal{T}_e}\right\}$. Additionally, the algebraic state variables to be estimated correspond to the values of magnitudes and phase angles of nodal voltages. These variables are grouped in the vectors $\boldsymbol{V}=\left[V_1\cdots V_{N_e}\right]^{\mathrm{T}}\in\mathbb{R}^{N_e}$ and ,$\boldsymbol{\theta}=\left[\theta_1\cdots\theta_{N_e}\right]^{\mathrm{T}}\in\mathbb{R}^{N_e}$, respectively, and in turn these vectors are grouped in a single vector denoted by

$$\boldsymbol{x_e}=\left[\boldsymbol{V}\quad\boldsymbol{\theta}\right]^{\mathrm{T}}\in\mathbb{R}^{2N_e}. \tag{2.1}$$

On the other hand, the set of physical measurements of electrical variables are obtained from the subsets of observable buses $\mathcal{N}_{oe}:=\{1,2,\ldots,N_{oe}\}\ni\mathcal{N}_{oe}\subset\mathcal{N}_e$ and observable transmission elements $\mathcal{T}_{oe}:=\left\{1,2,\ldots,N_{\mathcal{T}_{oe}}\right\}\ni\mathcal{T}_{oe}\subset\mathcal{T}_e$, respectively (where $\ni$ means such that). The measurements provided by a SCADA correspond to nodal voltage magnitudes: $\boldsymbol{V_k^{SCADA}}$, nodal injections of the active and reactive powers $\boldsymbol{P_k^{SCADA}}$ and $\boldsymbol{Q_k^{SCADA}}$, respectively, and the branch active and reactive power flows $\boldsymbol{P_{km}^{SCADA}}$ and $\boldsymbol{Q_{km}^{SCADA}}$, respectively. All these SCADA measurements are grouped in the vector $\boldsymbol{z_e^{SCADA}}\in\mathbb{R}^{M_e^{SCADA}}$:

$$\boldsymbol{z_e^{SCADA}}=\left[\{V_k^{SCADA}\}_{k\in\mathcal{N}_{oe}}\;\{P_k^{SCADA}\}_{k\in\mathcal{N}_{oe}}\;\{Q_k^{SCADA}\}_{k\in\mathcal{N}_{oe}}\;\{P_{km}^{SCADA}\}_{(km)\in\mathcal{T}_{oe}}\;\{Q_{km}^{SCADA}\}_{(km)\in\mathcal{T}_{oe}}\right]^{\mathrm{T}}. \tag{2.2}$$

Similarly, the measurements provided by PMU devices correspond to nodal voltage magnitudes $\boldsymbol{V_k^{PMU}}$, nodal phase angles $\boldsymbol{\theta_k^{PMU}}$, branch current magnitudes $\boldsymbol{I_{km}^{PMU}}$ and phase angles of branch currents $\boldsymbol{\theta_{I_{km}}^{PMU}}$. All these PMU measurements are grouped in the vector $\boldsymbol{z_e^{PMU}}\in\mathbb{R}^{M_e^{PMU}}$:

$$\boldsymbol{z_e^{PMU}}=\left[\{V_k^{PMU}\}_{k\in\mathcal{N}_{oe}}\;\{\theta_k^{PMU}\}_{k\in\mathcal{N}_{oe}}\;\{I_{km}^{PMU}\}_{(km)\in\mathcal{T}_{oe}}\;\{\theta_{I_{km}}^{PMU}\}_{(km)\in\mathcal{T}_{oe}}\right]^{\mathrm{T}}. \tag{2.3}$$

The total set of measurements in the power grid is represented by the vector $\boldsymbol{z}=\left[\boldsymbol{z_e^{SCADA}}\quad\boldsymbol{z_e^{PMU}}\right]^{\mathrm{T}}\in\mathbb{R}^M$ that commonly contains random errors. Hence, the mathematical representation of these physical measurements is through the nonlinear model:

$$\boldsymbol{z}=\hat{\boldsymbol{z}}(\boldsymbol{x_e})+\boldsymbol{\varepsilon}, \tag{2.4}$$

where $\hat{\boldsymbol{z}}(\boldsymbol{x_e}):\mathbb{R}^{2N_e}\to\mathbb{R}^M$ is a vector of nonlinear functions commonly referred to as the vector of estimated measurements, which mathematically relate the values of physical measurements $\boldsymbol{z}$ to the estimated values of algebraic variables $\boldsymbol{x}_e$. Furthermore, $\boldsymbol{\varepsilon} \in \mathbb{R}^M$ is the vector of uncorrelated measurement errors with a Gaussian probability distribution and zero mean.

Based on the information mentioned above, the static state estimation problem is formulated in this work as an equality constrained-based optimization problem: the minimization of the sum of the weighted squares of the differences between each physical measurement and its corresponding estimated measurement. Hence, the weighted least squares with equality constraints (WLS-EC) is mathematically expressed as

$$\begin{aligned} \underset{\boldsymbol{x}_e, \boldsymbol{r}}{\arg\min} \quad & \boldsymbol{J}(\boldsymbol{r}) = \frac{1}{2}\boldsymbol{r}^{\mathrm{T}}\boldsymbol{W}\boldsymbol{r} \\ \text{subject to:} \quad & \boldsymbol{c}(\boldsymbol{x}_e) = \boldsymbol{0} \\ & \boldsymbol{r} - \boldsymbol{z} + \hat{\boldsymbol{z}}(\boldsymbol{x}_e) = \boldsymbol{0}, \end{aligned} \tag{2.5}$$

where $\boldsymbol{J}(\boldsymbol{r}): \mathbb{R}^M \rightarrow \mathbb{R}$ is the objective function from the WLS approach and $\{r_i\}_{i=1}^{M}$ is the vector of measurements residuals, which are considered as explicit decision variables together with the components of vector $\boldsymbol{x}_e$. The residuals are weighted by the diagonal matrix $\boldsymbol{W} = \operatorname{diag}\left\{1/\sigma_i^2\right\}_{i=1}^{M}$, where $\{\sigma_i\}_{i=1}^{M}$ is the *i*-th standard deviation that reflects the *i*-th meter's level of accuracy. Furthermore, the estimated measurements of active $\{\hat{P}_k\}_{k\in\mathcal{N}_{tbe}}$ and reactive $\{\hat{Q}_k\}_{k\in\mathcal{N}_{tbe}}$ power injections must be equal to 0 at transition buses $\mathcal{N}_{tbe} := \{1, 2, \ldots, N_{tbe}\}$, as reported in Eqs. (C.5) and (C.6) of Appendix C, such that $\mathcal{N}_{tbe} \subseteq \mathcal{N}_{oe}$. Hence, these zero injection measurements are grouped in the vector of equality constraints $\boldsymbol{c}(\boldsymbol{x}_e): \mathbb{R}^{2N_e} \rightarrow \mathbb{R}^{2N_{tbe}}$.

## 2.3 Complementarity constraints

Let $\boldsymbol{a} \in \mathbb{R}^n$ and $\boldsymbol{b} \in \mathbb{R}^n$ be a pair of real vectors; the complementarity condition [Rosehart, *et al.*, 2005] must then satisfy the linear complementarity problem (2.6). This problem is referred to as a strict complementarity condition when $\boldsymbol{a} = \boldsymbol{0}$ and $\boldsymbol{b} \neq \boldsymbol{0}$ or when $\boldsymbol{a} \neq \boldsymbol{0}$ and $\boldsymbol{b} = \boldsymbol{0}$; otherwise, it is a non-strict complementarity condition, i.e., $\boldsymbol{a} = \boldsymbol{0}$ and $\boldsymbol{b} = \boldsymbol{0}$

$$a_i \geq 0 \quad b_i \geq 0 \quad a_i b_i = 0 \quad \forall i = 1,\ldots,n \,. \tag{2.6}$$

Generally, the complement operator "$\perp$" as well as inequality operators are jointly used to simplify the notation of complementarity conditions, so Eq. (2.6) equals $0 \leq \boldsymbol{a} \perp \boldsymbol{b} \geq 0$. By the same line of reasoning, let $\boldsymbol{h}(\boldsymbol{x}) : \mathbb{R}^n \to \mathbb{R}^n$ and $\boldsymbol{w}(\boldsymbol{x}) : \mathbb{R}^n \to \mathbb{R}^n$ be two nonlinear functions; the complementarity condition is then expressed as a nonlinear complementarity problem given by

$$h_i(\boldsymbol{x}) \geq 0 \quad w_i(\boldsymbol{x}) \geq 0 \quad h_i(\boldsymbol{x}) w_i(\boldsymbol{x}) = 0 \quad \forall i = 1,\ldots,n \,. \tag{2.7}$$

The complementarity conditions denoted by (2.6) and (2.7) can be transformed into the equality constraints (2.8) and (2.9), respectively, by using the Fischer-Burmeister merit function [Fischer, 1992], where the square root terms consider the positive square roots:

$$\varphi_i\left(a_i, b_i\right) = \sqrt{a_i^2 + b_i^2} - a_i - b_i = 0 \quad \forall i \;=\; 1,\ldots,n \,, \tag{2.8}$$

$$\varphi_i\left(h_i(\boldsymbol{x}), w_i(\boldsymbol{x})\right) = \sqrt{h_i^2(\boldsymbol{x}) + w_i^2(\boldsymbol{x})} - h_i(\boldsymbol{x}) - w_i(\boldsymbol{x}) = 0 \quad \forall i \;=\; 1,\ldots,n \,. \tag{2.9}$$

The key idea of this thesis is to incorporate the equality constraints provided by Fischer's function in the context of the proposed generalized static and dynamic state estimators.

## 2.4 Static state and parameter co-estimation

The co-estimation of states and parameters consists of simultaneously estimating the operating condition of an electric power system and the values of some transmission lines' parameters making up the database. The most important difference between different approaches to achieve this co-estimation consists of the type of parameters added to the original vector $\boldsymbol{x}_e$ given by (2.1). The mathematical formulations of three different methodologies are described in the following sections, considering that there is a set of transmission lines $\mathcal{T}_{eb} := \left\{1, 2, \ldots, N_{\mathcal{T}_{eb}}\right\} \ni \mathcal{T}_{eb} \subseteq \mathcal{T}_e$ with doubtful parameters that must be estimated: series conductance $\{g_{sekm}\}_{(sekm) \in \mathcal{T}_{eb}}$, series susceptance $\{b_{sekm}\}_{(sekm) \in \mathcal{T}_{eb}}$ and shunt susceptance $\{b_{shkm}\}_{(shkm) \in \mathcal{T}_{eb}}$.

### 2.4.1 Methodology 1: Estimation of conventional parameters of transmission lines

In this methodology, the magnitudes and phase angles of nodal voltages are simultaneously estimated together with the parameters of $N_{\mathcal{T}_{eb}}$ suspected transmission lines [Larson, *et al.*, 1970]. Therefore, the augmented vector of algebraic state variables is given by (2.10), where $\boldsymbol{V} \in \mathbb{R}^{N_e}$, $\boldsymbol{\theta} \in \mathbb{R}^{N_e}$, $\boldsymbol{g_{sekm}} \in \mathbb{R}^{N_{\mathcal{T}_{eb}}}$, $\boldsymbol{b_{sekm}} \in \mathbb{R}^{N_{\mathcal{T}_{eb}}}$ and $\boldsymbol{b_{shkm}} \in \mathbb{R}^{N_{\mathcal{T}_{eb}}}$:

$$\boldsymbol{x_{e\text{-}eb}} = \begin{bmatrix} \boldsymbol{V} & \boldsymbol{\theta} & \boldsymbol{g_{sekm}} & \boldsymbol{b_{sekm}} & \boldsymbol{b_{shkm}} \end{bmatrix}^{\mathrm{T}} \in \mathbb{R}^{2N_e + 3N_{\mathcal{T}_{eb}}}. \tag{2.10}$$

The optimization problem to be solved is represented by (2.11), where the measurement's vector of zero injections at transition buses is $\boldsymbol{c}(\boldsymbol{x_{e\text{-}eb}}) : \mathbb{R}^{2N_e + 3N_{\mathcal{T}_{eb}}} \to \mathbb{R}^{2N_{tbe}}$ $\{\hat{P}_k\}_{k \in \mathcal{N}_{tbe}}$ $\{\hat{Q}_k\}_{k \in \mathcal{N}_{tbe}}$ $\mathcal{N}_{tbe} := \{1, 2, \ldots, N_{tbe}\}$ (see Eqs. (C.5) and (C.6)), and $\hat{\boldsymbol{z}}(\boldsymbol{x_{e\text{-}eb}}) : \mathbb{R}^{2N_e + 3N_{\mathcal{T}_{eb}}} \to \mathbb{R}^M$ represents the vector of estimated measurements:

$$\begin{aligned} \underset{\boldsymbol{x_{e\text{-}eb}}, \boldsymbol{r}}{\arg\min} \quad & \boldsymbol{J}(\boldsymbol{r}) = \frac{1}{2} \boldsymbol{r}^{\mathrm{T}} \boldsymbol{W} \boldsymbol{r} \\ \text{subject to:} \quad & \boldsymbol{c}(\boldsymbol{x_{e\text{-}eb}}) = \boldsymbol{0} \\ & \boldsymbol{r} - \boldsymbol{z} + \hat{\boldsymbol{z}}(\boldsymbol{x_{e\text{-}eb}}) = \boldsymbol{0}. \end{aligned} \tag{2.11}$$

### 2.4.2 Methodology 2: Estimation of normalized lengths of transmission lines

The main goal of this methodology reported in [Abur & Gómez Expósito, 2004] is the estimation of the normalized lengths of transmission lines $\{L_{N,i}\}_{i=1}^{N_{\mathcal{T}_{eb}}}$, defined as the ratio between original lengths $\{L_{org,i}\}_{i=1}^{N_{\mathcal{T}_{eb}}}$, which are obtained from the system database, and real lengths $\{L_{real,i}\}_{i=1}^{N_{\mathcal{T}_{eb}}}$, which are the actual lengths due to either system operating conditions or aging conditions:

$$L_{N,i} = \frac{L_{org,i}}{L_{real,i}} \qquad \forall\, i = 1, \ldots, N_{\mathcal{T}_{eb}}, \tag{2.12}$$

where $N_{\mathcal{T}_{eb}}$ is the number of transmission lines with parameters that are to be estimated.

Note from (2.12) that the normalized length is equal to 1 if and only if the real length is equal to the original length. Since a variation in the real length affects the normalized length, it is reasonable to consider the normalized length as a state variable. Hence, the state variables to be estimated by this formulation are magnitudes and phase angles of nodal voltages together with normalized lengths of transmission lines with parameters that are suspected of being erroneous. Hence, the augmented state vector is represented by

$$\boldsymbol{x}_{\boldsymbol{e\text{-}eb}} = \begin{bmatrix} \boldsymbol{V} & \boldsymbol{\theta} & \boldsymbol{L_N} \end{bmatrix}^{\mathrm{T}} \in \mathbb{R}^{2N_e + N_{\mathcal{T}_{eb}}}, \tag{2.13}$$

where $\boldsymbol{V} \in \mathbb{R}^{N_e}$, $\boldsymbol{\theta} \in \mathbb{R}^{N_e}$ and $\boldsymbol{L_N} \in \mathbb{R}^{N_{\mathcal{T}_{eb}}}$ is the normalized length's vector.

The optimization problem to be solved by methodology 2 is the one given by (2.11). The main difference between methodology 1 and methodology 2, however, corresponds to the set of decision variables for the optimization problem. Once the parameters and nodal voltages have been estimated, the series and shunt parameters of the $i$-th transmission line are calculated using the estimated normalized length [Romay, *et al.*, 2019]:

$$\hat{g}_{sekm,i} = \frac{g^{err}_{sekm,i}}{\hat{L}_{N,i}} \quad \forall i = 1, \ldots, N_{\mathcal{T}_{eb}}, \tag{2.14}$$

$$\hat{b}_{sekm,i} = \frac{b^{err}_{sekm,i}}{\hat{L}_{N,i}} \quad \forall i = 1, \ldots, N_{\mathcal{T}_{eb}}, \tag{2.15}$$

$$\hat{b}_{shkm,i} = b^{err}_{shkm,i} \hat{L}_{N,i} \quad \forall i = 1, \ldots, N_{\mathcal{T}_{eb}}, \tag{2.16}$$

where $\{\hat{g}_{sekm,i}\}_{i=1}^{N_{\mathcal{T}_{eb}}}$ and $\{g^{err}_{sekm,i}\}_{i=1}^{N_{\mathcal{T}_{eb}}}$ (resp. $\{\hat{b}_{sekm,i}\}_{i=1}^{N_{\mathcal{T}_{eb}}}$ and $\{b^{err}_{sekm,i}\}_{i=1}^{N_{\mathcal{T}_{eb}}}$) are the calculated and erroneous series conductance (resp. susceptance), respectively, while $\{\hat{b}_{shkm,i}\}_{i=1}^{N_{\mathcal{T}_{eb}}}$ and $\{b^{err}_{shkm,i}\}_{i=1}^{N_{\mathcal{T}_{eb}}}$ are the calculated and erroneous shunt susceptance, respectively.

### 2.4.3 Methodology 3: Estimation of transmission lines power flows

This methodology simultaneously estimates nodal voltage magnitudes, phase angles and power flows through transmission elements with parameters that are unknown [Alsac, *et al.*, 1998]. The circuit model used for representing unknown transmission elements is shown in Fig. 2.1, while the vector of variables to be estimated in this model is given by:

$$\boldsymbol{x}_{\boldsymbol{e\text{-}eb}} = \left[\boldsymbol{V} \quad \boldsymbol{\theta} \quad \boldsymbol{P}_{\boldsymbol{st}} \quad \boldsymbol{Q}_{\boldsymbol{st}} \quad \boldsymbol{P}_{\boldsymbol{ss}} \quad \boldsymbol{Q}_{\boldsymbol{ss}} \quad \boldsymbol{P}_{\boldsymbol{ts}} \quad \boldsymbol{Q}_{\boldsymbol{ts}} \quad \boldsymbol{P}_{\boldsymbol{tt}} \quad \boldsymbol{Q}_{\boldsymbol{tt}}\right]^{\mathrm{T}} \in \mathbb{R}^{2N_e + 8N_{\mathcal{T}_{eb}}} . \qquad (2.17)$$

By considering the $i$-th unknown transmission line, $\{V_{ebk,i}\}_{i=1}^{N_{\mathcal{T}_{eb}}}$ and $\{\theta_{ebk,i}\}_{i=1}^{N_{\mathcal{T}_{eb}}}$ (resp. $\{V_{ebm,i}\}_{i=1}^{N_{\mathcal{T}_{eb}}}$ and $\{\theta_{ebm,i}\}_{i=1}^{N_{\mathcal{T}_{eb}}}$ ) are voltage magnitude and phase angle at sending bus $k$ (resp. at receiving bus $m$), respectively. Furthermore, $\{P_{st,i}\}_{i=1}^{N_{\mathcal{T}_{eb}}}$ and $\{Q_{st,i}\}_{i=1}^{N_{\mathcal{T}_{eb}}}$ (resp. $\{P_{ts,i}\}_{i=1}^{N_{\mathcal{T}_{eb}}}$ and $\{Q_{ts,i}\}_{i=1}^{N_{\mathcal{T}_{eb}}}$ ) are the active and reactive power flows from internal node $s$ to internal node $t$ (resp. from internal node $t$ to internal node $s$), respectively. Lastly, $\{P_{ss,i}\}_{i=1}^{N_{\mathcal{T}_{eb}}}$ (resp. $\{P_{tt,i}\}_{i=1}^{N_{\mathcal{T}_{eb}}}$ ) and $\{Q_{ss,i}\}_{i=1}^{N_{\mathcal{T}_{eb}}}$ (resp. $\{Q_{tt,i}\}_{i=1}^{N_{\mathcal{T}_{eb}}}$ ) are the active and reactive power flows through the shunt branches connected at the internal node $s$ (resp. $t$), respectively.

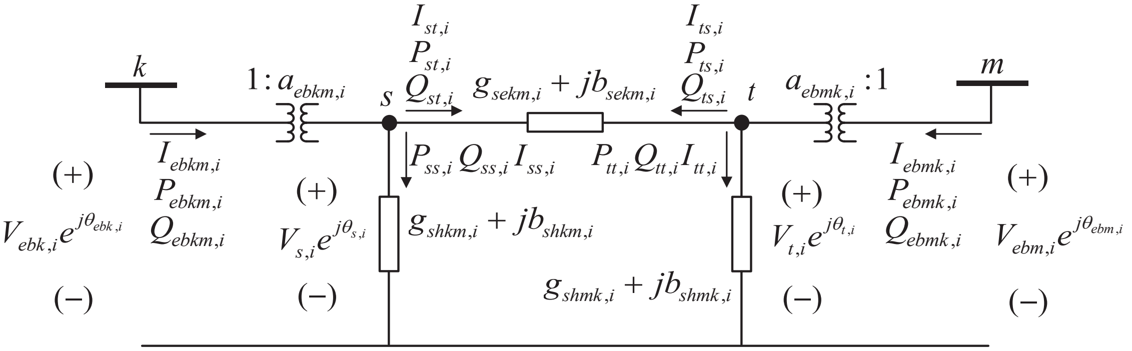

Fig. 2.1 Unified branch model representing the $i$-th transmission element.

Mathematical equations relating the series and shunt parameters to power flowing through the π circuit representing the $i$-th transmission line are obtained from Fig. 2.1. The operating conditions based on the branch currents injected at the internal buses are given by [Romay, *et al.*, 2019]

$$\begin{aligned}\mathrm{Re}\left[I_{st,i}+I_{ts,i}\right]=&\frac{P_{st,i}}{a_{ebkm,i}\,V_{ebk,i}}\cos\left(\theta_{ebk,i}\right)+\frac{Q_{st,i}}{a_{ebkm,i}\,V_{ebk,i}}\sin\left(\theta_{ebk,i}\right)\\&+\frac{P_{ts,i}}{a_{ebmk,i}\,V_{ebk,i}}\cos\left(\theta_{ebm,i}\right)+\frac{Q_{ts,i}}{a_{ebmk,i}\,V_{ebk,i}}\sin\left(\theta_{ebm,i}\right)=0\end{aligned}\qquad\forall i=1,\ldots,N_{\mathcal{T}_{eb}}\,, \tag{2.18}$$

$$\begin{aligned}\mathrm{Im}\left[I_{st,i}+I_{ts,i}\right]=&\frac{P_{st,i}}{a_{ebkm,i}V_{ebk,i}}\sin\left(\theta_{ebk,i}\right)-\frac{Q_{st,i}}{a_{ebkm,i}V_{ebk,i}}\cos\left(\theta_{ebk,i}\right)\\&+\frac{P_{ts,i}}{a_{ebmk,i}V_{ebm,i}}\sin\left(\theta_{ebm,i}\right)-\frac{Q_{ts,i}}{a_{ebmk,i}V_{ebm,i}}\cos\left(\theta_{ebm,i}\right)=0\end{aligned}\qquad\forall i=1,\ldots,N_{\mathcal{T}_{eb}}\,, \tag{2.19}$$

where $N_{\mathcal{T}_{eb}}$ is the number of transmission lines with unknown parameters. The variable $\{I_{st,i}\}_{i=1}^{N_{\mathcal{T}_{eb}}}$ (resp. $\{I_{ts,i}\}_{i=1}^{N_{\mathcal{T}_{eb}}}$) denotes the complex current flowing from bus *s* to bus *t* (resp. from bus *t* to bus *s*). Lastly, Re[.] (resp. Im[.]) represents the real (resp. imaginary) part of the complex current.

On the other hand, the operating conditions of shunt branches in terms of power flows [Romay, *et al.*, 2019] are represented by

$$\mathrm{Re}\left[y_{shkm,i}-y_{shmk,i}\right]=\frac{P_{ss,i}}{a^2_{ebkm,i}V_{ebk,i}}-\frac{P_{tt,i}}{a^2_{ebmk,i}V_{ebm,i}}=0\quad\forall i=1,\ldots,N_{\mathcal{T}_{eb}}\,, \tag{2.20}$$

$$\mathrm{Im}\left[y_{shkm,i}-y_{shmk,i}\right]=-\frac{Q_{ss,i}}{a^2_{ebkm,i}V_{ebk,i}}+\frac{Q_{tt,i}}{a^2_{ebmk,i}V_{ebm,i}}=0\quad\forall i=1,\ldots,N_{\mathcal{T}_{eb}}\,, \tag{2.21}$$

where $\{y_{shkm,i}\}_{i=1}^{N_{\mathcal{T}_{eb}}}$ (resp. $\{y_{shmk,i}\}_{i=1}^{N_{\mathcal{T}_{eb}}}$) is the complex admittance connected to the internal bus *s* (resp. *t*).

The optimization problem to be solved by this methodology is given by (2.22), where $\mathrm{Re}\left[\boldsymbol{I}_{st}(\boldsymbol{x}_{e\text{-}eb})+\boldsymbol{I}_{ts}(\boldsymbol{x}_{e\text{-}eb})\right]\in\mathbb{R}^{N_{\mathcal{T}_{eb}}}$ (resp. $\mathrm{Im}\left[\boldsymbol{I}_{st}(\boldsymbol{x}_{e\text{-}eb})+\boldsymbol{I}_{ts}(\boldsymbol{x}_{e\text{-}eb})\right]\in\mathbb{R}^{N_{\mathcal{T}_{eb}}}$) is the vector with elements given by the sum of the real (resp. imaginary) part of the complex currents injected at both terminals of the series branches of unknown transmission lines as given by (2.18) (resp. (2.19)). Similarly, $\mathrm{Re}\left[\boldsymbol{y}_{\boldsymbol{shkm}}(\boldsymbol{x}_{\boldsymbol{e\text{-}eb}})-\boldsymbol{y}_{\boldsymbol{shmk}}(\boldsymbol{x}_{\boldsymbol{e\text{-}eb}})\right]\in\mathbb{R}^{N_{\mathcal{T}_{eb}}}$ (resp. $\mathrm{Im}\left[\boldsymbol{y}_{\boldsymbol{shkm}}(\boldsymbol{x}_{\boldsymbol{e\text{-}eb}})-\boldsymbol{y}_{\boldsymbol{shmk}}(\boldsymbol{x}_{\boldsymbol{e\text{-}eb}})\right]\in\mathbb{R}^{N_{\mathcal{T}_{eb}}}$ ) is the vector with elements given by the differences of the real (resp. imaginary) part of the complex admittances connected to both internal buses as represented by (2.20) (resp. (2.21)). All other variables and functions have previously been described:

$$\begin{array}{ll}\underset{x_{e\text{-}eb},r}{\arg\min} & \boldsymbol{J}(\boldsymbol{r})=\dfrac{1}{2}\boldsymbol{r}^{\mathrm{T}}\boldsymbol{W}\boldsymbol{r}\\ \text{subject to:} & \boldsymbol{c}(\boldsymbol{x}_{\boldsymbol{e\text{-}eb}})=\boldsymbol{0}\\ & \boldsymbol{r}-\boldsymbol{z}+\hat{\boldsymbol{z}}(\boldsymbol{x}_{\boldsymbol{e\text{-}eb}})=\boldsymbol{0}\\ & \mathrm{Re}\left[\boldsymbol{I}_{\boldsymbol{st}}(\boldsymbol{x}_{\boldsymbol{e\text{-}eb}})+\boldsymbol{I}_{\boldsymbol{ts}}(\boldsymbol{x}_{\boldsymbol{e\text{-}eb}})\right]=\boldsymbol{0}\\ & \mathrm{Im}\left[\boldsymbol{I}_{\boldsymbol{st}}(\boldsymbol{x}_{\boldsymbol{e\text{-}eb}})+\boldsymbol{I}_{\boldsymbol{ts}}(\boldsymbol{x}_{\boldsymbol{e\text{-}eb}})\right]=\boldsymbol{0}\\ & \mathrm{Re}\left[\boldsymbol{y}_{\boldsymbol{shkm}}(\boldsymbol{x}_{\boldsymbol{e\text{-}eb}})-\boldsymbol{y}_{\boldsymbol{shmk}}(\boldsymbol{x}_{\boldsymbol{e\text{-}eb}})\right]=\boldsymbol{0}\\ & \mathrm{Im}\left[\boldsymbol{y}_{\boldsymbol{shkm}}(\boldsymbol{x}_{\boldsymbol{e\text{-}eb}})-\boldsymbol{y}_{\boldsymbol{shmk}}(\boldsymbol{x}_{\boldsymbol{e\text{-}eb}})\right]=\boldsymbol{0}.\end{array} \tag{2.22}$$

Once the optimization problem (2.22) has been solved, the magnitude and phase angle of the voltage measured between buses *s* and *t* of the *i*-th transmission element are obtained by means of (2.23) and (2.24) [Romay, *et al.*, 2019], respectively:

$$\begin{aligned}\hat{V}_{st,i}=\Big[&\left[a_{ebkm,i}\hat{V}_{ebk,i}\cos\left(\hat{\theta}_{ebk,i}\right)-a_{ebmk,i}\hat{V}_{ebm,i}\cos\left(\hat{\theta}_{ebm,i}\right)\right]^{2}\\ &+\left[a_{ebkm,i}\hat{V}_{ebk,i}\sin\left(\hat{\theta}_{ebk,i}\right)-a_{ebmk,i}\hat{V}_{ebm,i}\sin\left(\hat{\theta}_{ebm,i}\right)\right]^{2}\Big]^{1/2}\end{aligned}\quad \forall i=1,\ldots,N_{\mathcal{T}_{eb}}\ , \tag{2.23}$$

$$\hat{\theta}_{st,i}=\tan^{-1}\left[\frac{a_{ebkm,i}\hat{V}_{ebk,i}\sin\left(\hat{\theta}_{ebk,i}\right)-a_{ebmk,i}\hat{V}_{ebm,i}\sin\left(\hat{\theta}_{ebm,i}\right)}{a_{ebkm,i}\hat{V}_{ebm,i}\cos\left(\hat{\theta}_{ebm,i}\right)-a_{ebmk,i}\hat{V}_{ebm,i}\cos\left(\hat{\theta}_{ebm,i}\right)}\right]\quad \forall i=1,\ldots,N_{\mathcal{T}_{eb}}\ . \tag{2.24}$$

Finally, parameters of the *i*-th unknown transmission line can be determined by the following set of equations [Romay, *et al.*, 2019]:

$$\begin{aligned}\hat{g}_{sekm,i} = & \frac{\hat{P}_{st,i}}{a_{ebkm,i}\hat{V}_{ebk,i}\hat{V}_{st,i}}\cos\left(\hat{\theta}_{st,i}\right)\cos\left(\hat{\theta}_{ebk,i}\right) \\ & +\frac{\hat{Q}_{st,i}}{a_{ebkm,i}\hat{V}_{ebk,i}\hat{V}_{st,i}}\cos\left(\hat{\theta}_{st,i}\right)\sin\left(\hat{\theta}_{ebk,i}\right) \\ & +\frac{\hat{P}_{st,i}}{a_{ebkm,i}\hat{V}_{ebk,i}\hat{V}_{st,i}}\sin\left(\hat{\theta}_{st,i}\right)\sin\left(\hat{\theta}_{ebk,i}\right) \\ & -\frac{\hat{Q}_{st,i}}{a_{ebkm,i}\hat{V}_{ebk,i}\hat{V}_{st,i}}\sin\left(\hat{\theta}_{st,i}\right)\cos\left(\hat{\theta}_{ebk,i}\right)\end{aligned} \quad \forall i = 1,\ldots,N_{\mathcal{T}_{eb}}\ , \tag{2.25}$$

$$\begin{aligned}\hat{b}_{sekm,i} = & \frac{\hat{P}_{st,i}}{a_{ebkm,i}\hat{V}_{ebk,i}\hat{V}_{st,i}}\cos\left(\hat{\theta}_{st,i}\right)\sin\left(\hat{\theta}_{ebk,i}\right) \\ & -\frac{\hat{Q}_{st,i}}{a_{ebkm,i}\hat{V}_{ebk,i}\hat{V}_{st,i}}\cos\left(\hat{\theta}_{st,i}\right)\cos\left(\hat{\theta}_{ebk,i}\right) \\ & -\frac{\hat{P}_{st,i}}{a_{ebkm,i}\hat{V}_{ebk,i}\hat{V}_{st,i}}\sin\left(\hat{\theta}_{st,i}\right)\cos\left(\hat{\theta}_{ebk,i}\right) \\ & -\frac{\hat{Q}_{st,i}}{a_{ebkm,i}\hat{V}_{ebk,i}\hat{V}_{st,i}}\sin\left(\hat{\theta}_{st,i}\right)\sin\left(\hat{\theta}_{ebk,i}\right)\end{aligned} \quad \forall i = 1,\ldots,N_{\mathcal{T}_{eb}}\ , \tag{2.26}$$

$$\hat{g}_{shkm,i} = \frac{\hat{P}_{ss,i}}{a^2_{ebkm,i}\hat{V}_{ebk,i}^{\ 2}} \quad \forall i = 1,\ldots,N_{\mathcal{T}_{eb}}\ , \tag{2.27}$$

$$\hat{b}_{shkm,i} = \frac{-\hat{Q}_{ss,i}}{a^2_{ebkm,i}\hat{V}_{ebk,i}^{\ 2}} \quad \forall i = 1,\ldots,N_{\mathcal{T}_{eb}}\ . \tag{2.28}$$

### 2.4.4 Case studies

The performances of methodologies described in Sections 2.4.1 to 2.4.3 are evaluated by using the IEEE-14 bus benchmark system [University of Washington, 2018]. The mathematical programming language AMPL® [Fourer, *et al*., 2003] is used for the implementation of the optimization problems, which are solved by using the Knitro® solver [Ziena Optimization LLC, 2014] with an interior point algorithm and a convergence tolerance of $1\times10^{-8}$. The choice of AMPL is due to its capability to express and solve highly complex nonlinear optimization problems using an algebraic notation, which substantially facilitates the implementation and validation of proposed optimization problems. The set of ideal measurements is generated from a power flow study. A Gaussian random error is added to each ideal measurement considering a zero mean and the following standard deviations [Alcaide-Moreno, *et al.*, 2015]: $\left\{\sigma_{V_k^{SCADA}} = 0.004\right\}_{k\in\mathcal{N}_{oe}}$, $\left\{\sigma_{P_{km}^{SCADA}} = 0.008\right\}_{(km)\in\mathcal{T}_{oe}}$, $\left\{\sigma_{Q_{km}^{SCADA}} = 0.008\right\}_{(km)\in\mathcal{T}_{oe}}$, $\left\{\sigma_{P_k^{SCADA}} = 0.01\right\}_{k\in\mathcal{N}_{oe}}$, $\left\{\sigma_{Q_k^{SCADA}} = 0.01\right\}_{k\in\mathcal{N}_{oe}}$, $\left\{\sigma_{V_k^{PMU}} = 0.002\right\}_{k\in\mathcal{N}_{oe}}$, , $\left\{\sigma_{\left|I_{km}^{PMU}\right|} = 0.002\right\}_{(km)\in\mathcal{T}_{oe}}$ and $\left\{\sigma_{\theta_{I_{km}}^{PMU}} = 0.0017\right\}_{(km)\in\mathcal{T}_{oe}}$. The PMU current equations are handled in rectangular form. Therefore, the corresponding standard deviations are derived using the error propagation theory [Zamora-Cárdenas, *et al.*, 2014] as shown by (2.29) and (2.30):

$$\left\{\sigma_{I_{realkm}^{PMU}} = \sqrt{\left[\sigma_{\left|I_{km}^{PMU}\right|}\cos\left(\theta_{I_{km}}\right)\right]^2 + \left[\sigma_{\theta_{I_{km}}^{PMU}}\left|I_{km}\right|\sin\left(\theta_{I_{km}}\right)\right]^2}\right\}_{(realkm)\in\mathcal{T}_{oe}}, \tag{2.29}$$

$$\left\{\sigma_{I_{imagkm}^{PMU}} = \sqrt{\left[\sigma_{\left|I_{km}^{PMU}\right|}\sin\left(\theta_{I_{km}}\right)\right]^2 + \left[\sigma_{\theta_{I_{km}}^{PMU}}\left|I_{km}\right|\cos\left(\theta_{I_{km}}\right)\right]^2}\right\}_{(imagkm)\in\mathcal{T}_{oe}}. \tag{2.30}$$

Methodologies 1 and 2 consider initial values of parameters that are to be estimated at 30% with respect to (w.r.t.) the nominal database values; this agrees with the error level reported in [Kusic & Garrison, 2004]. Furthermore, the active and reactive power flows are initialized in 1.0 p.u. and 0.0 p.u., respectively, in methodology 3. This is due to the best parameter estimations being obtained by using these initial conditions. Three case studies are performed using the hybrid set of measurements (SCADA and PMU) as depicted in Fig. 2.2, which is composed of 83 SCADA and PMU measurements.

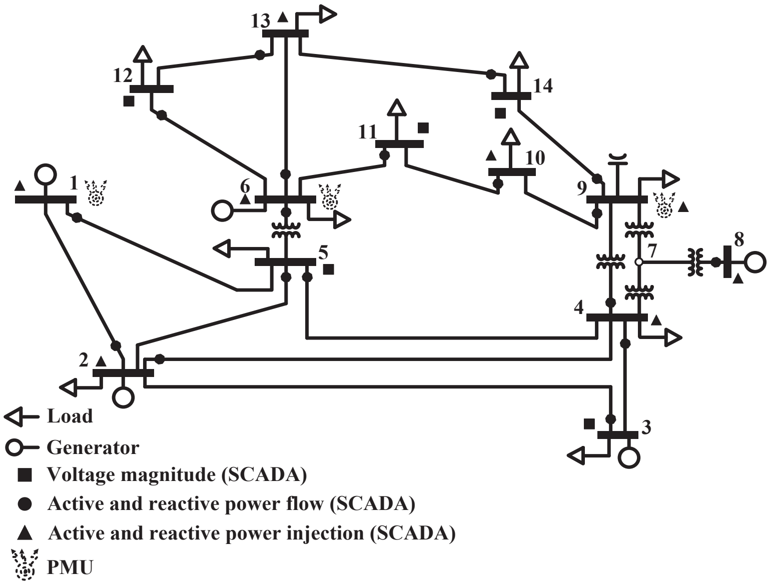

Fig. 2.2 Measurement diagram of IEEE 14-bus power system.

All case studies consider that there is a set of suspected lines $\mathcal{T}_{eb} := \left\{1, 2, \ldots, N_{\mathcal{T}_{eb}}\right\}$ with parameters that must be corrected through an estimation process. Apart from the system state estimation, the parameters of the following transmission lines are also estimated. In Case Study 1, the parameters of lines 1-2, 1-5 and 2-3 are estimated such that $N_{\mathcal{T}_{eb}} = 3$. Two suspected transmission lines are added in Case Study 2 such that $N_{\mathcal{T}_{eb}} = 5$, and the parameters of the following transmission lines are estimated: 1-2, 1-5, 2-3, 2-4 and 2-5. Lastly, the parameters of lines 1-2, 1-5, 2-3, 2-4, 2-5 and 3-4 are estimated in Case Study 3 so that $N_{\mathcal{T}_{eb}} = 6$. Even though these transmission lines are electrically close to each other, they are selected as suspected electric components because of their location at the transmission level and for their greatest values of $\{x_{km}/r_{km}\}_{(km)\in\mathcal{T}_e}$ ratios, which implies that they have the highest power transfer capacities. Lastly, the redundancy coefficients for each case are presented in Table 2.1. These redundancies are obtained by the division of the number of measurements by the number of state variables to be estimated. Table 2.1 clearly shows that methodology 2 offers the best redundancy level, while the opposite occurs with methodology 3. This is because the smaller the number of transmission line parameters added to the original state vector, the better the level of redundancy.

Table 2.1 Measurement redundancy for each case.

| **Case** | **Methodology** | | |
|---|---|---|---|
| | **1** | **2** | **3** |
| 1 | 2.305556 | 2.766667 | 1.627451 |
| 2 | 1.976190 | 2.593750 | 1.238806 |
| 3 | 1.844444 | 2.515152 | 1.106667 |

The relative errors of estimated parameters w.r.t. nominal database values are reported in Table 2.2 to Table 2.4 for the Case Studies 1 to 3, respectively. Each Case Study is solved by using all state and parameter estimation methodologies described in Sections 2.4.1 to 2.4.3. Cleary from the results, not all methodologies can provide relative errors of the suspected transmission lines per case below 30%, which corresponds to the error level of parameters that electric companies commonly have in their databases [Kusic & Garrison, 2004]. Methodology 2 yields the best performance because it provides the smallest percentage of relative errors for all cases studies despite both the number of parameters to be estimated and the closeness of transmission lines under consideration. In a comparison of the errors reported in Table 2.2 for methodologies 1 and 3, it can be noticed that both methodologies offer almost the same percentage errors of parameter estimations. Methodology 1 performs better than methodology 3, however, when the number of transmission line parameters to be estimated increases, as shown in

Table 2.3 and Table 2.4, then these two methodologies provide very poor parameter estimates because their percentage of relative errors are higher than 30% w.r.t. nominal database values: these methodologies provide relative errors significantly higher than those reported in [Kusic & Garrison, 2004].

Table 2.2 Percentage of relative errors of parameter estimations for case 1.

| **Parameter** | **Bus *k*** | **Bus *m*** | **Methodology** | | |
|---|---|---|---|---|---|
| | | | **1** | **2** | **3** |
| Series resistance | 1 | 2 | 6.11182598 | 0.35916704 | 5.40516278 |
| | 1 | 5 | 21.92342596 | 0.08533360 | 33.65179756 |
| | 2 | 3 | 10.26654699 | 0.35234107 | 9.19576839 |
| Series reactance | 1 | 2 | 1.00232600 | 0.35916704 | 0.82020975 |
| | 1 | 5 | 0.79529887 | 0.08533360 | 2.41345285 |
| | 2 | 3 | 0.53596500 | 0.35234107 | 0.97771660 |
| Shunt susceptance | 1 | 2 | 18.58795178 | 0.35916704 | 18.52873965 |
| | 1 | 5 | 100.00000000 | 0.08533360 | 186.90284172 |
| | 2 | 3 | 26.65483057 | 0.35234107 | 25.55636024 |

Table 2.3 Percentage of relative errors of parameter estimations for case 2.

| Parameter | Bus *k* | Bus *m* | Methodology | | |
|---|---|---|---|---|---|
| | | | 1 | 2 | 3 |
| Series resistance | 1 | 2 | 53.13114185 | 2.22625351 | 307.53338797 |
| | 1 | 5 | 7.97429645 | 1.30585164 | 834.84282118 |
| | 2 | 3 | 39.19100042 | 1.06816057 | 323.06341859 |
| | 2 | 4 | 38.04667823 | 4.87373194 | 359.46478384 |
| | 2 | 5 | 67.47757602 | 6.96658394 | 319.02131259 |
| Series reactance | 1 | 2 | 9.78431679 | 2.22625351 | 16.21187305 |
| | 1 | 5 | 2.04447145 | 1.30585164 | 430.01254175 |
| | 2 | 3 | 2.38017919 | 1.06816057 | 25.05925175 |
| | 2 | 4 | 6.38276318 | 4.87373194 | 38.88703141 |
| | 2 | 5 | 12.16517391 | 6.96658394 | 73.13636512 |
| Shunt susceptance | 1 | 2 | 7.84209462 | 2.22625351 | 70.92538220 |
| | 1 | 5 | 99.92530009 | 1.30585164 | 91.98136804 |
| | 2 | 3 | 32.86198084 | 1.06816057 | 155.14263500 |
| | 2 | 4 | 19.09312531 | 4.87373194 | 87.80916629 |
| | 2 | 5 | 57.20182083 | 6.96658394 | 92.80301586 |

Table 2.4 Percentage of relative errors of parameter estimations for case 3.

| Parameter | Bus *k* | Bus *m* | Methodology | | |
|---|---|---|---|---|---|
| | | | 1 | 2 | 3 |
| Series resistance | 1 | 2 | 4.67166320 | 4.54421732 | 4225.85958697 |
| | 1 | 5 | 19.82396461 | 0.24475548 | 324.56518137 |
| | 2 | 3 | 45.70198275 | 3.59890420 | 1234.51995792 |
| | 2 | 4 | 6.01631147 | 1.73308003 | 2034.59091167 |
| | 2 | 5 | 31.28260930 | 9.01220620 | 3777.00419996 |
| | 3 | 4 | 42.50632704 | 8.29681225 | 683.79760761 |
| Series reactance | 1 | 2 | 10.58824717 | 4.54421732 | 2727.30774328 |
| | 1 | 5 | 0.59416680 | 0.24475548 | 215.44772930 |
| | 2 | 3 | 45.11319579 | 3.59890420 | 1947.75496631 |
| | 2 | 4 | 12.28230117 | 1.73308003 | 2662.90732500 |
| | 2 | 5 | 4.40249284 | 9.01220620 | 2758.52471518 |
| | 3 | 4 | 112.97536549 | 8.29681225 | 221.42638251 |
| Shunt susceptance | 1 | 2 | 39.71374409 | 4.54421732 | 1501.05759383 |
| | 1 | 5 | 99.26001047 | 0.24475548 | 11.40247213 |
| | 2 | 3 | 100.00000000 | 3.59890420 | 172.58468712 |
| | 2 | 4 | 23.88065266 | 1.73308003 | 831.35616878 |
| | 2 | 5 | 254.03394970 | 9.01220620 | 1352.02904341 |
| | 3 | 4 | 99.90033614 | 8.29681225 | 973.44626656 |

As the name implies, the observability concept regards observations or physical measurements embedded in the power system. A system is said to be observable if enough information is obtained from the set of measurements to directly estimate the system operating state [Abur & Gómez Expósito, 2004]. An observability analysis can be performed before solving the optimization problems (2.11) and (2.22) to ensure that a state estimation study is possible. For Case Studies 1 through 3, the observability of state and parameters is assumed from the set of measurements in Fig. 2.2.

Table 2.5 Values of objective functions and Chi-squared tests for each case.

| **Case** | **Methodology** | | | | | |
|---|---|---|---|---|---|---|
| | **1** | | **2** | | **3** | |
| | $\boldsymbol{J}(\boldsymbol{r})$ | $\chi^2$ | $\boldsymbol{J}(\boldsymbol{r})$ | $\chi^2$ | $\boldsymbol{J}(\boldsymbol{r})$ | $\chi^2$ |
| 1 | 22.447 | 32.001 | 25.234 | 35.497 | 22.191 | 23.097 |
| 2 | 16.252 | 28.471 | 21.561 | 34.335 | 16.251 | 13.148 |
| 3 | 16.331 | 26.692 | 18.365 | 33.752 | 16.232 | 7.754 |

Estimation theory indicates that the objective function should follow a Chi-square distribution, so a statistical test can be performed on the resulting objective function to verify this property. The statistical test used is the Chi-square test which determines a threshold value for the objective function, if the resulting objective function is below this value then the results are considered as reliable, if the objective function exceeds this threshold value then the results provided are not reliable. The optimality function's value $\boldsymbol{J}(\boldsymbol{r})$ of the estimation process as well as the Chi-squared $\chi^2$ test's value are shown in Table 2.5 for each Case Study. The Chi-squared test is performed by using a significance level of 0.05 [Abur & Gómez Expósito, 2004] and degrees of freedom obtained as the difference between available measurements and state variables. Note that the objective function values of methodology 1 do not exceed the Chi-squared test values in any of the Case Studies. Nevertheless, estimates of parameters are completely incorrect for methodology 1 as reported from Table 2.2 to Table 2.4. This represents its main drawback because it minimizes the WLS-based objective function below the Chi-squared test value and one may erroneously consider the provided parameter estimates as correct. On the other hand, methodology 3 shows a completely different behavior because the objective function surpasses the Chi-squared limits in cases 2 and 3, as reported in Table 2.5. In addition, for Case Study 1, the resulting value of the objective function of methodology 3 is almost the same as the Chi-squared limit. Therefore, from the Chi-square test, the results provided by this methodology are not reliable, which can be verified from Table 2.2 to Table 2.4. This behavior is a consequence of the poor redundancy generated by methodology 3 when the number of transmission line parameters is augmented. Lastly, methodology 2 offers the best performance because their objective functions do not exceed the limit of the Chi-square tests per case, as shown in Table 2.5, and the relative percentage errors are below 30%, which is the level of error encountered in the electric companies databases [Kusic & Garrison, 2004].

## 2.5 Static state and topology co-estimation

The static state and topology co-estimation refers to simultaneously estimating the system operating state and all circuit breakers statuses at explicitly modeled power substations in the power grid. To formulate this co-estimation problem, it must be considered that in addition to the set of system transmission buses $\mathcal{N}_e := \{1,2,\ldots,N_e\}$ interconnected through transmission elements $\mathcal{T}_e := \left\{1,2,\ldots,N_{\mathcal{T}_e}\right\}$, there exists a set of buses $\mathcal{N}_{se} := \{1,2,\ldots,N_{se}\}$ explicitly modeled at power substations that are interconnected through a set of circuit breakers $\mathcal{T}_{cb} := \left\{1,2,\ldots,N_{\mathcal{T}_{cb}}\right\}$. In this case, the number of circuit breakers is given by $N_{\mathcal{T}_{cb}} = N_{\mathcal{T}_{ccb}} + N_{\mathcal{T}_{ocb}} + N_{\mathcal{T}_{ucb}}$, where $N_{\mathcal{T}_{ccb}}$ and $N_{\mathcal{T}_{ocb}}$ correspond to the number of circuit breakers with known statuses: closed and open breakers, respectively. Furthermore, $N_{\mathcal{T}_{ucb}}$ denotes the number of circuit breakers with unknown statuses. Lastly, the active $\{P_{km}\}_{\{k,m\}\in\mathcal{N}_{se}}$ and reactive $\{Q_{km}\}_{\{k,m\}\in\mathcal{N}_{se}}$ powers that flow through these breakers are considered as state variables that are to be estimated. Therefore, the augmented state vector is represented by (2.31), where $\boldsymbol{V} \in \mathbb{R}^{N_e+N_{se}}$, $\boldsymbol{\theta} \in \mathbb{R}^{N_e+N_{se}}$, $\boldsymbol{P_{cb}} \in \mathbb{R}^{N_{\mathcal{T}_{cb}}}$ and $\boldsymbol{Q_{cb}} \in \mathbb{R}^{N_{\mathcal{T}_{cb}}}$:

$$\boldsymbol{x_{e\text{-}cb}} = \begin{bmatrix} \boldsymbol{V} & \boldsymbol{\theta} & \boldsymbol{P_{cb}} & \boldsymbol{Q_{cb}} \end{bmatrix}^{\mathrm{T}} \in \mathbb{R}^{2N_e+2N_{se}+2N_{\mathcal{T}_{cb}}}. \tag{2.31}$$

In [Monticelli & Garcia, 1991; Monticelli, 1993; Monticelli, 1993; Alsac, *et al.*, 1998], the use of operational constraints for circuit breakers with known statuses is proposed by assuming subsets of closed $\mathcal{T}_{ccb} := \left\{1,2,\ldots,N_{\mathcal{T}_{ccb}}\right\} \ni \mathcal{T}_{ccb} \subset \mathcal{T}_{cb}$ and open $\mathcal{T}_{ocb} := \left\{1,2,\ldots,N_{\mathcal{T}_{ocb}}\right\} \ni \mathcal{T}_{ocb} \subset \mathcal{T}_{cb}$ circuit breakers, respectively. Furthermore, the closed and open breakers are connected to the following subset of nodes: $\mathcal{N}_{ccb} := \{1,2,\ldots,N_{ccb}\} \ni \mathcal{N}_{ccb} \subseteq \mathcal{N}_{se}$ and $\mathcal{N}_{ocb} := \{1,2,\ldots,N_{ocb}\} \ni \mathcal{N}_{ocb} \subseteq \mathcal{N}_{se}$, respectively.

If the *i*-th closed breaker is connected between nodes *k* and *m*, the voltage drop across its terminals must be null such that the breaker's operating conditions are mathematically defined by

$$\mathrm{OC}_{ccb}(\boldsymbol{x}_{\boldsymbol{e\text{-}cb}})_i = \begin{bmatrix} \theta_k - \theta_m \\ V_k - V_m \end{bmatrix} = \begin{bmatrix} 0 \\ 0 \end{bmatrix} \quad , \quad \begin{array}{c} \forall \; \{k,m\} \in \mathcal{N}_{ccb}, \\ \forall i \in \mathcal{T}_{ccb}. \end{array} \tag{2.32}$$

On the other hand, the operating conditions for the *i*-th open circuit breaker connecting nodes *k* and *m* are given by the zero power flow through it:

$$\mathrm{OC}_{ocb}(\boldsymbol{x}_{\boldsymbol{e\text{-}cb}})_i = \begin{bmatrix} P_{km} \\ Q_{km} \end{bmatrix} = \begin{bmatrix} 0 \\ 0 \end{bmatrix} \quad , \quad \begin{array}{c} \forall \; \{k,m\} \in \mathcal{N}_{ocb}, \\ \forall i \in \mathcal{T}_{ocb}. \end{array} \tag{2.33}$$

Based on the conditions mentioned, a new set of constraints are proposed to estimate the unknown statuses of circuit breakers composing the subset $\mathcal{T}_{ucb} := \left\{1, 2, \ldots, N_{\mathcal{T}_{ucb}}\right\} \ni \mathcal{T}_{ucb} \subset \mathcal{T}_{cb}$ and which are interconnected through the subset of nodes $\mathcal{N}_{ucb} := \{1, 2, \ldots, N_{ucb}\} \ni \mathcal{N}_{ucb} \subseteq \mathcal{N}_{se}$. In this context, circuit breakers are considered with unknown statuses if their operating statuses are not explicitly known or if the power system's operator does not have absolute confidence in the breaker statuses provided by the network configurator. These operating conditions are derived from applying the concept of complementarity constraints to Eqs. (2.32) and (2.33). The first stage of this derivation results in the complementarity constraints (2.34) and (2.35) associated with the *i*-th breaker with an unknown status connected between nodes *k* and *m*. Note that these equations include quadratic terms in order to fulfill the non-negativity condition associated with these types of constraints:

$$0 \le (\theta_k - \theta_m)^2 \perp P_{km}^2 \ge 0 \,, \quad \forall \{k,m\} \in \mathcal{N}_{ucb}, \tag{2.34}$$

$$0 \le (V_k - V_m)^2 \perp Q_{km}^2 \ge 0 \,, \quad \forall \{k,m\} \in \mathcal{N}_{ucb}. \tag{2.35}$$

The main drawback of directly using (2.34) and (2.35), however, is that in a substation with several breakers with unknown statuses the estimated values of active and reactive power flows can be 0 for some circuit breakers that are actually closed. Similarly, the estimated values of power flows through breakers that are actually open can be different than

0. Hence, the estimated state variables may take values that do not correctly represent the real operating conditions of circuit breakers with unknown statuses. The incorrect estimation of the active and reactive powers that flow through breakers with unknown statuses is because of the decoupling of complementarity conditions (2.34) and (2.35). Hence, it is necessary to couple all state variables composing the complementarity conditions representing the breaker's unknown status.

The drawbacks mentioned above are overcome by formulating a single complementarity constraint that simultaneously considers the two possible breakers' operating statuses: open or closed. In the former operating condition, both active and reactive power flows are 0, which can be mathematically represented in one single constraint expressed in terms of the apparent power:

$$\Phi_{ucb}(\boldsymbol{x}_{\boldsymbol{e\text{-}cb}})_i = P_{km}^2 + Q_{km}^2 = 0, \quad \forall \{k,m\} \in \mathcal{N}_{ucb}, \ \forall i \in \mathcal{T}_{ucb}. \tag{2.36}$$

On the other hand, the voltage drop and voltage phase angle difference are both 0 when the breaker is closed. These two conditions can be merged in a single constraint expressed in terms of the rectangular components of both nodal voltages:

$$\Gamma_{ucb}(\boldsymbol{x}_{\boldsymbol{e\text{-}cb}})_i = (\mathrm{Re}(\vec{V}_k) - \mathrm{Re}(\vec{V}_m))^2 + (\mathrm{Im}(\vec{V}_k) - \mathrm{Im}(\vec{V}_m))^2 = 0 \ , \ \forall \ \{k,m\} \in \mathcal{N}_{ucb}, \ \forall i \in \mathcal{T}_{ucb} \ . \tag{2.37}$$

The merging Eqs. (2.36) and (2.37) with the complement operator "$\perp$" results in the proposed nonlinear complementarity constraint for breakers with unknown statuses:

$$\mathrm{OC}_{ucb}(\boldsymbol{x}_{\boldsymbol{e\text{-}cb}})_i = 0 \le \underbrace{\left(P_{km}^2 + Q_{km}^2\right)}_{\Phi_{ucb}(\boldsymbol{x}_{\boldsymbol{e\text{-}cb}})_i} \perp \underbrace{\begin{pmatrix} (\mathrm{Re}(\vec{V}_k) - \mathrm{Re}(\vec{V}_m))^2 \\ +(\mathrm{Im}(\vec{V}_k) - \mathrm{Im}(\vec{V}_m))^2 \end{pmatrix}}_{\Gamma_{ucb}(\boldsymbol{x}_{\boldsymbol{e\text{-}cb}})_i} \ge 0 \ , \quad \begin{matrix} \forall \ \{k,m\} \in \mathcal{N}_{ucb}, \\ \forall i \in \mathcal{T}_{ucb}. \end{matrix} \tag{2.38}$$

The complementarity condition (2.38) correctly represents the possible open or closed operating condition associated with an unknown status of a circuit breaker because only one of two constraints equals 0. Including (2.38) in the state and topology co-optimization problem for the simultaneous estimation of all state variables associated with this type of breaker requires transforming (2.38) into an equality constraint by using the

Fischer-Burmeister merit function [Fischer, 1992], where the square root term considers the positive square root:

$$\mathrm{OC}_{ucb}(x_{e\text{-}cb})_i = \sqrt{\Phi(\boldsymbol{x_{e\text{-}cb}})_i^2 + \Gamma(\boldsymbol{x_{e\text{-}cb}})_i^2} - \Phi(\boldsymbol{x_{e\text{-}cb}})_i - \Gamma(\boldsymbol{x_{e\text{-}cb}})_i = 0\ ,\ \forall i \in \mathcal{T}_{ucb}\,. \tag{2.39}$$

Based on the information mentioned above, the static state and topology co-estimation is performed by solving the optimization problem given by (2.40), where three possible breaker statuses are considered: closed, open and unknown:

$$\begin{aligned}
&\underset{x_{e\text{-}cb},r}{\arg\min} && \boldsymbol{J}(\boldsymbol{r}) = \frac{1}{2}\boldsymbol{r}^{\mathrm{T}}\boldsymbol{W}\boldsymbol{r} && \\
&\text{subject to:} && \boldsymbol{c_{te}}(\boldsymbol{x_{e\text{-}cb}}) = \boldsymbol{0} && \boldsymbol{c_{te}}(\boldsymbol{x_{e\text{-}cb}}) : \mathbb{R}^{2N_e+2N_{se}+2N_{\mathcal{T}_{cb}}} \to \mathbb{R}^{2N_{tbe}+2N_{sbe}} \\
& && \boldsymbol{r} - \boldsymbol{z} + \hat{\boldsymbol{z}}(\boldsymbol{x_{e\text{-}cb}}) = \boldsymbol{0} && \hat{\boldsymbol{z}}(\boldsymbol{x_{e\text{-}cb}}) : \mathbb{R}^{2N_e+2N_{se}+2N_{\mathcal{T}_{cb}}} \to \mathbb{R}^{M} \\
& && \mathbf{OC}_{\boldsymbol{ccb}}(\boldsymbol{x_{e\text{-}cb}}) = \mathbf{0} && \mathbf{OC}_{\boldsymbol{ccb}}\left(\boldsymbol{x_{e\text{-}cb}}\right) : \mathbb{R}^{2N_e+2N_{se}+2N_{\mathcal{T}_{cb}}} \to \mathbb{R}^{2N_{\mathcal{T}_{ccb}}} \\
& && \mathbf{OC}_{\boldsymbol{ocb}}(\boldsymbol{x_{e\text{-}cb}}) = \mathbf{0} && \mathbf{OC}_{\boldsymbol{ocb}}\left(\boldsymbol{x_{e\text{-}cb}}\right) : \mathbb{R}^{2N_e+2N_{se}+2N_{\mathcal{T}_{cb}}} \to \mathbb{R}^{2N_{\mathcal{T}_{ocb}}} \\
& && \mathbf{OC}_{\boldsymbol{ucb}}(\boldsymbol{x_{e\text{-}cb}}) = \mathbf{0} && \mathbf{OC}_{\boldsymbol{ucb}}(\boldsymbol{x_{e\text{-}cb}}) : \mathbb{R}^{2N_e+2N_{se}+2N_{\mathcal{T}_{cb}}} \to \mathbb{R}^{N_{\mathcal{T}_{ucb}}}\,,
\end{aligned} \tag{2.40}$$

where $\boldsymbol{J}(\boldsymbol{r})\!: \mathbb{R}^M \to \mathbb{R}$ is the objective function from the WLS approach and $\boldsymbol{r} \in \mathbb{R}^M$ is the vector of measurements' residuals, which are considered as explicit decision variables together with the components of vector $\boldsymbol{x_{e\text{-}cb}}$. The diagonal matrix $\boldsymbol{W} = \mathrm{diag}\left\{1/\sigma_i^2\right\}_{i=1}^{M}$ weights vector $\boldsymbol{r}$, where $\left\{\sigma_i\right\}_{i=1}^{M}$ is the *i*-th standard deviation that reflects the *i*-th meter's level of accuracy. Furthermore, $\boldsymbol{c_{te}}(\boldsymbol{x_{e\text{-}cb}})$ corresponds to the set of structural constraints associated with the zero injection measurements at the transitions' buses located in the transmission system and explicitly modeled substations. The mathematical representation of these zero injection measurements are reported in Eqs. (C.5) and (C.6) of Appendix C. The operating constraints $\mathbf{OC}_{\boldsymbol{ccb}}(\boldsymbol{x_{e\text{-}cb}})$, $\mathbf{OC}_{\boldsymbol{ocb}}(\boldsymbol{x_{e\text{-}cb}})$ and $\mathbf{OC}_{\boldsymbol{ucb}}(\boldsymbol{x_{e\text{-}cb}})$ correspond to the closed, open and unknown statuses of circuit breakers, respectively. Lastly, the set of physical and estimated measurements are given by $\boldsymbol{z} = \left[\boldsymbol{z_e^{SCADA}} \;\; \boldsymbol{z_e^{PMU}}\right]^{\mathrm{T}} \in \mathbb{R}^M$ and $\hat{\boldsymbol{z}}(\boldsymbol{x_{e\text{-}cb}})$, respectively.

In order to identify unknown statuses of breakers from estimated power flows, a comparative test is proposed in this thesis. After the optimization problem of (2.40) is solved, the absolute values of estimated active and reactive power flow through those breakers are compared with the values of three times the active and reactive power flow measurements' standard deviations: $3\sigma_{P_{km}^{SCADA}}$ and $3\sigma_{Q_{km}^{SCADA}}$, respectively. This proposed comparison is based on the fact that power flow measurement errors follow a normal distribution [Abur & Gómez Expósito, 2004] with mean values equal to 0 and standard deviations of measurement devices which are equal to $\sigma_{P_{km}^{SCADA}}$ and $\sigma_{Q_{km}^{SCADA}}$. Thus, 99.73% of random values of this distribution are clustered within the range of $\pm 3\sigma_{P_{km}^{SCADA}}$ and $\pm 3\sigma_{Q_{km}^{SCADA}}$, respectively. Consequently, it is acceptable to consider $3\sigma_{P_{km}^{SCADA}}$ and $3\sigma_{Q_{km}^{SCADA}}$ as limit values that can adopt power flows of circuit breakers in the open condition. Therefore, if the estimated active and reactive power flows of the corresponding switching device are lower than these values, that circuit breaker is identified as open. If at least one of them is greater than the limit value, that circuit breaker is identified as closed.

It is important to mention that the static state and topology co-estimation requires explicitly incorporating the substations in a node-breaker model, which results in an increase of the state vector dimensionality according to the number of power substations. Note that this eventually limits its application in large-scale electrical systems. Even though this can be overcome by modeling only a few selected substations at the bus-breaker level [Simoes Costa, *et al.*, 2007] or applying decentralized state estimation at substation level [Silva, *et al.*, 2013], this issue is beyond of the scope of this thesis.

### 2.5.1 Case studies

The performance of the proposed methodology is evaluated by using the IEEE 24-bus power system [Probability Methods Subcommittee, 1979; Billinton, *et al.*, 1985] and the COPEL-55 bus power system that supplies the metropolitan area of Curitiba, Brazil [Vosgerau F. , 2011]. The mathematical programming language AMPL® [Fourer, *et al.*, 2003] is used for the proposal's implementation as well as the Knitro® solver [Ziena Optimization LLC, 2014] with a quadratic sequential programming algorithm for the optimization problem solution. This is due to the best estimations being obtained by using this solution algorithm. The case studies and the corresponding numerical results for each power system are described in the following sections.

### 2.5.1.1 IEEE-24 bus power system

The substations at buses 14 and 16 of the IEEE 24-bus benchmark system [Probability Methods Subcommittee, 1979; Billinton, *et al.*, 1985] are modeled at the physical level. The former is composed of a ring configuration, while the substation at node 16 has a breaker and a half configuration, respectively. The total number of switching devices included in these substations is 13. The measurement scheme is shown in Fig. 2.3, which is composed of 143 SCADA measurements: 23 nodal voltage magnitude measurements, 46 active power flow measurements, 46 reactive power flow measurements, 16 active power injection measurements and 16 reactive power injection measurements. Furthermore, the breaker statuses shown in this figure correspond to the true topology.

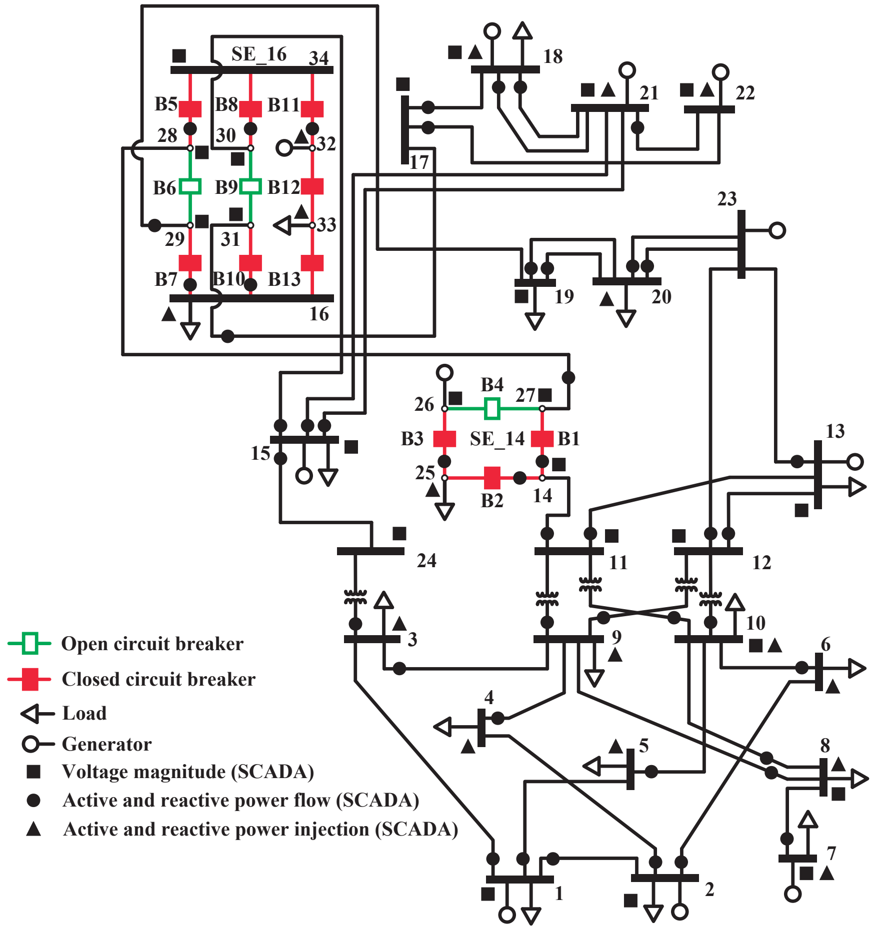

Fig. 2.3 Measurement diagram of the IEEE-24 bus power system with substations 14 and 16 modeled at the section level.

All SCADA measurements are generated by adding Gaussian random noise to the solution of a power flow program that explicitly considers substation models as described in [Lourenco, *et al.*, 2010]. The measurements' standard deviations used by the random number generator are as follows [Andreoli, *et al.*, 2014]: $\left\{\sigma_{V_k^{SCADA}} = 0.005\right\}_{k\in\mathcal{N}_e,\mathcal{N}_{se}}$, $\left\{\sigma_{P_{km}^{SCADA}} = 0.03\right\}_{\left(P_{km}^{SCADA}\right)\in\mathcal{T}_e,\mathcal{T}_{cb}}$, $\left\{\sigma_{Q_{km}^{SCADA}} = 0.03\right\}_{\left(Q_{km}^{SCADA}\right)\in\mathcal{T}_e,\mathcal{T}_{cb}}$, $\left\{\sigma_{P_k^{SCADA}} = 0.03\right\}_{k\in\mathcal{N}_e,\mathcal{N}_{se}}$ and $\left\{\sigma_{Q_k^{SCADA}} = 0.03\right\}_{k\in\mathcal{N}_e,\mathcal{N}_{se}}$. A tolerance of $1\times10^{-4}$ is considered for the sequential quadratic algorithm convergence and the nodal voltage magnitudes, and phase angles are initialized at flat start. This tolerance is used because the algorithm produces estimations more quickly than if a smaller tolerance is used. For closed switching devices, initial values of 1.0 p.u. are used for active and reactive power flows. On the other hand, the initialization of active and reactive power flows through open and unknown circuit breakers is set at $1\times10^{-5}$ p.u., respectively. Lastly, three case studies are simulated to verify the performance of the proposed optimization problem which are described below.

The first case assumes unknown operating statuses for breakers B1 and B5, while the others have the statuses given in Fig. 2.3 such that $N_{\mathcal{T}_{ucb}} = 2$, $N_{\mathcal{T}_{ccb}} = 8$ and $N_{\mathcal{T}_{ocb}} = 3$. The objective is to estimate the statuses of B1 and B5 from the proposed optimization problem represented by (2.40) and the redundancy given in Fig. 2.3. In order to validate the effectiveness of the proposed methodology, the results are compared with the ones obtained by the methodology described in [da Silva, *et al.*, 2016]. For this purpose, this methodology was also implemented in AMPL® by using the same standard deviations previously described, a weighting factor of $k_w = 0.01$ and an interior point algorithm with a convergence tolerance of $1\times10^{-4}$. The estimated power flows and unknown statuses for unknown breakers by using both methodologies are reported in Table 2.6, which also shows the absolute errors in the active and reactive power flows estimations obtained from both methodologies. The values of these absolute errors clearly show that estimated flows of B1 and B5 by the proposed approach are very close to those given by the methodology described in [da Silva, *et al*., 2016]. Furthermore, the proposal correctly estimates the unknown statuses of circuit breakers for the given simulation conditions.

Table 2.6 Results for case 1 of IEEE-24 bus power system.

| **Breaker** | **Estimated values** | | | | | | **Error** | |
|---|---|---|---|---|---|---|---|---|
| | **[da Silva, *et al*., 2016]** | | | **Proposed** | | | | |
| | **$P_{km}$ (p.u.)** | **$Q_{km}$ (p.u.)** | **Status** | **$P_{km}$ (p.u.)** | **$Q_{km}$ (p.u.)** | **Status** | **$P_{km}$ (p.u.)** | **$Q_{km}$ (p.u.)** |
| B1 | -3.69 | 0.06 | Closed | -3.71 | 0.06 | Closed | 0.02 | 0.00 |
| B5 | -3.79 | -0.41 | Closed | -3.78 | -0.41 | Closed | 0.01 | 0.00 |

The second case assumed that breakers B8, B9 and B10 have unknown statuses, while the others are known (as seen Fig. 2.3) such that $N_{\mathcal{T}_{ucb}} = 3$, $N_{\mathcal{T}_{ccb}} = 8$ and $N_{\mathcal{T}_{ocb}} = 2$. The proposed optimization problem and the methodology proposed in [da Silva, *et al*., 2016] are used to determining those statuses as well as the entire system operating condition. Table 2.7 reports the results for breakers B8, B9 and B10 from which it is concluded that the estimator obtains correct estimated values of power flows and statuses of unknown circuit breakers.

Table 2.7 Results for case 2 of IEEE-24 bus power system.

| **Breaker** | **Estimated values** | | | | | | **Error** | |
|---|---|---|---|---|---|---|---|---|
| | **[da Silva, *et al*., 2016]** | | | **Proposed** | | | | |
| | **$P_{km}$ (p.u.)** | **$Q_{km}$ (p.u.)** | **Status** | **$P_{km}$ (p.u.)** | **$Q_{km}$ (p.u.)** | **Status** | **$P_{km}$ (p.u.)** | **$Q_{km}$ (p.u.)** |
| B8 | 1.20 | -0.26 | Closed | 1.20 | -0.26 | Closed | 0.01 | 0.00 |
| B9 | 0.00 | 0.00 | Open | 0.00 | 0.01 | Open | 0.00 | 0.00 |
| B10 | -3.24 | -0.36 | Closed | -3.24 | -0.36 | Closed | 0.00 | 0.00 |

Lastly, the third case regards all breakers at the substations of Fig. 2.3 as unknown, such that $N_{\mathcal{T}_{ucb}} = 13$, $N_{\mathcal{T}_{ccb}} = 0$ and $N_{\mathcal{T}_{ocb}} = 0$. Hence, the objective is to estimate all switching devices statuses based on the available measurements by using the proposed methodology as well as the methodology reported in [da Silva, *et al*., 2016]. The power flows and statuses estimations of all circuit breakers are reported in Table 2.8, which newly validate the effectiveness of the proposed approach.

Table 2.8 Results for case 3 of IEEE-24 bus power system.

| Breaker | Estimated values | | | | | | Error | |
|---|---|---|---|---|---|---|---|---|
| | **[da Silva, *et al.*, 2016]** | | | **Proposed** | | | **$P_{km}$ (p.u.)** | **$Q_{km}$ (p.u.)** |
| | **$P_{km}$ (p.u.)** | **$Q_{km}$ (p.u.)** | **Status** | **$P_{km}$ (p.u.)** | **$Q_{km}$ (p.u.)** | **Status** | | |
| B1 | -3.69 | 0.06 | Closed | -3.69 | 0.06 | Closed | 0.00 | 0.00 |
| B2 | 1.96 | 0.38 | Closed | 1.96 | 0.38 | Closed | 0.00 | 0.00 |
| B3 | 0.02 | 0.20 | Closed | 0.02 | 0.20 | Closed | 0.00 | 0.00 |
| B4 | -0.03 | 0.00 | Open | -0.03 | 0.00 | Open | 0.00 | 0.00 |
| B5 | -3.79 | -0.41 | Closed | -3.79 | -0.41 | Closed | 0.00 | 0.00 |
| B6 | 0.00 | -0.01 | Open | 0.00 | 0.00 | Open | 0.00 | 0.01 |
| B7 | 1.29 | -0.46 | Closed | 1.29 | -0.46 | Closed | 0.00 | 0.00 |
| B8 | 1.20 | -0.26 | Closed | 1.20 | -0.26 | Closed | 0.00 | 0.00 |
| B9 | 0.00 | 0.00 | Open | 0.00 | 0.00 | Open | 0.00 | 0.00 |
| B10 | -3.24 | -0.36 | Closed | -3.24 | -0.36 | Closed | 0.00 | 0.00 |
| B11 | 2.58 | 0.66 | Closed | 2.58 | 0.66 | Closed | 0.00 | 0.00 |
| B12 | -1.01 | -0.60 | Closed | -1.01 | -0.60 | Closed | 0.00 | 0.00 |
| B13 | 1.51 | 0.70 | Closed | 1.51 | 0.70 | Closed | 0.00 | 0.00 |

### 2.5.1.2 COPEL-55 bus power system

The substation at bus 55 of the COPEL 55-bus power system [Vosgerau F. , 2011] is explicitly considered for this case study with a total number of circuit breakers equal to $N_{\mathcal{T}_{cb}} = 30$. The entire system as well as the measurement scheme are shown in Fig. 2.4, where the latter is composed of 305 measurements: 30 nodal voltage magnitude measurements, 103 active power flow measurements, 103 reactive power flow measurements, 54 active power injection measurements and 15 reactive power injection measurements. SCADA measurements are generated by adding Gaussian random noise to the power flow results, while the measurements' standard deviations are considered as follows [Alcaide-Moreno, *et al.*, 2015]: $\left\{\sigma_{V_k^{SCADA}} = 0.004\right\}_{k\in\mathcal{N}_e,\mathcal{N}_{se}}$, $\left\{\sigma_{P_{km}^{SCADA}} = 0.008\right\}_{\left(P_{km}^{SCADA}\right)\in\mathcal{T}_e,\mathcal{T}_{cb}}$, $\left\{\sigma_{Q_{km}^{SCADA}} = 0.008\right\}_{\left(P_{km}^{SCADA}\right)\in\mathcal{T}_e,\mathcal{T}_{cb}}$, $\left\{\sigma_{P_k^{SCADA}} = 0.01\right\}_{k\in\mathcal{N}_e,\mathcal{N}_{se}}$ and $\left\{\sigma_{Q_k^{SCADA}} = 0.01\right\}_{k\in\mathcal{N}_e,\mathcal{N}_{se}}$. The same convergence tolerance and circuit breakers' initial conditions for the sequential quadratic algorithm as described in Section 2.5.1.1 for the IEEE 24-bus benchmark system are used. The extreme case where all breakers at the substation 55 are unknown is simulated, so that $N_{\mathcal{T}_{ucb}} = 30$, $N_{\mathcal{T}_{ccb}} = 0$ and $N_{\mathcal{T}_{ocb}} = 0$. The objective is to estimate all switching devices statuses based on the available measurements through the proposed approach and the one reported in [da Silva, *et al*., 2016]. For that purpose, the latter is implemented in AMPL® by using the standard deviations previously described with a weighting factor of $k_w = 1\times10^{-6}$ and solved by employing an interior point algorithm with a convergence tolerance of $1\times10^{-4}$. The estimation results of power flows and breakers' statuses are reported in Table 2.9. A comparison of these results as well as the absolute values of the differences between active and reactive power flow estimations obtained from both methodologies demonstrate the validity of the proposed approach.

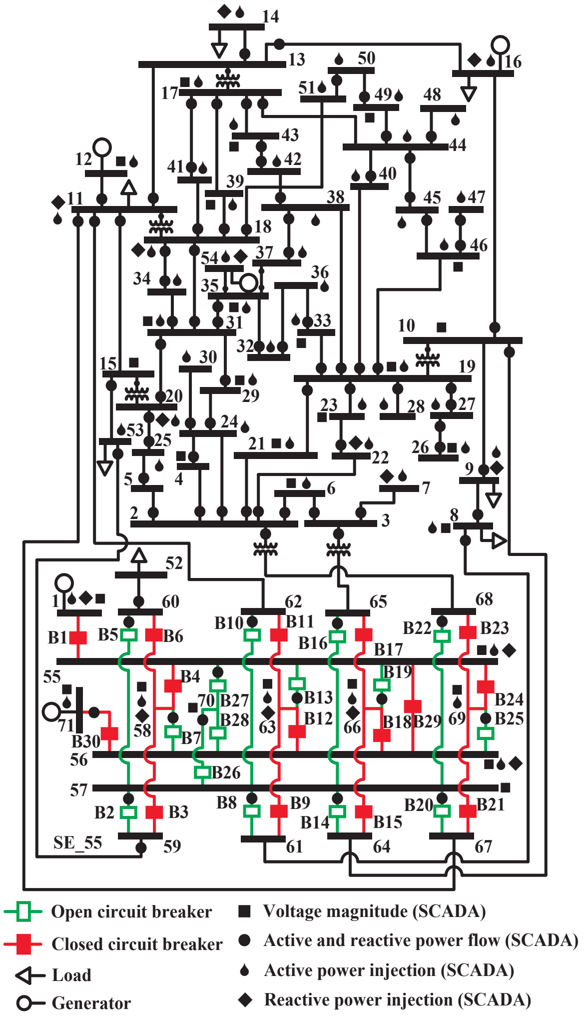

Fig. 2.4 Measurement diagram of the COPEL-55 bus power system with substation 55 explicitly modeled.

Table 2.9 Results for COPEL-55 bus power system.

| **Breaker** | **Estimated values** | | | | | | **Error** | |
|---|---|---|---|---|---|---|---|---|
| | **[da Silva, *et al.*, 2016]** | | | **Proposed** | | | **$P_{km}$ (p.u.)** | **$Q_{km}$ (p.u.)** |
| | **$P_{km}$ (p.u.)** | **$Q_{km}$ (p.u.)** | **Status** | **$P_{km}$ (p.u.)** | **$Q_{km}$ (p.u.)** | **Status** | | |
| B1 | 3.74 | 0.48 | Closed | 3.74 | 0.48 | Closed | 0.00 | 0.00 |
| B2 | 0.00 | -0.01 | Open | 0.00 | -0.01 | Open | 0.00 | 0.00 |
| B3 | 0.37 | 0.09 | Closed | 0.37 | 0.09 | Closed | 0.00 | 0.00 |
| B4 | 1.40 | 0.36 | Closed | 1.40 | 0.36 | Closed | 0.00 | 0.00 |
| B5 | 0.00 | 0.00 | Open | 0.00 | 0.00 | Open | 0.00 | 0.00 |
| B6 | 0.94 | 0.26 | Closed | 0.94 | 0.26 | Closed | 0.00 | 0.00 |
| B7 | 0.00 | -0.01 | Open | 0.00 | -0.01 | Open | 0.00 | 0.00 |
| B8 | 0.00 | 0.01 | Open | 0.00 | 0.01 | Open | 0.00 | 0.00 |
| B9 | 0.59 | -0.22 | Closed | 0.59 | -0.22 | Closed | 0.00 | 0.00 |
| B10 | 0.00 | 0.01 | Open | 0.00 | 0.01 | Open | 0.00 | 0.00 |
| B11 | 0.17 | -0.19 | Closed | 0.17 | -0.19 | Closed | 0.00 | 0.00 |
| B12 | 0.45 | -0.04 | Closed | 0.45 | -0.04 | Closed | 0.00 | 0.00 |
| B13 | 0.01 | 0.01 | Open | 0.01 | 0.01 | Open | 0.00 | 0.00 |
| B14 | 0.00 | 0.00 | Open | 0.00 | 0.00 | Open | 0.00 | 0.00 |
| B15 | -0.91 | 0.05 | Closed | -0.91 | 0.05 | Closed | 0.00 | 0.00 |
| B16 | 0.01 | 0.01 | Open | 0.01 | 0.01 | Open | 0.00 | 0.00 |
| B17 | -0.50 | -0.07 | Closed | -0.50 | -0.07 | Closed | 0.00 | 0.00 |
| B18 | 1.47 | 0.01 | Closed | 1.46 | 0.01 | Closed | 0.00 | 0.00 |
| B19 | 0.00 | 0.00 | Open | 0.00 | 0.00 | Open | 0.00 | 0.00 |
| B20 | 0.00 | 0.00 | Open | 0.00 | 0.00 | Open | 0.00 | 0.00 |
| B21 | 0.07 | -0.08 | Closed | 0.07 | -0.07 | Closed | 0.00 | 0.00 |
| B22 | 0.00 | 0.00 | Open | 0.00 | 0.00 | Open | 0.00 | 0.00 |
| B23 | -0.51 | -0.09 | Closed | -0.51 | -0.09 | Closed | 0.00 | 0.00 |
| B24 | 0.49 | 0.15 | Closed | 0.49 | 0.15 | Closed | 0.00 | 0.00 |
| B25 | 0.00 | 0.01 | Open | 0.00 | 0.01 | Open | 0.00 | 0.00 |
| B26 | 0.00 | -0.01 | Open | 0.00 | -0.01 | Open | 0.00 | 0.00 |
| B27 | -0.01 | 0.00 | Open | -0.01 | 0.00 | Open | 0.00 | 0.00 |
| B28 | 0.01 | 0.01 | Open | 0.01 | 0.01 | Open | 0.00 | 0.00 |
| B29 | 1.73 | -0.03 | Closed | 1.73 | -0.02 | Closed | 0.00 | 0.00 |
| B30 | 0.20 | 0.00 | Closed | 0.20 | 0.00 | Closed | 0.00 | 0.00 |

## 2.6 Static state and temperature co-estimation

The proposed approach in this section regards the static state and temperature co-estimation of system nodal voltages and transmission lines' temperatures in a single frame of reference. For this purpose, a set of system transmission buses $\mathcal{N}_e := \{1, 2, \ldots, N_e\}$ interconnected through transmission elements $\mathcal{T}_e := \left\{1, 2, \ldots, N_{\mathcal{T}_e}\right\}$ is considered. Furthermore, some of these elements have temperature dependent parameters $\mathcal{T}_{tdb} := \left\{1, 2, \ldots, N_{\mathcal{T}_{tdb}}\right\} \ni \mathcal{T}_{tdb} \subseteq \mathcal{T}_e$ such that their corresponding conducture temperatures $\{T_{km}\}_{(km)\in\mathcal{N}_e}$ must be estimated. Considering the *i*-th transmission line connected from bus *k* to bus *m*, the corresponding temperature dependent series resistivity of the metallic conductor $r_{sekm,i}(T_{km,i}) : \mathbb{R} \rightarrow \mathbb{R}$ is represented by (2.41). In this case, $\{r_{sekm,i}\}_{i=1}^{N_{\mathcal{T}_{tdb}}}$ is the corresponding conductor resistivity, and $\{r_{refkm,i}\}_{i=1}^{N_{\mathcal{T}_{tdb}}}$ stands for conductor resistivity at the reference temperature. Furthermore, $\{T_{km,i}\}_{i=1}^{N_{\mathcal{T}_{tdb}}}$ denotes the conductor temperature, $\{T_{refkm,i}\}_{i=1}^{N_{\mathcal{T}_{tdb}}}$ is the reference temperature and $\{T_{Fkm,i}\}_{i=1}^{N_{\mathcal{T}_{tdb}}}$ represents the temperature constant that depends on the conductor material [Frank, *et al.*, 2013]:

$$r_{sekm,i}(T_{km,i}) = r_{refkm,i} \frac{T_{km,i}+T_{Fkm,i}}{T_{refkm,i}+T_{Fkm,i}} \quad \forall i = 1,\ldots, N_{\mathcal{T}_{tdb}} . \tag{2.41}$$

The series conductance $g_{sekm,i}(T_{km,i}) : \mathbb{R} \rightarrow \mathbb{R}$ and series susceptance $b_{sekm,i}(T_{km,i}) : \mathbb{R} \rightarrow \mathbb{R}$ of the *i*-th transmission line as a function of conductor temperature are expressed by (2.42) and (2.43), respectively, where $\{x_{sekm,i}\}_{i=1}^{N_{\mathcal{T}_{tdb}}}$ is the series reactance:

$$g_{sekm,i}(T_{km,i}) = \frac{r_{sekm,i}(T_{km,i})}{r_{sekm,i}^2(T_{km,i}) + x_{sekm,i}^2} \quad \forall i=1,\ldots,N_{\mathcal{T}_{tdb}} , \tag{2.42}$$

$$b_{sekm,i}(T_{km,i}) = \frac{-x_{sekm,i}}{r_{sekm,i}^2(T_{km,i}) + x_{sekm,i}^2} \quad \forall i=1,\ldots,N_{\mathcal{T}_{tdb}} . \tag{2.43}$$

The active power flows at both ends of this *i*-th transmission line are represented by (2.44) and (2.45), respectively:

$$\begin{aligned} P_{tbkm,i} = {} & V_{tbk,i}{}^2 g_{sekm,i}(T_{km,i}) \\ & - V_{tbk,i} V_{tbm,i} g_{sekm,i}(T_{km,i}) \cos(\theta_{tbk,i} - \theta_{tbm,i}) \quad \forall i = 1,\ldots, N_{\mathcal{T}_{tdb}} , \\ & - V_{tbk,i} V_{tbm,i} b_{sekm,i}(T_{km,i}) \sin(\theta_{tbk,i} - \theta_{tbm,i}) \end{aligned} \tag{2.44}$$

$$\begin{aligned} P_{tbmk,i} = {} & {V_{tbm,i}}^2 g_{sekm,i}(T_{km,i}) \\ & - V_{tbm,i} V_{tbk,i} g_{sekm,i}(T_{km,i}) \cos(\theta_{tbm,i} - \theta_{tbk,i}) \quad \forall i = 1,\ldots, N_{\mathcal{T}_{tdb}} \, . \\ & - V_{tbm,i} V_{tbk,i} b_{sekm,i}(T_{km,i}) \sin(\theta_{tbm,i} - \theta_{tbk,i}) \end{aligned} \tag{2.45}$$

Consequently, the transmission line's active power loss is given by

$$P_{Losstb,i} = P_{tbkm,i} + P_{tbmk,i} \quad \forall i = 1,\ldots, N_{\mathcal{T}_{tdb}} \, . \tag{2.46}$$

On the other hand, the nominal active power loss of the *i*-th transmission line can be calculated [Frank, *et al.*, 2013] from (2.47), where $\{I_{Ratingkm,i}\}_{i=1}^{N_{\mathcal{T}_{tdb}}}$ and $\{Z_{basekm,i}\}_{i=1}^{N_{\mathcal{T}_{tdb}}}$ represent the current line rating and the base impedance, respectively. Note that these data can be obtained from the system database:

$$P_{RatedLosstb,i} = I_{Ratingkm,i}^2 r_{refkm,i} Z_{basekm,i} \quad \forall i = 1,\ldots, N_{\mathcal{T}_{tdb}} \, . \tag{2.47}$$

Similarly, the ratio of the rated temperature rise to the rated active power loss is referred to as thermal resistance [Frank, *et al.*, 2013], which is mathematically expressed by (2.48). In this case, $\{T_{RatedRisetb,i}\}_{i=1}^{N_{\mathcal{T}_{tdb}}}$ stands for rated temperature rise above the ambient temperature, and $\{P_{RatedLosstb,i}\}_{i=1}^{N_{\mathcal{T}_{tdb}}}$ denotes the rated active power loss:

$$R_{\theta,i} = \frac{T_{RatedRisetb,i}}{P_{RatedLosstb,i}} \quad \forall i = 1,\ldots, N_{\mathcal{T}_{tdb}} \, . \tag{2.48}$$

Neglecting the heat gain caused by solar radiation in the heat balance equation as described in [Frank, *et al.*, 2013], an equation for the conductor temperature that only depends on the transmission line's active power losses is obtained:

$$T_{km,i} - T_{a,i} - P_{Losstb,i} R_{\theta,i} = 0 \quad \forall i = 1,\ldots, N_{\mathcal{T}_{tdb}} \, , \tag{2.49}$$

where $\{T_{a,i}\}_{i=1}^{N_{\mathcal{T}_{tdb}}}$ is the ambient temperature that is considered a known parameter from the system database.

Based on the information mentioned above, the conductor temperature $\{T_{km,i}\}_{i=1}^{N_{\mathcal{T}_{tdb}}}$ can be estimated for each transmission line by including the set of equality constraints (2.49) in the formulation of the static state estimation problem. In this context, the augmented state vector is given by (2.50), where $\boldsymbol{\theta} \in \mathbb{R}^{N_e}$ is the vector of nodal phase angles, $\boldsymbol{V} \in \mathbb{R}^{N_e}$ stands for the vector of nodal voltage magnitudes and $\boldsymbol{T_{km}} \in \mathbb{R}^{N_{\mathcal{T}_{tdb}}}$ is the vector of transmission line temperatures:

$$\boldsymbol{x_{e\text{-}tdb}} = \begin{bmatrix} \boldsymbol{V} & \boldsymbol{\theta} & \boldsymbol{T_{km}} \end{bmatrix}^{\mathrm{T}} \in \mathbb{R}^{2N_e + N_{\mathcal{T}_{tdb}}} . \tag{2.50}$$

Finally, the proposed optimization problem to be solved for the static state and temperature co-estimation is given by (2.51). In this case, $\boldsymbol{J}(\boldsymbol{r}) : \mathbb{R}^M \to \mathbb{R}$ is the objective function of the weighted least squares approach, $\boldsymbol{r} \in \mathbb{R}^M$ is the vector of measurements' residuals and $\boldsymbol{W} = \operatorname{diag}\left\{1/\sigma_i^2\right\}_{i=1}^{M}$ is the measurements' weighting matrix. The set of structural constraints is given by $\boldsymbol{c}(\boldsymbol{x_{e\text{-}tdb}}) : \mathbb{R}^{2N_e + N_{\mathcal{T}_{tdb}}} \to \mathbb{R}^{2N_{tbe}}$, which denotes the set of zero power injections at the transition buses $\mathcal{N}_{tbe} := \{1, 2, \ldots, N_{tbe}\} \ni \mathcal{N}_{tbe} \subset \mathcal{N}_e$ (see Eqs. (C.5) and (C.6) in Appendix C). Furthermore, $\boldsymbol{z} \in \mathbb{R}^M$ is the vector of SCADA and PMU physical measurements, which are obtained from the subsets of observable transmission buses $\mathcal{N}_{oe} := \{1, 2, \ldots, N_{oe}\}$ and observable transmission elements $\mathcal{T}_{oe} := \left\{1, 2, \ldots, N_{\mathcal{T}_{oe}}\right\}$, while $\hat{\boldsymbol{z}}(\boldsymbol{x_{e\text{-}tdb}}) : \mathbb{R}^{2N_e + N_{\mathcal{T}_{tdb}}} \to \mathbb{R}^M$ stands for the vector of estimated measurements. Lastly, $\boldsymbol{T}(\boldsymbol{x_{e\text{-}tdb}}) : \mathbb{R}^{2N_e + N_{\mathcal{T}_{tdb}}} \to \mathbb{R}^{N_{\mathcal{T}_{tdb}}}$ represents the set of constraints imposed by temperatures of transmission, as shown in (2.49) :

$$\begin{aligned} \underset{\boldsymbol{x_{e\text{-}tdb}},\, \boldsymbol{r}}{\arg\min} \quad & \boldsymbol{J}(\boldsymbol{r}) = \frac{1}{2}\boldsymbol{r}^{\mathrm{T}}\boldsymbol{W}\boldsymbol{r} \\ \text{subject to:} \quad & \boldsymbol{c}(\boldsymbol{x_{e\text{-}tdb}}) = \boldsymbol{0} \\ & \boldsymbol{r} - \boldsymbol{z} + \hat{\boldsymbol{z}}(\boldsymbol{x_{e\text{-}tdb}}) = \boldsymbol{0} \\ & \boldsymbol{T}(\boldsymbol{x_{e\text{-}tdb}}) = \boldsymbol{0}. \end{aligned} \tag{2.51}$$

## 2.6.1 Case studies

The general scheme of the Mexican interconnected power system (MIPS) [PRODESEN, 2018] is presented in Fig. 2.5, which encompasses seven regional control areas. The performance of the proposed methodology is shown by analyzing a MIPS 7659-bus model. The proposed approach is implemented by using the mathematical programming language AMPL® [Fourer, *et al*., 2003], while the constrained optimization problem (2.51) is solved through the Knitro® solver [Ziena Optimization LLC, 2014] with an interior point algorithm considering a convergence tolerance of $1\times10^{-4}$. SCADA and PMU measurements are generated by adding Gaussian random noise to the solution of a power flow program that includes conductor temperatures. This program was developed following the approach reported in [Frank, *et al*., 2013]. On the other hand, the material used to build the transmission lines is aluminum such that $\{T_{Fkm,i} = 228.1^\circ \mathrm{C}\}_{i=1}^{N_{\mathcal{T}_{tdb}}}$. Additionally, all transmission lines are subjected to an ambient temperature of $\{T_{a,i} = 25^\circ \mathrm{C}\}_{i=1}^{N_{\mathcal{T}_{tdb}}}$, and the parameters' reference temperature given in the database is equal to the ambient temperature of system lines: $\{T_{refkm,i} = T_{a,i}\}_{i=1}^{N_{\mathcal{T}_{tdb}}}$. Lastly, the rated temperature rise of $\{T_{RatedRisetb,i} = 35^\circ \mathrm{C}\}_{i=1}^{N_{\mathcal{T}_{tdb}}}$ above the ambient temperature is considered for all transmission lines.

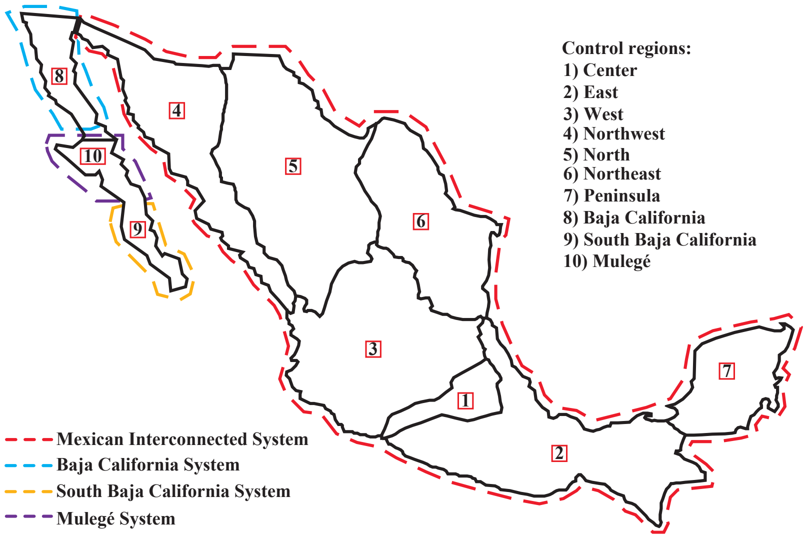

Fig. 2.5 Mexican interconnected power system.

In order to perform the state and parameter co-estimation, the measurement scheme is composed of 32,687 measurements: 2553 nodal voltage magnitude measurements, 9286 active power flows measurements, 9286 reactive power flow measurements, 5106 active power injection measurements, 5106 reactive power injection measurements, 192 PMU measurements of nodal voltage magnitudes, 192 PMU measurements of voltage phase angles, and 483 PMU measurements of real and imaginary components of branch currents, respectively. Since 15,317 algebraic variables must be estimated, the system has a redundancy coefficient of 2.1340. Within this context, the following measurements' standard deviations are considered [Alcaide-Moreno, *et al.*, 2015]: $\left\{\sigma_{V_k^{SCADA}} = 0.004\right\}_{k\in\mathcal{N}_e}$, $\left\{\sigma_{P_{km}^{SCADA}} = 0.008\right\}_{\left(P_{km}^{SCADA}\right)\in\mathcal{T}_e}$, $\left\{\sigma_{Q_{km}^{SCADA}} = 0.008\right\}_{\left(Q_{km}^{SCADA}\right)\in\mathcal{T}_e}$, $\left\{\sigma_{P_k^{SCADA}} = 0.01\right\}_{k\in\mathcal{N}_e}$, $\left\{\sigma_{Q_k^{SCADA}} = 0.01\right\}_{k\in\mathcal{N}_e}$, $\left\{\sigma_{V_k^{PMU}} = 0.002\right\}_{k\in\mathcal{N}_e}$, $\left\{\sigma_{\theta_k^{PMU}} = 0.002\right\}_{k\in\mathcal{N}_e}$, $\left\{\sigma_{\left|I_{km}^{PMU}\right|} = 0.002\right\}_{\left|I_{km}^{PMU}\right|\in\mathcal{T}_e}$ and $\left\{\sigma_{\theta_{I_{km}}^{PMU}} = 0.002\right\}_{\theta_{I_{km}}^{PMU}\in\mathcal{T}_e}$.

To verify that the proposed temperature estimator provides accurate values, Table 2.10 shows the results of estimated values of temperature and series resistance values of the transmission lines that exceed their power ratings with respect to those provided by the temperature-dependent power flow study [Frank, *et al.*, 2013]. The relative percentage errors of the temperatures and series resistances are also shown. As can be observed, the highest temperature error presents a value of 0.8805% and the highest series resistance error is equal to 0.1923%, which implies that the proposed estimator obtains accurate estimates.

Table 2.10 Comparison of temperature-dependent power flow and temperature estimation methodologies.

| **Line number** | **Power flow** | | **Proposed Co-estimation** | | **Error $T_{km}$ (%)** | **Error $r_{km}$ (%)** |
|---|---|---|---|---|---|---|
| | **$T_{km}$ (°C)** | **$r_{km}$ (p.u.)** | **$T_{km}$ (°C)** | **$r_{km}$ (p.u.)** | | |
| 530 | 52.7237 | 0.0013 | 52.9409 | 0.0013 | 0.4118 | 0.0773 |
| 531 | 52.7237 | 0.0013 | 52.9409 | 0.0013 | 0.4118 | 0.0773 |
| 1942 | 60.4434 | 0.0152 | 60.8614 | 0.0152 | 0.6916 | 0.1449 |
| 2139 | 36.9074 | 0.0043 | 36.979 | 0.0043 | 0.1941 | 0.0270 |
| 2144 | 63.2329 | 0.0038 | 63.2304 | 0.0038 | 0.0040 | 0.0009 |
| 2917 | 63.7336 | 0.0014 | 64.2948 | 0.0014 | 0.8805 | 0.1923 |

The estimated values by the proposed approach associated with the operating temperatures and temperature-dependent series resistance parameters are reported in Table 2.11. For the sake of space and the size of the system under analysis, these reported results only correspond to those transmission lines exceeding their nominal ratings. For comparison purposes, the estimated power (MVA) flowing through the overloaded lines according to both the proposed approach and the conventional static state estimation given by (2.5) is also shown in Table 2.11. Within this context, the series resistances in the system database and the power rating value (MVA) of the corresponding transmission line are shown in this table of results. Lastly, the relative percentage error of the estimated value of temperature-dependent series resistance to the value given in the system database is also reported. These results permit us to be aware of the error when considering the database parameters to performing power system studies.

As expected, the line with the highest percentage error of series resistance corresponds to the line with the highest estimated conductor temperature: line 2917. Furthermore, the computed MVA power exceeds some transmission lines' nominal ratings when the operating temperatures are considered as state variables, unlike the results obtained when using the conventional static state estimation. Therefore, it is essential to include conductor temperatures within the state estimation process to monitor transmission line nominal ratings because it can assist control center operators in detecting an electric power system's insecure operating condition.

Table 2.11 Results of the proposed temperature estimator for the Mexican-7659 bus power system.

| **Line number** | **Database $r_{km}$ (p.u.)** | **Estimated values** | | **Error $r_{km}$ (%)** | **Estimated power** | | **Rating (MVA)** |
|---|---|---|---|---|---|---|---|
| | | **$T_{km}$ (°C)** | **$r_{km}$ (p.u.)** | | **Without $T_{km}$ (MVA)** | **With $T_{km}$ (MVA)** | |
| 530 | 0.0012 | 52.9409 | 0.0013 | 11.0395 | 59.1970 | 62.3447 | 61.9506 |
| 531 | 0.0012 | 52.9409 | 0.0013 | 11.0395 | 59.1970 | 62.3447 | 61.9506 |
| 1942 | 0.0133 | 60.8614 | 0.0152 | 14.1689 | 70.8344 | 74.9609 | 74.1151 |
| 2139 | 0.0041 | 36.9790 | 0.0043 | 4.7329 | 115.6092 | 121.6621 | 121.3410 |
| 2144 | 0.0033 | 63.2304 | 0.0038 | 15.1049 | 422.5479 | 445.0359 | 443.7594 |
| 2917 | 0.0012 | 64.2948 | 0.0014 | 15.5254 | 166.0968 | 178.0187 | 173.3217 |

## 2.7 Conclusions

First, a comparative study of three WLS-based simultaneous state and parameter estimation methods at the system level has been performed in this thesis by using a hybrid set of SCADA and PMU measurements. The main difference between these methodologies is the type of variables incorporated into the optimization problem of static state estimation. Methodology 1 uses admittances of the π model of transmission lines. Furthermore, methodology 2 uses normalized line lengths, and methodology 3 uses power flows of the associated π circuit as variables to be estimated. Numerical results showed that methodology 2 is the best approach for estimating parameters of several transmission lines because it provides the smallest percentage error values of parameter estimations with respect to the nominal database values. In addition, methodology 2 does not significantly increase the size of the state vector to be estimated; consequently, it provides the best redundancy level of all methodologies considered.

On the other hand, a static estimator that simultaneously estimates the system's operating state and breakers' statuses by using a hybrid set of SCADA and PMU measurements is proposed in this thesis. The novelty of this proposal is as follows. Firstly, two new operating constraints for each breaker with unknown status are proposed based on the complementarity approach. Secondly, the proposed breakers' operating constraints are directly included in the static state estimation problem as equality constraints derived by employing the Fischer-Burmeister merit function. Lastly, the unknown statuses of breakers are directly estimated together with nodal voltages in a unified framework of analysis. The results numerically demonstrate that the proposed approach can satisfactorily estimate the breakers' statuses considering a given measurement redundancy, even though all circuit breakers at power substations included in the system are initially considered as unknown.

Finally, a methodology is proposed for the state and transmission line temperature co-estimation by using a hybrid set of SCADA and PMU measurements. This is achieved by including a temperature-based equality constraints to the static state estimation problem. The numerical results show that some lines violate their nominal transmission ratings by regarding the effect of temperature compared with the case where this variable is not considered within the static state estimation. These results validate the need to consider the temperature dependence of transmission lines for the appropriate power system security assessment.

# Chapter

# 3 Transient stability assessment considering hard limits on dynamic states

## 3.1 Introduction

This chapter centers on presenting a fundamentally different, comprehensive and general approach for directly including hard limits of controllers in the formulation and solution of the transient stability problem. Within this context three main specific contributions are presented as follows. Firstly, hard limits are simultaneously and automatically checked and, when applicable, enforced or liberated at each step of the time-domain simulation. Secondly, the solution process is not reinitialized at the time at which a non-windup controller changes its control operating mode because the system's dynamic structure remains unaltered during the entire time-domain simulation: differential equations are not transformed into algebraic equations and vice versa. Lastly, the proposal does not require adjustments of parameter values to correctly represent hard limits, unlike the approach that uses saturation functions for the treatment of limits.

## 3.2 Dynamic modeling of power systems

Power system stability is generally defined as [Kundur, 1994]: *"the property of a power system that enables it to remain in a state of operating equilibrium under normal operating conditions and to regain an acceptable state of equilibrium after being subjected to a disturbance"*. Examples of large disturbances in power systems can be faults in the transmission network or the shutdown of a major generating unit. In the area of rotor angle stability, [Anderson & Fouad, 2003] stated: *"If one of these large impacts occurs, the synchronous machines may lose synchronism. This problem is referred to in the literature as the transient stability problem"*. This chapter is focused in this area of study.

The power grid electromechanical dynamics with constrained dynamics states is mathematically described by a set of differential-algebraic equations (DAEs) with double-sided inequality constraints (DSICs) given by

$$
\begin{aligned}
&\dot{\boldsymbol{\gamma}} = \boldsymbol{f}(\boldsymbol{x},\boldsymbol{y},\boldsymbol{\beta},\boldsymbol{\tau},\boldsymbol{\mu}) \qquad \boldsymbol{f}:\mathbb{R}^{n+w+p+2N_{wl}} \rightarrow \mathbb{R}^{n+N_{wl}}\\
&\dot{\boldsymbol{\psi}}_{\boldsymbol{nwl}} = \boldsymbol{f}_{\boldsymbol{nwl}}(\boldsymbol{x},\boldsymbol{y},\boldsymbol{\beta},\boldsymbol{\psi}) \quad \boldsymbol{f}_{\boldsymbol{nwl}}:\mathbb{R}^{n+w+p+N_{nwl}} \rightarrow \mathbb{R}^{N_{nwl}}\\
&\mathbf{0} = \boldsymbol{g}(\boldsymbol{x},\boldsymbol{y},\boldsymbol{\beta}) \qquad \boldsymbol{g}:\mathbb{R}^{n+w+p} \rightarrow \mathbb{R}^{w}\\
&\boldsymbol{\psi}^{\mathbf{min}} \le \boldsymbol{\psi} \le \boldsymbol{\psi}^{\mathbf{max}}\\
&\boldsymbol{\mu}^{\mathbf{min}} \le \boldsymbol{\mu} \le \boldsymbol{\mu}^{\mathbf{max}}\\
&\boldsymbol{x} \in \mathrm{X}_{de} \subset \mathbb{R}^{n} \quad \boldsymbol{y} \in \Upsilon_{ae} \subset \mathbb{R}^{w} \quad \boldsymbol{\beta} \in \mathrm{B}_{pe} \subset \mathbb{R}^{p}\\
&\boldsymbol{\psi} \in \Psi_{N_{nwl}} \subset \mathbb{R}^{N_{nwl}} \quad \boldsymbol{\tau} \in \mathrm{T}_{N_{wl}} \subset \mathbb{R}^{N_{wl}} \quad \boldsymbol{\mu} \in \mathrm{M}_{N_{wl}} \subset \mathbb{R}^{N_{wl}}.
\end{aligned} \tag{3.1}
$$

In the parameter-state space of $\mathrm{X}_{de}$, $\Upsilon_{ae}$, $\mathrm{B}_{pe}$, $\Psi_{N_{nwl}}$, $\mathrm{T}_{N_{wl}}$ and $\mathrm{M}_{N_{wl}}$, $\boldsymbol{x}$ is the vector of dynamic states related to both generators and all controllers without non-windup and windup limiters, while the vectors $\boldsymbol{\psi}$ and $\boldsymbol{\tau}$ correspond to the controllers outputs with non-windup and windup limiters, respectively. Furthermore $\boldsymbol{\mu}$ corresponds to the dummy variables' vector located at windup limiters outputs which are used to obtain limited values of dynamic states in a transient stability study. On the other hand, $\boldsymbol{y}$ is the vector of network's algebraic variables that change instantaneously with variations of dynamic states, while $\boldsymbol{\beta}$ is a vector of time-invariant parameters associated with control devices and electrical components of the transmission grid. The rate of change of $\boldsymbol{x}$, $\boldsymbol{\tau}$ and $\boldsymbol{\mu}$ is explicitly modelled by the set of functions $\dot{\boldsymbol{\gamma}} = \boldsymbol{f}(\boldsymbol{x},\boldsymbol{y},\boldsymbol{\beta},\boldsymbol{\tau},\boldsymbol{\mu})$, while the dynamics of non-windup limiters' outputs $\boldsymbol{\psi}$ are modelled by $\dot{\boldsymbol{\psi}}_{\boldsymbol{nwl}} = \boldsymbol{f}_{\boldsymbol{nwl}}(\boldsymbol{x},\boldsymbol{y},\boldsymbol{\beta},\boldsymbol{\psi})$. All these dynamics evolutions are constrained by algebraic equations $\mathbf{0} = \boldsymbol{g}(\cdot) = \boldsymbol{g}(\boldsymbol{x},\boldsymbol{y},\boldsymbol{\beta})$ representing both the power interchange between synchronous machine stators and the transmission system, as well as power balance equations in each network's node. Furthermore, those dynamics are also constrained by the double-sided inequality constraints $\boldsymbol{\psi}^{\mathbf{min}} \le \boldsymbol{\psi} \le \boldsymbol{\psi}^{\mathbf{max}}$ and $\boldsymbol{\mu}^{\mathbf{min}} \le \boldsymbol{\mu} \le \boldsymbol{\mu}^{\mathbf{max}}$, which impose the upper and lower physical bounds associated with non-windup and windup limiters, respectively. These hard limits are shown in Fig. 3.1 (a) and Fig. 3.1(b), respectively.

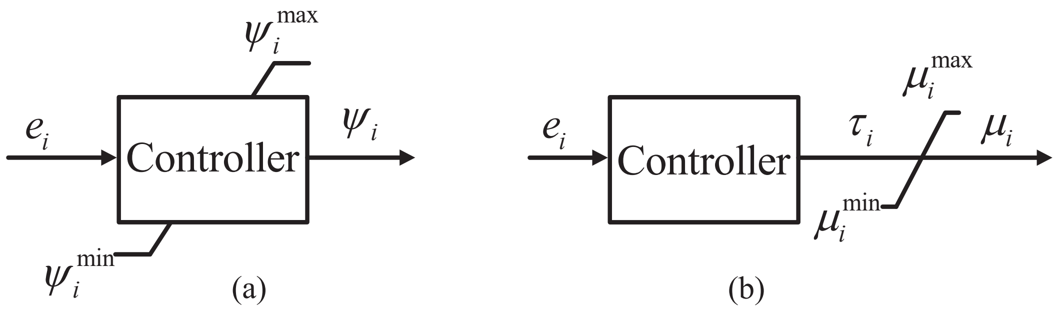

Fig. 3.1 (a) *i*-th non-windup limiter and (b) *i*-th windup limiter.

When the controller's output of the *i*-th non-windup limiter reaches one of its limits, it is set at the violated limit until the derivative of $\psi_i$ changes sign [Milano, 2010]. As long as the value of $\psi_i$ remains constant, the system dynamics reduce its dimension in one: $d\psi_i/dt = 0$. On the other hand, in the *i*-th windup limiter, the controller's output $\tau_i$ is not limited, but if its value is out of the range of limits, the dummy variable $\mu_i$ is set to the violated limit: if $\tau_i > \mu_i^{\max}$ (resp. $\tau_i < \mu_i^{\min}$), $\mu_i = \mu_i^{\max}$ (resp. $\mu_i = \mu_i^{\min}$). The limitation ceases as soon as the value of $\tau_i$ is back within limits: if $\mu_i^{\min} \le \tau_i \le \mu_i^{\max}$ such that $\mu_i = \tau_i$. Note that all the aforementioned operations are traditionally performed based on "if" conditional tests, which are the guiding principle for conducting limit revisions in transient stability simulations.

## 3.3 Representation of hard limits on dynamic states

By applying the concepts described in Section 2.3, the new representations of non-windup and windup limiters based on complementarity are obtained as shown in Fig. 3.2 (a) and Fig. 3.2 (b), respectively.

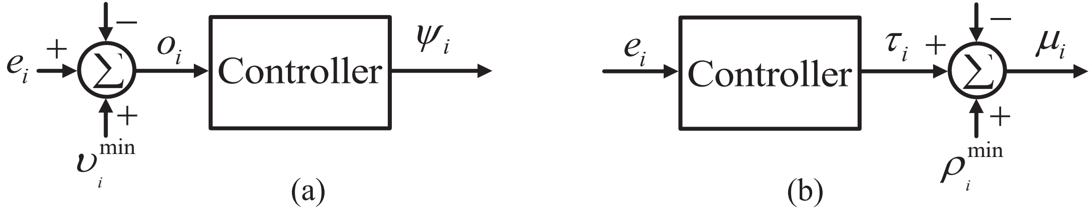

Fig. 3.2 (a) *i*-th complementarity-based non-windup limiter and
(b) *i*-th complementarity-based windup limiter.

Consequently, by applying the complementarity condition, the DSICs $\boldsymbol{\psi}^{\mathbf{min}} \leq \boldsymbol{\psi} \leq \boldsymbol{\psi}^{\mathbf{max}}$ are replaced by (3.2) and (3.3), while $\boldsymbol{\mu}^{\mathbf{min}} \leq \boldsymbol{\mu} \leq \boldsymbol{\mu}^{\mathbf{max}}$ are substituted by (3.4) and (3.5):

$$0 \leq \left(\psi_i^{\max} - \psi_i\right) \perp \left(\upsilon_i^{\max}\right) \geq 0 \Leftrightarrow \left(\psi_i^{\max} - \psi_i\right) \upsilon_i^{\max} = 0 \quad \forall i = 1, ..., \mathbb{R}^{N_{nwl}}, \tag{3.2}$$

$$0 \leq \left(\psi_i - \psi_i^{\min}\right) \perp \left(\upsilon_i^{\min}\right) \geq 0 \Leftrightarrow \left(\psi_i - \psi_i^{\min}\right) \upsilon_i^{\min} = 0 \quad \forall i = 1, ..., \mathbb{R}^{N_{nwl}}, \tag{3.3}$$

$$0 \leq \left(\mu_i^{\max} - \mu_i\right) \perp \left(\rho_i^{\max}\right) \geq 0 \Leftrightarrow \left(\mu_i^{\max} - \mu_i\right) \rho_i^{\max} = 0 \quad \forall i = 1, ..., \mathbb{R}^{N_{wl}}, \tag{3.4}$$

$$0 \leq \left(\mu_i - \mu_i^{\min}\right) \perp \left(\rho_i^{\min}\right) \geq 0 \Leftrightarrow \left(\mu_i - \mu_i^{\min}\right) \rho_i^{\min} = 0 \quad \forall i = 1, ..., \mathbb{R}^{N_{wl}}. \tag{3.5}$$

Note that the above equations consider four new vectors of complementarity variables: $\boldsymbol{\upsilon}^{\mathbf{max}}$, $\boldsymbol{\upsilon}^{\mathbf{min}} \in \mathbb{R}^{N_{nwl}}$ for non-windup limiters and $\boldsymbol{\rho}^{\mathbf{max}}$, $\boldsymbol{\rho}^{\mathbf{min}} \in \mathbb{R}^{N_{wl}}$ for windup limiters. In the complementarity representation of a non-windup limiter, the controller's input $e_i$ is altered by including $\upsilon_i^{\max}$ and $\upsilon_i^{\min}$, as shown in Fig. 3.2 (a), such that the new controller input $o_i$ is equal to $o_i = e_i + \upsilon_i^{\min} - \upsilon_i^{\max}$. At the time at which $\psi_i > \psi_i^{\max}$ during the numerical solution of the transient stability problem, the values of the complementarity variables provided by the solution are $\upsilon_i^{\min} = 0$ and $\upsilon_i^{\max} > 0$. Since $\upsilon_i^{\max} > 0$, $\psi_i$ is automatically set to the violated limit to satisfy (3.2): $\psi_i = \psi_i^{\max}$. In this case, the input $o_i$ is also reduced to a value $o_i = e_i - \upsilon_i^{\max}$ that causes $d\psi_i / dt = 0$ to be satisfied for the period of time in which $\psi_i$ remains fixed at the limit value. These numerical results are maintained until $d\psi_i / dt$ evolves in a direction opposite to that which caused the limit violation, which occurs when $\upsilon_i^{\max}$ is newly 0. A similar line of reasoning applies when $\psi_i < \psi_i^{\min}$.

On the other hand, the windup controller's output $\tau_i$ is not limited and is free to vary. Furthermore, the variables $\rho_i^{\min}$ and $\rho_i^{\max}$ change the dummy variable $\mu_i$ of the *i*-th windup limiter such that the algebraic equation that relates $\mu_i$ and $\tau_i$ is $\eta_i(\mu_i, \tau_i, \rho_i) = \mu_i - \tau_i - \rho_i^{\min} + \rho_i^{\max} = 0$. Lastly, the limiter action is as follows. If

$\mu_i^{\min} \le \tau_i \le \mu_i^{\max}, \rho_i^{\max} = \rho_i^{\min} = 0$; however, if $\tau_i > \mu_i^{\max}$ (resp. $\tau_i < \mu_i^{\min}$), $\mu_i = \mu_i^{\max}$ and $\rho_i^{\max} > 0$ (resp. $\mu_i = \mu_i^{\min}$ and $\rho_i^{\min} > 0$) [Romay, *et al.*, 2021]. Limiting ceases only when the value of $\tau_i$ newly comes within limits.

Lastly, Eqs. (3.2) to (3.5) are transformed to equality constraints (3.6) to (3.9) by applying the Fischer-Burmeister merit function and considering positive square roots:

$$\varphi_i^{\max} = \sqrt{\left(\psi_i^{\max} - \psi_i\right)^2 + \left(\upsilon_i^{\max}\right)^2} - \left(\psi_i^{\max} - \psi_i\right) - \left(\upsilon_i^{\max}\right) = 0 \quad \forall i = 1,\ldots,\mathbb{R}^{N_{nwl}}, \tag{3.6}$$

$$\varphi_i^{\min} = \sqrt{\left(\psi_i - \psi_i^{\min}\right)^2 + \left(\upsilon_i^{\min}\right)^2} - \left(\psi_i - \psi_i^{\min}\right) - \left(\upsilon_i^{\min}\right) = 0 \quad \forall i = 1,\ldots,\mathbb{R}^{N_{nwl}}, \tag{3.7}$$

$$\phi_i^{\max} = \sqrt{\left(\mu_i^{\max} - \mu_i\right)^2 + \left(\rho_i^{\max}\right)^2} - \left(\mu_i^{\max} - \mu_i\right) - \left(\rho_i^{\max}\right) = 0 \quad \forall i = 1,\ldots,\mathbb{R}^{N_{wl}}, \tag{3.8}$$

$$\phi_i^{\min} = \sqrt{\left(\mu_i - \mu_i^{\min}\right)^2 + \left(\rho_i^{\min}\right)^2} - \left(\mu_i - \mu_i^{\min}\right) - \left(\rho_i^{\min}\right) = 0 \quad \forall i = 1,\ldots,\mathbb{R}^{N_{wl}}. \tag{3.9}$$

## 3.4 Generalized formulation of the transient stability problem with hard limits

The set of complementarity constraints (3.6) and (3.7) for non-windup limiters are grouped in a single vector $\boldsymbol{\varphi}_{\boldsymbol{nwl}} = \left[\boldsymbol{\varphi}^{\mathbf{max}} \ \boldsymbol{\varphi}^{\mathbf{min}}\right]^{\mathrm{T}} \in \mathbb{R}^{2N_{nwl}}$, while the complementarity constraints (3.8) and (3.9) for windup limiters are merged in a vector $\boldsymbol{\phi}_{\boldsymbol{wl}} = \left[\boldsymbol{\phi}^{\mathbf{max}} \ \boldsymbol{\phi}^{\mathbf{min}}\right]^{\mathrm{T}} \in \mathbb{R}^{2N_{wl}}$. Furthermore, the vectors of complementarity variables for the non-windup and windup limiters are denoted by $\boldsymbol{\upsilon} = \left[\boldsymbol{\upsilon}^{\mathbf{max}} \ \boldsymbol{\upsilon}^{\mathbf{min}}\right]^{\mathrm{T}} \in \mathbb{R}^{2N_{nwl}}$ and $\boldsymbol{\rho} = \left[\boldsymbol{\rho}^{\mathbf{max}} \ \boldsymbol{\rho}^{\mathbf{min}}\right]^{\mathrm{T}} \in \mathbb{R}^{2N_{wl}}$, respectively. Additionally, $\boldsymbol{\eta}_{\boldsymbol{wl}} \in \mathbb{R}^{N_{wl}}$ is a vector that gathers the algebraic equations of windup limiters: $\{\eta_i(\mu_i, \tau_i, \rho_i) = \mu_i - \tau_i - \rho_i^{\min} + \rho_i^{\max} = 0\}_{i=1}^{N_{wl}}$. Based on the aforementioned, the proposed set of differential-algebraic equations based on complementarity constraints is obtained for the treatment of hard limits on dynamic states as follows:

$$
\begin{array}{ll}
\dot{\boldsymbol{\gamma}} = \boldsymbol{f}(\boldsymbol{x},\boldsymbol{y},\boldsymbol{\beta},\boldsymbol{\tau},\boldsymbol{\mu}) & \boldsymbol{f}:\mathbb{R}^{n+w+p+2N_{wl}} \rightarrow \mathbb{R}^{n+N_{wl}} \\
\dot{\boldsymbol{\psi}}_{\boldsymbol{nwl}} = \boldsymbol{f}_{\boldsymbol{nwl}}(\boldsymbol{x},\boldsymbol{y},\boldsymbol{\beta},\boldsymbol{\psi},\boldsymbol{\upsilon}) & \boldsymbol{f}_{\boldsymbol{nwl}}:\mathbb{R}^{n+w+p+3N_{nwl}} \rightarrow \mathbb{R}^{N_{nwl}} \\
\mathbf{0} = \boldsymbol{g}(\boldsymbol{x},\boldsymbol{y},\boldsymbol{\beta}) & \boldsymbol{g}:\mathbb{R}^{n+w+p} \rightarrow \mathbb{R}^{w} \\
\mathbf{0} = \boldsymbol{\eta}_{\boldsymbol{wl}}(\boldsymbol{\tau},\boldsymbol{\mu},\boldsymbol{\rho}) & \boldsymbol{\eta}_{\boldsymbol{wl}}:\mathbb{R}^{4N_{wl}} \rightarrow \mathbb{R}^{N_{wl}} \\
\mathbf{0} = \varphi_{\boldsymbol{nwl}}(\boldsymbol{\psi},\boldsymbol{\upsilon}) & \varphi_{\boldsymbol{nwl}}:\mathbb{R}^{3N_{nwl}} \rightarrow \mathbb{R}^{2N_{nwl}} \\
\mathbf{0} = \boldsymbol{\phi}_{\boldsymbol{wl}}(\boldsymbol{\mu},\boldsymbol{\rho}) & \boldsymbol{\phi}_{\boldsymbol{wl}}:\mathbb{R}^{3N_{wl}} \rightarrow \mathbb{R}^{2N_{wl}} \\
\multicolumn{2}{l}{\boldsymbol{x}\in \mathrm{X}_{de} \subset \mathbb{R}^{n} \quad \boldsymbol{y}\in \Upsilon_{ae} \subset \mathbb{R}^{w} \quad \boldsymbol{\beta}\in \mathrm{B}_{pe} \subset \mathbb{R}^{p}} \\
\multicolumn{2}{l}{\boldsymbol{\psi}\in \Psi_{N_{nwl}} \subset \mathbb{R}^{N_{nwl}} \quad \boldsymbol{\tau}\in \mathrm{T}_{N_{wl}} \subset \mathbb{R}^{N_{wl}} \quad \boldsymbol{\mu}\in \mathrm{M}_{N_{wl}} \subset \mathbb{R}^{N_{wl}}} \\
\multicolumn{2}{l}{\quad\quad \boldsymbol{\upsilon}\in \mathrm{U}_{N_{nwl}} \subset \mathbb{R}^{2N_{nwl}} \quad \boldsymbol{\rho}\in \mathrm{P}_{N_{wl}} \subset \mathbb{R}^{2N_{wl}},}
\end{array}
\tag{3.10}
$$

where the DSICs $\boldsymbol{\psi}^{\mathbf{min}} \leq \boldsymbol{\psi} \leq \boldsymbol{\psi}^{\mathbf{max}}$ are replaced by the complementarity constraint equations $\boldsymbol{\varphi}_{\boldsymbol{nwl}}$. Similarly, the set of DSICs $\boldsymbol{\mu}^{\mathbf{min}} \leq \boldsymbol{\mu} \leq \boldsymbol{\mu}^{\mathbf{max}}$ is replaced by $\boldsymbol{\phi}_{\boldsymbol{wl}}$, while the set of algebraic equations $\boldsymbol{\eta}_{\boldsymbol{wl}}(\boldsymbol{\tau},\boldsymbol{\mu},\boldsymbol{\rho})$ relating to the output and dummy variables in the windup limiters, i.e., $\boldsymbol{\mu}$ and $\boldsymbol{\tau}$, has also been added to the set of equations (3.10).

The set of differential-algebraic equations (3.10) is converted into a set of difference-algebraic equations, in which the trapezoidal rule is applied to algebraize all differential equations, except the ones associated with non-windup controllers $\dot{\boldsymbol{\psi}}_{\boldsymbol{nwl}} = \boldsymbol{f}_{\boldsymbol{nwl}}(\boldsymbol{x},\boldsymbol{y},\boldsymbol{\beta},\boldsymbol{\psi},\boldsymbol{\upsilon})$ for a time-domain (TD) simulation. This last set of differential equations requires special treatment to avoid possible inaccuracies in the calculated values of $\{\psi_i\}_{i=1}^{N_{nwl}}$, particularly during the switching operations that occur at the inception and clearing of faults with values of the complementarity variables higher than 0. In this case, $\boldsymbol{f}_{\boldsymbol{nwl}}(\boldsymbol{x},\boldsymbol{y},\boldsymbol{\beta},\boldsymbol{\psi},\boldsymbol{\upsilon})$ is split into two terms: $\boldsymbol{f}_{\boldsymbol{nwl}}(.) = \boldsymbol{u}(\boldsymbol{x},\boldsymbol{y},\boldsymbol{\beta},\boldsymbol{\psi}) + \boldsymbol{q}(\boldsymbol{\beta},\boldsymbol{\upsilon})$, which is algebraized by using the trapezoidal and backward Euler rules, respectively, for the entire period of study [Romay, *et al.*, 2021]. Based on the aforementioned, the resulting set of nonlinear difference-algebraic equations are given by (3.11), where $\Delta t$ is the integration time step, and the superscripts $k+1$ and $k$ denote the time instants $t_{k+1}$ and $t_k$, respectively, at which functions and variables are evaluated. Furthermore, the subscripts $nwl$ and $wl$ denote non-windup and windup limiters, respectively. Lastly, $N_{nwl}$ and $N_{wl}$ symbolize the number of non-windup and windup limiters, respectively:

$$\begin{aligned}
&\boldsymbol{F}_1(\cdot)=\boldsymbol{\gamma}^{k+1}-\boldsymbol{\gamma}^{k}-0.5\Delta t(\boldsymbol{f}(\cdot)^{k+1}+\boldsymbol{f}(\cdot)^{k})=\mathbf{0} && \boldsymbol{F}_1(\cdot):\mathbb{R}^{n+w+p+2N_{wl}}\rightarrow\mathbb{R}^{n+N_{wl}}\\
&\boldsymbol{F}_2(\cdot)=\boldsymbol{\psi}_{nwl}^{k+1}-\boldsymbol{\psi}_{nwl}^{k}-0.5\Delta t(\boldsymbol{u}(\cdot)^{k+1}+\boldsymbol{u}(\cdot)^{k})-\Delta t\boldsymbol{q}(\boldsymbol{\beta},\boldsymbol{\upsilon})^{k+1}=\mathbf{0} && \boldsymbol{F}_2(\cdot):\mathbb{R}^{n+w+p+3N_{nwl}}\rightarrow\mathbb{R}^{N_{nwl}}\\
&\mathrm{G}(\cdot)=\boldsymbol{g}(\boldsymbol{x},\boldsymbol{y},\boldsymbol{\beta})^{k+1}=\mathbf{0} && \mathrm{G}(\cdot):\mathbb{R}^{n+w+p}\rightarrow\mathbb{R}^{w}\\
&\boldsymbol{\eta}_{wl}(\cdot)=\boldsymbol{\eta}_{wl}(\boldsymbol{\tau},\boldsymbol{\mu},\boldsymbol{\rho})^{k+1}=\mathbf{0} && \boldsymbol{\eta}_{wl}(\cdot):\mathbb{R}^{4N_{wl}}\rightarrow\mathbb{R}^{N_{wl}}\\
&\varphi_{nwl}(\cdot)=\varphi_{nwl}(\boldsymbol{\psi},\boldsymbol{\upsilon})^{k+1}=\mathbf{0} && \varphi_{nwl}(\cdot):\mathbb{R}^{3N_{nwl}}\rightarrow\mathbb{R}^{2N_{nwl}}\\
&\boldsymbol{\phi}_{wl}(\cdot)=\boldsymbol{\phi}_{wl}(\boldsymbol{\mu},\boldsymbol{\rho})^{k+1}=\mathbf{0} && \boldsymbol{\phi}_{wl}(\cdot):\mathbb{R}^{3N_{wl}}\rightarrow\mathbb{R}^{2N_{wl}}.
\end{aligned}\tag{3.11}$$

This proposed approach directly incorporates the limits on controllers' dynamic states as part of the formulation of the transient stability problem. In this context, dynamic and algebraic state variables are grouped into the vector $\boldsymbol{x}_{tsa}\in\mathbb{R}^{n+w+3N_{nwl}+4N_{wl}}$ as shown in (3.12) , where $\boldsymbol{x}$, $\boldsymbol{\psi}$ and $\boldsymbol{\tau}$ are added in $\boldsymbol{x}_{de}$. On the other hand, $\boldsymbol{y}$ and $\boldsymbol{\mu}$ are appended to $\boldsymbol{y}_{ae}$, while $\boldsymbol{\upsilon}$ and $\boldsymbol{\rho}$ are grouped into $\boldsymbol{\xi}_{cc}$:

$$\boldsymbol{x}_{tsa}=\begin{bmatrix}\boldsymbol{x}_{de} & \boldsymbol{y}_{ae} & \boldsymbol{\xi}_{cc}\end{bmatrix}^{\mathrm{T}}.\tag{3.12}$$

By merging $\boldsymbol{F}_1(\cdot)$ and $\boldsymbol{F}_2(\cdot)$ in one single set of difference equations $\boldsymbol{\Gamma}(\cdot):\mathbb{R}^{n+w+p+2N_{wl}+3N_{nwl}}\rightarrow\mathbb{R}^{n+N_{wl}+N_{nwl}}$ and all algebraic equations of $\boldsymbol{\eta}_{wl}(\cdot)$, $\boldsymbol{\varphi}_{nwl}(\cdot)$ and $\boldsymbol{\phi}_{wl}(\cdot)$ that are associated with hard limits in another one single set denoted by $\boldsymbol{\Phi}(\cdot):\mathbb{R}^{3N_{nwl}+4N_{wl}}\rightarrow\mathbb{R}^{2N_{nwl}+3N_{wl}}$, the Newton-Raphson (NR) algorithm provides a unified solution of (3.11) for both dynamic and algebraic state variables $\boldsymbol{x}_{tsa}$ at a given time instant $k+1$ by iteratively solving the linearized problem given in (3.13). In this case, the set $\boldsymbol{G}(\cdot):\mathbb{R}^{n+w+p}\rightarrow\mathbb{R}^{w}$ is composed of all algebraic nodal power mismatch equations and the power exchanged between synchronous machines and the transmission system. Furthermore, the vector $\{\boldsymbol{F}(\boldsymbol{x}_{tsa})\}_{k+1}^{i}\in\mathbb{R}^{n+w+3N_{nwl}+4N_{wl}}$ is given by (3.14), and the Jacobian matrix $\{\boldsymbol{J}\}_{k+1}^{i}\in\mathbb{R}^{(n+w+3N_{nwl}+4N_{wl})\times(n+w+3N_{nwl}+4N_{wl})}$ is given in (3.15), while the vector of increments in dynamic and algebraic variables $\{\Delta\boldsymbol{x}_{tsa}\}_{k+1}^{i}\in\mathbb{R}^{n+w+3N_{nwl}+4N_{wl}}$ is reported in (3.16). Lastly, $\{\boldsymbol{x}_{tsa}\}_{k+1}^{i}$ is updated by $\{\boldsymbol{x}_{tsa}\}_{k+1}^{i}=\{\boldsymbol{x}_{tsa}\}_{k+1}^{i-1}+\{\Delta\boldsymbol{x}_{tsa}\}_{k+1}^{i}$ during the iterative solution process until the convergence's test $\max(\mathrm{abs}(\{\Delta\boldsymbol{x}_{tsa}\}_{k+1}^{i}))\leq\mathrm{tol}$ is satisfied:

$$\{\boldsymbol{J}\}_{k+1}^{i}\{\Delta\boldsymbol{x}_{tsa}\}_{k+1}^{i}=-\{\boldsymbol{F}(\boldsymbol{x}_{tsa})\}_{k+1}^{i}\,, \tag{3.13}$$

$$\{\boldsymbol{F}(\boldsymbol{x}_{tsa})\}_{k+1}^{i}=\begin{bmatrix}\boldsymbol{\Gamma}(\cdot) & \boldsymbol{G}(\cdot) & \boldsymbol{\Phi}(\cdot)\end{bmatrix}_{k+1}^{i,\mathrm{T}}, \tag{3.14}$$

$$\{\boldsymbol{J}\}_{k+1}^{i}=\begin{bmatrix}\partial\boldsymbol{\Gamma}^{k+1}/\partial\boldsymbol{x}_{de} & \partial\boldsymbol{\Gamma}^{k+1}/\partial\boldsymbol{y}_{ae} & \partial\boldsymbol{\Gamma}^{k+1}/\partial\boldsymbol{\xi}_{cc}\\ \partial\boldsymbol{G}^{k+1}/\partial\boldsymbol{x}_{de} & \partial\boldsymbol{G}^{k+1}/\partial\boldsymbol{y}_{ae} & \boldsymbol{0}\\ \partial\boldsymbol{\Phi}^{k+1}/\partial\boldsymbol{x}_{de} & \partial\boldsymbol{\Phi}^{k+1}/\partial\boldsymbol{y}_{ae} & \partial\boldsymbol{\Phi}^{k+1}/\partial\boldsymbol{\xi}_{cc}\end{bmatrix}^{i}, \tag{3.15}$$

$$\{\Delta\boldsymbol{x}_{tsa}\}_{k+1}^{i}=\begin{bmatrix}\Delta\boldsymbol{x}_{de} & \Delta\boldsymbol{y}_{ae} & \Delta\boldsymbol{\xi}_{cc}\end{bmatrix}_{k+1}^{i,\mathrm{T}}. \tag{3.16}$$

Please note that the proposed transient stability problem represented by (3.13) increases the dimension of the traditional transient stability problem given in (3.1) by $2N_{nwl}+3N_{wl}$ algebraic equations, where the system of equations is completely determined because the same number of algebraic variables are added to the problem. The application of the proposed approach implemented in a program using the MATLAB® platform, however, has been satisfactorily performed by using a conventional computing system with Intel Core i7 @ 2.93 GHz and 8 GB of RAM memory.

## 3.5 Case studies

### 3.5.1 WSCC 3-Machine, 9-bus power system

The effectiveness of the proposed approach is numerically illustrated in the 3-machine, 9-bus WSCC system [Sauer & Pai, 1998], which is presented in Fig. 3.3. This system is composed of 9 buses, 3 synchronous machines, 6 transmission lines and 3 power transformers. The two-axis generator model [Sauer & Pai, 1998] adopted in this thesis is equipped with the excitation system IEEE DC1A [IEEE Power and Energy Society, 2016], a mechanical-hydraulic speed-governing system and a tandem-compound, single reheat steam turbine [IEEE Committee Report, 1973]. The excitation system's amplifiers have non-windup limiters for maintaining their voltage magnitudes outputs within the range of $0\le V_{R,i}\le 2.5\,\text{p.u.},\ \forall i=1,2,3.$ On the other hand, each governor-controlled valve at the inlet of the steam turbine has a windup limitation in obtaining mechanical power between specified limits of $0\le P_{gov,i}\le 1.7\,\text{p.u.},\ \forall i=1,2,3.$

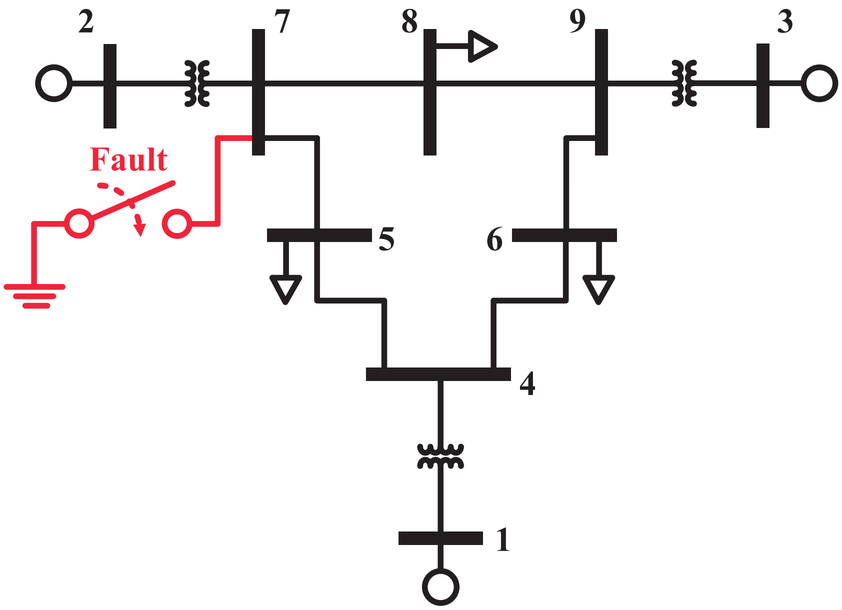

Fig. 3.3 One-line diagram of WSCC 9-bus power system.

From a steady-state operating point obtained from a power flow study, a self-clearing fault is simulated at bus 7 as shown in Fig. 3.3, which is incepted at $t = 10$ s and cleared after 8 cycles. For this contingency, a transient stability study is performed by solving the proposed Newton-based formulation (3.13) at each time instant $k+1$ for a time period of 40 s with a time step $\Delta t = 0.01$ s. The tolerance for the convergence's test $\max(\mathrm{abs}(\{\Delta \boldsymbol{x}_{tsa}\}_{k+1}^{i})) \leq \mathrm{tol}$ is set to $\mathrm{tol} = 1 \times 10^{-5}$. To validate the results obtained with the proposed approach, the case study is also simulated in the Simulink® environment by using its own user models for representing the aforementioned controllers and limiters. Please note that in the Simulink®-based simulation, limits are checked by using conditional tests and the concept of zero-crossing [The MathWorks, Inc., 1990-2004].

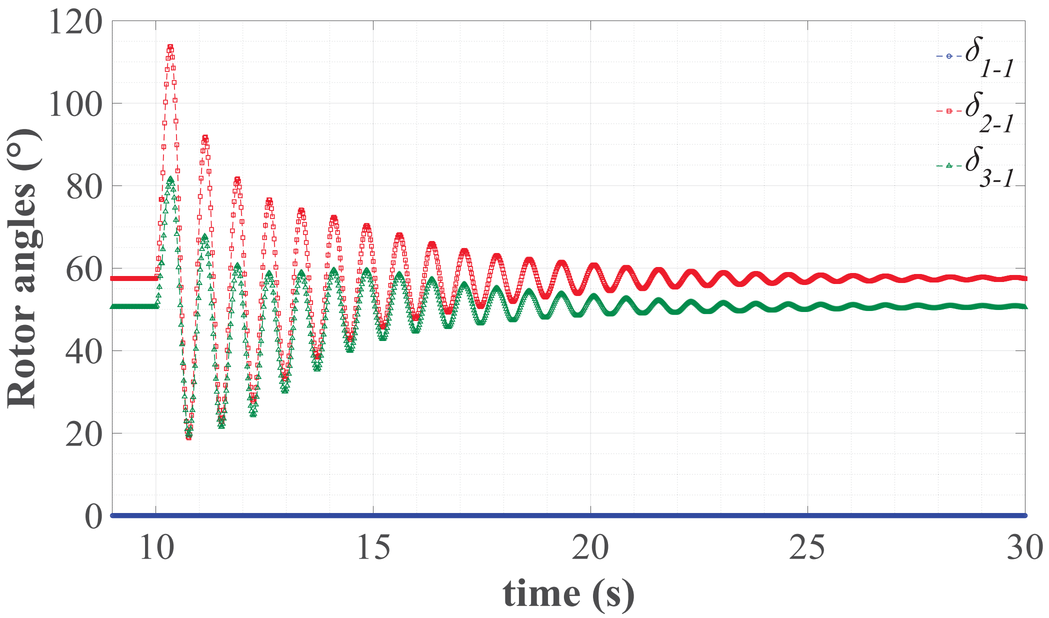

Fig. 3.4 Relative rotor angles of the WSCC 9-bus power system.

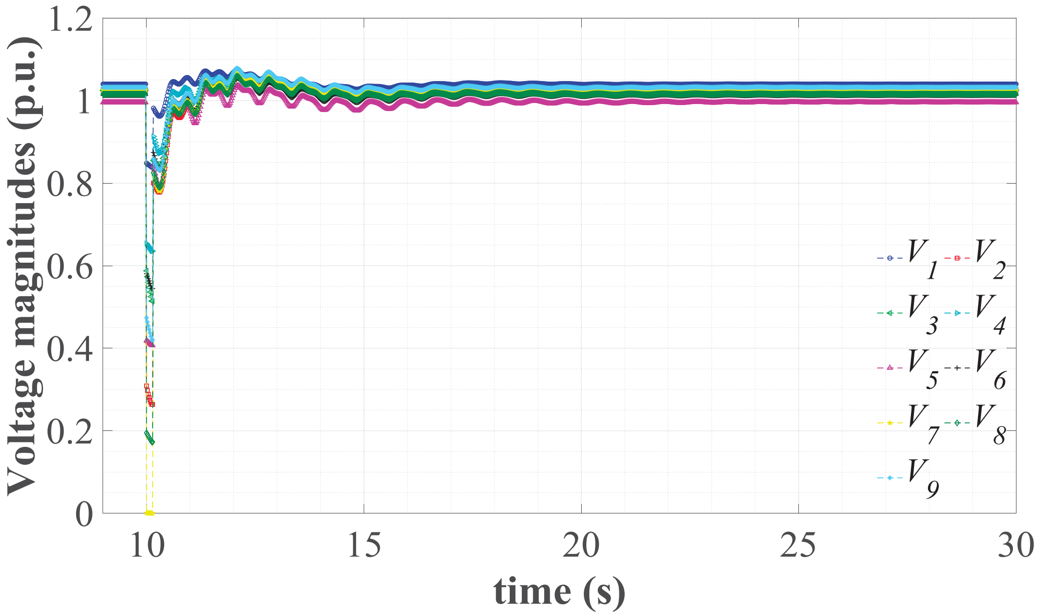

Fig. 3.5 Nodal voltage magnitudes of the WSCC-9 bus power system.

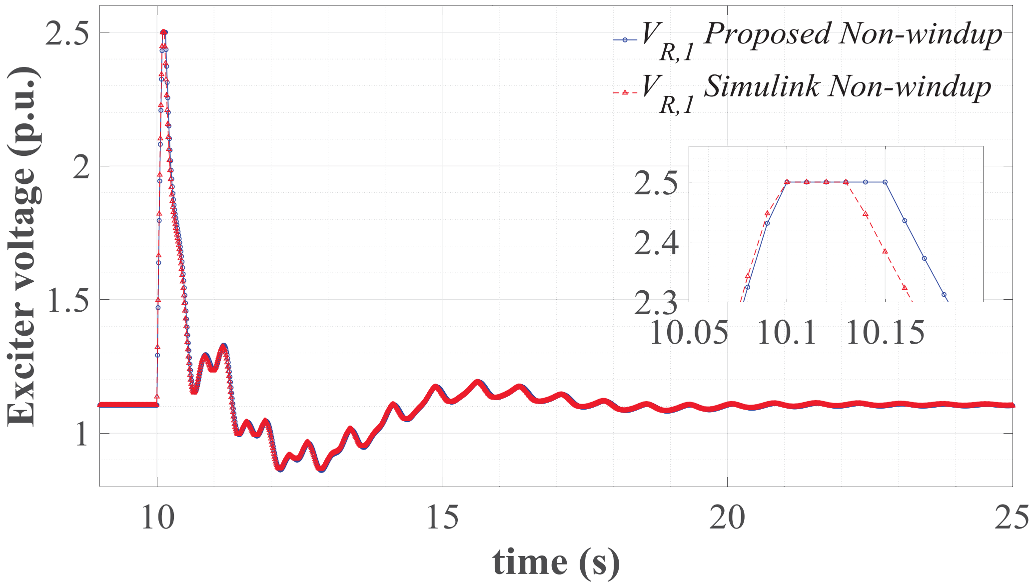

Fig. 3.6 Voltage magnitude profile of the exciter's amplifier in generator 1.

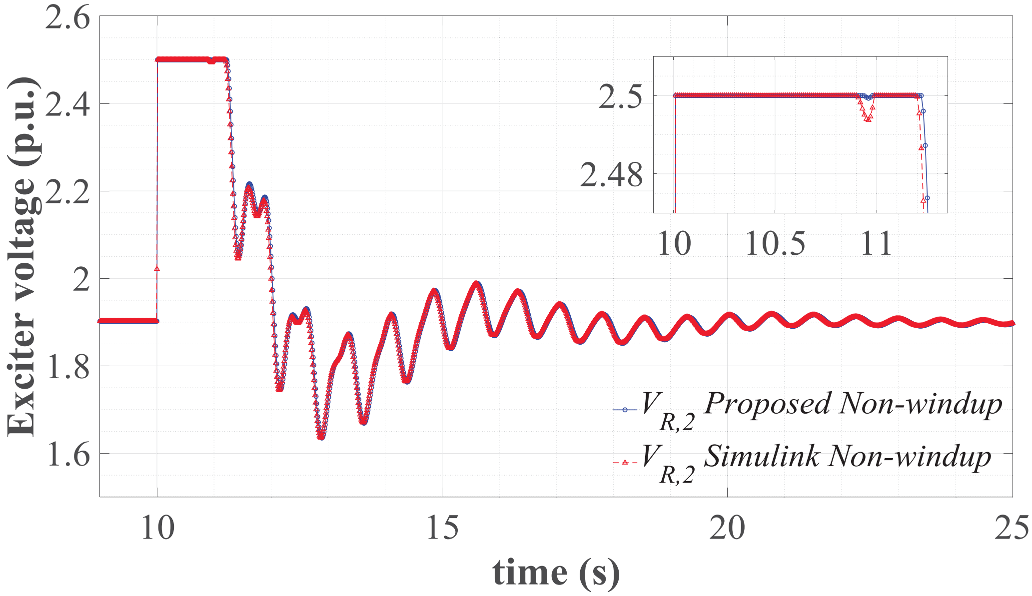

Fig. 3.7 Voltage magnitude profile of the exciter's amplifier in generator 2.

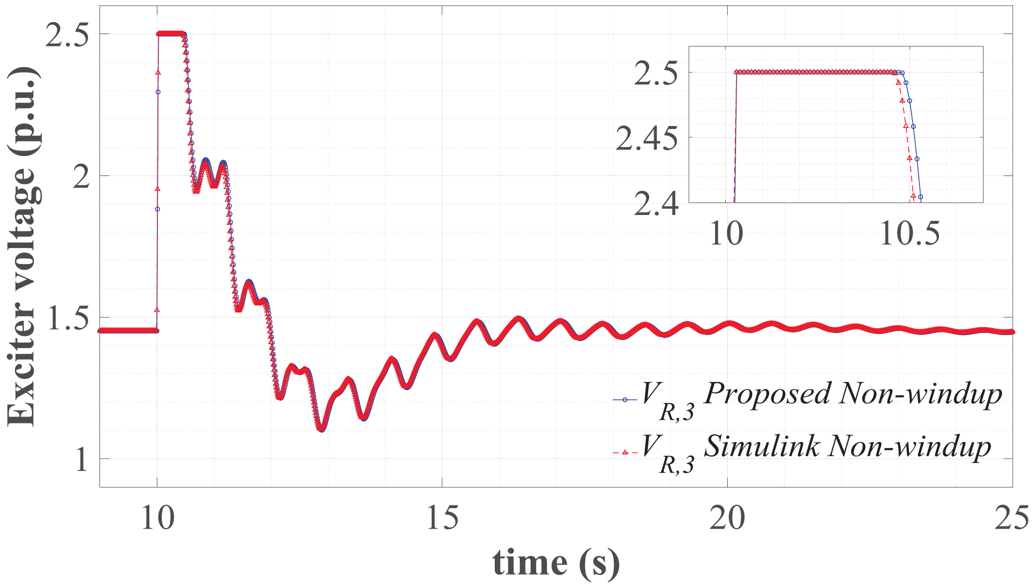

Fig. 3.8 Voltage magnitude profile of the exciter's amplifier in generator 3.

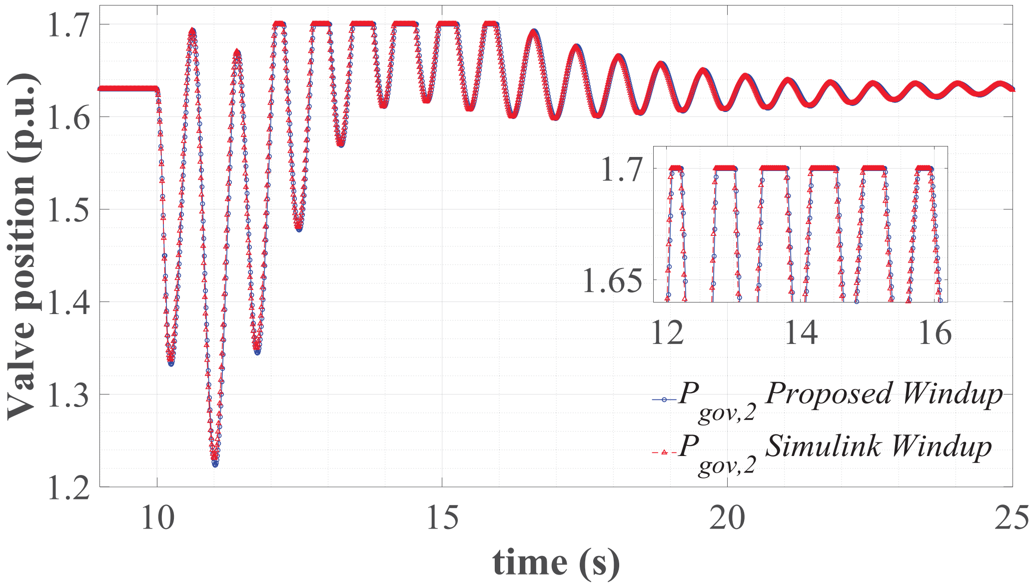

Fig. 3.9 Evolution of the governor valve position in generator 2.

From the results of these studies, the relative rotor angle and voltage magnitude trajectories shown in Fig. 3.4 and Fig. 3.5, respectively, clearly show that the system withstands the contingency such that the pre-fault equilibrium point is transiently stable. On the other hand, several controller outputs violated their output limits after the contingency occurred. Regarding the excitation system's amplifiers, the upper limit of $V_{R,1}$ for generator 1 is quickly reached during the period of time of $10.10 \le t \le 10.15$ s. A similar behavior occurs for $V_{R,2}$ and $V_{R,3}$ of generators 2 and 3, respectively, but over a longer period of time: $10.01 \le t \le 11.22$ and $10.03 \le t \le 10.47$, respectively. Within this context, the amplifier's outputs of the excitation systems embedded in generators 1, 2 and 3 are shown in Fig. 3.6, Fig. 3.7 and Fig. 3.8, respectively. On the other hand, the governor valve position evolution for generator 2 is shown in Fig. 3.9, where it is observed that the maximum level of $P_{gov,2}$ is reached at different periods of time. Note from these figures that the same results were arrived at by both the proposed approach and the Simulink®-based simulation but by using different techniques to prevent the controller outputs from exceeding the specified limits of 2.5 for non-windup limiters and 1.7 for windup limiters. This confirms that the proposed approach accurately handles hard limits on dynamic states, independently of the type of limiter used by the controllers, at each step of the time-domain simulation performed for solving the transient stability problem.

### 3.5.2 Mexican 46-machine, 190-bus power system

In this section, the proposal is applied to an equivalent model of the Mexican interconnected power system [Pizano-Martínez, *et al.*, 2014] consisting of 190 buses, 46 synchronous machines, 180 transmission lines, 83 power transformers and 26 shunt elements, with its schematic one-line diagram shown in Fig. 3.10. The models of generators and controllers are those described in Section 3.5.1. In this context, the excitation system's amplifiers $\{V_{R,i}\}_{i=1}^{46}$ have non-windup limiters with their lower limit set at $\{V_{R,i}^{\min} = 0 \text{ p.u.}\}_{i=1}^{46}$, and their corresponding upper limits specified as reported in Table 3.1. By the same token, the governor-controlled valves at the inlets of the steam turbines $\{P_{gov,i}\}_{i=1}^{46}$ have windup limiters with lower limits that are $\{P_{gov,i}^{\min} = 0 \text{ p.u.}\}_{i=1}^{46}$, and their corresponding upper limits are presented in Table 3.2.

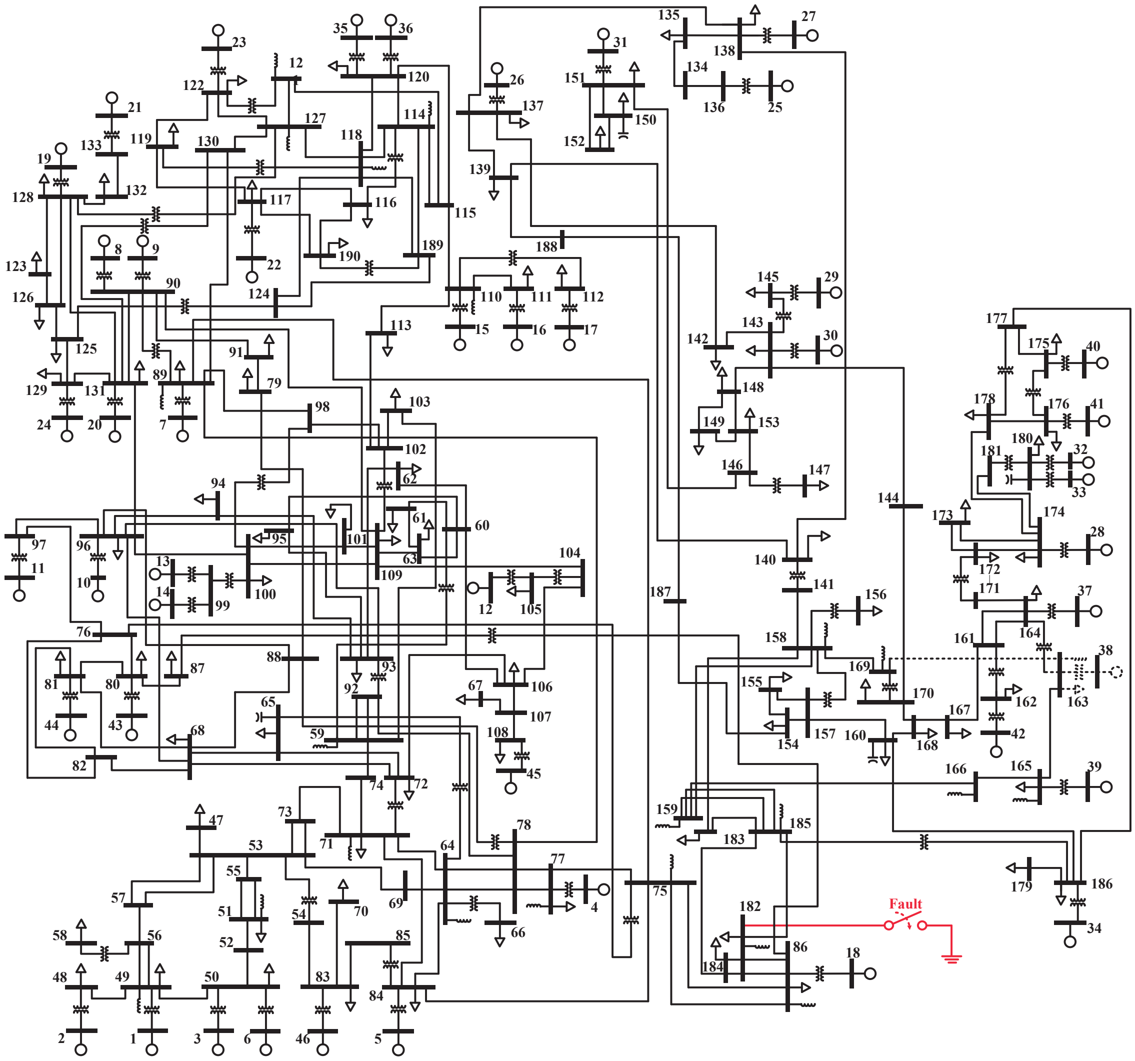

Fig. 3.10 One-line diagram of the Mexican 190-bus power system.

Table 3.1 Upper limits of non-windup limiters for the Mexican 190-bus power system.

| **Machine number** | 1 | 2,3,16,<br>25,41 | 4,42 | 5,24 | 6,11,13,<br>15,21,28,<br>43,45 | 7 | 8,37-39 | 9 | 10 |
|---|---|---|---|---|---|---|---|---|---|
| **Upper limit (p.u.)** | 20.0 | 5.0 | 7.0 | 8.0 | 4.0 | 8.4 | 6.0 | 9.4 | 14.0 |
| **Machine number** | 12 | 14 | 17 | 18 | 19 | 20 | 22 | 23 | 26 |
| **Upper limit (p.u.)** | 6.4 | 3.0 | 3.6 | 7.5 | 4.1 | 5.4 | 10.4 | 5.3 | 10.0 |
| **Machine number** | 27 | 29 | 30 | 31 | 32-34,40 | 35 | 36 | 44 | 46 |
| **Upper limit (p.u.)** | 12.0 | 4.5 | 83.0 | 18.0 | 9.0 | 11.0 | 54.0 | 3.0 | 16.0 |

Table 3.2 Upper limits of windup limiters for the Mexican 190-bus power system.

| **Machine number** | 1-12,18,34 | 13-17,19-24 | 25-33,35-36 | 37-46 |
|---|---|---|---|---|
| **Upper limit (p.u.)** | 16 | 10 | 14 | 12 |

A self-clearing fault is applied at bus 182, as shown in Fig. 3.10, which is incepted at time *t*=10s for 8 cycles. For this contingency, a transient stability study is performed for a time period of 30 s with a time step equal to $\Delta t = 0.01$ s and $\mathrm{tol} = 1 \times 10^{-5}$. After the fault clearance, the system dynamics evolve to the pre-fault operating condition: the equilibrium point is transiently stable for this disturbance. This transiently stable behavior is schematically shown in Fig. 3.11 and Fig. 3.12 for the relative rotor angles and nodal voltage magnitudes, respectively. The outputs of 37 amplifiers, however, reached their maximum limit values and then returned within limits during the period of time $10.01 \le t \le 10.81$ s. On the other hand, the dynamic states of all steam valves never violated their limits. This numerical simulation was also performed by using the Simulink® environment with the models of controllers and the handling of limits described in Section 3.5.1, where the same results were arrived at. A comparison of the results obtained for $V_{R,4}$, $V_{R,5}$, $V_{R,18}$ and $V_{R,34}$ of generators connected to buses 4, 5, 18 and 34, which are the closest to the fault, are shown in Fig. 3.13, Fig. 3.14, Fig. 3.15 and Fig. 3.16, respectively. Please note that these transient responses are very close to each other, which newly verifies that the proposed and conditional test methods for handling hard limits during the time-domain simulation are in good agreement.

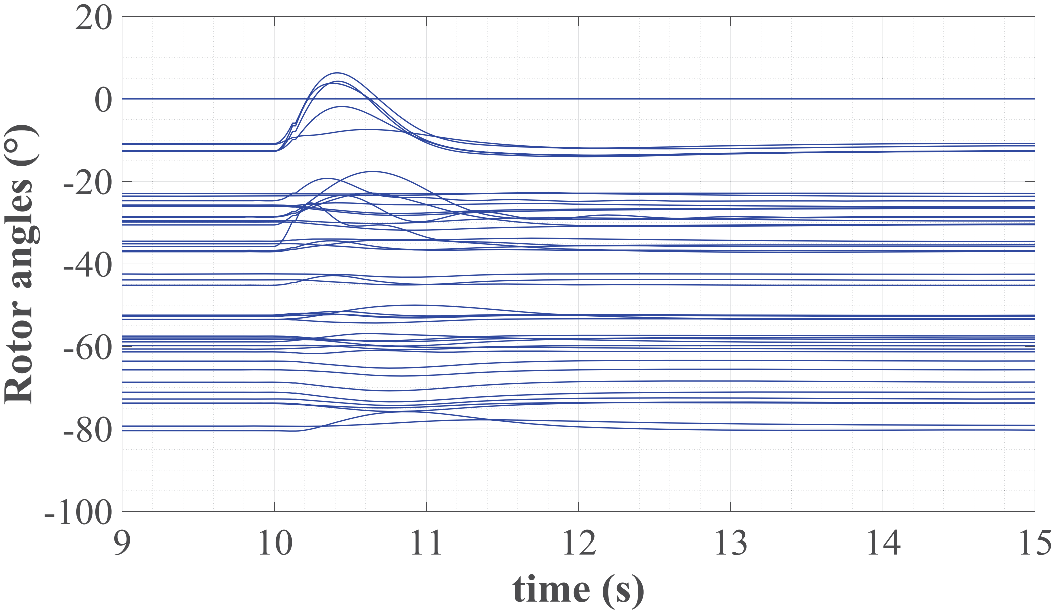

Fig. 3.11 Relative rotor angles of Mexican 190-bus power system.

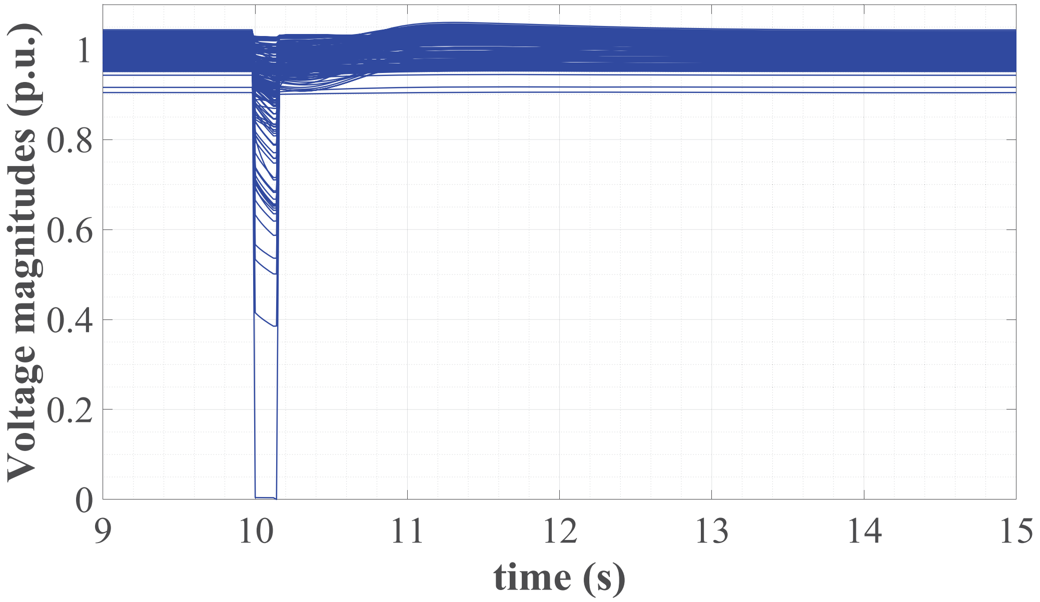

Fig. 3.12 Nodal voltage magnitudes of Mexican 190-bus power system.

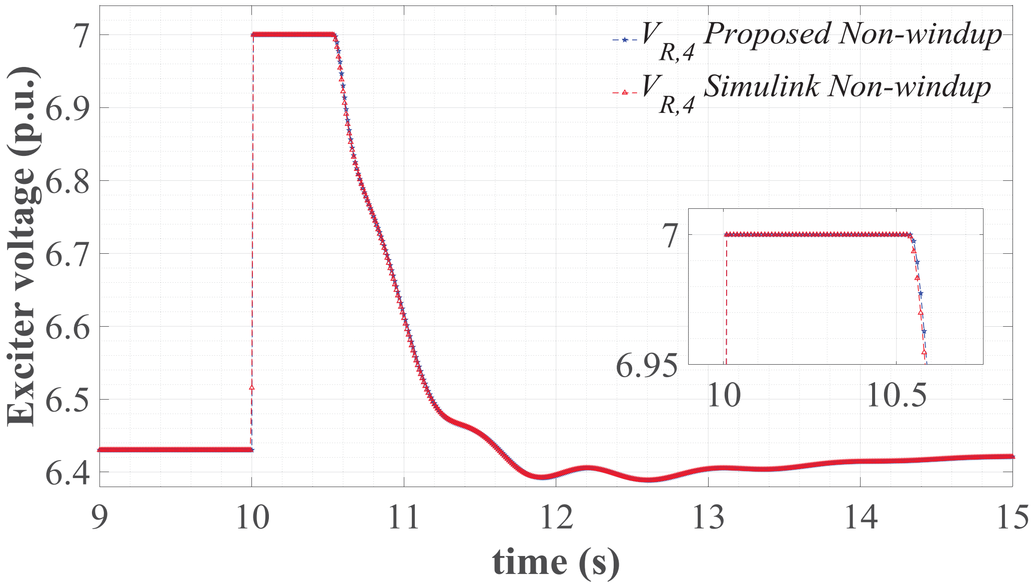

Fig. 3.13 Voltage magnitude profile of the exciter's amplifier in generator 4.

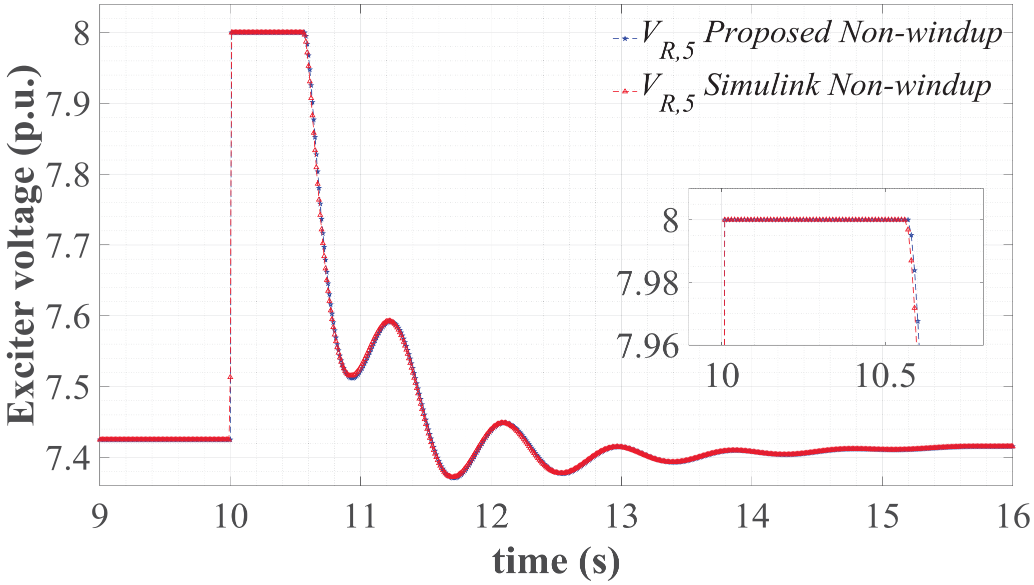

Fig. 3.14 Voltage magnitude profile of the exciter's amplifier in generator 5.

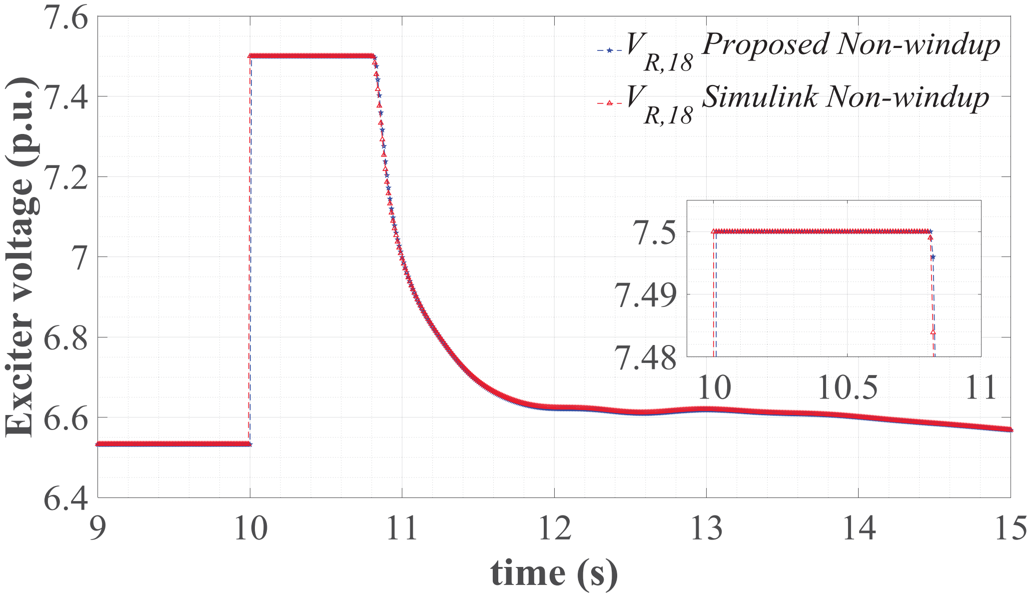

Fig. 3.15 Voltage magnitude profile of the exciter's amplifier in generator 18.

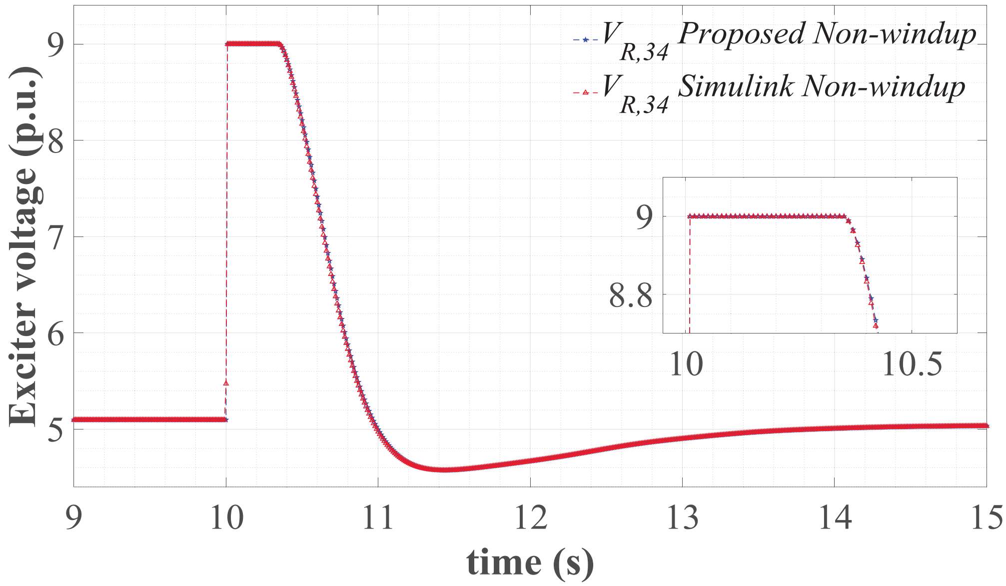

Fig. 3.16 Voltage magnitude profile of the exciter's amplifier in generator 34.

## 3.6 Conclusions

A new practical approach for directly including hard limits on dynamics states in the formulation and solution of the transient stability problem has been proposed in this chapter. This goal is achieved by representing hard limits as equality constraints, which are directly included in the set of differential-algebraic equations representing the power system dynamics. Note that the number of algebraic state variables increases in this structure-preserving formulation of the transient stability problem, i.e., two complementarity variables for each limiter. This proposal is rather attractive, however, because non-windup and windup limits are simultaneously and automatically checked, and enforced in the case of violations, at each step of the time-domain simulation. The effectiveness of the proposed approach for preventing the controllers' dynamic states from exceeding specified limits has been numerically demonstrated and validated.

# Chapter

# 4 Generalized wide area dynamic state estimation

## 4.1 Introduction

A new approach for a generalized estimation of dynamic and algebraic state variables to improve the situational awareness of electric power systems based on PMU measurements is reported in this chapter. Two main specific contributions characterize the proposed approach. Firstly, the proposal is formulated based on the structure-preserving concept where both dynamic and algebraic state variables are simultaneously estimated in a single frame of reference. Secondly, inequality constraints on dynamic states are directly incorporated in the problem's formulation on the basis of the complementarity theory and the Fischer-Burmeister merit function. This allows the automatic enforcing of any of the controller's operational limits, which may be violated during the wide area state estimation process and avoiding the need for a dedicated limit checking process.

## 4.2 Conventional formulation of the dynamic estimation problem

The conventional dynamic state estimation (DSE) refers to the process of estimating the values of dynamic variables that define the system's time evolution under the occurrence of a perturbation. Traditionally, the conventional formulation of estimating dynamic variables is based on the Kalman filter theory and the unscented transformation [Singh & Pal, 2019]. Within the context of power systems, the DSE has been focused on the estimation of dynamic states of synchronous machines, which are grouped in the vector $\boldsymbol{\lambda} \in \mathbb{R}^a$ and based on the set of measurements provided by a PMU connected to the generator's terminals. This set of measurements $\boldsymbol{z}$ is composed of the real $V_{realp}^{PMU} \in \mathbb{R}$ and imaginary $V_{imagp}^{PMU} \in \mathbb{R}$ components of the nodal voltage as well as the real $I_{realp}^{PMU} \in \mathbb{R}$ and imaginary $I_{imagp}^{PMU} \in \mathbb{R}$ components of the nodal current injection at the synchronous machine endpoints. All these measurements are grouped in the vector $\boldsymbol{z} = \begin{bmatrix} V_{realp}^{PMU} & V_{imagp}^{PMU} & I_{realp}^{PMU} & I_{imagp}^{PMU} \end{bmatrix}^{\mathrm{T}} \in \mathbb{R}^{M_e^{PMU}}$.

Based on the information mentioned above, the mathematical model of the nonlinear continuous time system is given by the set of differential-algebraic equations:

$$
\begin{aligned}
&\dot{\boldsymbol{\lambda}} = \boldsymbol{f}\left(\boldsymbol{\lambda},\boldsymbol{\varsigma},\boldsymbol{\beta}\right)+\boldsymbol{\varpi} \quad \boldsymbol{f}:\mathbb{R}^{a+b+p}\rightarrow\mathbb{R}^{a}\\
&\boldsymbol{z} = \hat{\boldsymbol{z}}\left(\boldsymbol{\lambda},\boldsymbol{\varsigma},\boldsymbol{\beta}\right)+\boldsymbol{\varepsilon} \quad \hat{\boldsymbol{z}}:\mathbb{R}^{a+b+p}\rightarrow\mathbb{R}^{M_e^{PMU}}\\
&\boldsymbol{\lambda}\in \mathrm{X}_{sm}\subset\mathbb{R}^{a} \quad \boldsymbol{\varsigma}\in \mathrm{C}_{in}\subset\mathbb{R}^{b} \quad \boldsymbol{\beta}\in \mathrm{B}_{smp}\subset\mathbb{R}^{p}\\
&\boldsymbol{z}\in \mathrm{Z}_{me}\subset\mathbb{R}^{M_e^{PMU}} \quad \boldsymbol{\varpi}\in \mathrm{W}_{pr}\subset\mathbb{R}^{a} \quad \boldsymbol{\varepsilon}\in \mathrm{E}_{me}\subset\mathbb{R}^{M_e^{PMU}}.
\end{aligned}
\tag{4.1}
$$

In this model, $\dot{\boldsymbol{\lambda}}$ represents a vector of differential equations associated with a synchronous machine with its dynamic variables to be estimated grouped in $\boldsymbol{\lambda}$, $\boldsymbol{\varsigma}$ is a vector of known input variables to the synchronous machine, and $\boldsymbol{\beta}$ is a vector containing the synchronous machine's parameters. On the other hand, $\boldsymbol{z}$ is the vector of measurements provided by the PMU connected at the generator's terminals, while $\hat{\boldsymbol{z}}$ is the vector of estimated measurements corresponding to the mathematical representations of those available measurements $\boldsymbol{z}$. In addition, $\boldsymbol{\varpi}\sim(\mathbf{0},\boldsymbol{Q})$ represents a random Gaussian noise vector associated with the dynamic model of the synchronous machine. This noise has a mean that equals $\mathbf{0}$ and a covariance matrix $\boldsymbol{Q}=\mathrm{diag}\{\sigma^2_{\mathrm{process},i}\}_{i=1}^{a}$. Similarly, $\boldsymbol{\varepsilon}\sim(\mathbf{0},\boldsymbol{R})$ is the random Gaussian noise vector associated with the available PMU measurements with a mean that equals $\mathbf{0}$ and covariance matrix $\boldsymbol{R}=\mathrm{diag}\{\sigma^2_{\mathrm{meas},i}\}_{i=1}^{M_e^{PMU}}$.

The nonlinear continuous time system of (4.1) can be transformed into the nonlinear discrete-time system (4.2) through the following two steps. Firstly, the trapezoidal rule of integration is analytically applied to the set of differential equations $\dot{\boldsymbol{\lambda}}$, which results in the first set of difference equations $\boldsymbol{\lambda}^{k+1}$. Secondly, the nonlinear measurement model $\boldsymbol{z}$ is expressed as a set of discrete equations $\boldsymbol{z}^{k+1}$. In the resulting set of discrete-time equations (4.2), $k+1$ is the index for the current discrete-time value $t_{k+1}$, $k$ is the index for the previous discrete time value $t_k$ at which variables and functions were evaluated. Furthermore $\boldsymbol{\lambda}^k, \boldsymbol{f}(\cdot)^k$ and $\boldsymbol{\varpi}^k$ are known, while $\Delta t = t_{k+1}-t_k$ is the time step of integration determined by the PMU sampling rate:

$$
\begin{aligned}
&\boldsymbol{\lambda}^{k+1} = \boldsymbol{\lambda}^{k} + 0.5\Delta t(\boldsymbol{f}(\cdot)^{k+1} + \boldsymbol{f}(\cdot)^{k}) + \boldsymbol{\varpi}^{k} = \boldsymbol{d}(\cdot)^{k+1} + \boldsymbol{\varpi}^{k} \quad && \boldsymbol{d}:\mathbb{R}^{a+b+p} \to \mathbb{R}^{a} \\
&\boldsymbol{z}^{k+1} = \hat{\boldsymbol{z}}(.)^{k+1} + \boldsymbol{\varepsilon}^{k+1} && \hat{\boldsymbol{z}}:\mathbb{R}^{a+b+p} \to \mathbb{R}^{M_e^{PMU}} \\
&\boldsymbol{\lambda} \in \mathrm{X}_{sm} \subset \mathbb{R}^{a} \quad \boldsymbol{\varsigma} \in \mathrm{C}_{in} \subset \mathbb{R}^{b} \quad \boldsymbol{\beta} \in \mathrm{B}_{smp} \subset \mathbb{R}^{p} \\
&\boldsymbol{z} \in \mathrm{Z}_{me} \subset \mathbb{R}^{M_e^{PMU}} \quad \boldsymbol{\varpi} \in \mathrm{W}_{pr} \subset \mathbb{R}^{a} \quad \boldsymbol{\varepsilon} \in \mathrm{E}_{me} \subset \mathbb{R}^{M_e^{PMU}} .
\end{aligned}
\tag{4.2}
$$

The unscented Kalman filter is a straightforward approach to implement and does not require the computation of Jacobian matrices of both the dynamic process and the estimated measurements, which is why this method is preferred in the literature over linearization-based methods [Liu, *et al.*, 2020]. Hence, the unscented Kalman filter is applied to (4.2) for estimating $\hat{\boldsymbol{\lambda}}^{k+1} \in \mathbb{R}^{a}$ in $t_{k+1}$ with the information of the previous state estimation $\hat{\boldsymbol{\lambda}}^{k} \in \mathbb{R}^{a}$ in $t_k$. This estimation process consists of two stages: the prediction and correction stage. In the former stage, the filter performs a prediction of new values for both the dynamic state variables and the covariance matrix from $t_k$ to $t_{k+1}$ by using the time update equations (4.3) through (4.6) [Gibbs, 2011]. The prediction stage begins by generating a set of sigma point vectors $\hat{\boldsymbol{S}}_k^{(i)} \in \mathbb{R}^{2a}$ $\forall i = 0,...,2a$, which are calculated with the unscented transformation (4.3). In this case, $\hat{\boldsymbol{\lambda}}_k^{+} \in \mathbb{R}^{a}$ is the vector of *a posteriori* dynamic variables in $t_k$. Furthermore, $\boldsymbol{P}_k^{+} \in \mathbb{R}^{a \times a}$ is the *a posteriori* covariance matrix in $t_k$, $\sqrt{\boldsymbol{P}_k^{+}} \in \mathbb{R}^{a \times a}$ is the Cholesky factorization of $\boldsymbol{P}_k^{+}$. Lastly, $\kappa = \sqrt{4+\eta}$, $\eta = ((0.0001^2 \times 3) - 4)$ and $\left\langle \sqrt{\boldsymbol{P}_k^{+}} \right\rangle_i \in \mathbb{R}^{a}$ represents the *i*-th column of $\sqrt{\boldsymbol{P}_k^{+}}$. Once the sigma point vectors $\hat{\boldsymbol{S}}_k^{(i)}$ have been obtained in $t_k$, they are transformed into a modified set of sigma point vectors $\hat{\boldsymbol{\chi}}_{k+1}^{(i)} \in \mathbb{R}^{a}$ in $t_{k+1}$ through the prediction function $\boldsymbol{d}(\cdot)$, as shown in (4.4). Lastly, based on the set of predicted vectors $\hat{\boldsymbol{\chi}}_{k+1}^{(i)} \in \mathbb{R}^{a}$ $\forall i = 0,...,2a$, the *a priori* state estimation vector $\hat{\boldsymbol{\lambda}}_{k+1}^{-} \in \mathbb{R}^{a}$ and the *a priori* covariance matrix $\boldsymbol{P}_{k+1}^{-} \in \mathbb{R}^{a \times a}$ in $t_{k+1}$ are predicted from (4.5) and (4.6) , respectively. In this case, $W_0^{\text{mean}} = \eta/(4+\eta)$, $W_0^{\text{cov}} = (\eta/(4+\eta)) + (3 - 0.0001^2)$ and $W_i^{\text{mean}} = W_i^{\text{cov}} = 1/(8+2\eta), \forall i = 1,...,2a$ [Grassidis & Junkins, 2012]:

$$\begin{aligned}
\hat{\boldsymbol{S}}_k^{(0)} &= \hat{\boldsymbol{\lambda}}_k^{+}, \\
\hat{\boldsymbol{S}}_k^{(i)} &= \hat{\boldsymbol{\lambda}}_k^{+} + \kappa \left\langle \sqrt{\boldsymbol{P}_k^{+}} \right\rangle_i \qquad \forall i = 1,\ldots,a, \\
\hat{\boldsymbol{S}}_k^{(a+i)} &= \hat{\boldsymbol{\lambda}}_k^{+} - \kappa \left\langle \sqrt{\boldsymbol{P}_k^{+}} \right\rangle_i \qquad \forall i = 1,\ldots,a,
\end{aligned} \tag{4.3}$$

$$\hat{\boldsymbol{\chi}}_{k+1}^{(i)} = \boldsymbol{d}(\hat{\boldsymbol{S}}_k^{(i)}) \quad \forall i = 0,\ldots,2a, \tag{4.4}$$

$$\hat{\boldsymbol{\lambda}}_{k+1}^{-} = \sum_{i=0}^{2a} W_i^{\text{mean}} \hat{\boldsymbol{\chi}}_{k+1}^{(i)}, \tag{4.5}$$

$$\boldsymbol{P}_{k+1}^{-} = \sum_{i=0}^{2a} W_i^{\text{cov}} \left( \hat{\boldsymbol{\chi}}_{k+1}^{(i)} - \hat{\boldsymbol{\lambda}}_{k+1}^{-} \right) \left( \hat{\boldsymbol{\chi}}_{k+1}^{(i)} - \hat{\boldsymbol{\lambda}}_{k+1}^{-} \right)^{\mathrm{T}} + \boldsymbol{Q}_{k+1}. \tag{4.6}$$

The predicted values $\hat{\boldsymbol{\lambda}}_{k+1}^{-}$ and $\boldsymbol{P}_{k+1}^{-}$ are refined by considering the PMU's measurements available at $t_{k+1}$. This correction stage begins by computing a new set of sigma point vectors $\boldsymbol{\vartheta}_{k+1}^{(i)} \in \mathbb{R}^{M_e^{PMU}}$ through the evaluation of the estimated measurements $\hat{\boldsymbol{z}}(.)$ at the modified sigma point vectors $\hat{\boldsymbol{\chi}}_{k+1}^{(i)}$, as reported in (4.7). This new set of sigma point vectors are in turn used for obtaining a new set of weighed estimated measurements $\hat{\boldsymbol{z}}_{k+1}^{-} \in \mathbb{R}^{M_e^{PMU}}$ at $t_{k+1}$ as given by (4.8). The predicted measurement covariance matrix $\boldsymbol{P}_{k+1}^{zz} \in \mathbb{R}^{M_e^{PMU} \times M_e^{PMU}}$ and the cross-covariance matrix $\boldsymbol{P}_{k+1}^{\lambda z} \in \mathbb{R}^{a \times M_e^{PMU}}$ between $\hat{\boldsymbol{\lambda}}_{k+1}^{-}$ and $\hat{\boldsymbol{z}}_{k+1}^{-}$ are then calculated from (4.9) and (4.10), respectively. Finally, the Kalman gain matrix $\boldsymbol{K}_{k+1}$, the corrected state estimation vector $\hat{\boldsymbol{\lambda}}_{k+1}^{+} \in \mathbb{R}^{a}$ and the corrected covariance matrix $\boldsymbol{P}_{k+1}^{+} \in \mathbb{R}^{a \times a}$ in $t_{k+1}$ are calculated as given by (4.11), (4.12) and (4.13), respectively [Simon, 2006]:

$$\boldsymbol{\vartheta}_{k+1}^{(i)} = \hat{\boldsymbol{z}}(\hat{\boldsymbol{\chi}}_{k+1}^{(i)}) \quad \forall i = 0,\ldots,2a. \tag{4.7}$$

$$\hat{\boldsymbol{z}}_{k+1}^{-} = \sum_{i=0}^{2a} W_i^{\text{mean}} \boldsymbol{\vartheta}_{k+1}^{(i)}. \tag{4.8}$$

$$\boldsymbol{P}_{k+1}^{zz} = \sum_{i=0}^{2a} W_i^{\text{cov}} \left( \boldsymbol{\vartheta}_{k+1}^{(i)} - \hat{\boldsymbol{z}}_{k+1}^{-} \right) \left( \boldsymbol{\vartheta}_{k+1}^{(i)} - \hat{\boldsymbol{z}}_{k+1}^{-} \right)^{\mathrm{T}} + \boldsymbol{R}_{k+1}, \tag{4.9}$$

$$\boldsymbol{P}_{k+1}^{\lambda z}=\sum_{i=0}^{2a}W_i^{\text{cov}}\left(\hat{\boldsymbol{\chi}}_{k+1}^{(i)}-\hat{\boldsymbol{\lambda}}_{k+1}^{-}\right)\left(\boldsymbol{\vartheta}_{k+1}^{(i)}-\hat{\boldsymbol{z}}_{k+1}^{-}\right)^{\mathrm{T}}, \tag{4.10}$$

$$\boldsymbol{K}_{k+1}=\boldsymbol{P}_{k+1}^{\lambda z}\left(\boldsymbol{P}_{k+1}^{zz}\right)^{-1}, \tag{4.11}$$

$$\hat{\boldsymbol{\lambda}}_{k+1}^{+}=\hat{\boldsymbol{\lambda}}_{k+1}^{-}+\boldsymbol{K}_{k+1}\left(\boldsymbol{z}^{k+1}-\hat{\boldsymbol{z}}_{k+1}^{-}\right), \tag{4.12}$$

$$\boldsymbol{P}_{k+1}^{+}=\boldsymbol{P}_{k+1}^{-}-\boldsymbol{K}_{k+1}\boldsymbol{P}_{k+1}^{zz}\boldsymbol{K}_{k+1}^{\mathrm{T}}. \tag{4.13}$$

The vector of dynamic variables estimated by the unscented Kalman filter at $t_{k+1}$ is $\hat{\boldsymbol{\lambda}}^{k+1}=\hat{\boldsymbol{\lambda}}_{k+1}^{+}$. This estimation is used to determine the vector of dynamic variables in the next time instant. This estimation is recursively obtained through Eqs. (4.3) through (4.13) by considering $\hat{\boldsymbol{\lambda}}_{k}^{+}=\hat{\boldsymbol{\lambda}}_{k+1}^{+}$, $\boldsymbol{P}_{k}^{+}=\boldsymbol{P}_{k+1}^{+}$.

Even though the application of the unscented Kalman filter is simple and easy to understand, the conventional formulation of the dynamic state estimation problem based on this filter has the following drawbacks.

1. The dynamic variables of synchronous machines that have a PMU connected to their terminals are estimated in a decentralized manner.
2. The estimation process is locally performed at generation buses and neglects the algebraic variables of the transmission system nodal voltages.
3. The estimation requires knowledge of the input vector to the synchronous machine at each time instant, which is not always available in a practical context.
4. The estimated values of dynamic variables associated with control devices are not set to their corresponding physical limits in case of limit violations during the estimation process.

Based on the information mentioned above, the following section proposes a wide area state estimation process where both dynamic and algebraic state variables are simultaneously estimated in a unified framework of analysis. This proposed approach overcomes the Kalman filter-based dynamic estimation disadvantages.

## 4.3 Wide area dynamic state estimation

The proposed wide area dynamic state estimation (WADSE) refers to the process of estimating both dynamic and algebraic state variables in an unified structure-preserving framework of analysis. Based on Fig. 4.1, the electric power system consists of a set of nodes $\mathcal{N} := \{1,2,\ldots,N\}$ interconnected through a set of transmission elements $\mathcal{T} := \{1,2,\ldots,N_{\mathcal{T}}\}$. The dynamic variables to be estimated are associated with synchronous machines and their controllers, while the estimated algebraic variables correspond to all nodal voltages at the transmission network. Hence, the generalized WADSE is formulated by including the dynamic modeling of synchronous machines and their controllers in the tracking state estimation problem. This results in an unified framework of analysis where both dynamic and algebraic state variables are simultaneously estimated in a single frame of reference.

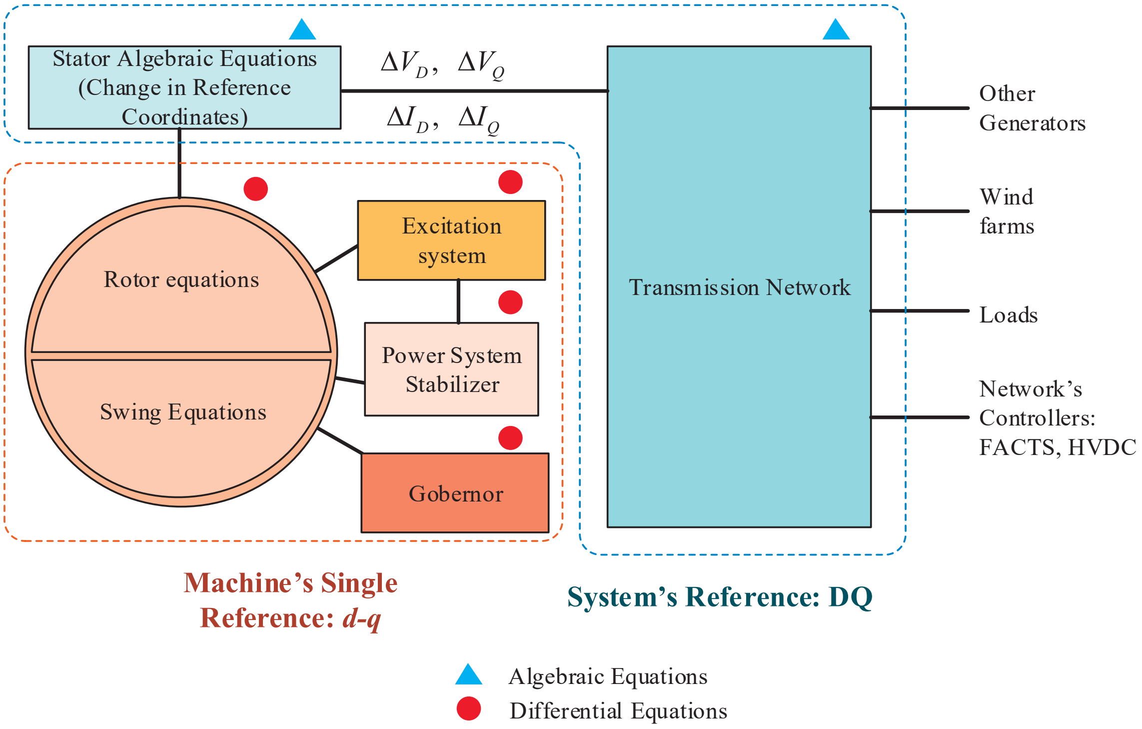

Fig. 4.1 Structure-preserving power system model.

### 4.3.1 Dynamic modeling of synchronous machines and controllers

The WADSE formulation starts with the set of constrained-based differential-algebraic equations associated with the synchronous machines and their controller units, as given by

$$
\begin{aligned}
&\dot{\boldsymbol{\gamma}} = \boldsymbol{f}(\boldsymbol{x},\boldsymbol{y},\boldsymbol{\beta},\boldsymbol{\tau},\boldsymbol{\mu}) && \boldsymbol{f}:\mathbb{R}^{n+w+p+2N_{wl}} \rightarrow \mathbb{R}^{n+N_{wl}}\\
&\dot{\boldsymbol{\psi}}_{\boldsymbol{nwl}} = \boldsymbol{f}_{\boldsymbol{nwl}}(\boldsymbol{x},\boldsymbol{y},\boldsymbol{\beta},\boldsymbol{\psi}) && \boldsymbol{f}_{\boldsymbol{nwl}}:\mathbb{R}^{n+w+p+N_{nwl}} \rightarrow \mathbb{R}^{N_{nwl}}\\
&\boldsymbol{0} = \boldsymbol{I}_{\boldsymbol{dq}}^{\boldsymbol{DQ}}(\boldsymbol{x},\boldsymbol{y},\boldsymbol{\beta}) && \boldsymbol{I}_{\boldsymbol{dq}}^{\boldsymbol{DQ}}:\mathbb{R}^{n+w+p} \rightarrow \mathbb{R}^{w}\\
&\boldsymbol{\psi}^{\mathbf{min}} \le \boldsymbol{\psi} \le \boldsymbol{\psi}^{\mathbf{max}}\\
&\boldsymbol{\mu}^{\mathbf{min}} \le \boldsymbol{\mu} \le \boldsymbol{\mu}^{\mathbf{max}}\\
&\boldsymbol{x} \in \mathrm{X}_{dv} \subset \mathbb{R}^{n} \quad \boldsymbol{y} \in \Upsilon_{av} \subset \mathbb{R}^{w} \quad \boldsymbol{\beta} \in \mathrm{B}_{ep} \subset \mathbb{R}^{p}\\
&\boldsymbol{\psi} \in \Psi_{N_{nwl}} \subset \mathbb{R}^{N_{nwl}} \quad \boldsymbol{\tau} \in \mathrm{T}_{N_{wl}} \subset \mathbb{R}^{N_{wl}} \quad \boldsymbol{\mu} \in \mathrm{M}_{N_{wl}} \subset \mathbb{R}^{N_{wl}}.
\end{aligned}
\tag{4.14}
$$

In the parameter state space of $\mathrm{X}_{dv}$, $\Upsilon_{av}$, $\mathrm{B}_{ep}$, $\Psi_{N_{nwl}}$, $\mathrm{T}_{N_{wl}}$ and $\mathrm{M}_{N_{wl}}$, all dynamic states associated with generators and controllers without non-windup and windup limiters are grouped in vector $\boldsymbol{x}$. Similarly, the controllers outputs with non-windup and windup limiters are lumped in vectors $\boldsymbol{\psi}$ and $\boldsymbol{\tau}$, respectively, while the dummy variables at windup limiters' outputs correspond to the elements of vector $\boldsymbol{\mu}$. On the other hand, $\boldsymbol{y}$ is the vector of algebraic variables associated with the synchronous machines $\boldsymbol{y}_{\boldsymbol{dq}}$ and transmission network $\boldsymbol{y}_{\boldsymbol{DQ}}$ such that $\boldsymbol{y} = \left[\boldsymbol{y}_{\boldsymbol{dq}}\ \boldsymbol{y}_{\boldsymbol{DQ}}\right]^{\mathrm{T}}$, while $\boldsymbol{\beta}$ is a vector of time-invariant parameters associated with the synchronous machines and their controllers. The evolution of dynamic states $\boldsymbol{x}$, $\boldsymbol{\tau}$ and  is explicitly modeled by the set of functions $\dot{\boldsymbol{\gamma}} = \boldsymbol{f}(\boldsymbol{x},\boldsymbol{y},\boldsymbol{\beta},\boldsymbol{\tau},\boldsymbol{\mu})$, while the evolution of non-windup limiters' outputs $\boldsymbol{\psi}$ are modeled by $\dot{\boldsymbol{\psi}}_{\boldsymbol{nwl}} = \boldsymbol{f}_{\boldsymbol{nwl}}(\boldsymbol{x},\boldsymbol{y},\boldsymbol{\beta},\boldsymbol{\psi})$. All these dynamics are constrained by the stator algebraic equations $\boldsymbol{0} = \boldsymbol{I}_{\boldsymbol{dq}}^{\boldsymbol{DQ}}(\cdot) = \boldsymbol{I}_{\boldsymbol{dq}}^{\boldsymbol{DQ}}(\boldsymbol{x},\boldsymbol{y},\boldsymbol{\beta})$, which are expressed in polar form in terms of the state and network variables. Furthermore, the system's dynamics are also constrained by the double-sided inequality constraints $\boldsymbol{\psi}^{\mathbf{min}} \le \boldsymbol{\psi} \le \boldsymbol{\psi}^{\mathbf{max}}$ and $\boldsymbol{\mu}^{\mathbf{min}} \le \boldsymbol{\mu} \le \boldsymbol{\mu}^{\mathbf{max}}$, which limit the dynamic variables associated with non-windup and windup limiters, respectively. Lastly, $N_{nwl}$ and $N_{wl}$ denote the number of non-windup and windup limiters, respectively.

The complementarity-based representation of $\boldsymbol{\psi}^{\mathbf{min}} \le \boldsymbol{\psi} \le \boldsymbol{\psi}^{\mathbf{max}}$ and $\boldsymbol{\mu}^{\mathbf{min}} \le \boldsymbol{\mu} \le \boldsymbol{\mu}^{\mathbf{max}}$ in terms of the Fischer-Burmeister merit function results in the following set of equations:

$$
\varphi_i^{\max} = \sqrt{\left(\psi_i^{\max} - \psi_i\right)^2 + \left(\upsilon_i^{\max}\right)^2} - \left(\psi_i^{\max} - \psi_i\right) - \left(\upsilon_i^{\max}\right) = 0 \quad \forall i = 1,\ldots,\mathbb{R}^{N_{nwl}}, \tag{4.15}
$$

$$\varphi_i^{\min} = \sqrt{\left(\psi_i - \psi_i^{\min}\right)^2 + \left(\upsilon_i^{\min}\right)^2} - \left(\psi_i - \psi_i^{\min}\right) - \left(\upsilon_i^{\min}\right) = 0 \quad \forall i = 1,\ldots,\mathbb{R}^{N_{nwl}}\ , \tag{4.16}$$

$$\phi_i^{\max} = \sqrt{\left(\mu_i^{\max} - \mu_i\right)^2 + \left(\rho_i^{\max}\right)^2} - \left(\mu_i^{\max} - \mu_i\right) - \left(\rho_i^{\max}\right) = 0 \quad \forall i = 1,\ldots,\mathbb{R}^{N_{wl}}\ , \tag{4.17}$$

$$\phi_i^{\min} = \sqrt{\left(\mu_i - \mu_i^{\min}\right)^2 + \left(\rho_i^{\min}\right)^2} - \left(\mu_i - \mu_i^{\min}\right) - \left(\rho_i^{\min}\right) = 0 \quad \forall i = 1,\ldots,\mathbb{R}^{N_{wl}}\ . \tag{4.18}$$

The non-windup limiters' equality constraints (4.15) and (4.16) are clustered in the vector $\boldsymbol{\varphi}_{\boldsymbol{nwl}} = \left[\boldsymbol{\varphi}^{\mathbf{max}}\ \boldsymbol{\varphi}^{\mathbf{min}}\right]^{\mathrm{T}} \in \mathbb{R}^{2N_{nwl}}$, while the vector $\boldsymbol{\phi}_{\boldsymbol{wl}} = \left[\boldsymbol{\phi}^{\mathbf{max}}\ \boldsymbol{\phi}^{\mathbf{min}}\right]^{\mathrm{T}} \in \mathbb{R}^{2N_{wl}}$ gathers the equality constraints (4.17) and (4.18) associated with windup limiters. Furthermore, the complementarity auxiliary variables associated with non-windup limiters and windup limiters can be grouped to form the vectors $\boldsymbol{\upsilon} = \left[\boldsymbol{\upsilon}^{\mathbf{max}}\ \boldsymbol{\upsilon}^{\mathbf{min}}\right]^{\mathrm{T}} \in \mathbb{R}^{2N_{nwl}}$ and $\boldsymbol{\rho} = \left[\boldsymbol{\rho}^{\mathbf{max}}\ \boldsymbol{\rho}^{\mathbf{min}}\right]^{\mathrm{T}} \in \mathbb{R}^{2N_{wl}}$, respectively. Finally, all algebraic equations relating $\mu_i$ and $\tau_i$ in the windup limiters $\{\eta_i = \mu_i - \tau_i - \rho_i^{\min} + \rho_i^{\max} = 0\}_{i=1}^{N_{wl}}$ are grouped in the vector $\boldsymbol{\eta}_{\boldsymbol{wl}} \in \mathbb{R}^{N_{wl}}$.

Based on the information mentioned above, the set of constrained-based DAEs given in (4.14) is transformed into (4.19):

$$\begin{aligned}
&\dot{\boldsymbol{\gamma}} = \boldsymbol{f}(\boldsymbol{x},\boldsymbol{y},\boldsymbol{\beta},\boldsymbol{\tau},\boldsymbol{\mu}) && \boldsymbol{f}:\mathbb{R}^{n+w+p+2N_{wl}} \rightarrow \mathbb{R}^{n+N_{wl}}\\
&\dot{\boldsymbol{\psi}}_{\boldsymbol{nwl}} = \boldsymbol{f}_{\boldsymbol{nwl}}(\boldsymbol{x},\boldsymbol{y},\boldsymbol{\beta},\boldsymbol{\psi},\boldsymbol{\upsilon}) && \boldsymbol{f}_{\boldsymbol{nwl}}:\mathbb{R}^{n+w+p+3N_{nwl}} \rightarrow \mathbb{R}^{N_{nwl}}\\
&\mathbf{0} = \boldsymbol{I}_{\boldsymbol{dq}}^{\boldsymbol{DQ}}(\boldsymbol{x},\boldsymbol{y},\boldsymbol{\beta}) && \boldsymbol{I}_{\boldsymbol{dq}}^{\boldsymbol{DQ}}:\mathbb{R}^{n+w+p} \rightarrow \mathbb{R}^{w}\\
&\mathbf{0} = \boldsymbol{\eta}_{\boldsymbol{wl}}(\boldsymbol{\tau},\boldsymbol{\mu},\boldsymbol{\rho}) && \boldsymbol{\eta}_{\boldsymbol{wl}}:\mathbb{R}^{4N_{wl}} \rightarrow \mathbb{R}^{N_{wl}}\\
&\mathbf{0} = \boldsymbol{\varphi}_{\boldsymbol{nwl}}(\boldsymbol{\psi},\boldsymbol{\upsilon}) && \boldsymbol{\varphi}_{\boldsymbol{nwl}}:\mathbb{R}^{3N_{nwl}} \rightarrow \mathbb{R}^{2N_{nwl}}\\
&\mathbf{0} = \boldsymbol{\phi}_{\boldsymbol{wl}}(\boldsymbol{\mu},\boldsymbol{\rho}) && \boldsymbol{\phi}_{\boldsymbol{wl}}:\mathbb{R}^{3N_{wl}} \rightarrow \mathbb{R}^{2N_{wl}}\\
&\boldsymbol{x} \in \mathrm{X}_{dv} \subset \mathbb{R}^{n},\ \boldsymbol{y} \in \Upsilon_{av} \subset \mathbb{R}^{w},\ \boldsymbol{\beta} \in \mathrm{B}_{ep} \subset \mathbb{R}^{p},\\
&\boldsymbol{\psi} \in \Psi_{N_{nwl}} \subset \mathbb{R}^{N_{nwl}},\ \boldsymbol{\tau} \in \mathrm{T}_{N_{wl}} \subset \mathbb{R}^{N_{wl}},\ \boldsymbol{\mu} \in \mathrm{M}_{N_{wl}} \subset \mathbb{R}^{N_{wl}},\\
&\qquad \boldsymbol{\upsilon} \in \mathrm{U}_{N_{nwl}} \subset \mathbb{R}^{2N_{nwl}},\ \boldsymbol{\rho} \in \mathrm{P}_{N_{wl}} \subset \mathbb{R}^{2N_{wl}},
\end{aligned} \tag{4.19}$$

where the subscripts *nwl* and *wl* denote non-windup and windup limiters, respectively. Note that in this new proposal the resulting set of complementarity-based equality constraints, representing all inequality constraints associated with non-windup and windup limiters, are directly added to the dynamic formulation for performing the automatic check of the operating limits and, when applicable, for the automatic enforcing of any of those limits, which may be violated during the system's dynamic evolution.

Lastly, the set of equations are discretized for its direct inclusion in the WADSE formulation, which results in (4.20):

$$\begin{array}{ll}
\boldsymbol{F}_1(\cdot)^{k+1} = \boldsymbol{\gamma}^{k+1} - \boldsymbol{\gamma}^{k} - 0.5\Delta t(\boldsymbol{f}(\cdot)^{k+1} + \boldsymbol{f}(\cdot)^{k}) = \mathbf{0} & \boldsymbol{F}_1(\cdot): \mathbb{R}^{n+w+p+2N_{wl}} \rightarrow \mathbb{R}^{n+N_{wl}} \\
\boldsymbol{F}_2(\cdot)^{k+1} = \boldsymbol{\psi}_{nwl}^{k+1} - \boldsymbol{\psi}_{nwl}^{k} - 0.5\Delta t(\boldsymbol{u}(\cdot)^{k+1} + \boldsymbol{u}(\cdot)^{k}) - \Delta t\boldsymbol{q}(\boldsymbol{\beta},\boldsymbol{\upsilon})^{k+1} = \mathbf{0} & \boldsymbol{F}_2(\cdot): \mathbb{R}^{n+w+p+3N_{nwl}} \rightarrow \mathbb{R}^{N_{nwl}} \\
\boldsymbol{G}(\cdot)^{k+1} = \boldsymbol{I}_{dq}^{DQ}(\boldsymbol{x},\boldsymbol{y},\boldsymbol{\beta})^{k+1} = \mathbf{0} & \boldsymbol{G}(\cdot): \mathbb{R}^{n+w+p} \rightarrow \mathbb{R}^{w} \\
\boldsymbol{\eta}_{wl}(\cdot)^{k+1} = \boldsymbol{\eta}_{wl}(\boldsymbol{\tau},\boldsymbol{\mu},\boldsymbol{\rho})^{k+1} = \mathbf{0} & \boldsymbol{\eta}_{wl}(\cdot): \mathbb{R}^{4N_{wl}} \rightarrow \mathbb{R}^{N_{wl}} \\
\boldsymbol{\varphi}_{nwl}(\cdot)^{k+1} = \boldsymbol{\varphi}_{nwl}(\boldsymbol{\psi},\boldsymbol{\upsilon})^{k+1} = \mathbf{0} & \boldsymbol{\varphi}_{nwl}(\cdot): \mathbb{R}^{3N_{nwl}} \rightarrow \mathbb{R}^{2N_{nwl}} \\
\boldsymbol{\phi}_{wl}(\cdot)^{k+1} = \boldsymbol{\phi}_{wl}(\boldsymbol{\mu},\boldsymbol{\rho})^{k+1} = \mathbf{0} & \boldsymbol{\phi}_{wl}(\cdot): \mathbb{R}^{3N_{wl}} \rightarrow \mathbb{R}^{2N_{wl}}.
\end{array} \tag{4.20}$$

In this case, all differential equations $\dot{\boldsymbol{\gamma}}$ have been discretized through the analytical application of the trapezoidal rule, which results in $\boldsymbol{F}_1(\cdot)^{k+1}$. On the other hand, sustained and bounded numerical oscillations can occur with the trapezoidal rule of integration when discontinuities take place during the dynamic simulation, such as switching operations and transitions associated with the setting of limits. Hence, the phenomenon could occur with the discretization of differential equations $\dot{\boldsymbol{\psi}}_{nwl}$. This drawback is overcome by spliting $\dot{\boldsymbol{\psi}}_{nwl}$ into the two terms $\boldsymbol{f}_{nwl}(\cdot) = \boldsymbol{u}(\boldsymbol{x},\boldsymbol{y},\boldsymbol{\beta},\boldsymbol{\psi}) + \boldsymbol{q}(\boldsymbol{\beta},\boldsymbol{\upsilon})$, where the first and second terms are algebraized by using the trapezoidal and backward Euler rules of integration, respectively, for the entire period of study [Romay, *et al.*, 2021]. This discretization results in $\boldsymbol{F}_2(\cdot)^{k+1}$. Within the context of the discretization process, $\Delta t$ is the integration time step, and the superscripts $k+1$ and $k$ denote the time instants $t_{k+1}$ and $t_k$, respectively, at which functions and variables are evaluated.

For the sake of simplicity in the nomenclature, the set of equations (4.20) can be further reduced by merging all discretized differential equations in one single set of equations denoted by $\boldsymbol{\Gamma}(\cdot)^{k+1} = \begin{bmatrix} \boldsymbol{F}_1(\cdot)^{k+1} & \boldsymbol{F}_2(\cdot)^{k+1} \end{bmatrix}^{\mathrm{T}} : \mathbb{R}^{n+w+p+2N_{wl}+3N_{nwl}} \rightarrow \mathbb{R}^{n+N_{wl}+N_{nwl}}$. Similarly, all algebraic equations associated with hard limits of controllers $\boldsymbol{\eta}_{\boldsymbol{wl}}(\cdot)^{k+1}$, $\boldsymbol{\varphi}_{\boldsymbol{nwl}}(\cdot)^{k+1}$ and $\boldsymbol{\phi}_{\boldsymbol{wl}}(\cdot)^{k+1}$ are grouped in a single vector of algebraic equations $\boldsymbol{\Phi}(\cdot)^{k+1} = \left[\boldsymbol{\eta}_{\boldsymbol{wl}}(\cdot)^{k+1} \quad \boldsymbol{\varphi}_{\boldsymbol{nwl}}(\cdot)^{k+1} \quad \boldsymbol{\phi}_{\boldsymbol{wl}}(\cdot)^{k+1}\right]^{\mathrm{T}} : \mathbb{R}^{3N_{nwl}+7N_{wl}} \rightarrow \mathbb{R}^{2N_{nwl}+3N_{wl}}$. Lastly, all dynamic and algebraic state variables are clustered in one single vector $\boldsymbol{x}_{\boldsymbol{dav}} = \left[\boldsymbol{x}_{\boldsymbol{tdv}} \quad \boldsymbol{y}_{\boldsymbol{tav}} \quad \boldsymbol{\xi}_{\boldsymbol{cc}}\right]^{\mathrm{T}} \in \mathbb{R}^{n+w+3N_{nwl}+4N_{wl}}$, where $\boldsymbol{x}$, $\boldsymbol{\psi}$ and $\boldsymbol{\tau}$ are added in $\boldsymbol{x}_{\boldsymbol{tdv}}$. On the other hand, $\boldsymbol{y}$ and $\boldsymbol{\mu}$ are appended to $\boldsymbol{y}_{\boldsymbol{tav}}$, while $\boldsymbol{\upsilon}$ and $\boldsymbol{\rho}$ are grouped in $\boldsymbol{\xi}_{\boldsymbol{cc}}$. Based on the information mentioned above, the set of equations (4.20) is transformed into (4.21):

$$\begin{aligned} &\boldsymbol{\Gamma}(\boldsymbol{x}_{\boldsymbol{dav}})^{k+1} = \mathbf{0} \\ &\boldsymbol{G}(\boldsymbol{x}_{\boldsymbol{dav}})^{k+1} = \mathbf{0} \\ &\boldsymbol{\Phi}(\boldsymbol{x}_{\boldsymbol{dav}})^{k+1} = \mathbf{0}. \end{aligned} \tag{4.21}$$

Lastly, the set of equations $\boldsymbol{\Gamma}(\boldsymbol{x}_{\boldsymbol{dav}})^{k+1}$, $\boldsymbol{G}(\boldsymbol{x}_{\boldsymbol{dav}})^{k+1}$ and $\boldsymbol{\Phi}(\boldsymbol{x}_{\boldsymbol{dav}})^{k+1}$ are directly added to the tracking state estimation problem to obtain the proposed WADSE approach.

### 4.3.2 Tracking static state estimation approach

The weighted least squares-based algorithm remains as the most widely used technique in the majority of static state estimation practical programs. Furthermore, the tracking state estimation consists of the sequential application of a static state estimator and upgraded sets of measurements to track the evolution of algebraic state variables after a disturbance.

The objective of the static state estimation is to find the best estimate state of the algebraic state variables $\hat{\boldsymbol{y}}_{\boldsymbol{DQ}}$ of the true state $\boldsymbol{y}_{\boldsymbol{DQ}}$ that best fits the set of measurements $\boldsymbol{z} = \hat{\boldsymbol{z}}(\boldsymbol{y}_{\boldsymbol{DQ}}) + \boldsymbol{\varepsilon}$. Assuming a set of $M_e^{PMU}$ synchronized phasor measurements $\boldsymbol{z} \in \mathbb{R}^{M_e^{PMU}}$, $\hat{\boldsymbol{z}}(\boldsymbol{y}_{\boldsymbol{DQ}}) \in \mathbb{R}^{M_e^{PMU}}$ is a vector of estimated measurements relating $\boldsymbol{z}$ and $\hat{\boldsymbol{y}}_{\boldsymbol{DQ}}$ through the mathematical representation of $\boldsymbol{z}$. On the other hand, $\boldsymbol{\varepsilon} \in \mathbb{R}^{M_e^{PMU}}$ is the vector of uncorrelated measurement errors with zero mean and with a specified probability distribution function representing imperfections of real measuring devices.

In addition to the PMU measurements, which are subject to errors, there are some “perfect” measurements related to nodes with no loads. In these nodes, the net power injected from the network is 0 such that this power mismatch equation can be included into the state estimator in two different ways: i) as a set of measurements with a small variance or ii) as a set of equality constraints $\boldsymbol{c}(\boldsymbol{y}_{\boldsymbol{DQ}})=\mathbf{0}$, where $\boldsymbol{c}(\boldsymbol{y}_{\boldsymbol{DQ}})\in\mathbb{R}^{N_{zi}}$ and $\mathcal{N}_{zi}:=\{1,2,\ldots,N_{zi}\}$, $\mathcal{N}_{zi}\subset\mathcal{N}$ is the set of nodes with zero injections of active and reactive powers (see Eqs. (C.5) and (C.6) ). Since the former approach could lead to ill-conditioning during the iterative solution process, the second approach is the one used in practice, which results in a constrained-based state estimator.

Based on the information mentioned above, the constrained-based WLS optimization takes on the following form:

$$\begin{aligned} \underset{\boldsymbol{y}_{\boldsymbol{DQ}},\boldsymbol{r}}{\arg\min}: \quad & \boldsymbol{J}(\boldsymbol{r})=\frac{1}{2}\boldsymbol{r}^{\mathrm{T}}\boldsymbol{W}\boldsymbol{r} \\ \text{subject to}: \quad & \boldsymbol{r}-\boldsymbol{z}+\hat{\boldsymbol{z}}(\boldsymbol{y}_{\boldsymbol{DQ}})=\mathbf{0} \\ & \boldsymbol{c}(\boldsymbol{y}_{\boldsymbol{DQ}})=\mathbf{0}. \end{aligned} \tag{4.22}$$

Note that in this formulation the vector of measurements’ residuals $\boldsymbol{r}\in\mathbb{R}^{M_e^{PMU}}$ is considered unknown so that all residuals are also decision variables of the optimization problem.

The static state estimation can be used to track the system evolution after a disturbance, even during non-quasi static operation conditions, with no model for the dynamic behavior of the system [Alcaide-Moreno, *et al.*, 2018]. Since the PMUs are available in a very short period of time (30 or more samples per second), the tracking state estimation provides the system’s operating state at the discrete time $k+1$ by solving the following discrete optimization problem:

$$\begin{aligned} \underset{\boldsymbol{y}_{\boldsymbol{DQ}},\boldsymbol{r}}{\arg\min}: \quad & \boldsymbol{J}(\boldsymbol{r})=\frac{1}{2}\boldsymbol{r}^{k+1,\mathrm{T}}\boldsymbol{W}^{k+1}\boldsymbol{r}^{k+1} \\ \text{subject to}: \quad & \boldsymbol{r}^{k+1}-\boldsymbol{z}^{k+1}+\hat{\boldsymbol{z}}(\boldsymbol{y}_{\boldsymbol{DQ}})^{k+1}=\mathbf{0} \\ & \boldsymbol{c}(\boldsymbol{y}_{\boldsymbol{DQ}})^{k+1}=\mathbf{0}, \end{aligned} \tag{4.23}$$

where $\boldsymbol{J}(\boldsymbol{r})\colon \mathbb{R}^{M_e^{PMU}} \to \mathbb{R}$ is the objective function of weighted least squares (WLS) approach, $\boldsymbol{r}^{k+1}$ is the residual vector at $t_{k+1}$, $\boldsymbol{W}^{k+1} = \operatorname{diag}\left\{1/(\sigma_{\text{meas},i}^{k+1})^2\right\}_{i=1}^{M_e^{PMU}}$ is the measurement weighting matrix at $t_{k+1}$ with standard deviations $\left\{\sigma_{\text{meas},i}^{k+1}\right\}_{i=1}^{M_e^{PMU}}$, and $\boldsymbol{z}^{k+1} \in \mathbb{R}^{M_e^{PMU}}$ is the vector of available PMU measurements at $t_{k+1}$ including nodal voltage phasors, branch current phasors and nodal frequencies.

### 4.3.3 Generalized WADSE approach

The generalized WADSE is mathematically formulated through the co-optimization of both the set of constrained DAEs associated with the synchronous machines and their controllers and the set of $M_e^{PMU}$ synchronized phasor measurements collected in a given period of time from the subsets of observable nodes $\mathcal{N}_{oe} := \{1, 2, \ldots, N_{oe}\}$, $\mathcal{N}_{oe} \subset \mathcal{N}$ and observable transmission elements $\mathcal{T}_{oe} := \left\{1, 2, \ldots, N_{\mathcal{T}_{oe}}\right\}$, $\mathcal{T}_{oe} \subset \mathcal{T}$ :

$$
\begin{aligned}
\underset{\boldsymbol{x_{dav}},\boldsymbol{r}}{\text{arg min:}} \quad & \boldsymbol{J}(\boldsymbol{r}) = \frac{1}{2}\boldsymbol{r}^{k+1,\mathrm{T}}\boldsymbol{W}^{k+1}\boldsymbol{r}^{k+1} \\
\text{subject to:} \quad & \boldsymbol{r}^{k+1}\text{-}\boldsymbol{z}^{k+1}+\hat{\boldsymbol{z}}(\boldsymbol{x_{dav}})^{k+1} = \boldsymbol{0} \\
& \boldsymbol{c}(\boldsymbol{x_{dav}})^{k+1} = \boldsymbol{0} \\
& \boldsymbol{\Gamma}(\boldsymbol{x_{dav}})^{k+1} = \boldsymbol{0} \\
& \boldsymbol{L}(\boldsymbol{x_{dav}})^{k+1} = \boldsymbol{0} \\
& \boldsymbol{\Phi}(\boldsymbol{x_{dav}})^{k+1} = \boldsymbol{0}.
\end{aligned}
\tag{4.24}
$$

The PMU's measurements collected at discrete time $k$+1 from the $i$-th node correspond to nodal voltage magnitudes $\{V_i^{PMU}\}_{i\in\mathcal{N}_{oe}}$, nodal voltage phase angles $\{\theta_i^{PMU}\}_{i\in\mathcal{N}_{oe}}$, the real (resp. imaginary) part of the branch complex current flowing from node $i$ to node $j$ of a transmission element $\mathcal{T}_{km}$: $\left\{\Re\left(\vec{i}_{ij}^{\,PMU}\right)\right\}_{\mathcal{T}_{ij}\in\mathcal{T}_{oe}}$ (resp. $\left\{\Im\left(\vec{i}_{ij}^{\,PMU}\right)\right\}_{\mathcal{T}_{ij}\in\mathcal{T}_{oe}}$) and the nodal frequency $\{f_i^{PMU}\}_{i\in\mathcal{N}_{oe}}$. All these measurements are grouped in the vector $\boldsymbol{z}^{k+1} = \left[\boldsymbol{V}_{k+1}^{\boldsymbol{PMU}} \quad \boldsymbol{\theta}_{k+1}^{\boldsymbol{PMU}} \quad \Re\left(\vec{\boldsymbol{I}}_{k+1}^{\boldsymbol{PMU}}\right) \quad \Im\left(\vec{\boldsymbol{I}}_{k+1}^{\boldsymbol{PMU}}\right) \quad \boldsymbol{f}_{k+1}^{\boldsymbol{PMU}}\right]^{\mathrm{T}} \in \mathbb{R}^{M_e^{PMU}}$.

## 4.4 Initial conditions

To perform the WADSE, it is necessary to know the system's equilibrium point before the disturbance occurrence, which provides the initial conditions required for any dynamic study. Hence, the initial conditions for the nodal voltages, i.e., the network's algebraic state variables $\boldsymbol{y}_{\boldsymbol{DQ}}^{0}$, are completely defined by the power flow solution. These values are in turn used to obtain the initial conditions for the machine's stator algebraic variables $\boldsymbol{y}_{\boldsymbol{dq}}^{0}$. Since the initial conditions are associated with an equilibrium point, the change rate of dynamic variables is **0**. Hence, the initial conditions of dynamic variables and the controller's inputs are calculated by solving the algebraic equations resulting from setting the derivatives equal to **0**: $\boldsymbol{f}(\cdot)=\boldsymbol{0}$ and $\boldsymbol{f}_{\boldsymbol{nwl}}(\cdot)=\boldsymbol{0}$. In addition, complementarity variables of non-windup and windup limiters are set to null values: $\boldsymbol{\upsilon}^{0}=\boldsymbol{0}$ and $\boldsymbol{\rho}^{0}=\boldsymbol{0}$, under the assumption that the initial values of dynamic states are within limits. On the other hand, the proposed methodology considers that the initial values of the dynamic and algebraic variables for the WADSE at a given time are equal to the values estimated in the previous time instant. Lastly, the complementarity variables will have values of 1e-4 ($\boldsymbol{\upsilon}^{k+1}=(1e-4)\times\mathbf{i}_{2N_{nwl}}\in\mathbb{R}^{2N_{nwl}}$ and $\boldsymbol{\rho}^{k+1}=(1e-4)\times\mathbf{i}_{2N_{wl}}\in\mathbb{R}^{2N_{wl}}$) where $\mathbf{i}_{2N_{nwl}}$ and $\mathbf{i}_{2N_{wl}}$ are vectors composed of unitary values to avoid indeterminations in the complementarity constraints when starting with values of complementarity variables exactly equal to **0**.

## 4.5 Bad data analysis

Many robust techniques for the detection and identification of measurements with gross errors have been proposed in the literature within the context of dynamic state estimation [Zhao J. , 2018; Zhao & Mili, 2019; Zhao & Mili, 2019; Zhao, *et al.*, 2019], however, the purpose of this work is not a rigorous study of robust estimation or bad data detection and identification. Hence, the bad data analysis implemented in this work is the one proposed and detailed in [Martínez-Parrales, *et al.*, 2020], which is briefly described below. This procedure is applied after each WADSE solution process for each time instant and is executed in the four stages below.

- **Stage 1:** First, all measurements with absolute estimated residuals greater than three times their corresponding standard deviations are grouped in a set of suspected erroneous measurements $\mathcal{SBD}_1$, which is mathematically defined by (4.25). If $\mathcal{SBD}_1$ is an empty set, then there are no gross measurements in $t_{k+1}$:

$$\text{if}\{\left|\hat{r}_i^{k+1}\right| > 3\sigma_{\text{meas},i}^{k+1}\}_{i=1}^{M_e^{PMU}} \quad \therefore i \in \mathcal{SBD}_1. \tag{4.25}$$

- **Stage 2:** A threshold filter is applied to the set $\mathcal{SBD}_1$ to remove all measurements with normalized estimated residuals lower than the threshold value $\text{Th}_{\text{se}} = 0.5(\text{LNER}-3)+3$, where $\text{LNER} = \max(\{\left|\hat{r}_i^{k+1}\right| / \sigma_{\text{meas},i}^{k+1}\}_{i\in\mathcal{SBD}_1})$. This results in a reduced set of suspected erroneous measurements $\mathcal{SBD}_2$. The information mentioned above is mathematically described by

$$\begin{aligned} &\text{if}\{\left|\hat{r}_i^{k+1}\right| / \sigma_{\text{meas},i}^{k+1} > \text{Th}_{\text{se}}\}_{i\in\mathcal{SBD}_1} \;\therefore i \in \mathcal{SBD}_2 \\ &\text{if}\{\left|\hat{r}_i^{k+1}\right| / \sigma_{\text{meas},i}^{k+1} < \text{Th}_{\text{se}}\}_{i\in\mathcal{SBD}_1} \;\therefore i \notin \mathcal{SBD}_2. \end{aligned} \tag{4.26}$$

- **Stage 3:** A smearing effect filter is applied to the set $\mathcal{SBD}_2$ to identify the erroneous measurements. This identification process is as follows. Firstly, the measurement with the largest normalized estimated residual $\text{LNER} = \max(\{\left|\hat{r}_i^{k+1}\right| / \sigma_{\text{meas},i}^{k+1}\}_{i\in\mathcal{SBD}_2})$ is identified as a bad datum and transferred to the set of identified bad data $\mathcal{IBD}$. Secondly, all measurements correlated to the identified bad datum are eliminated from $\mathcal{SBD}_2$. Finally, the identification process mentioned above is repeated for the rest of measurements in $\mathcal{SBD}_2$ until this set is empty: $\mathcal{SBD}_2 = \varnothing$. In this proposal, the correlation between measurements is determined from an incidence matrix $A_{inc} \in \mathbb{R}^{M_e^{PMU} \times (n+w+3N_{nwl}+4N_{wl})}$ with its (*i*,*j*)-element equal to 1 if the *i*-th measurement depends on the *j*-th state variable; otherwise, the element has a null value. If the (*i*,*j*)-element of $A_{inc}$ equals 1, the unitary elements in the *j*-th column correspond to the measurements that are correlated with the *i*-th measurement.

- **Stage 4:** Finally, all measurements belonging to the set $\mathcal{IBD}$ are corrected according to (4.27) and the generalized WADSE given by (4.24) at $t_{k+1}$ is solved again using the new set of corrected measurements:

$$z_{i(\text{corrected})}^{k+1} = z_i^{k+1} - \hat{r}_i^{k+1} \quad \forall i \in \mathcal{IBD}. \tag{4.27}$$

## 4.6 Processing of PMU measurements

Since the typical PMUs' sample rate corresponds to at least 30 samples/second, it is valid to assume that all PMUs measurements are available at each discrete time at which the WADSE is performed. On the other hand, since there is a probability that some measurements collected in a given time $t_{k+1}$ contain gross errors, the post-estimation bad data analysis described in Section 4.5 is performed to obtain reliable results from the proposal.

Lastly, the WADSE formulation must consider a unified reference for the estimated and collected PMUs measurements associated with voltage phase angles in order to have a coherent estimation of the system's operating state at a given instant. For the purpose of this work, the estimation is performed considering no reference angle at one of the network's nodes of PMU measurements: all voltage and rotor phase angles are estimated with respect to the time dictated by the global positioning system (GPS).

## 4.7 WADSE algorithm

The generalized WADSE approach is implemented as described below.

- **Step 1:** Set $k = 0$ and calculate the initial conditions for all dynamic and algebraic state variables $\boldsymbol{x}_{\boldsymbol{dav}}^{0}$ at $t_0$ based on the procedure described in Section 4.4.
- **Step 2:** Solve the proposed WADSE given by (4.24) for a given discrete time $t_{k+1}$, using the set of PMU measurements $\boldsymbol{z}^{k+1}$ with a time tag at $t_{k+1}$.
- **Step 3:** Perform the bad data process as described in Section 4.5 at $t_{k+1}$.
- **Step 4:** If $t_{k+1} < t_{end}$, where $t_{end}$ is the last discrete time at which the estimation is performed, then set $k = k + 1$ and return to step 2.

## 4.8 Case studies

The performance of the proposed WADSE is evaluated by using the WSCC 9-bus power system and an equivalent 190-bus model of the Mexican interconnected power system, which are reported in [Sauer, *et al*., 2018] and [Pizano-Martínez, *et al*., 2014], respectively. The WADSE formulation is coded using the mathematical programming language AMPL® [Fourer, *et al*., 2003] , where the optimization problem is solved through the Knitro® solver [Ziena Optimization LLC, 2014] using a conjugate gradient algorithm and a feasibility tolerance of $1\times10^{-8}$ at each discrete time $t_{k+1}$. The set of differential equations is discretized considering a PMU's sampling rate of 50 samples per second such that $\Delta t = 0.02$ s. The initial values of dynamic and algebraic state variables at $t_0$ are calculated as described in Section 4.4. The database of the PMUs' synchronized measurements is generated by adding random noise to the results given by a transient stability study. This results in the following set of measurements: nodal voltage magnitudes $\{V_i^{SCADA}\}_{i\in\mathcal{N}_{oe}}$, nodal phase angles $\{\theta_i^{PMU}\}_{i\in\mathcal{N}_{oe}}$, real and imaginary components of the branch currents $\left\{\Re\left(\vec{i}_{ij}^{\,PMU}\right)\right\}_{\mathcal{T}_{ij}\in\mathcal{T}_{oe}}$ and $\left\{\Im\left(\vec{i}_{ij}^{\,PMU}\right)\right\}_{\mathcal{T}_{ij}\in\mathcal{T}_{oe}}$, respectively, and the nodal frequencies $\{f_i^{PMU}\}_{i\in\mathcal{N}_{oe}}$. Furthermore, the measurements' standard deviations at each discrete time $t_{k+1}$ are assumed to be as follows: $\left\{\sigma_{V_i^{PMU}}^{k+1} = 0.002\right\}_{i\in\mathcal{N}_{oe}}$, $\left\{\sigma_{\theta_i^{PMU}}^{k+1} = 0.0017\right\}_{i\in\mathcal{N}_{oe}}$, $\left\{\sigma_{\Re\left(\vec{i}_{ij}^{\,PMU}\right)}^{k+1} = \sigma_{\Im\left(\vec{i}_{ij}^{\,PMU}\right)}^{k+1} = 0.002\right\}_{\mathcal{T}_{ij}\in\mathcal{T}_{oe}}$, and $\left\{\sigma_{f_i^{PMU}}^{k+1} = 0.002\right\}_{i\in\mathcal{N}_{oe}}$. Lastly, all results associated with the estimated rotor and voltage phase angles are reported as relative angles measured with respect to the rotor angle of generator 1 for the WSCC 9-bus power system and generator 36 for the Mexican interconnected power system.

### 4.8.1 WSCC 3-machine, 9-bus power system (base case)

This system is composed of 9 buses, 6 transmission lines, 3 transformers and 3 synchronous machines. Each synchronous machine is mathematically represented through the two-axis generator model with an excitation system IEEE DC1A. The voltage magnitude output of the excitation system's amplifiers is bounded in the range of $0 \leq V_{R,i} \leq 2.5\,\text{p.u.}\ \forall i = 1,2,3$ by using non-windup limiters. On the other hand, all valves that control the inlet of steam to the turbines have a windup limiter for maintaining the mechanical power within limits of $0 \leq P_{gov,i} \leq 1.7\,\text{p.u.}\ \forall i = 1,2,3$. The set of PMU measurements with Gaussian noise is generated from a transient stability study associated with a self-clearing fault applied at bus 7 at $t = 10$ s and cleared after 8 cycles. In this case, the system is observable by the set of 24 measurements associated with four PMUs located at observable buses $\mathcal{N}_{oe} := \{1,2,5,8\}$, as shown in Fig. 4.2. The currents flowing from PMU nodes to the adjacent nodes compose the set of branch current measurements. Lastly, note that even though no measurements are located at the generator's node 3, the estimation of dynamic variables associated with this generator and its controllers is possible by applying the proposed approach. In this case, this is possible because the proposal estimates dynamic variables with the information of zero injection power constraints at node 9, with no need to have any measurement at node 3.

Since 18 algebraic variables have to be estimated, the system has a redundancy of 1.3333. Note that the number of dynamic and complementarity state variables to be estimated does not affect the system's redundancy. This redundancy depends only on algebraic state variables and the number of measurements at the transmission grid. Note that the proposed approach does not consider dynamic states' measurements and that the number of constraints added to (4.24) equals that number of state variables.

Figures 4.3 to 4.8 clearly show that the estimations of the relative rotor angle and angular speed trajectories of each generator compare well with the real trajectories obtained from the transient stability study. A similar observation can be done when comparing the estimations of nodal voltages at unobservable nodes, as shown in Figs. 4.9 to 4.18.

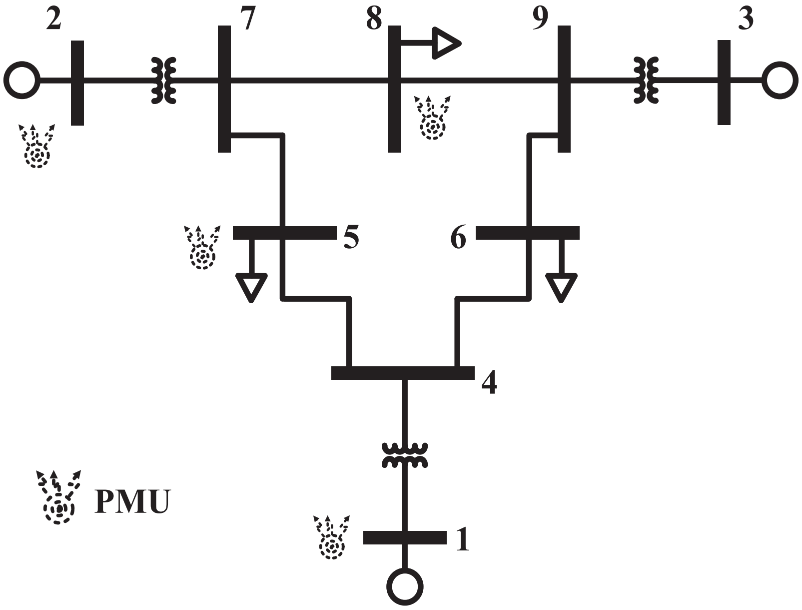

Fig. 4.2 Measurement diagram of WSCC 9-bus power system.

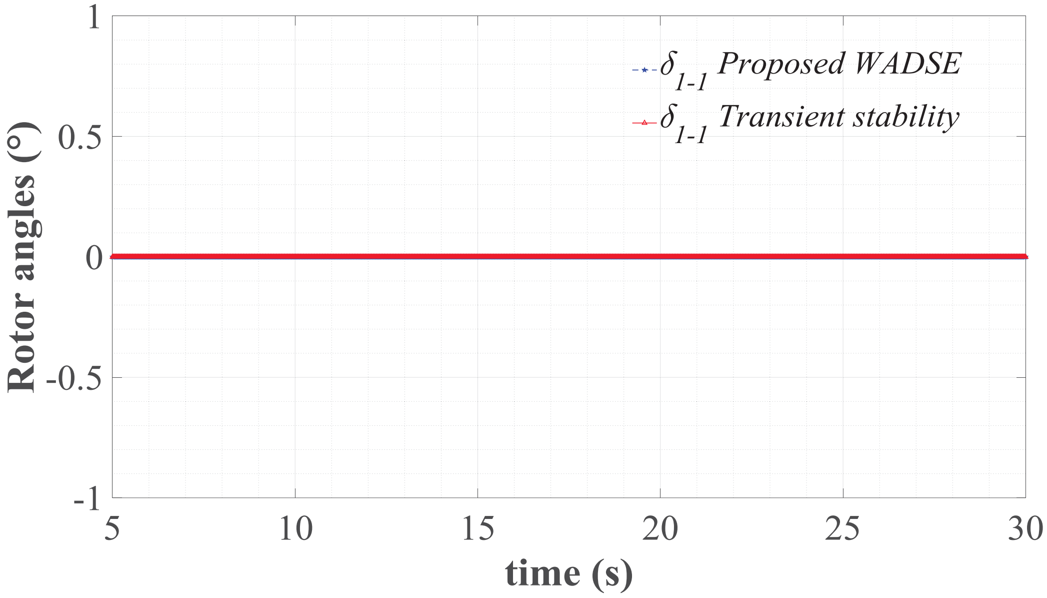

Fig. 4.3 Estimated and real relative rotor angles' trajectories of the machine connected at bus 1.

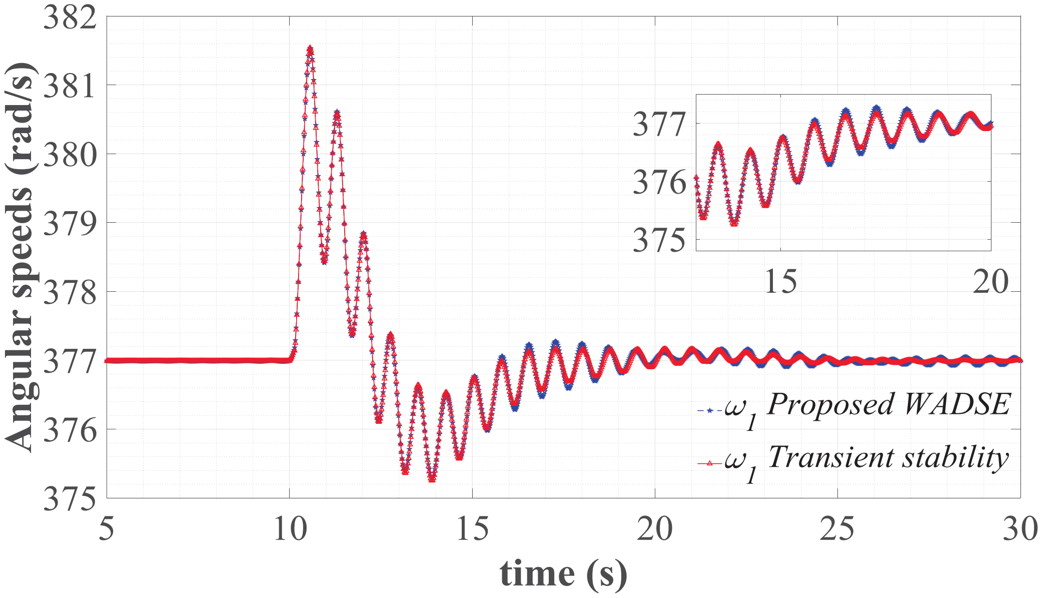

Fig. 4.4 Estimated and real angular speeds' trajectories of the machine connected at bus 1.

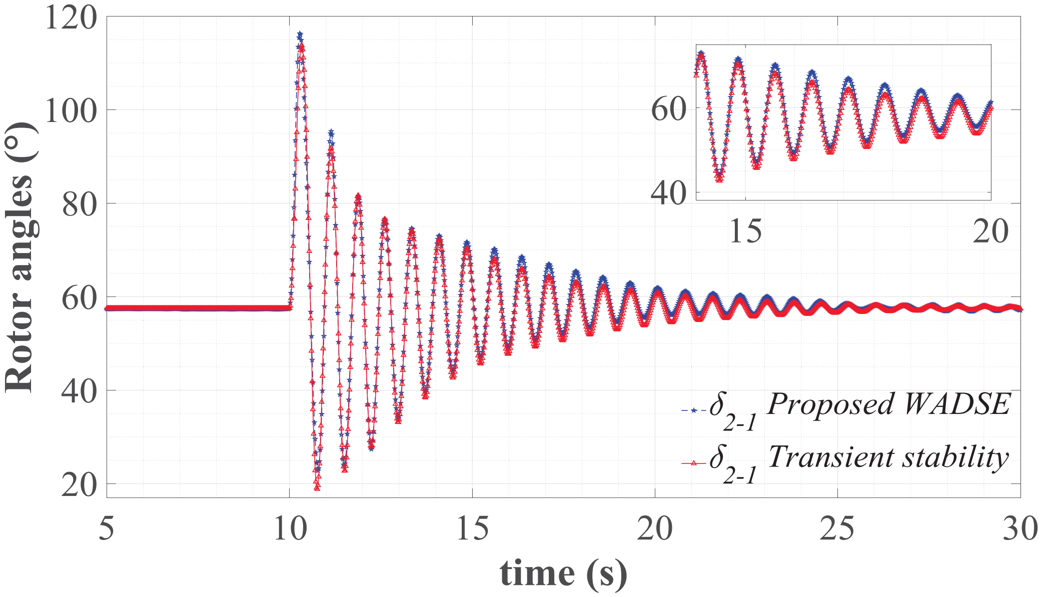

Fig. 4.5 Estimated and real relative rotor angles' trajectories of the machine connected at bus 2.

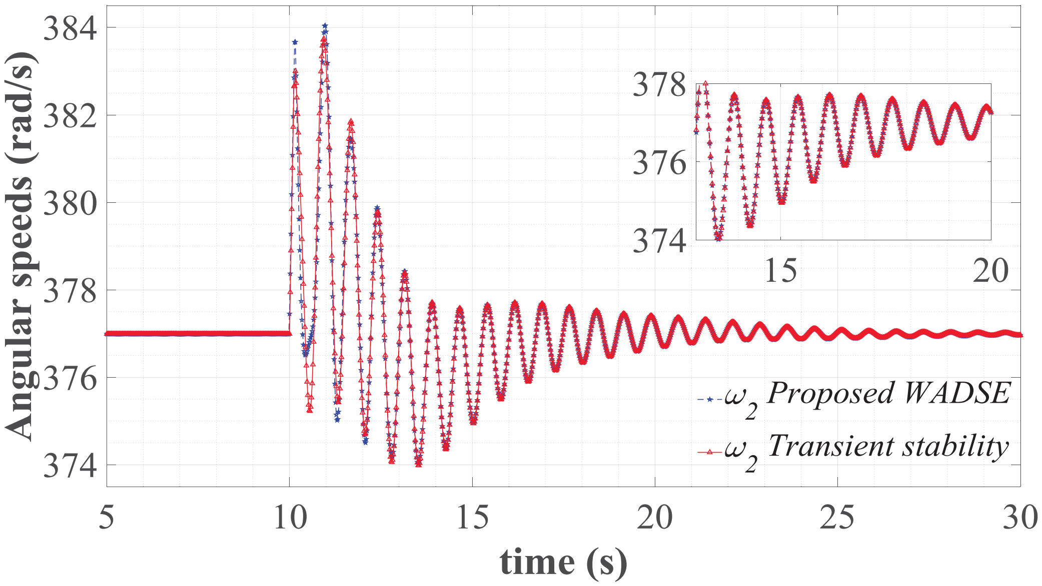

Fig. 4.6 Estimated and real angular speeds' trajectories of the machine connected at bus 2.

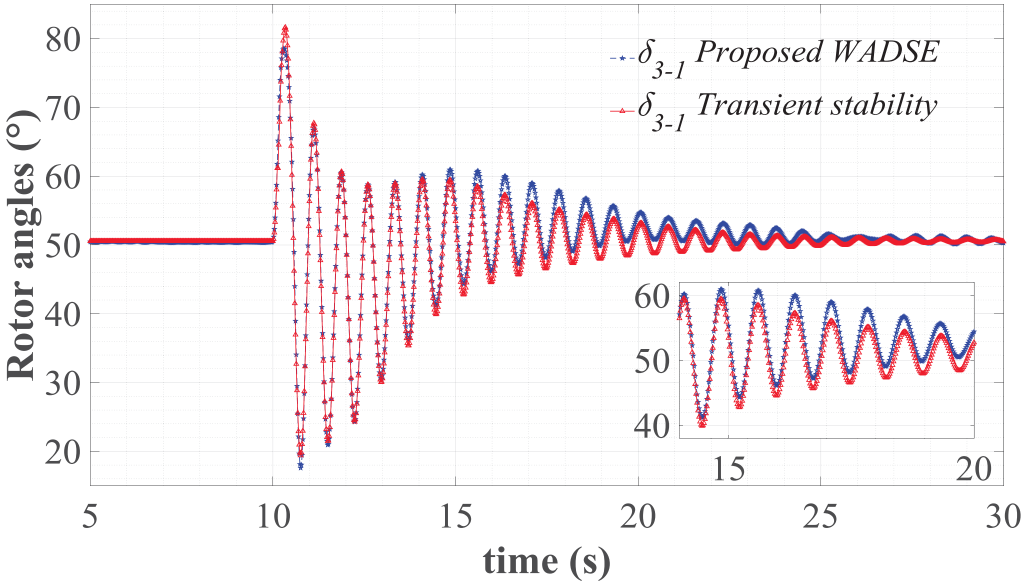

Fig. 4.7 Estimated and real relative rotor angles' trajectories of the machine connected at bus 3.

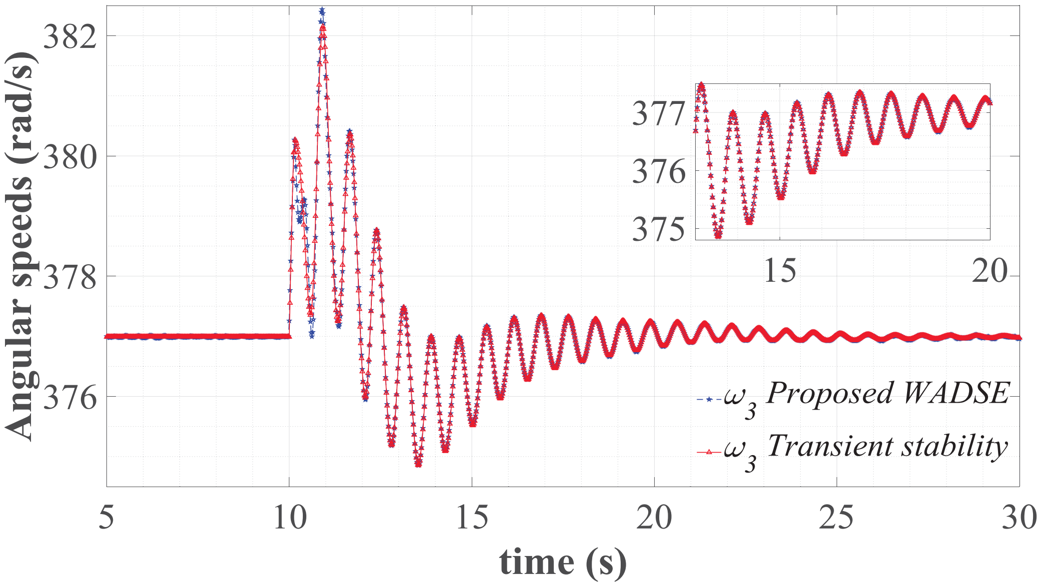

Fig. 4.8 Estimated and real angular speeds' trajectories of the machine connected at bus 3.

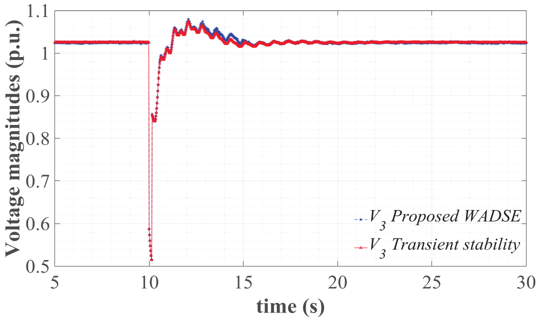

Fig. 4.9 Estimated and real nodal voltage magnitudes at bus 3.

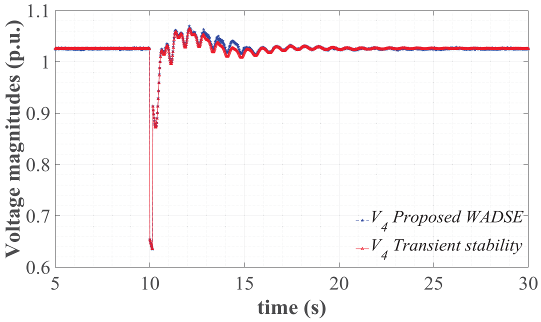

Fig. 4.10 Estimated and real nodal voltage magnitudes at bus 4.

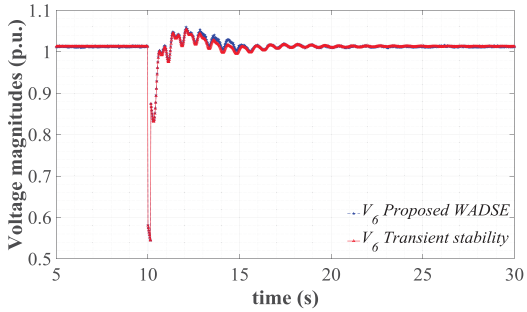

Fig. 4.11 Estimated and real nodal voltage magnitudes at bus 6.

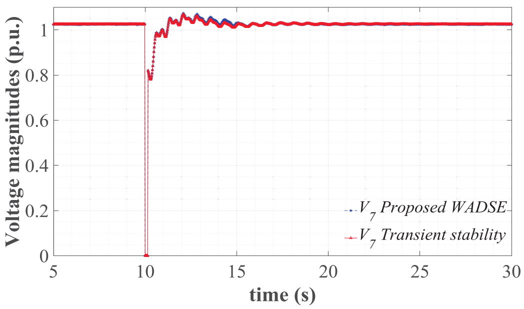

Fig. 4.12 Estimated and real nodal voltage magnitudes at bus 7.

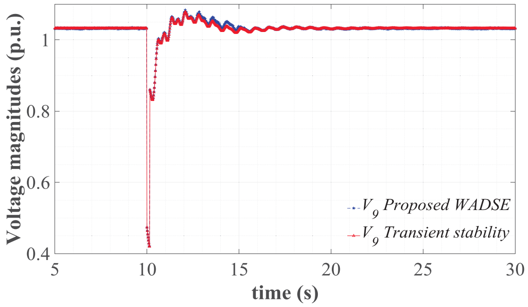

Fig. 4.13 Estimated and real nodal voltage magnitudes at bus 9.

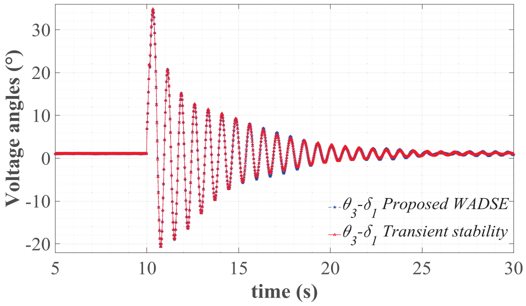

Fig. 4.14 Estimated and real nodal phase angles at bus 3.

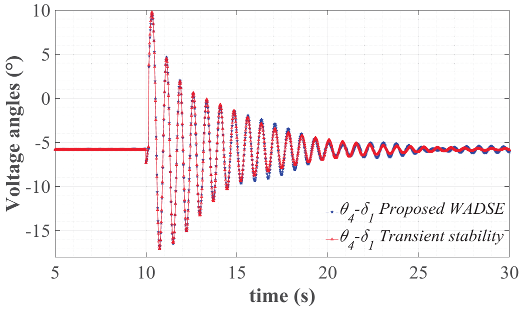

Fig. 4.15 Estimated and real nodal phase angles at bus 4.

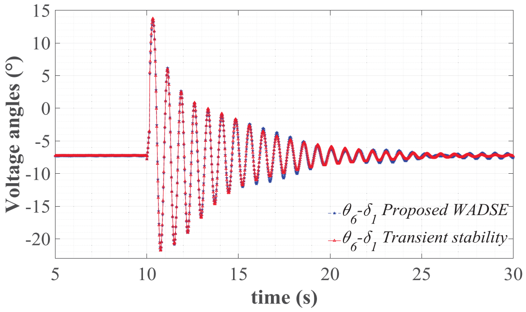

Fig. 4.16 Estimated and real nodal phase angles at bus 6.

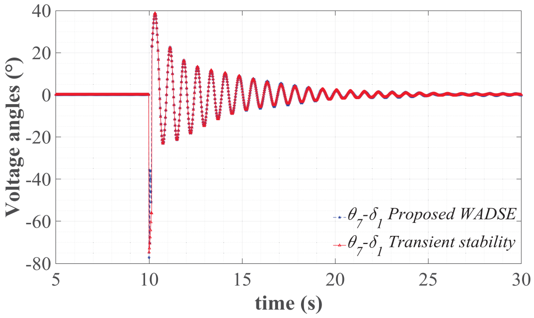

Fig. 4.17 Estimated and real nodal phase angles at bus 7.

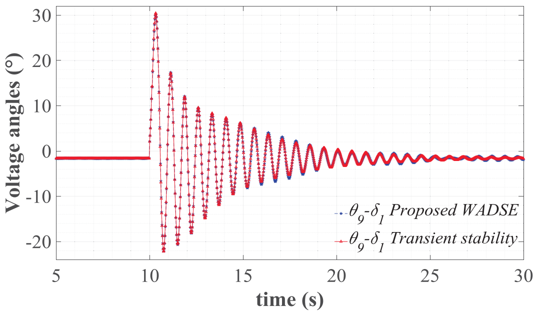

Fig. 4.18 Estimated and real nodal phase angles at bus 9.

In order to quantify the accuracy of the proposed approach, the mean absolute percentage errors (MAPEs) of dynamic variables and nodal voltages are computed by (4.28) through (4.30), where $N_{sm}$ corresponds to the number of synchronous machines and $N_{buses}$ is the total number of buses in the system. Note that this index depends on both the estimated and true values of state variables at a given discrete time.

$$\mathbf{MAPE}(\boldsymbol{x}^{k+1}) = \frac{1}{N_{sm}} \sum_{i=1}^{N_{sm}} \frac{\left|\hat{x}_i^{k+1} - x_i^{k+1}\right|}{x_i^{k+1}}, \tag{4.28}$$

$$\mathbf{MAPE}(\boldsymbol{V}^{k+1}) = \frac{1}{N_{buses}} \sum_{i=1}^{N_{buses}} \frac{\left|\hat{V}_i^{k+1} - V_i^{k+1}\right|}{V_i^{k+1}}, \tag{4.29}$$

$$\mathbf{MAPE}(\boldsymbol{\theta}^{k+1}) = \frac{1}{N_{buses}} \sum_{i=1}^{N_{buses}} \frac{\left|\hat{\theta}_i^{k+1} - \theta_i^{k+1}\right|}{\theta_i^{k+1}}. \tag{4.30}$$

The results of evaluating these indexes are shown in Figs. 4.19 to 4.24. The proposed approach effectiveness is evident since the MAPEs' low values mean accurate estimates.

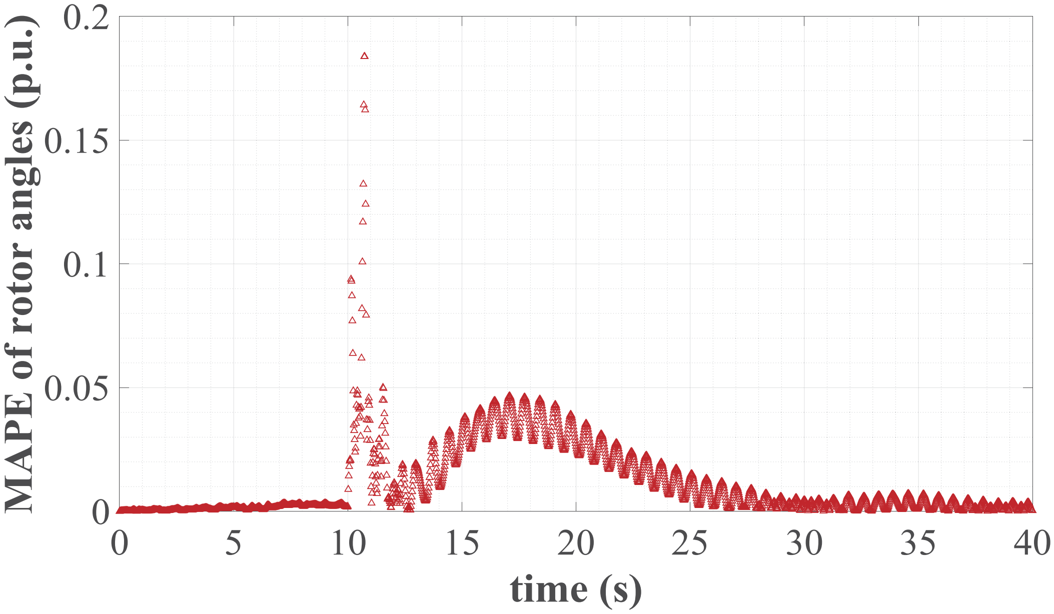

Fig. 4.19 MAPE values of rotor angles of synchronous machines in the WSCC 9-bus power system.

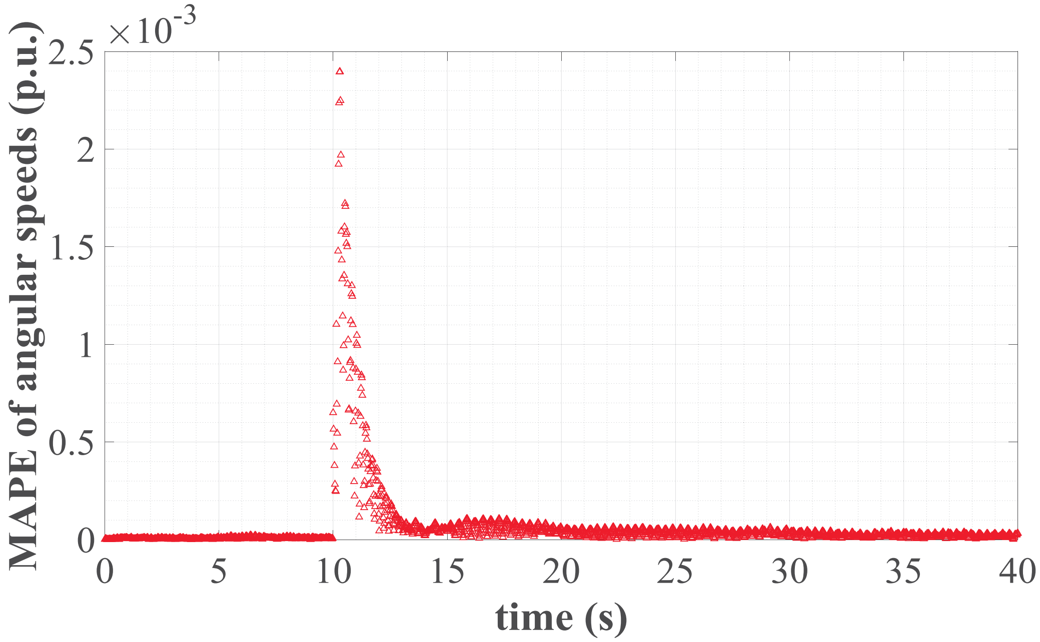

Fig. 4.20 MAPE values of angular speeds of synchronous machines in the WSCC 9-bus power system.

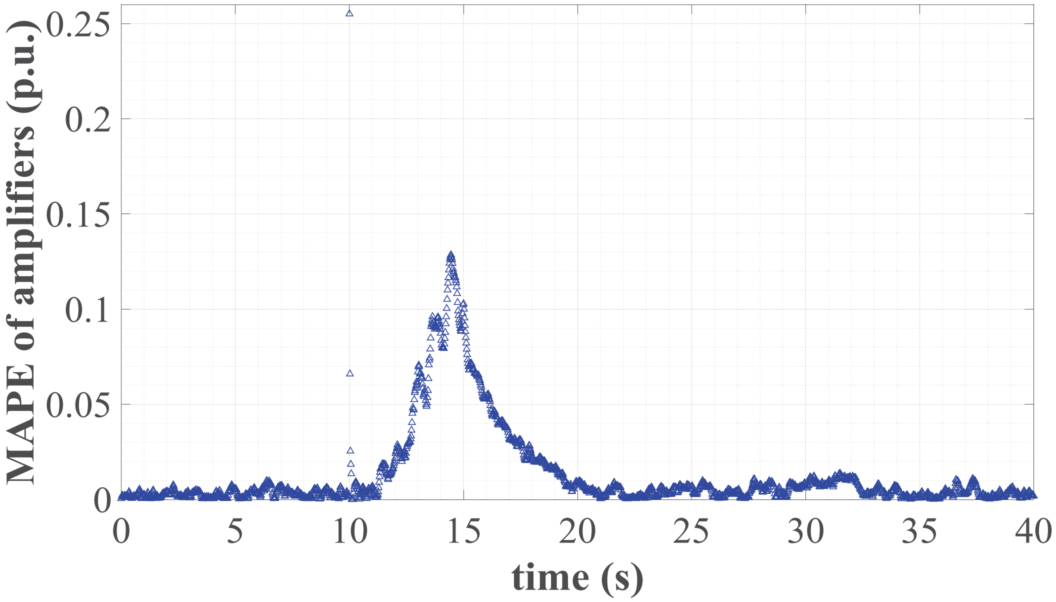

Fig. 4.21 MAPE values of amplifiers' scaled outputs of excitation systems in the WSCC 9-bus power system.

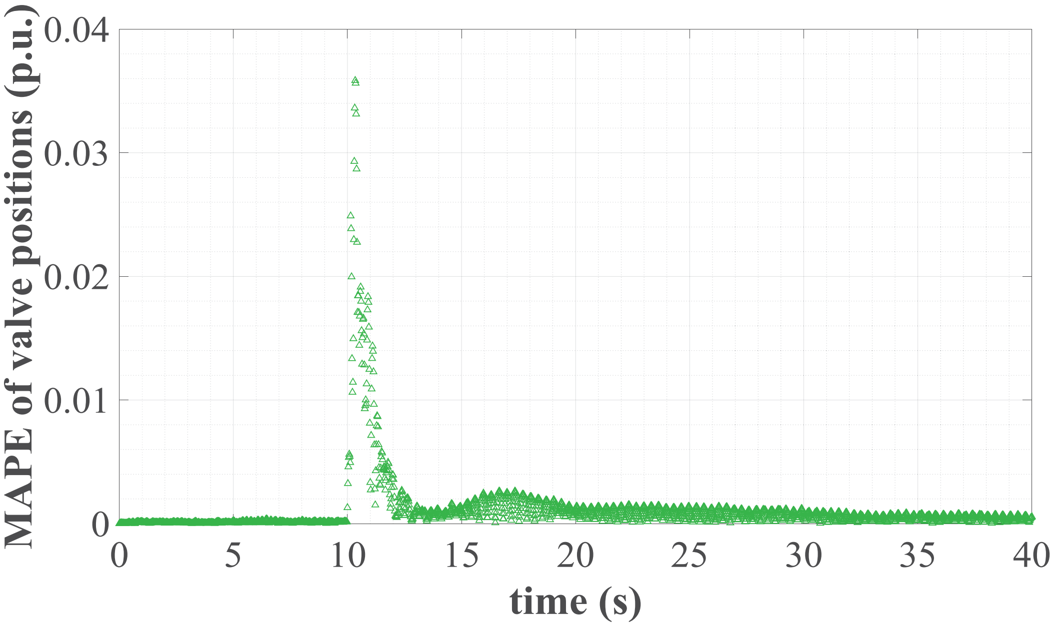

Fig. 4.22 MAPE values of steam valve positions of speed governing systems in the WSCC 9-bus power system.

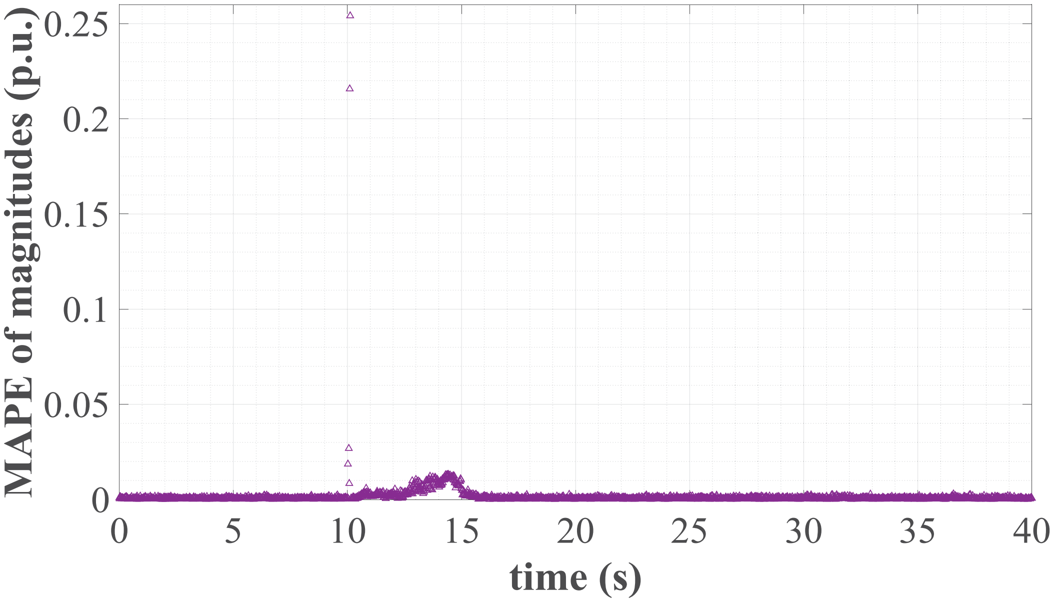

Fig. 4.23 MAPE values of nodal voltage magnitudes in the WSCC 9-bus power system.

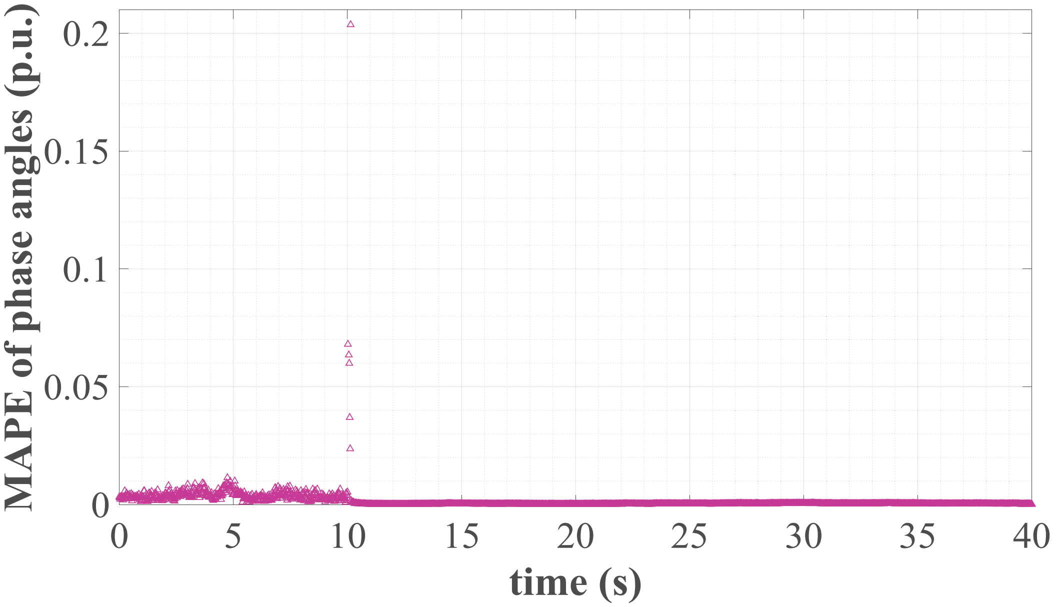

Fig. 4.24 MAPE values of nodal phase angles in the WSCC 9-bus power system.

Lastly, the estimations obtained for the rotor angle and angular speed trajectories associated with the generator embedded at node 3 are compared with the ones obtained by applying the unscented Kalman filter. In the latter case, measurements at node 3 are necessary for performing the local dynamic state estimation. Hence, these measurements are generated in the same way described above for the real and imaginary components of nodal voltage magnitude and phase angle as well as the current injected at node 3. All these measurements contain a random Gaussian noise with deviations of $\{\sigma_{\text{meas},i} = 0.002\}_{i=1}^{4}$, while the dynamic process is assumed to follow a Gaussian distribution with deviations of $\{\sigma_{\text{process},i} = 0.002\}_{i=1}^{4}$. The results of estimated rotor angle and angular speed applying both the WADSE proposal and the unscented Kalman filter are shown in Figs. 4.25 and 4.26, respectively, together with the real values obtained from the transient stability study. From these figures, it is clear that the proposed estimator and the Kalman-based estimator provide estimates of dynamic variables close to the real values, but with the important difference that unlike the proposed approach, the unscented Kalman filter requires measurements at the generator's terminal to perform the estimation of dynamic state variables.

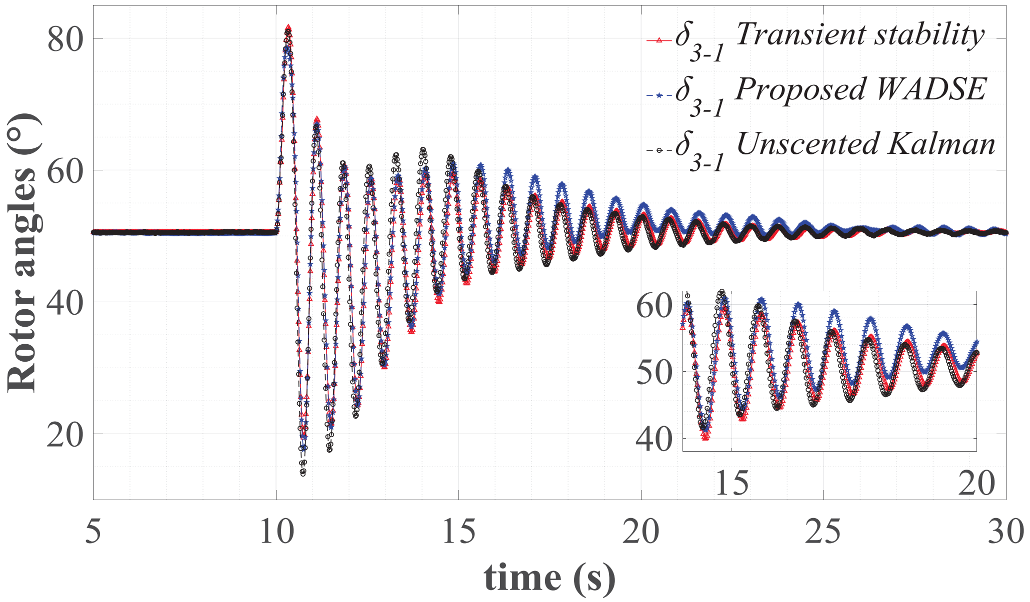

Fig. 4.25 Estimated and real relative rotor angles' trajectories of the machine connected at bus 3.

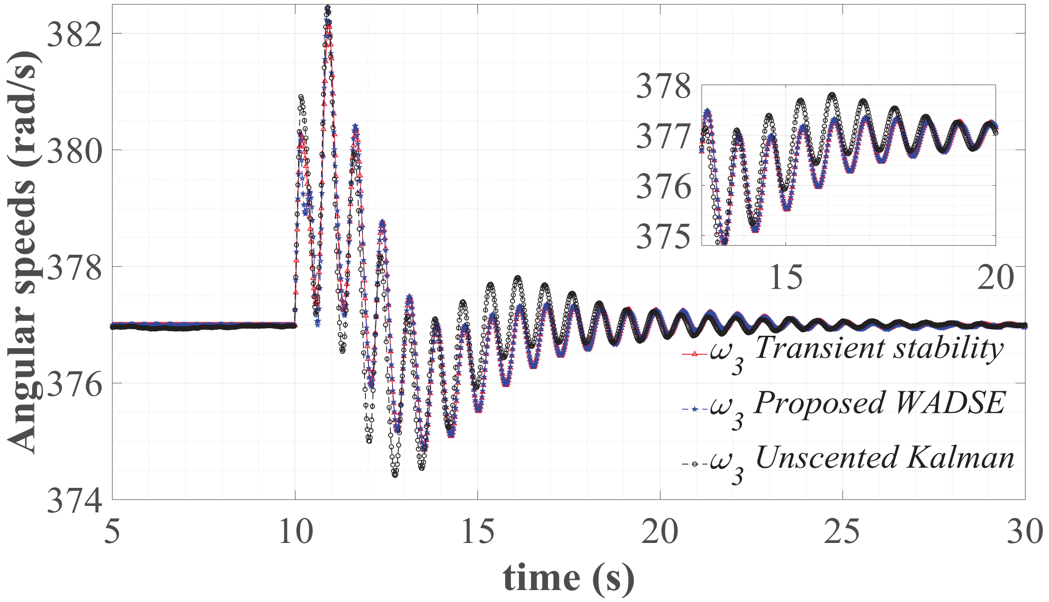

Fig. 4.26 Estimated and real angular speeds' trajectories of the machine connected at bus 3.

### 4.8.2 WSCC 3-machine, 9-bus power system (bad data)

Recent research reveals that the error distribution of PMU measurements is unlikely to follow a Gaussian probability distribution [Zhou, *et al.*, 2014; Wang, *et al.*, 2018]. Hence, the case study described in Section 4.8.1 is repeated but considers a Gaussian mixture probability distribution that is comprised of two Gaussian components. The *i*-th measurement's error is represented by the following parameters for the first (resp. second) Gaussian component: i) a mean of $\left\{-0.5\sigma_{\text{meas},i}^{k+1}\right\}_{i=1}^{M_e^{PMU}}$ (resp. $\left\{0.7\sigma_{\text{meas},i}^{k+1}\right\}_{i=1}^{M_e^{PMU}}$), ii) a standard deviation of $\left\{0.7\sigma_{\text{meas},i}^{k+1}\right\}_{i=1}^{M_e^{PMU}}$ (resp. $\left\{1.3\sigma_{\text{meas},i}^{k+1}\right\}_{i=1}^{M_e^{PMU}}$), and iii) a weight value equal to 0.7 (resp. 0.3). Furthermore, the measurements of both nodal voltage magnitudes and nodal phase angles available at buses 1 and 2 are assumed to have gross errors during the period of time $10 \le t \le 15$ s. These gross errors are generated by adding to each measurement a value of 60 times its corresponding standard deviation: $\left\{60\sigma_{V_i^{PMU}}^{k+1}\right\}_{i\in\{1,2\}}$ and $\left\{60\sigma_{\theta_i^{PMU}}^{k+1}\right\}_{i\in\{1,2\}}$, respectively. The bad data methodology described in Section 4.5 is used for the detection, identification and correction of measurements with gross errors. The latter is applied to keep the measurements' redundancy intact during the entire period in which the WADSE is performed. The estimated trajectories of the relative rotor angle, angular speed, amplifier's output and steam valve position for the synchronous machine connected at node 3 are shown from Figs. 4.27 to 4.30 together with the true trajectories obtained from the transient stability study. Please note that these estimated trajectories are determined by considering that there is no PMU measurement at node 3. In addition, the estimated and true trajectories of the steam valve position for the synchronous machine connected at node 2 are shown in Fig. 4.31.

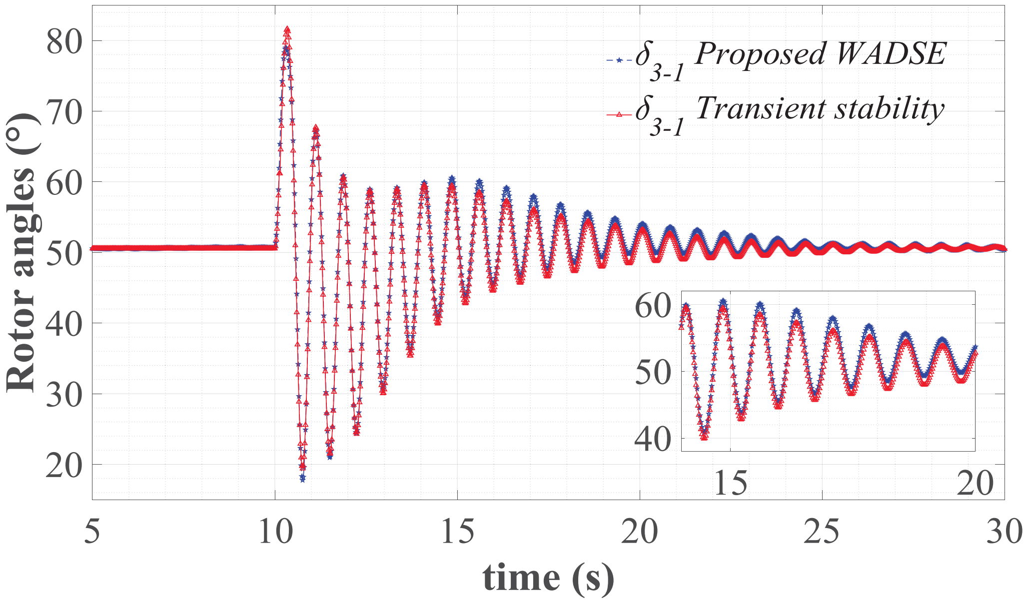

Fig. 4.27 Estimated and real relative rotor angles' trajectories of the machine connected at node 3.

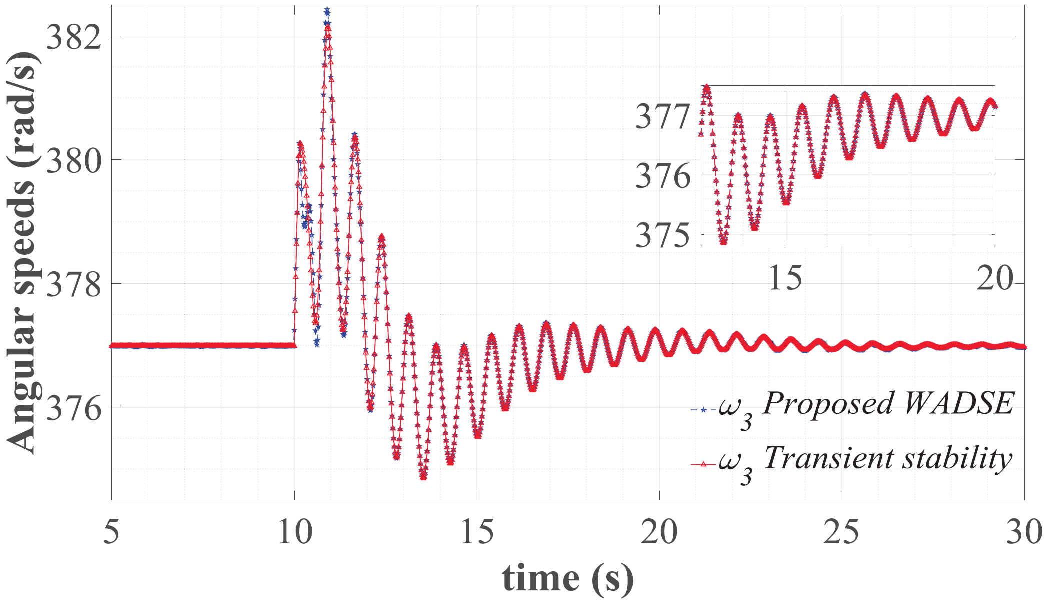

Fig. 4.28 Estimated and real angular speeds' trajectories of the machine connected at node 3.

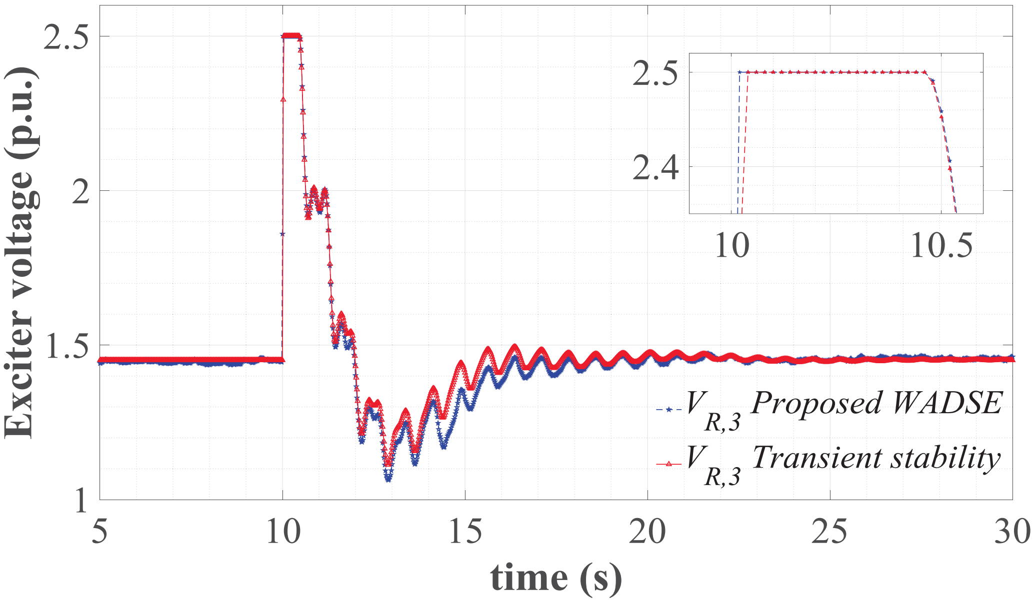

Fig. 4.29 Estimated and real amplifier scaled outputs' trajectories of the machine connected at node 3.

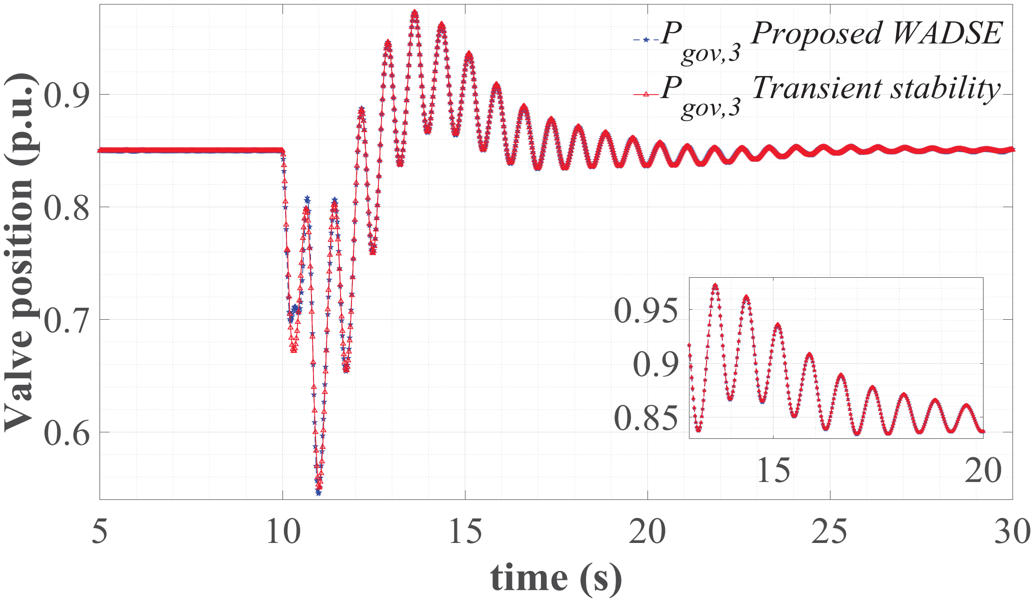

Fig. 4.30 Estimated and real steam valve positions' trajectories of the machine connected at node 3.

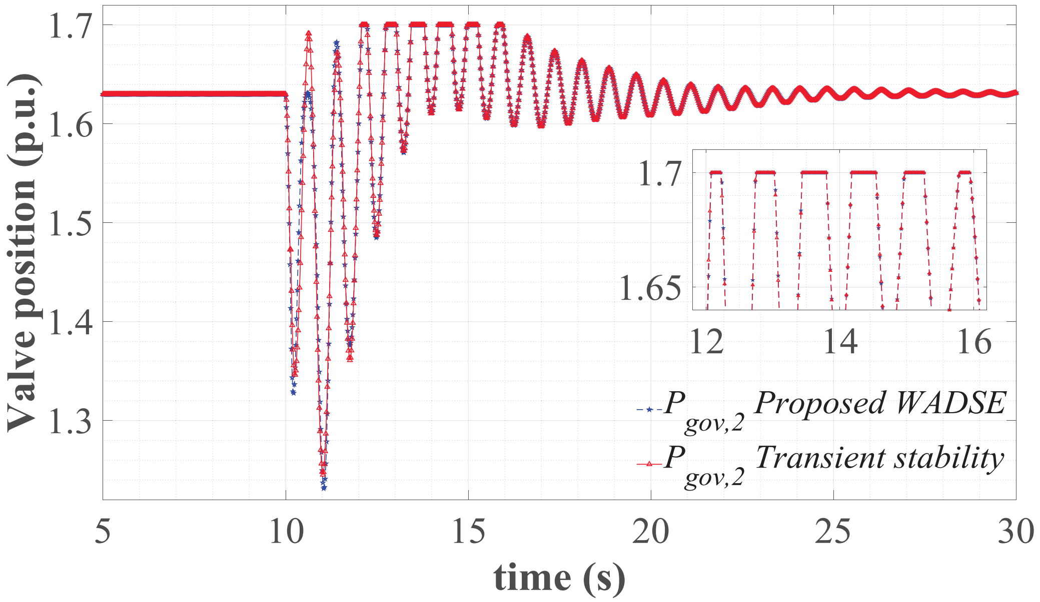

Fig. 4.31 Estimated and real steam valve positions' trajectories of the machine connected at node 2.

A comparison of the estimated and real trajectories clearly shows the effectiveness of the proposed approach for estimating dynamic state variables. From Figs. 4.29 and 4.31 it is also clear how the proposed method permits the simultaneous and automatic handling of both non-windup and windup hard limits on dynamic states during the WADSE solution process. Note from Fig. 4.29 how the WADSE correctly estimates the upper limit violation of the amplifier's output of the generator connected at bus 3 at a value of 2.5. This validates that the proposal succeeds in reproducing the action of non-windup limiters within the state estimation framework. In addition, Fig. 4.31 shows that the proposal also manages to estimate the behavior of windup limiters adequately because the estimated trajectory of the steam valve position of the generator connected at node 2 is set at a value of 1.7 at the same time instants given by the real trajectory. Finally, the implemented bad data analysis proposed in [Martínez-Parrales, *et al*., 2020] manages to correct the erroneous measurements contained between $10 \le t \le 15$ s since the estimated and real trajectories of the dynamic variables are very close over the entire period of time.

Lastly, the MAPE quality index associated with the estimation of both magnitudes and phase angles of nodal voltages is shown in Figs. 4.32 and 4.33, respectively. The low value of this index during the entire period of time of the state estimation process indicates the accuracy with which the WADSE estimates nodal voltage magnitudes.

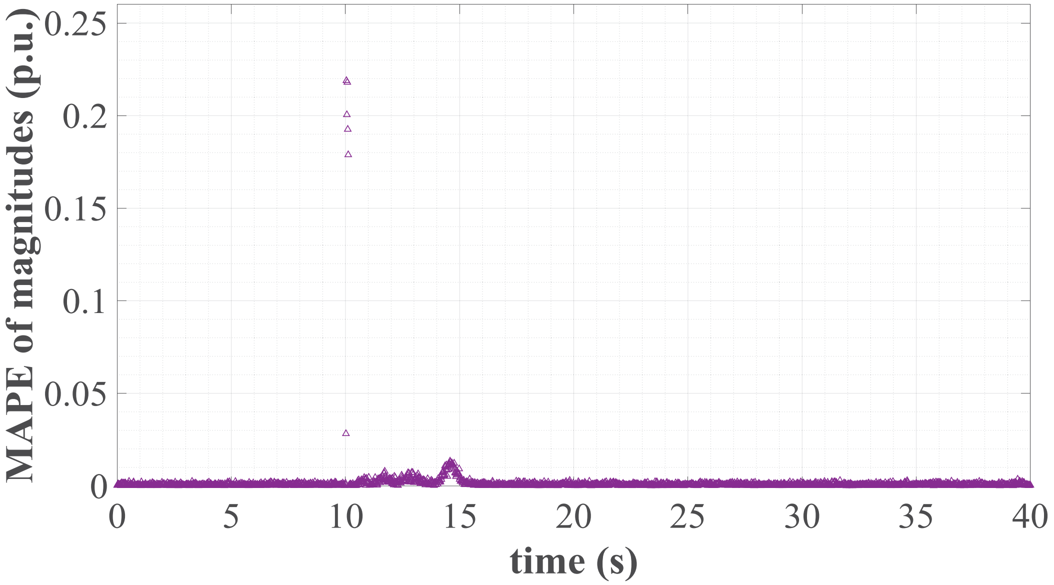

Fig. 4.32 MAPE values of nodal voltage magnitudes in the WSCC 9-bus power system.

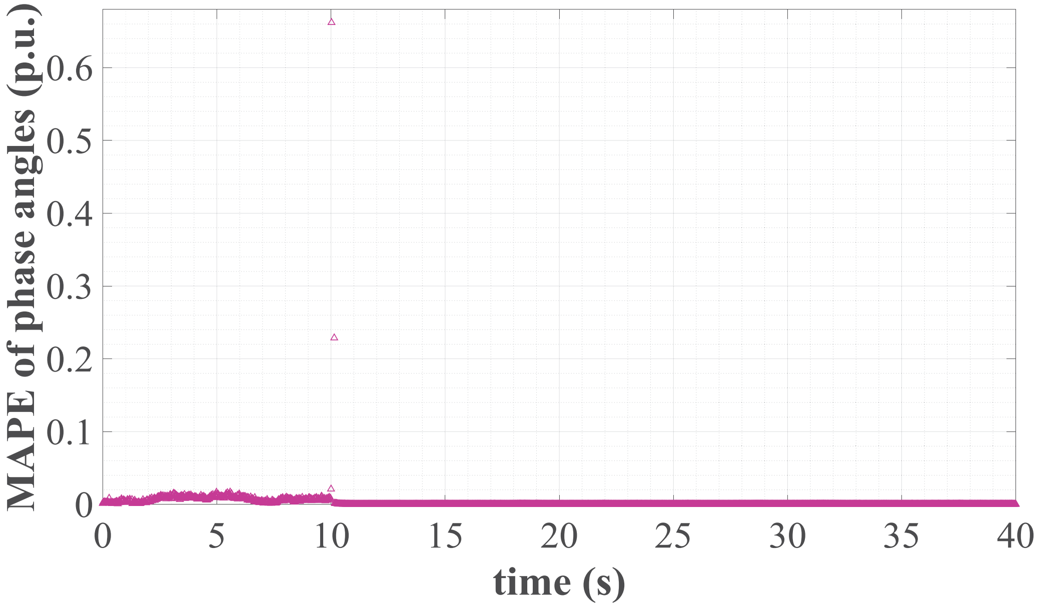

Fig. 4.33 MAPE values of nodal phase angles in the WSCC 9-bus power system.

### 4.8.3 Mexican 46-machine, 190 bus power system

The proposed approach is applied to an equivalent model of the Mexican interconnected power system (MIPS) that includes the northern, northeastern, western, central and southeastern control areas, as shown in Fig. 4.34.

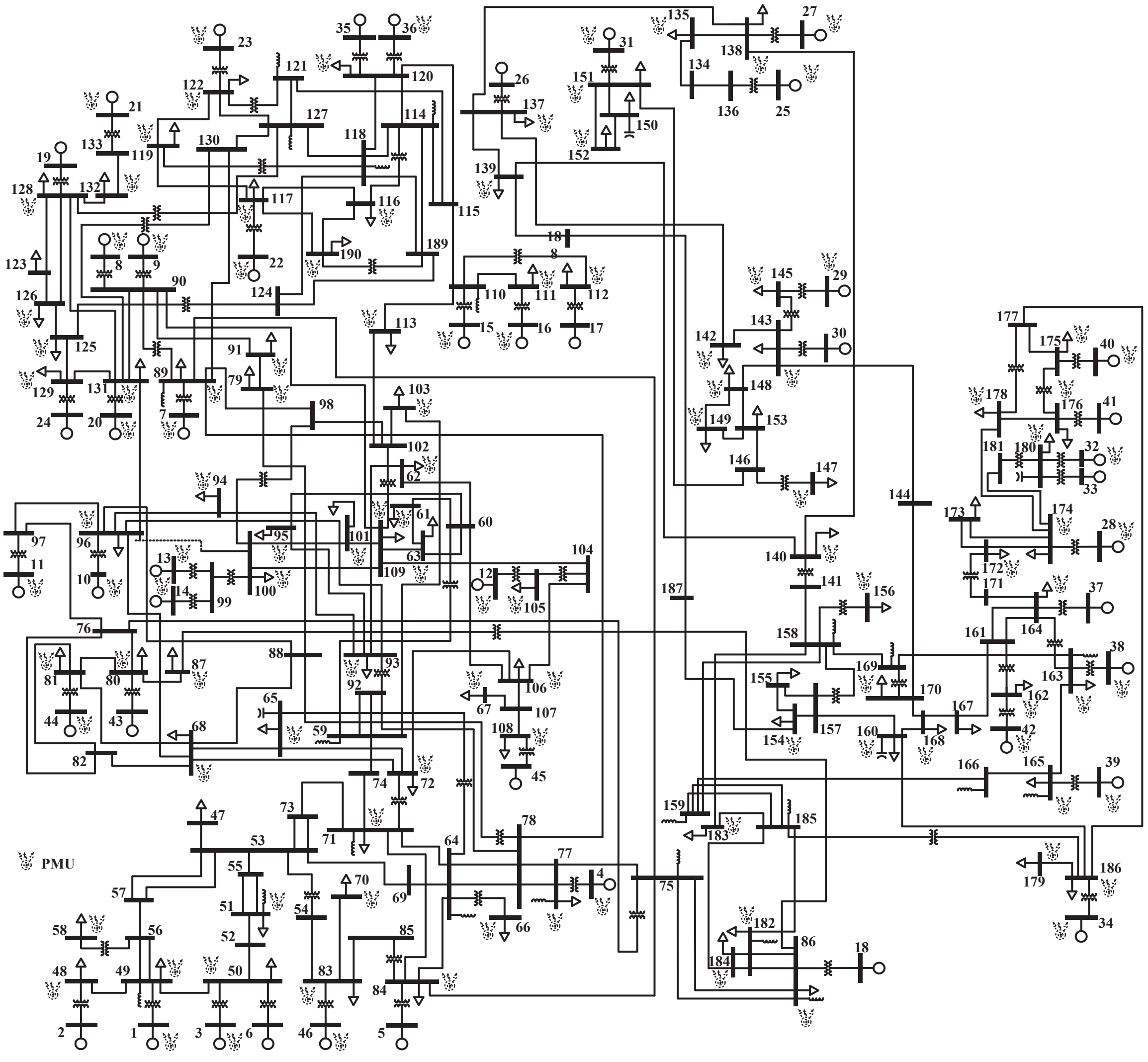

Fig. 4.34 Measurement diagram of the 190-bus MIPS.

This equivalent model is comprised of 190 nodes, 46 generators, 263 transmission elements, 90 loads and 26 shunt elements at voltage levels ranging from 400 kV to 115 kV. All generators have the same machine models and controls described in Section 4.8.1. Furthermore, the bounds of non-windup and windup limiters are those reported in Section

3.5.2. A transient stability study is performed for a time period of 30 s, where a self-clearing fault at bus 182 is incepted at $t = 10$ s and cleared after 8 cycles. The system withstands this contingency because both relative rotor angles and nodal voltage magnitudes return to the pre-fault conditions: the system is transiently stable for this contingency scenario.

The proposed estimator uses the results of the transient stability study and also adds a random noise to obtain the set of measurements at each sampling time $t_{k+1}$. As shown in Fig. 4.34, a set of 953 measurements is provided by 115 PMUs located in the following set of observable nodes: $\mathcal{N}_{oe} := \{$1, 3, 4, 7, 8, 9, 10, 11, 12, 13, 14, 15, 16, 20, 21, 22, 23, 25, 27, 28, 29, 31, 32, 34, 36, 38, 39, 40, 42, 44, 46, 48, 49, 50, 51, 58, 61, 62, 63, 65, 66, 67, 68, 70, 71, 72, 77, 79, 80, 81, 83, 84, 86, 87, 89, 91, 93, 94, 95, 96, 100, 101, 103, 105, 106, 108, 109, 111, 112, 113, 116, 117, 119, 120, 122, 125, 126, 128, 129, 131, 132, 135, 137, 138, 139, 140, 142, 143, 145, 147, 148, 149, 151, 152, 154, 156, 160, 162, 163, 164, 165, 168, 170, 172, 174, 175, 176, 178, 179, 180, 182, 183, 184, 186 and 190$\}$. The standard deviations of the different types of measurements are the ones reported in Section 4.8.1, while the random noise is assumed to be a Gaussian mixture probability distribution with two Gaussian components, with their data as reported in Section 4.8.2. Since the algebraic variables to be estimated are 380, the system's redundancy corresponds to 2.5078. Lastly, the measurements associated with the magnitudes and phase angles at nodes 4 and 34 have gross errors from $t = 10$ s to $t = 15$ s, which are generated as reported in Section 4.8.2.

The estimated and actual trajectories of the relative rotor angle, angular speed, the amplifier's output and the steam valve position of the machine connected at bus 18, which is the closest to the fault and does not have a PMU, are shown in Figs. 4.35 to 4.38, respectively. Note from these results that the proposed estimator obtains dynamic variables' estimations that are very close to the actual values attained by the transient stability study. Similarly, from Fig. 4.37 the WADSE manages to limit the exciter amplifier of the machine connected at node 18 to a value of 7.5. Hence, this result newly validates that the estimator is capable of reproducing the behavior of the non-windup limiter associated with this variable. Furthermore, the bad data process presents a good performance since it manages to correct the gross measurements. This statement is validated by the results mentioned above, which show that the estimated and real trajectories of dynamic variables are very close.

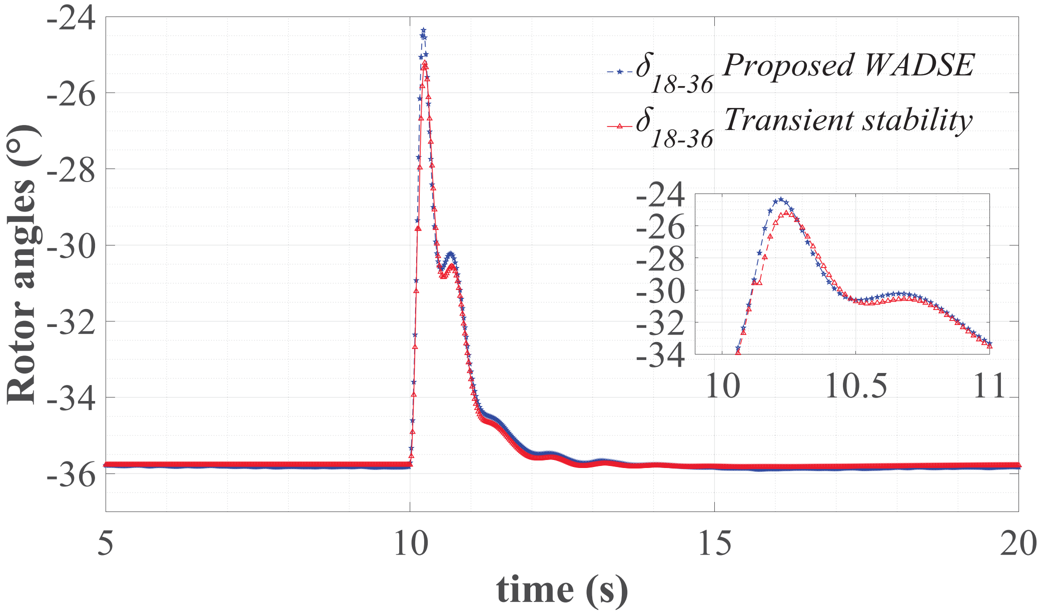

Fig. 4.35 Estimated rotor angle trajectory of the machine connected at node 18.

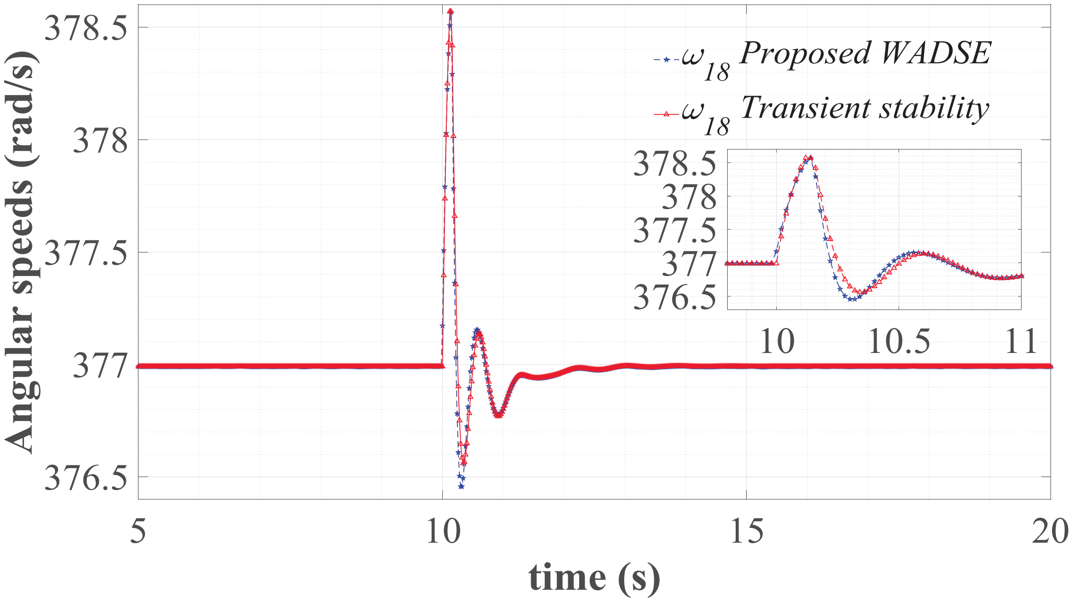

Fig. 4.36 Estimated angular speed trajectory of the machine connected at node 18.

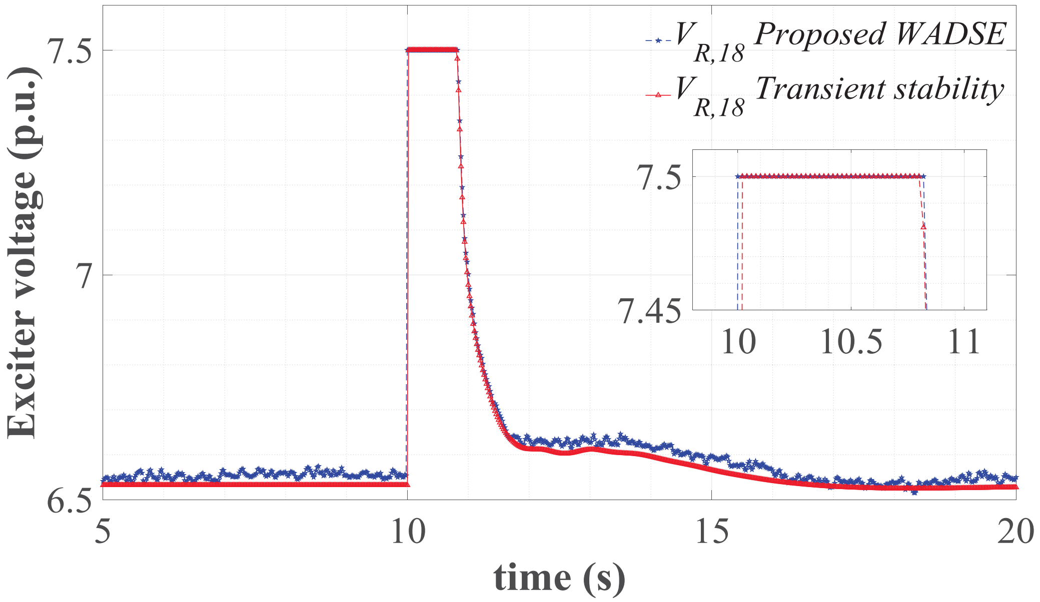

Fig. 4.37 Estimated amplifier scaled output trajectory of the machine connected at node 18.

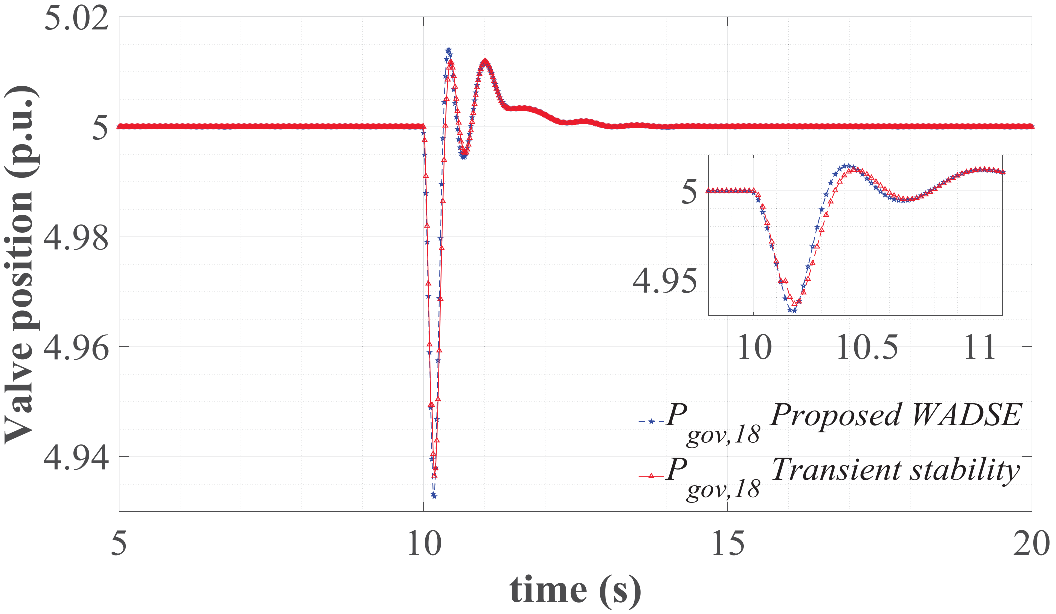

Fig. 4.38 Estimated steam valve position trajectory of the machine connected at node 18.

Once the estimated trajectories have been obtained by the proposed approach, it is possible to apply a moving average filter in order to smooth the results of the proposed WADSE. The key idea of the moving average filter is to apply an average every certain number of samples as described next. Let $\hat{\boldsymbol{x}} \in \mathbb{R}^{mf}$ be the variable without the filter, $\tilde{\boldsymbol{x}} \in \mathbb{R}^{mf}$ be the variable with the moving average filter and $nm$ be the number of samples in which the filter will be applied. The equation that defines the moving average filter is presented in (4.31):

$$\begin{aligned} \tilde{x}_i &= \frac{1}{i}\sum_{j=1}^{i}\hat{x}_j \quad \forall\, i = 1,\ldots,nm-1, \\ \tilde{x}_i &= \frac{1}{nm}\sum_{j=i-(nm-1)}^{i}\hat{x}_j \quad \forall\, i = nm,\ldots,mf. \end{aligned} \tag{4.31}$$

Figure 4.39 shows the scaled output of the generator's amplifier connected to node 19 without the filter and the same estimated trajectory with the moving average filter applied to every 9 samples. Note that the moving average filter applied to the estimated trajectory obtains a smoother trajectory with respect to the original, so the results provided by the WADSE can be improved using this technique.

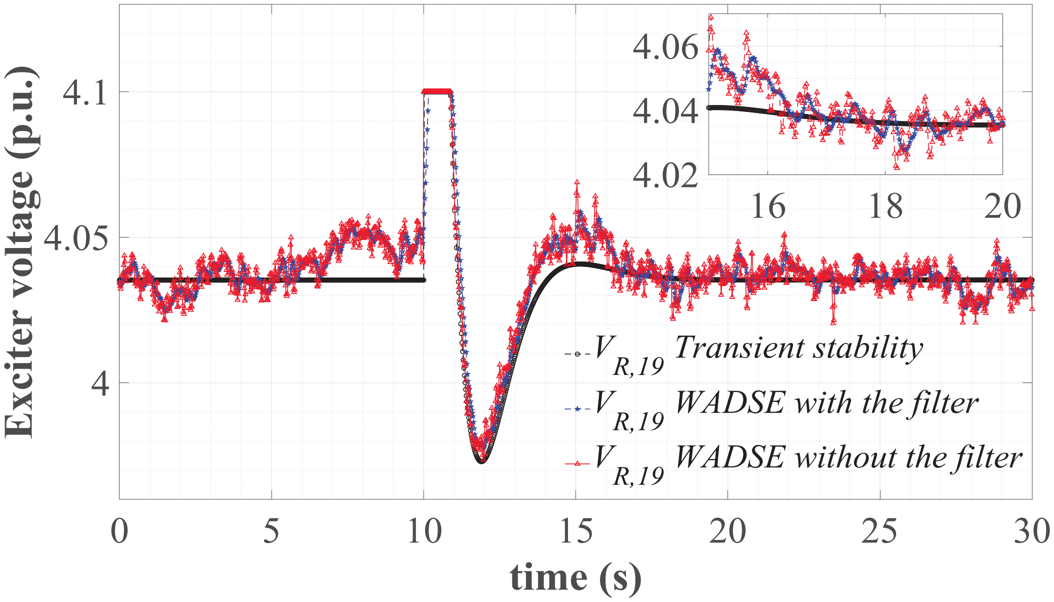

Fig. 4.39 Comparison of amplifier scaled outputs trajectories of the machine connected at node 19 with and without the moving average filter.

In order to quantify the accuracy of the proposed WADSE, the MAPE's values of the relative rotor angles, angular speeds, the amplifiers scaled outputs and the steam valve positions for the entire period of time are shown in Figs 4.40 to 4.43, respectively, while the MAPE values of magnitude and phase angles of nodal voltages are shown in Figs. 4.44 and 4.45, respectively.

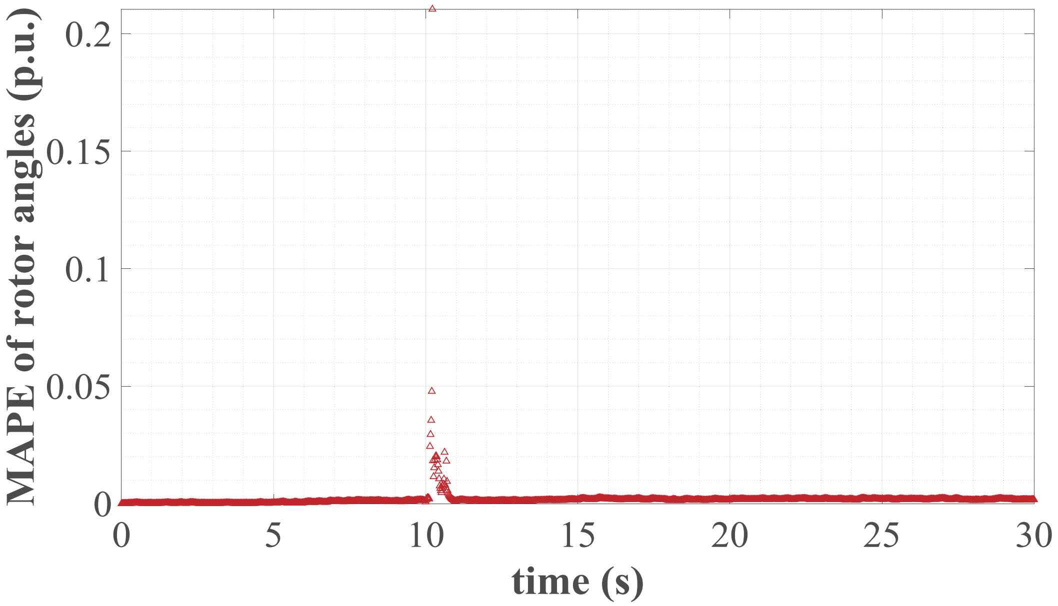

Fig. 4.40 MAPE values of rotor angles of synchronous machines in the 190-bus MIPS.

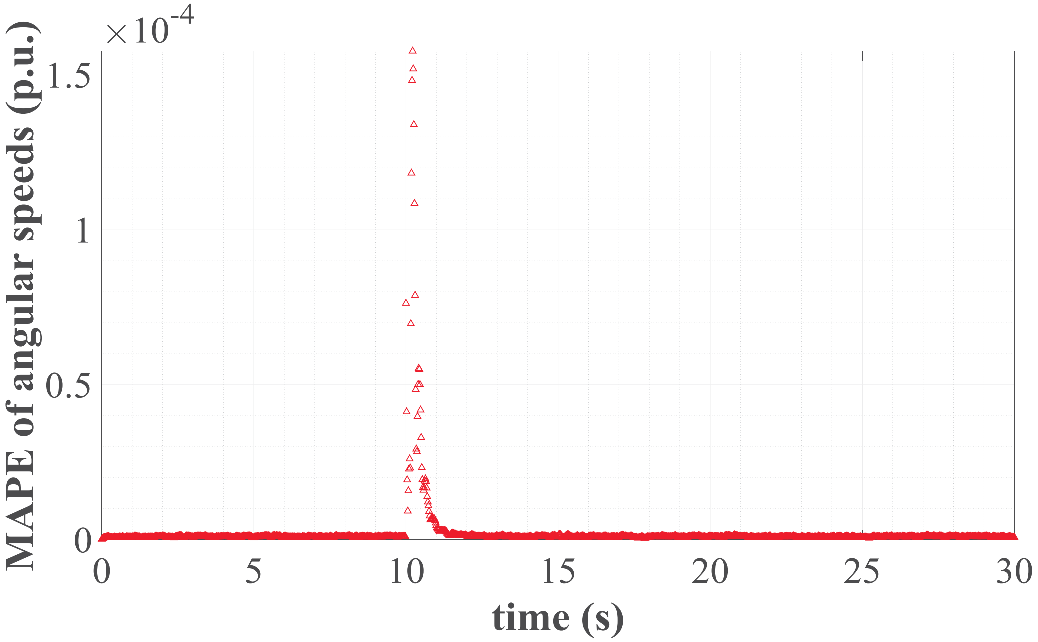

Fig. 4.41 MAPE values of angular speeds of synchronous machines in the 190-bus MIPS.

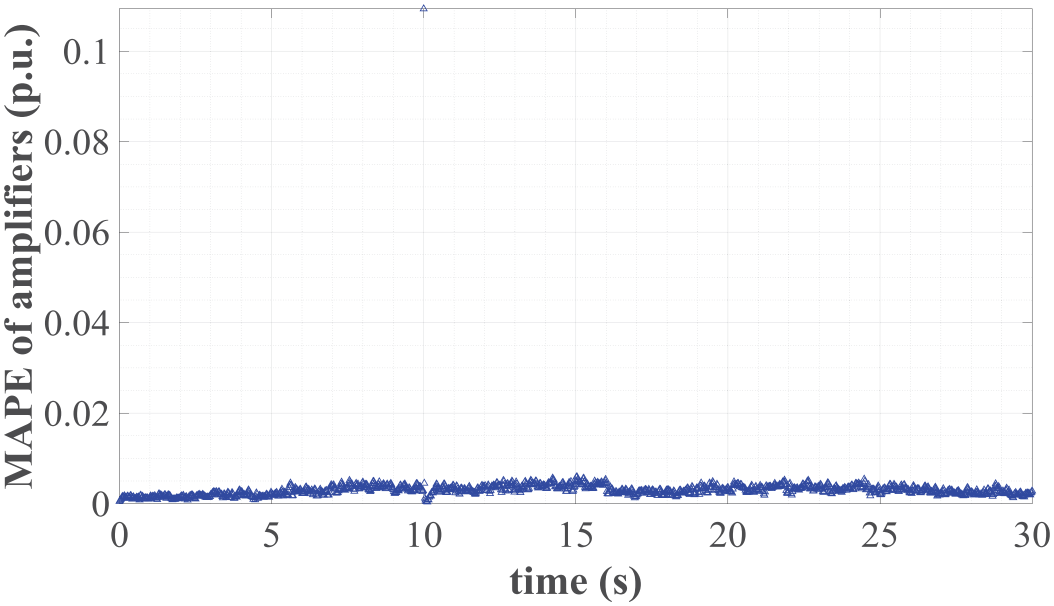

Fig. 4.42 MAPE values of amplifiers scaled outputs of excitation systems in the 190-bus MIPS.

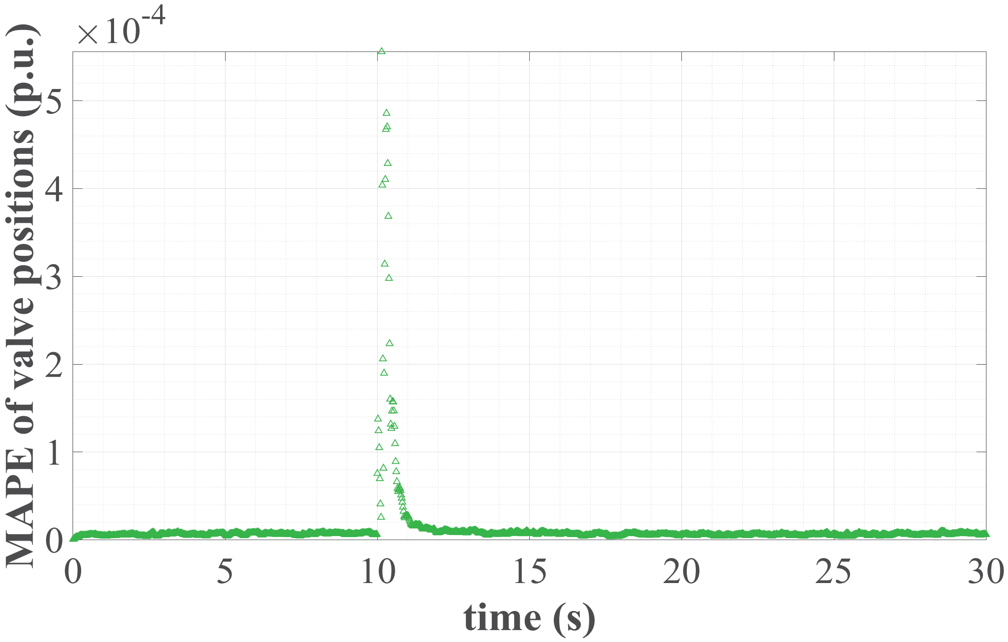

Fig. 4.43 MAPE values of steam valve positions of speed governing systems in the 190-bus MIPS.

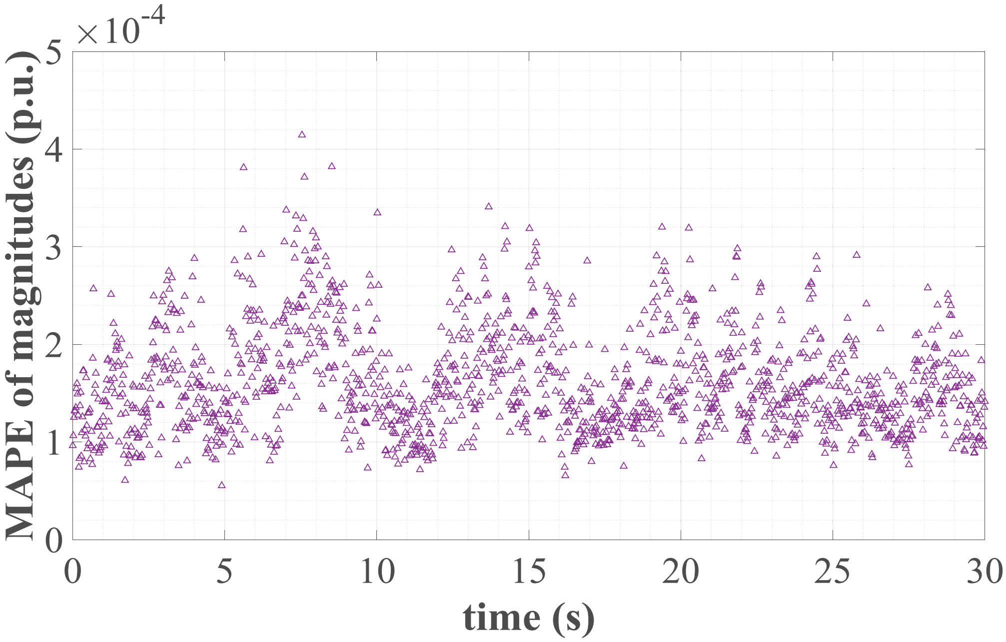

Fig. 4.44 MAPE values of nodal voltage magnitudes in the190-bus MIPS.

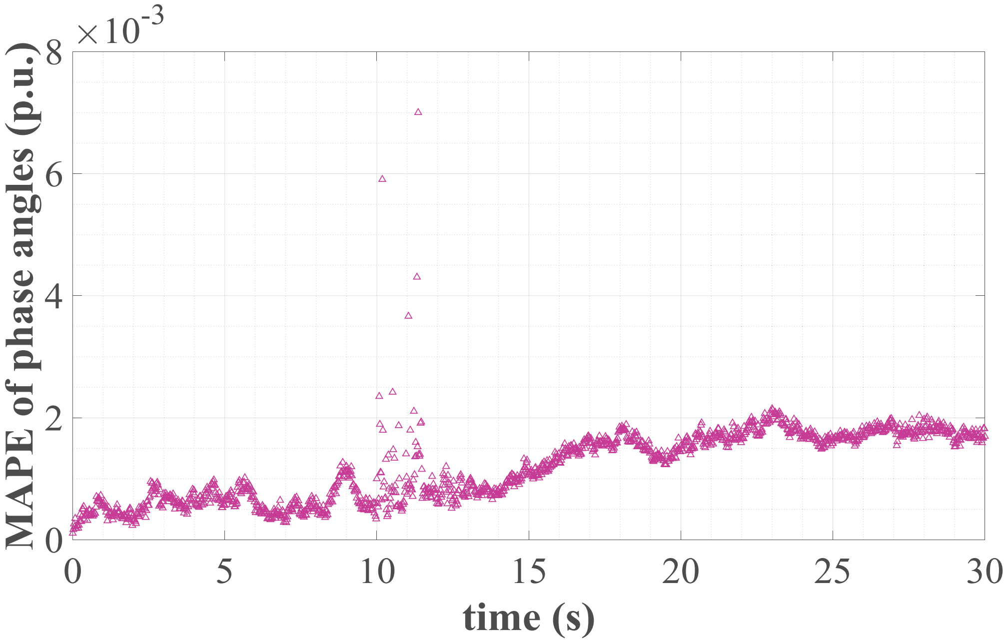

Fig. 4.45 MAPE values of nodal phase angles in the 190-bus MIPS.

From Figs. 4.41 and 4.43, it is clear that the MAPE values of angular speeds and steam valve positions are below 1.57e-4 and 5.56e-4, respectively, so the estimated variables adequately reproduce the real system's dynamics. On the other hand, from Figs. 4.40 and 4.42, it is observed that the highest MAPE value of rotor angles is equal to 0.2105 at $t = 10.22$

s and that the scaled outputs of amplifiers present the highest MAPE value equal to 0.1094 at $t = 10$ s. Note that these discrepancies occur when the fault in bus 182 is applied and between the time instants $10.01 \le t \le 10.81$ when 37 non-windup controllers violate their corresponding physical limits. Furthermore they only occur at the indicated time instants. On the other hand, throughout the entire simulation period except for the time instants mentioned above, MAPE values for rotor angles and scaled outputs of amplifiers are below 4.7e-2 and 5.6e-3, respectively. Hence, this also validates that the proposal can estimate the real MIPS' dynamics. Figure 4.44 clearly shows that MAPE values of nodal voltage magnitudes are below 4.14e-4, so these variables adequately reproduce the corresponding results obtained from the transient stability study. Finally, from Fig. 4.45 it is observed that the MAPE values of nodal phase angles are below 7.0e-3, so the proposal adequately tracks the corresponding results obtained from the transient stability study.

## 4.9 Conclusions

A new methodology is presented in this chapter for the generalized WADSE of electric power systems with the following characteristics. First, the proposal introduces equality constraints associated with difference equations of synchronous machines and their controls in the state estimation formulation. Second, it adds new equality constraints to state estimation formulation for the treatment of constrained dynamic variables by non-windup and windup limiters based on the complementarity theory and the Fischer-Burmeister merit function. Next, the proposed methodology is able to process time-tagged phasor measurements at sampling times determined from PMU reporting rates. Finally, it incorporates the bad data process of [Martínez-Parrales, *et al*., 2020] in the context of the generalized WADSE of electric power systems. The results show that the proposal correctly estimates algebraic and dynamic variables in a unified framework of analysis subject to non-Gaussian measurement uncertainty, constrained dynamic variables and large disturbances.

# Chapter

# 5 General conclusions and future work

## 5.1 General conclusions

The security assessment of power systems is an important task that must be performed to assure the secure and reliable operation of modern electrical networks. Among the computation tools used for a comprehensive and accurate security assessment, the state estimation study could be considered the cornerstone tool because it determines the electrical system's operating state from static and dynamic standpoints.

Based on the information mentioned above, this work proposes the solution of some state estimation's challenges regarding how the co-estimation of several types of state variables and parameters must be performed to facilitate the control actions to be selected for maintaining the power system in a normal operating state.

Regarding the co-estimation of nodal voltages and transmission line parameters, three different already proposed methodologies have been implemented and compared. The results obtained from the application of these methodologies clearly show that the one that estimates normalized transmission line lengths is the best approach for performing this kind of co-estimation.

In practice, one of the main problems for the off-line analysis and reproduction of disturbances occurring in power systems is associated with the parameter's database veracity. Experimental results show that the transmission lines' parameters depend on the temperature at which they are exposed. Hence, a practical method that permits the co-estimation of nodal voltages and temperature-dependent transmission line parameters are proposed in this work. The numerical analysis performed in the Mexican interconnected power system demonstrates that not considering this dependence results in estimates that do not reflect the real operating state. This is important because the operator can make incorrect control actions based on an unrealistic operating condition, especially in the context of remedial actions.

Following the same line of reasoning mentioned in the last paragraph, a new approach is also proposed for performing the co-estimation of state variables and unknown operating statuses of circuit breakers. Unlike other proposals, only one operating constraint is proposed for representing the two possible operating states of a circuit breaker: closed or open. This is achieved by using the concept of complementarity conditions. The proposed operating constraint is then transformed into an equality constraint by using the Fischer-Burmeister merit function, and it is directly included in the static state estimation formulation. Hence, the original formulation of the static state estimation problem remains unchanged but permits the additional estimation of the breaker's unknown operating statuses.

The complementarity constraint concept together with the Fischer-Burmeister merit function has been envisioned in this work as an attractive approach for directly including operating limits of electrical components into the transient stability problem. This work proposes for the first time the application of those concepts to take into account the operational limits of non-windup and windup controllers. Furthermore, the proposal goes beyond considering the controllers' limitations: it includes the controller's operating limits within the complementarity basis and formulating complementarity-based control constraints. This way of modeling the controllers' operation permits directly stating the existing relationships between the control laws and operational limits of the controllers in a single framework of analysis. In this case, the double-sided inequality constraints representing the controllers' limits are transformed into equality constraints by using the complementarity condition approach and the Fischer-Burmeister merit function. This resulting set of constraints are directly added to the set of differential-algebraic equations for performing the automatic check of the controllers' operating limits and, when applicable, the automatic enforcement during the iterative solution process of the transient stability problem. Hence, the *if*-based conditional tests for checking conventionally used violated limits are avoided.

Lastly, a proposed wide area dynamic state estimation (WADSE) approach permits the simultaneous estimation of dynamic and static state variables in a structure-preserving frame of reference. This proposed formulation consists of including the set of differential equations associated with the synchronous machines and their controllers in the conventional tracking state estimation problem. The proposed WADSE approach is capable of estimating algebraic variables related to the transmission system and dynamic variables associated with the synchronous machine model and their controllers, as well as the frequency at each system node: nodal frequency. Furthermore, the proposed estimation automatically sets the dynamic variables of controllers with non-windup and windup limiters to their corresponding physical limits in case of violations. Note that unlike the unscented Kalman approach, the proposal does not require knowledge of the synchronous machine terminals' input vector to estimate its corresponding dynamic variables. This represents a great advantage of the proposed approach with respect to the Kalman-based estimators: the estimation of algebraic and dynamical variables is not constrained by having a PMU installed at the synchronous generator terminals.

## 5.2 Future work

This thesis has described accurate and efficient methods for the co-estimation of different types of state variables suitable for both conventional measurements, synchronized measurements, and a combination of both measurements. New research can consider the following topics to extend this work.

- To develop a decentralized dynamic multi-area state estimation based on the WADSE approach.
- To develop a dynamic state estimation in the presence of HVDC links.
- To include stability indexes in the WADSE approach's formulation to automatically detect possible rotor, power, voltage, and/or frequency stability problems.
- To assess the minimal number of SCADA/PMU measurements needed for the proposed co-estimation and WADSE approaches.
- To merge the co-estimation of nodal voltages and unknown statuses of breakers and the WADSE approach for detecting islands during the occurrence of a disturbance in an electric power system.
- To apply the proposed modeling of non-windup and windup limiters based on complementarity in the context of small-signal stability studies.
- To implement the WADSE approach in a real-time simulator as OPAL-RT.

# *References*

Abur, A., & Gómez Expósito, A. (2004). *Power System State Estimation. Theory and Implementation* (1 ed.). CRC Press.

Abur, A., Kim, H., & Celik, M. (1995). Identifying the Unknown Circuit Breaker Statuses in Power Networks. *IEEE Transactions on Power Systems, 10*(4), 2029-2037. doi:10.1109/59.476072

Alcaide-Moreno, B., Fuerte-Esquivel, C., Castro, L., & Zamora-Cárdenas, E. (2015). Generalized state estimation of flexible ac transmission systems considering wind generators and primary frequency control. *Electric Power Components and Systems, 43*(13), 1534-1547. doi:10.1080/15325008.2015.1042596

Alcaide-Moreno, B., Fuerte-Esquivel, C., Glavic, M., & Van Cutsem, T. (2018). Electric Power Network State Tracking From Multirate Measurements. *IEEE Transactions on Instrumentation and Measurement, 67*(1), 33-44. doi:10.1109/TIM.2017.2754838

Alsac, O., Vempati, N., Stott, B., & Monticelli, A. (1998). Generalized State Estimation. *IEEE Transactions on Power Systems, 13*(3), 1069-1075. doi:10.1109/59.709101

Anderson, P., & Fouad, A. (2003). *Power system control and stability* (2 ed.). Wiley-IEEE Press.

Andreoli, E., Costa, A., & Clements, K. (2014). Topology Validation via Simultaneous State and Topology Estimation with Phasor Data Processing Capability. *2014 Power Systems Computation Conference.* Wroclaw, Poland. doi:10.1109/PSCC.2014.7038474

Billinton, Vohra, & Kumar. (1985). Effect of Station Originated Outages in a Composite System Adequacy Evaluation of the IEEE Reliability Test System. *IEEE Transactions on Power Apparatus and Systems, PAS-104*(10), 2649-2656. doi:10.1109/TPAS.1985.319105

Bockarjova, M., & Andersson, G. (2007). Transmission Line Conductor Temperature Impact on State Estimation Accuracy. *2007 IEEE Lausanne Power Tech.* Lausanne, Switzerland. doi:10.1109/PCT.2007.4538401

Castillo, M., Bretas, N., & London, J. (2012). Parameter Errors and Gross Errors Detection, Identification and Correction. *2012 IEEE Power and Energy Society General Meeting.* San Diego, CA, USA. doi:10.1109/PESGM.2012.6345543

Castillo, M., London, J., & Bretas, N. (2009). Identification and Estimation of Power System Branch Parameter Error. *2009 IEEE Power & Energy Society General Meeting.* Calgary, AB, Canada. doi:10.1109/PES.2009.5275219

Castillo, M., London, J., Bretas, N., Lefebvre, S., Prévost, J., & Lambert, B. (2011). Offline Detection, Identification and Correction of Branch Parameter Errors Based on Several Measurement Snapshots. *IEEE Transactions on Power Systems, 26*(2), 870-877. doi:10.1109/TPWRS.2010.2061876

Chen, Y., Rice, M., & Huang, Z. (2014). SCADA-rate parallel state estimation assessed with utility data. *2014 IEEE PES General Meeting | Conference & Exposition.* National Harbor, MD, USA. doi:10.1109/PESGM.2014.6939097

Clements, K., & Costa, S. (1998). Topology error identification using normalized Lagrange multipliers. *IEEE Transactions on Power Systems, 13*(2), 347-353. doi:10.1109/59.667350

da Silva, N., Simões Costa, A., Clements, K., & Andreoli, E. (2016). Simultaneous estimation of state variables and network topology for power system real-time modeling. *Electric Power Systems Research, 133*, 338-346. doi:10.1016/j.epsr.2015.12.029

Davis, K., Dutta, S., Overbye, T., & Gronquist, J. (2013). Estimation of Transmission Line Parameters from Historical Data. *2013 46th Hawaii International Conference on System Sciences.* Wailea, Maui, HI, USA. doi:10.1109/HICSS.2013.206

de la Villa Jaen, A., & Exposito, A. G. (2001). Modeling unknown circuit breakers in generalized state estimators. *2001 IEEE Porto Power Tech Proceedings.* Porto, Portugal. doi:10.1109/PTC.2001.964924

Debs, A. (1974). Estimation of Steady-State Power System Model Parameters. *IEEE Transactions on Power Apparatus and Systems, PAS-93*(5), 1260-1268. doi:10.1109/TPAS.1974.293849

Donmez, B., & Abur, A. (2020). A Parallel Framework for Robust State Estimation Using Node-Breaker Substation Models. *2020 IEEE PES Innovative Smart Grid Technologies Europe (ISGT-Europe).* The Hague, Netherlands. doi:10.1109/ISGT-Europe47291.2020.9248767

Donmez, B., Scioletti, G., & Abur, A. (2019). Robust State Estimation Using Node-Breaker Substation Models and Phasor Measurements. *2019 IEEE Milan PowerTech.* Milan, Italy. doi:10.1109/PTC.2019.8810449

Du, Y., & Liao, Y. (2012). On-line Estimation of Transmission Line Parameters, Temperature and Sag using PMU Measurements. *Electric Power Systems Research, 93*, 39-45. doi:10.1016/j.epsr.2012.07.007

Fischer, A. (1992). A special Newton-type optimization method. *Optimization, 24*(3-4), 269–284. doi:10.1080/02331939208843795

Fourer, R., M. Gay, D., & W. Kernighan, B. (2003). *AMPL: A modeling language for mathematical Programming* (2 ed.). Duxbury Thomson.

Frank, S., Sexauer, J., & Mohagheghi, S. (2013). Temperature-Dependent Power Flow. *IEEE Transactions on Power Systems, 28*(4), 4007-4018. doi:10.1109/TPWRS.2013.2266409

Gibbs, B. (2011). *Advanced Kalman Filtering, Least-Squares and Modeling: A Practical Handbook.* Hoboken, New Jersey: John Wiley.

Grassidis, J., & Junkins, J. (2012). *Optimal Estimation of Dynamic Systems* (2 ed.). New York: Taylor & Francis Group.

IEEE Committee Report. (1973). Dynamic Models for Steam and Hydro Turbines in Power System Studies. *IEEE Transactions on Power Apparatus and Systems, PAS-92*(6), 1904-1915. doi:10.1109/TPAS.1973.293570

IEEE Power and Energy Society. (2016). IEEE Recommended Practice for Excitation System Models for Power System Stability Studies. *IEEE Std 421.5-2016 (Revision of IEEE Std 421.5-2005)*, 1-207. doi:10.1109/IEEESTD.2016.7553421

Kundur, P. (1994). *Power system stability and control.* McGraw-Hill.

Kusic, G., & Garrison, D. (2004). Measurement of Transmission Line Parameters from SCADA Data. *IEEE PES Power Systems Conference and Exposition.* New York, NY, USA. doi:10.1109/PSCE.2004.1397479

Larson, R., Tinney, W., & Peschon, J. (1970). State Estimation in Power Systems, Part I: Theory and Feasibility. *IEEE Transactions on Power Apparatus and Systems, PAS-89*(3), 345-352. doi:10.1109/TPAS.1970.292711

Liao, Y. (2009). Some Algorithms for Transmission Line Parameter Estimation. *2009 41st Southeastern Symposium on System Theory.* Tullahoma, TN, USA. doi:10.1109/SSST.2009.4806781

Liao, Y., & Kezunovic, M. (2009). Online Optimal Transmission Line Parameter Estimation for Relaying Applications. *IEEE Transactions on Power Delivery, 24*(1), 96-102. doi:10.1109/TPWRD.2008.2002875

Lin, & Abur. (2018). Robust State Estimation Against Measurement and Network Parameter Errors. *IEEE Transactions on Power Systems, 33*(5), 4751-4759. doi:10.1109/TPWRS.2018.2794331

Lin, Y., & Abur, A. (2017). Robust Transformer Tap Estimation. *2017 IEEE Manchester PowerTech.* Manchester, UK. doi:10.1109/PTC.2017.7980919

Liu, H., Hu, F., Su, J., Wei, X., & Qin, R. (2020). Comparisons on Kalman-Filter-Based Dynamic State Estimation Algorithms of Power Systems. *IEEE Access, 8*, 51035-51043. doi:10.1109/ACCESS.2020.2979735

Liu, W., & Lim, S. (1995). Parameter Error Identification and Estimation in Power System State Estimation. *IEEE Transactions on Power Systems, 10*(1), 200-209. doi:10.1109/59.373943

London, J., Mili, L., & Bretas, N. (2004). An observability Analysis Method for a Combined Parameter and State Estimation of a Power Systems. *2004 International Conference on Probabilistic Methods Applied to Power Systems.* Ames, IA, USA.

Lourenco, E. M., Coelho, E. P., & Pal, B. C. (2015). Topology Error and Bad Data Processing in Generalized State Estimation. *IEEE Transactions on Power Systems, 30*(6), 3190-3200. doi:10.1109/TPWRS.2014.2379512

Lourenco, M., Costa, S., & Ribeiro, R. (2010). Steady-State Solution for Power Networks Modeled at Bus Section Level. *IEEE Transactions on Power Systems, 25*(1), 10-20. doi:10.1109/TPWRS.2009.2036466

Lourenco, M., Costa, S., Clements, A., & Cernev, A. (2006). A Topology Error Identification Method Directly Based on Collinearity Tests. *IEEE Transactions on Power Systems, 21*(4), 1920-1929. doi:10.1109/TPWRS.2006.881113

Martínez-Parrales, R., Fuerte-Esquivel, C., & Alcaide-Moreno, B. (2020). Analysis of Bad Data in Power System State Estimation Under Non-Gaussian Measurement Noise. *Electric Power Systems Research, 186*. doi:10.1016/j.epsr.2020.106424

Meneghetti, R., Simões Costa, A., Miranda, V., & Brüning Ascari, L. (2020). Information Theoretic Generalized State Estimation in power systems. *Electric Power Systems Research, 182*. doi:10.1016/j.epsr.2020.106251

Milano, F. (2010). *Power system modelling and scripting.* Berlin, Germany: Springer.

Mishra, C., Centeno, V. A., & Pal, A. (2015). Kalman-filter based recursive regression for three-phase line parameter estimation using synchrophasor measurements. *2015 IEEE Power & Energy Society General Meeting.* Denver, CO, USA. doi:10.1109/PESGM.2015.7285678

Moawwad, A., El-Saadany, E., & El Moursi, M. (2018). Dynamic security-constrained automatic generation control (AGC) of integrated AC/DC power networks. *IEEE Transactions on Power Systems, 33*(4), 3875-3885. doi:10.1109/TPWRS.2017.2770151

Monticelli, A. (1993). Modeling Circuit Breakers in Weighted Least Squares State Estimation. *IEEE Transactions on Power Systems, 8*(3), 1143-1149. doi:10.1109/59.260883

Monticelli, A. (1993). The impact of modeling short circuit branches in state estimation. *IEEE Transactions on Power Systems, 8*(1), 364-370. doi:10.1109/59.221219

Monticelli, A. (2000). Testing equality constraint hypotheses in weighted least squares state estimators. *IEEE Transactions on Power Systems, 15*(3), 950-954. doi:10.1109/59.871718

Monticelli, A., & Garcia, A. (1991). Modeling zero impedance branches in power system state estimation. *IEEE Transactions on Power Systems, 6*(4), 1561-1570. doi:10.1109/59.117003

Olarte, A., & Diaz, H. (2008). Transmission Line's Parameter Estimation Using State Estimation Algorithms. *2008 IEEE Power and Energy Society General Meeting-Conversion and Delivery of Electrical Energy in the 21st Century.* Pittsburgh, PA, USA. doi:10.1109/PES.2008.4596139

Ortega, A., & Milano, F. (2016). Generalized model of VSC-based energy storage systems for transient stability analysis. *IEEE Transactions on Power Systems, 31*(5), 3369-3380. doi:10.1109/TPWRS.2015.2496217

Ozdemir, & Gol. (2015). A robust parameter estimation method based on LAV estimator. *2015 Modern Electric Power Systems (MEPS).* Wroclaw, Poland. doi:10.1109/MEPS.2015.7477163

Pereira, C., Saraiva, T., Miranda, V., Costa, S., Lourengo, M., & Clements, A. (2001). Comparison of approaches to identify topology errors in the scope of state estimation studies. *2001 IEEE Porto Power Tech Proceedings.* Porto, Portugal. doi:10.1109/PTC.2001.964921

Pico, H., Aliprantis, D., & Lin, X. (2017). Transient stability assessment of power systems with uncertain renewable generation. *Proc. 10th Bulk Power Syst. Dynamics and Control Symp.*, (pp. 1-13).

Pizano-Martínez, A., Fuerte-Esquivel, C., Zamora-Cardenas, E., & Ruiz-Vega, D. (2014). Selective transient stability-constrained optimal power flow using a SIME and trajectory sensitivity unified analysis. *Electric Power Systems Research, 109*, 32-44. doi:10.1016/j.epsr.2013.12.003

Probability Methods Subcommittee. (1979). IEEE Reliability Test System. *IEEE Transactions on Power Apparatus and Systems, PAS-98*(6), 2047-2054. doi:10.1109/TPAS.1979.319398

PRODESEN. (2018). *Development Program for the National Electrical System 2018-2032.* Technical report, Secretaría de Energía. Retrieved 02 13, 2021, from https://base.energia.gob.mx/prodesen/PRODESEN2018/PRODESEN18.pdf

Rakpenthai, C., & Uatrongjit, S. (2017). Power System State and Transmission Line Conductor Temperature Estimation. *IEEE Transactions on Power Systems, 32*(3), 1818-1827. doi:10.1109/TPWRS.2016.2601072

Romay, O., Fuerte-Esquivel, C., Zamora-Cárdenas, E., & Gutierrez-Martínez, V. (2019). Methodologies for parameter and state estimation in electric power systems: A comparative analysis. *2019 IEEE International Autumn Meeting on Power, Electronics and Computing (ROPEC).* Ixtapa, Mexico. doi:10.1109/ROPEC48299.2019.9057032

Romay, O., Martínez-Parrales, R., & Fuerte-Esquivel, C. (2021). Transient Stability Assessment Considering Hard Limits on Dynamic States. *IEEE Transactions on Power Systems, 36*(1). doi:10.1109/TPWRS.2020.3025430

Rosehart, W., Roman, C., & Schellenberg, A. (2005). Optimal power flow with complementarity constraints. *IEEE Transactions on Power Systems, 20*(2), 813-822. doi:10.1109/TPWRS.2005.846171

Sauer, P., & Pai, M. (1998). *Power system dynamics and stability.* New Jersey: Prentice Hall.

Sauer, P., Pai, M., & Chow, J. (2018). *Power System Dynamics and Stability With Synchrophasor Measurement and Power System Toolbox* (1 ed.). Wiley-IEEE Press.

Silva, S., Simoes Costa, A., & Clements, K. (2013). Hierarchical state estimation based on state & topology coestimation at substation level. *2013 IEEE Grenoble Conference.* Grenoble, France. doi:10.1109/PTC.2013.6652499

Simoes Costa, A., Lourenco, M., & Colzani, L. (2007). Reduced Anomaly Zone Determination for Topology Error Processing in Generalized State Estimation. *2007 IEEE Lausanne Power Tech.* Lausanne, Switzerland. doi:10.1109/PCT.2007.4538306

Simon, D. (2006). *Optimal State Estimation: Kalman, H Infinity, and Nonlinear Approaches.* Hoboken, New Jersey: John Wiley.

Singh, A., & Pal, B. (2019). *Dynamic Estimation and Control of Power Systems* (1 ed.). Academic Press.

Slutsker, I., Mokhtari, S., & Clements, K. (1996). Real Time Recursive Parameter Estimation in Energy Management Systems. *IEEE Transactions on Power Systems, 11*(3), 1393-1399. doi:10.1109/59.535680

The MathWorks, Inc. (1990-2004). *Simulink® Simulation and Model-Based Design.* MA: The MathWorks Inc.

Tian, G., Zhou, Q., Birari, R., Qi, J., & Qu, Z. (2020). A Hybrid-Learning Algorithm for Online Dynamic State Estimation in Multimachine Power Systems. *IEEE Transactions on Neural Networks and Learning Systems, 31*(12), 5497-5508. doi:10.1109/TNNLS.2020.2968486

University of Washington. (2018, 09 16). *Power Systems Test Case Archive*. (U. E. Engineering, Editor) Retrieved 12 14, 2020, from https://labs.ece.uw.edu/pstca/

Venkatraman, A., Shchetinin, D., & Hug, G. (2019). A Computationally Efficient Solution Algorithm for Least Absolute Value State Estimation Problem. *2019 IEEE PES Innovative Smart Grid Technologies Europe (ISGT-Europe).* Bucharest, Romania. doi:10.1109/ISGTEurope.2019.8905683

Vosgerau, F. (2011). *Coestimação de estados e topologia em sistemas de potência.* Florianópolis, Universidade Federal de Santa Catarina, Brazil: M.Sc. Thesis. Retrieved from https://repositorio.ufsc.br/xmlui/handle/123456789/95320

Vosgerau, F., Costa, A., Clements, K., & Lourenco, E. (2010). Power System State and Topology Coestimation. *2010 IREP Symposium-Bulk Power System Dynamics and Control–VIII (IREP).* Rio de Janeiro, Brazil. doi:10.1109/IREP.2010.5563282

Wang, S., Zhao, J., Huang, Z., & Diao, R. (2018). Assessing Gaussian Assumption of PMU Measurement Error Using Field Data. *IEEE Transactions on Power Delivery, 33*(6), 3233-3236. doi:10.1109/TPWRD.2017.2762927

Wang, W., Tse, C., & Wang, S. (2020). Dynamic State Estimation of Power Systems by p-Norm Nonlinear Kalman Filter. *IEEE Transactions on Circuits and Systems I: Regular Papers, 67*(5), 1715-1728. doi:10.1109/TCSI.2020.2965141

Zamora-Cárdenas, E., Alcaide-Moreno, B., & Fuerte-Esquivel, C. (2014). State estimation of flexible AC transmission systems considering synchronized phasor measurements. *Electric Power Systems Research, 106*, 120-133. doi:10.1016/j.epsr.2013.08.004

Zhang, Y., & Larsson, M. (2010). Static Error Identification: Application to Line Parameter Estimation. *2010 International Conference on Power System Technology.* Zhejiang, China. doi:10.1109/POWERCON.2010.5666599

Zhao, J. (2018). Dynamic State Estimation with Model Uncertainties Using H-infinity Extended Kalman Filter. *IEEE Transactions on Power Systems, 33*(1), 1099-1100. doi:10.1109/TPWRS.2017.2688131

Zhao, J., & Mili, L. (2019). A Decentralized H-Infinity Unscented Kalman Filter for Dynamic State Estimation Against Uncertainties. *IEEE Transactions on Smart Grid, 10*(5), 4870-4880. doi:10.1109/TSG.2018.2870327

Zhao, J., & Mili, L. (2019). Robust Unscented Kalman Filter for Power System Dynamic State Estimation With Unknown Noise Statistics. *IEEE Transactions on Smart Grid, 10*(2), 1215-1224. doi:10.1109/TSG.2017.2761452

Zhao, J., Gómez-Expósito, A., Netto, M., Mili, L., Abur, A., Terzija, V., . . . Sakis Meliopoulos, A. (2019). Power System Dynamic State Estimation: Motivations, Definitions, Methodologies, and Future Work. *IEEE Transactions on Power Systems, 34*(4), 3188-3198. doi:10.1109/TPWRS.2019.2894769

Zhao, J., Mili, L., & Abdelhadi, A. (2017). Robust dynamic state estimator to outliers and cyber attacks. *2017 IEEE Power & Energy Society General Meeting.* Chicago, IL, USA. doi:10.1109/PESGM.2017.8274708

Zhao, J., Mili, L., & Gómez-Expósito, A. (2019). Constrained Robust Unscented Kalman Filter for Generalized Dynamic State Estimation. *IEEE Transactions on Power Systems, 34*(5), 3637-3646. doi:10.1109/TPWRS.2019.2909000

Zhao, J., Netto, M., & Mili, L. (2017). A Robust Iterated Extended Kalman Filter for Power System Dynamic State Estimation. *IEEE Transactions on Power Systems, 32*(4), 3205-3216. doi:10.1109/TPWRS.2016.2628344

Zhao, J., Netto, M., Huang, Z., Yu, S., Gomez-Exposito, A., Wang, S., . . . Rouhani, A. (2020). Roles of Dynamic State Estimation in Power System Modeling, Monitoring and Operation. *IEEE Transactions on Power Systems*, 1-1. doi:10.1109/TPWRS.2020.3028047

Zhao, J., Zheng, Z., Wang, S., Huang, R., Bi, T., Mili, L., & Huang, Z. (2020). Correlation-Aided Robust Decentralized Dynamic State Estimation of Power Systems With Unknown Control Inputs. *IEEE Transactions on Power Systems, 35*(3), 2443-2451. doi:10.1109/TPWRS.2019.2953256

Zhou, N., Huang, Z., Meng, D., Elbert, S., Wang, S., & Diao, R. (2014). *Capturing Dynamics in the Power Grid: Formulation of Dynamic State Estimation through Data Assimilation.* Richland, Washington, USA: Pacific Northwest National Laboratory. Retrieved 02 13, 21, from https://www.osti.gov/biblio/1172467

Zhou, N., Meng, D., Huang, Z., & Welch, G. (2015). Dynamic State Estimation of a Synchronous Machine Using PMU Data: A Comparative Study. *IEEE Transactions on Smart Grid, 6*(1), 450-460. doi:10.1109/TSG.2014.2345698

Zhu, J., & Abur, A. (2006). Identification of network parameter errors. *IEEE Transactions on Power Systems, 21*(2), 586-592. doi:10.1109/TPWRS.2006.873419

Ziena Optimization LLC. (2014). *KNITRO Documentation Release 9.1.* (Artelys, Ed.)

# Appendix A Power system component models

## A.1 Synchronous machine

The synchronous machines are represented by the fourth-order model. The dynamic circuit associated with the *i*-th synchronous machine is shown in Fig. A.1:

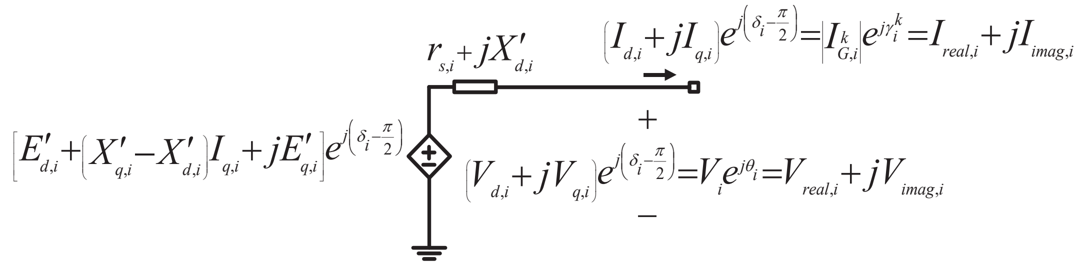

Fig. A.1 Dynamic circuit of the *i*-th synchronous machine.

On the other hand, the 4-th order model for this *i*-th synchronous machine is given by:

$$\frac{dE'_{q,i}}{dt}=-\frac{1}{T'_{d0,i}}E'_{q,i}-\frac{\left(X_{d,i}-X'_{d,i}\right)}{T'_{d0,i}}I_{d,i}+\frac{1}{T'_{d0,i}}E_{fd,i}\ \forall i=1,\ldots,N_{sm}, \tag{A.1}$$

$$\frac{dE'_{d,i}}{dt}=-\frac{1}{T'_{q0,i}}E'_{d,i}+\frac{\left(X_{q,i}-X'_{q,i}\right)}{T'_{q0,i}}I_{q,i}\ \forall i=1,\ldots,N_{sm}, \tag{A.2}$$

$$\frac{d\delta_i}{dt}=\omega_i-\omega_s\ \forall i=1,\ldots,N_{sm}, \tag{A.3}$$

$$\frac{d\omega_i}{dt}=\frac{\omega_s}{2H_i}T_{m,i}-\frac{\omega_s}{2H_i}T_{e,i}-\frac{\omega_sD_i}{2H_i}\left(\omega_i-\omega_s\right)\ \forall i=1,\ldots,N_{sm}, \tag{A.4}$$

where:

- $N_{sm}$ is the total number of synchronous machines.
- $T'_{d0,i}$ is the open circuit transient time constant on the direct axis of the *i*-th machine (s).
- $T'_{q0,i}$ is the open circuit transient time constant on the quadrature axis of the *i*-th machine (s).

- $X_{d,i}$ is the synchronous reactance on the direct axis of the *i*-th machine (p.u.).
- $X'_{d,i}$ is the transient reactance on the direct axis of the *i*-th machine (p.u.).
- $X_{q,i}$ is the synchronous reactance on the quadrature axis of the *i*-th machine (p.u.).
- $X'_{q,i}$ is the transient reactance on the quadrature axis of the *i*-th machine (p.u.).
- $I_{d,i}$ is the current on the direct axis of the *i*-th machine (p.u.).
- $I_{q,i}$ is the current on the quadrature axis of the *i*-th machine (p.u.).
- $\delta_i$ is the rotor angle of the *i*-th machine (rad).
- $H_i$ is the inertia constant of the *i*-th machine (MW/MVA).
- $D_i$ is the damping coefficient of the *i*-th machine (p.u.).
- $\omega_i$ is the angular velocity of the *i*-th machine (rad/s).
- $\omega_s$ is the synchronous angular velocity of the *i*-th machine (rad/s).
- $E'_{d,i}$ is the transient voltage on the direct axis of the *i*-th machine (p.u.).
- $E'_{q,i}$ is the transient voltage on the quadrature axis of the *i*-th machine (p.u.).
- $T_{m,i}$ is the mechanical power produced by the turbine of the *i*-th machine (p.u.).
- $T_{e,i}$ is the electrical power produced by the generator of the *i*-th machine (p.u.).

## A.2 Excitation system

The IEEE Type 1 excitation system is shown in Fig. A.2 and it is composed of the self-excited DC exciter, the signal amplifier, the stabilization circuit and the measurement transducers.

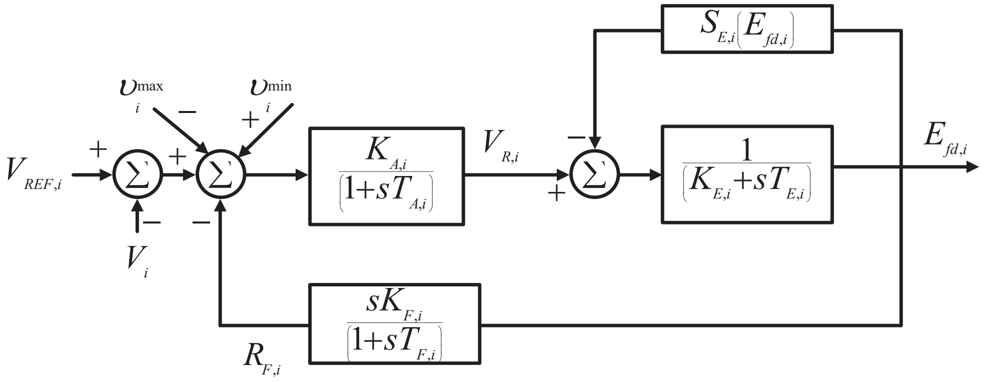

Fig. A.2 Block diagram of DC1A exciter of the *i*-th synchronous machine.

The differential equations of the IEEE type 1 exciter are given by:

$$\frac{dE_{fd,i}}{dt}=-\frac{1}{T_{E,i}}E_{fd,i}\left[K_{E,i}+S_{E,i}\left(E_{fd,i}\right)\right]+\frac{1}{T_{E,i}}V_{R,i}\ \ \forall i=1,\ldots,N_{sm}, \qquad \text{(A.5)}$$

$$\frac{dV_{R,i}}{dt}=\frac{K_{A,i}}{T_{A,i}}\upsilon_i^{\min}-\frac{K_{A,i}}{T_{A,i}}\upsilon_i^{\max}-\frac{1}{T_{A,i}}V_{R,i}-\frac{K_{A,i}}{T_{A,i}}R_{F,i}+\frac{K_{A,i}}{T_{A,i}}\left(V_{REF,i}-V_i\right)\ \ \forall i=1,\ldots,N_{sm}, \qquad \text{(A.6)}$$

$$\frac{dR_{F,i}}{dt}=-\frac{1}{T_{F,i}}R_{F,i}+\frac{K_{F,i}}{T_{E,i}T_{F,i}}V_{R,i}-\frac{K_{F,i}}{T_{E,i}T_{F,i}}E_{fd,i}\left[K_{E,i}+S_{E,i}\left(E_{fd,i}\right)\right]\ \ \forall i=1,\ldots,N_{sm}, \qquad \text{(A.7)}$$

where:

- $N_{sm}$ is the total number of synchronous machines.
- $E_{fd,i}$ is the field voltage of the *i*-th machine (p.u.).
- $T_{E,i}$ is the exciter time constant of the *i*-th machine (s).
- $K_{E,i}$ is the self-excited gain of the *i*-th machine.
- $S_{E,i}\left(E_{fd,i}\right)=A_{ex,i}e^{B_{ex,i}E_{fd,i}}$ is the exciter saturation function of the *i*-th machine. $A_{ex,i}$ and $B_{ex,i}$ are saturation constants.
- $V_{R,i}$ is the scaled output of exciter amplifier of the *i*-th machine (p.u.).
- $T_{A,i}$ is the amplifier time constant of the *i*-th machine (s).
- $K_{A,i}$ is the gain of the exciter amplifier of the *i*-th machine.

- $R_{F,i}$ is the scaled output of stabilizing transformer of the *i*-th machine (p.u.).
- $T_{F,i}$ is the amplifier time constant of the *i*-th machine (s).
- $K_{F,i}$ is the gain of the stabilizing transformer of the *i*-th machine.
- $\upsilon_i^{\min}$ is the complementarity variable for the minimum limit of the non-windup limiter (p.u.).
- $\upsilon_i^{\max}$ is the complementarity variable for the maximum limit of the non-windup limiter (p.u.).
- $V_{REF,i}$ is the exciter reference voltage magnitude of the *i*-th machine (p.u.).
- $V_i$ is the voltage magnitude at generator terminals of the *i*-th machine (p.u.).

## A.3 Governor and turbine

This work assumes that the speed-governing system is of the mechanical-hydraulic type, as shown in Fig. A.3, and it consists of a fly ball speed governor, hydraulic amplifier, linkage mechanism and speed changer.

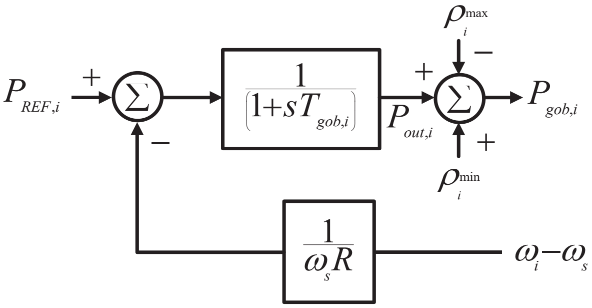

Fig. A.3 Block diagram of the speed governor of the *i*-th synchronous machine.

The differential-algebraic equations associated with this model are given by

$$\frac{dP_{out,i}}{dt} = -\frac{1}{T_{gob,i}}P_{out,i} + \frac{1}{T_{gob,i}}P_{REF,i} - \frac{1}{T_{gob,i}R_i\omega_s}\left(\omega_i - \omega_s\right) \ \forall i = 1,\ldots,N_{sm}, \tag{A.8}$$

$$P_{gob,i} = P_{out,i} + \rho_i^{\min} - \rho_i^{\max} \ \forall i = 1,\ldots,N_{sm}, \tag{A.9}$$

where:

- $N_{sm}$ is the total number of synchronous machines.
- $P_{out,i}$ is the unlimited steam inlet valve position that adjusts the mechanical power applied to the turbine shaft of the *i*-th machine (p.u.).
- $P_{gob,i}$ is the limited steam inlet valve position that adjusts the mechanical power applied to the turbine shaft of the *i*-th machine (p.u.).
- $P_{REF,i}$ is the reference power of the governor of the *i*-th machine (p.u.).
- $T_{gob,i}$ is the time constant of the governor of the *i*-th machine (s).
- $R_i$ is the speed regulation of the governor of the *i*-th machine (p.u.).
- $\rho_i^{\min}$ is the complementarity variable for the minimum limit of the windup limiter (p.u.).
- $\rho_i^{\max}$ is the complementarity variable for the maximum limit of the windup limiter (p.u.).

The turbine model used in this thesis is known as a tandem-compound single reheat steam turbine and it is shown in Fig. A.4.

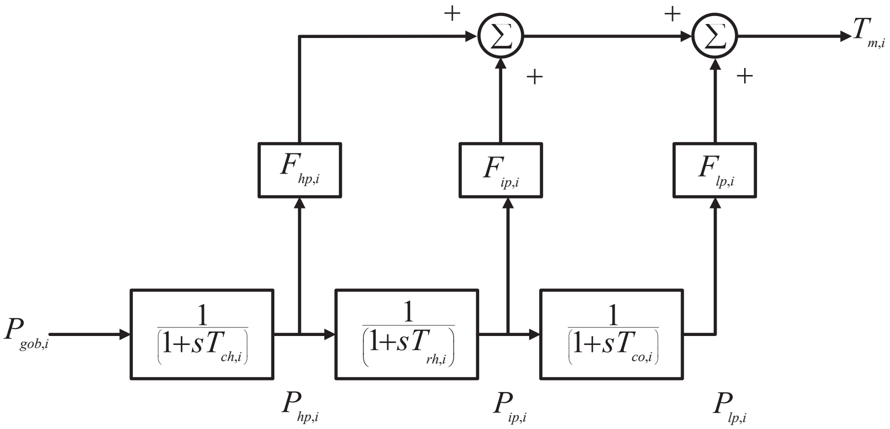

Fig. A.4 Block diagram of single reheat steam turbine of the *i*-th synchronous machine.

The differential equations representing this turbine model are given by

$$\frac{dP_{hp,i}}{dt} = \frac{1}{T_{ch,i}} P_{gob,i} - \frac{1}{T_{ch,i}} P_{hp,i} \quad \forall i = 1,\ldots,N_{sm}, \tag{A.10}$$

$$\frac{dP_{ip,i}}{dt} = \frac{1}{T_{rh,i}} P_{hp,i} - \frac{1}{T_{rh,i}} P_{ip,i} \;\; \forall i = 1,\ldots,N_{sm}, \tag{A.11}$$

$$\frac{dP_{lp,i}}{dt} = \frac{1}{T_{co,i}} P_{ip,i} - \frac{1}{T_{co,i}} P_{lp,i} \;\; \forall i = 1,\ldots,N_{sm}, \tag{A.12}$$

where:

- $N_{sm}$ is the total number of synchronous machines.
- $P_{hp,i}$ is the position of steam inlet valve to high pressure stage of the *i*-th machine (p.u.).
- $P_{ip,i}$ is the position of steam inlet valve to intermediate pressure stage of the *i*-th machine (p.u.).
- $P_{lp,i}$ is the position of steam inlet valve to low pressure stage of the *i*-th machine (p.u.).
- $T_{ch,i}$ is the time delay of the steam chest together with inlet piping of the *i*-th machine (s).
- $T_{rh,i}$ is the reheater time delay of the *i*-th machine (s).
- $T_{co,i}$ is the time delay of crossover piping of the *i*-th machine (s).

The electrical power produced by the *i*-th synchronous generator without considering the stator subtransient dynamics is expressed by

$$T_{e,i} = E'_{d,i} I_{d,i} + E'_{q,i} I_{q,i} + \left( X'_{q,i} - X'_{d,i} \right) I_{d,i} I_{q,i} \;\; \forall i = 1,\ldots,N_{sm}. \tag{A.13}$$

The mechanical power produced by the turbine of the *i*-th synchronous generator is represented by

$$T_{m,i} = P_{hp,i} F_{hp,i} + P_{ip,i} F_{ip,i} + P_{lp,i} F_{lp,i} \;\; \forall i = 1,\ldots,N_{sm}, \tag{A.14}$$

where:

- $N_{sm}$ is the total number of synchronous machines.

- $F_{hp,i}$ is the portion of the total turbine power developed in the high pressure stage of the *i*-th machine.
- $F_{ip,i}$ is the portion of the total turbine power developed in the intermediate pressure stage of the *i*-th machine.
- $F_{lp,i}$ is the portion of the total turbine power developed in the low pressure stage of the *i*-th machine.

## A.4 Complementarity equations

The complementarity equations of the non-windup limiters are given by

$$\sqrt{\left(V_{R,i}-\upsilon_i^{\min}\right)^2+\left(\upsilon_i^{\min}\right)^2}-\left(V_{R,i}-\upsilon_i^{\min}\right)-\left(\upsilon_i^{\min}\right)\ \forall i=1,\ldots,N_{sm}, \tag{A.15}$$

$$\sqrt{\left(\upsilon_i^{\max}-V_{R,i}\right)^2+\left(\upsilon_i^{\max}\right)^2}-\left(\upsilon_i^{\max}-V_{R,i}\right)-\left(\upsilon_i^{\max}\right)\ \forall i=1,\ldots,N_{sm}. \tag{A.16}$$

The windup limiter complementarity equations corresponds to

$$\sqrt{\left(P_{gob,i}-\rho_i^{\min}\right)^2+\left(\rho_i^{\min}\right)^2}-\left(P_{gob,i}-\rho_i^{\min}\right)-\left(\rho_i^{\min}\right)\ \forall i=1,\ldots,N_{sm}, \tag{A.17}$$

$$\sqrt{\left(\rho_i^{\max}-P_{gob,i}\right)^2+\left(\rho_i^{\max}\right)^2}-\left(\rho_i^{\max}-P_{gob,i}\right)-\left(\rho_i^{\max}\right)\ \forall i=1,\ldots,N_{sm}, \tag{A.18}$$

where:

- $N_{sm}$ is the total number of synchronous machines.

## A.5 Stator algebraic equations

The mathematical equations contained in the vector of algebraic stator equations $\boldsymbol{I_{dq}^{DQ}}(.)$ used in the WADSE formulation are associated with the algebraic equations of the *i*-th synchronous machine stator:

$$E'_{d,i}-V_i\sin\left(\delta_i-\theta_i\right)-R_{s,i}I_{d,i}+X'_{q,i}I_{q,i}=0\ \forall i=1,\ldots,N_{sm}, \tag{A.19}$$

$$E'_{q,i}-V_i\cos\left(\delta_i-\theta_i\right)-R_{s,i}I_{q,i}-X'_{d,i}I_{d,i}=0\ \forall i=1,\ldots,N_{sm}, \tag{A.20}$$

where:

- $N_{sm}$ is the total number of synchronous machines.
- $V_i$ is the voltage magnitude at generator terminals of the *i*-th machine (p.u.).
- $\theta_i$ is the nodal phase angle of the *i*-th machine (rad).
- $R_{s,i}$ is the stator resistance of the *i*-th machine (p.u.).

## A.6 Algebraic power balance equations

The vector of algebraic equations $\boldsymbol{g}(.)$ used to formulate the transient stability problem incorporates the algebraic stator equations $\boldsymbol{I}_{\boldsymbol{dq}}^{\boldsymbol{DQ}}(.)$ described in the previous section and the power balance equations at generation, transition and load buses. In this context, the algebraic power balance equations for generation buses are expressed by

$$\begin{aligned} &I_{d,i}V_i\sin\left(\delta_i-\theta_i\right)+I_{q,i}V_i\cos\left(\delta_i-\theta_i\right)-P_{L,i}\left(\frac{V_i}{V_i^0}\right)^2 \\ &-\sum_{k=1}^{N_{buses}}V_iV_k\left|Y_{ik}\right|\cos\left(\theta_i-\theta_k-\alpha_{ik}\right)=0 \end{aligned} \qquad \forall i=1,\ldots,N_{sm}\,, \tag{A.21}$$

$$\begin{aligned} &I_{d,i}V_i\cos\left(\delta_i-\theta_i\right)-I_{q,i}V_i\sin\left(\delta_i-\theta_i\right)-Q_{L,i}\left(\frac{V_i}{V_i^0}\right)^2 \\ &-\sum_{k=1}^{N_{buses}}V_iV_k\left|Y_{ik}\right|\sin\left(\theta_i-\theta_k-\alpha_{ik}\right)=0 \end{aligned} \qquad \forall i=1,\ldots,N_{sm}\,, \tag{A.22}$$

where:

- $N_{sm}$ is the total number of synchronous machines in the system.
- $N_{buses}$ is the total number of buses in the system.
- $\left|Y_{ik}\right|$ is the magnitude (p.u.) of the complex component of $Y_{bus}$ in the row *i* and column *k*.
- $\alpha_{ik}$ is the angle (rad) of the complex component of $Y_{bus}$ in the row *i* and column *k*.
- $P_{L,i}$ is the active power of the load connected at the *i*-th generation node (p.u.).
- $Q_{L,i}$ is the reactive power of the load connected at the *i*-th generation node (p.u.).

- $V_i$ is the voltage magnitude at the *i*-th node (p.u.).
- $V_i^0$ is the initial voltage magnitude at the *i*-th node (p.u.).

The algebraic power balance equations for transition buses are given by

$$\sum_{k=1}^{N_{buses}} V_i V_k \left|Y_{ik}\right| \cos\left(\theta_i - \theta_k - \alpha_{ik}\right) = 0 \quad \forall i = 1, \ldots, N_{tbe}\,, \tag{A.23}$$

$$\sum_{k=1}^{N_{buses}} V_i V_k \left|Y_{ik}\right| \sin\left(\theta_i - \theta_k - \alpha_{ik}\right) = 0 \quad \forall i = 1, \ldots, N_{tbe}\,, \tag{A.24}$$

where:

- $N_{tbe}$ is the total number of transition buses in the system.
- $N_{buses}$ is the total number of buses in the system.
- $\left|Y_{ik}\right|$ is the magnitude (p.u.) of the complex component of $Y_{bus}$ in the row *i* and column *k*.
- $\alpha_{ik}$ is the angle (rad) of the complex component of $Y_{bus}$ in the row *i* and column *k*.
- $V_i$ is the voltage magnitude at the *i*-th node (p.u.).

The algebraic power balance equations for load buses are given by

$$P_{L,i}\left(\frac{V_i}{V_i^0}\right)^2 + \sum_{k=1}^{N_{buses}} V_i V_k \left|Y_{ik}\right| \cos\left(\theta_i - \theta_k - \alpha_{ik}\right) = 0 \quad \forall i = 1, \ldots, N_{buses} - N_{sm} - N_{tbe}\,, \tag{A.25}$$

$$Q_{L,i}\left(\frac{V_i}{V_i^0}\right)^2 + \sum_{k=1}^{N_{buses}} V_i V_k \left|Y_{ik}\right| \sin\left(\theta_i - \theta_k - \alpha_{ik}\right) = 0 \quad \forall i = 1, \ldots, N_{buses} - N_{sm} - N_{tbe}\,, \tag{A.26}$$

where:

- $N_{buses} - N_m - N_{tbe}$ is the number of load buses in the system.
- $N_{buses}$ is the total number of buses in the system.
- $N_{sm}$ is the total number of synchronous machines in the system.
- $N_{tbe}$ is the total number of transition buses in the system.

- $\left| Y_{ik} \right|$ is the magnitude (p.u.) of the complex component of $Y_{bus}$ in the row *i* and column *k*.
- $\alpha_{ik}$ is the angle (rad) of the complex component of $Y_{bus}$ in the row *i* and column *k*.
- $P_{L,i}$ is the active power of the load connected at the *i*-th load node (p.u.).
- $Q_{L,i}$ is the reactive power of the load connected at the *i*-th load node (p.u.).
- $V_i$ is the voltage magnitude at the *i*-th node (p.u.).
- $V_i^0$ is the initial voltage magnitude at the *i*-th node (p.u.).

# Appendix B Discretization of differential equations

## B.1 Unscented Kalman filter

The mathematical equations contained in the vector of discretized functions $\boldsymbol{d}(.)$ used by the unscented Kalman filter are presented below. In this case, the discretization by trapezoidal rule of the 4-th order model of a synchronous machine connected to the $p$-th node is represented by:

$$\begin{aligned} E'^{k+1}_q = {} & \frac{2T'_{d0}-\Delta t}{2T'_{d0}+\Delta t}E'^{k}_q + \frac{-\left(X_d-X'_d\right)\Delta t}{2T'_{d0}+\Delta t}I^{k+1}_d + \frac{\Delta t}{2T'_{d0}+\Delta t}E^{k+1}_{fd} \\ & + \frac{-\left(X_d-X'_d\right)\Delta t}{2T'_{d0}+\Delta t}I^{k}_d + \frac{\Delta t}{2T'_{d0}+\Delta t}E^{k}_{fd}, \end{aligned} \tag{B.1}$$

$$E'^{k+1}_d = \frac{2T'_{q0}-\Delta t}{2T'_{q0}+\Delta t}E'^{k}_d + \frac{\left(X_q-X'_q\right)\Delta t}{2T'_{q0}+\Delta t}I^{k+1}_q + \frac{\left(X_q-X'_q\right)\Delta t}{2T'_{q0}+\Delta t}I^{k}_q, \tag{B.2}$$

$$\delta^{k+1}_p = \delta^{k}_p + \frac{\Delta t}{2}\Delta\omega^{k+1}_p + \frac{\Delta t}{2}\Delta\omega^{k}_p, \tag{B.3}$$

$$\begin{aligned} \Delta\omega^{k+1}_p = {} & \frac{4H_p-\omega_s D_p\Delta t}{4H_p+\omega_s D_p\Delta t}\Delta\omega^{k} + \frac{\omega_s\Delta t}{4H_p+\omega_s D_p\Delta t}T^{k+1}_m + \frac{-\omega_s\Delta t}{4H_p+\omega_s D_p\Delta t}T^{k+1}_e \\ & + \frac{\omega_s\Delta t}{4H_p+\omega_s D_p\Delta t}T^{k}_m + \frac{-\omega_s\Delta t}{4H_p+\omega_s D_p\Delta t}T^{k}_e, \end{aligned} \tag{B.4}$$

where:

- $k+1$ and $k$ denote the time instants $t_{k+1}$ and $t_k$, respectively, at which variables are evaluated.
- $\Delta\omega_p = \omega_p - \omega_s$ is the angular velocity deviation of the machine connected to the $p$-th node (rad/s).

## B.2 WADSE

The mathematical equations contained in the vectors of discretized functions $\boldsymbol{f}(.)$, $\boldsymbol{p}(.)$ and $\boldsymbol{q}(.)$ used in the WADSE formulation are obtained as follows. The synchronous machines are represented by the 4-th order model with its corresponding equations discretized by using by trapezoidal rule:

$$\begin{aligned} E'^{k+1}_{q,i} = E'^{k}_{q,i} &+ \frac{\Delta t}{2}\left( -\frac{1}{T'_{d0,i}} E'^{k+1}_{q,i} - \frac{\left(X_{d,i} - X'_{d,i}\right)}{T'_{d0,i}} I^{k+1}_{d,i} + \frac{1}{T'_{d0,i}} E^{k+1}_{fd,i} \right) \\ &+ \frac{\Delta t}{2}\left( -\frac{1}{T'_{d0,i}} E'^{k}_{q,i} - \frac{\left(X_{d,i} - X'_{d,i}\right)}{T'_{d0,i}} I^{k}_{d,i} + \frac{1}{T'_{d0,i}} E^{k}_{fd,i} \right) \end{aligned} \quad \forall i = 1, \ldots, N_{sm}\,, \tag{B.5}$$

$$\begin{aligned} E'^{k+1}_{d,i} = E'^{k}_{d,i} &+ \frac{\Delta t}{2}\left( -\frac{1}{T'_{q0,i}} E'^{k+1}_{d,i} + \frac{\left(X_{q,i} - X'_{q,i}\right)}{T'_{q0,i}} I^{k+1}_{q,i} \right) \\ &+ \frac{\Delta t}{2}\left( -\frac{1}{T'_{q0,i}} E'^{k}_{d,i} + \frac{\left(X_{q,i} - X'_{q,i}\right)}{T'_{q0,i}} I^{k}_{q,i} \right) \end{aligned} \quad \forall i = 1, \ldots, N_{sm}\,, \tag{B.6}$$

$$\delta^{k+1}_{i} = \delta^{k}_{i} + \frac{\Delta t}{2}\left(\omega^{k+1}_{i} - \omega_{s}\right) + \frac{\Delta t}{2}\left(\omega^{k}_{i} - \omega_{s}\right) \quad \forall i = 1, \ldots, N_{sm}\,, \tag{B.7}$$

$$\begin{aligned} \omega^{k+1}_{i} = \omega^{k}_{i} &+ \frac{\Delta t}{2}\left( \frac{\omega_{s}}{2H_{i}} T^{k+1}_{m,i} - \frac{\omega_{s}}{2H_{i}} T^{k+1}_{e,i} - \frac{\omega_{s} D_{i}}{2H_{i}}\left(\omega^{k+1}_{i} - \omega_{s}\right) \right) \\ &+ \frac{\Delta t}{2}\left( \frac{\omega_{s}}{2H_{i}} T^{k}_{m,i} - \frac{\omega_{s}}{2H_{i}} T^{k}_{e,i} - \frac{\omega_{s} D_{i}}{2H_{i}}\left(\omega^{k}_{i} - \omega_{s}\right) \right) \end{aligned} \quad \forall i = 1, \ldots, N_{sm}\,. \tag{B.8}$$

The excitation system equations are discretized by using the trapezoidal and backward Euler rules. The former is applied to the equations representing the DC exciter output and the stabilization circuit, which correspond to (B.9) and (B.11), respectively. On the other hand, a combination of the trapezoidal and backward Euler rules is applied to the equation associated with the signal amplifier output given by (B.10):

$$\begin{aligned} E^{k+1}_{fd,i} = E^{k}_{fd,i} &+ \frac{\Delta t}{2}\left( -\frac{1}{T_{E,i}} E^{k+1}_{fd,i}\left[K_{E,i} + S_{E,i}\left(E^{k+1}_{fd,i}\right)\right] + \frac{1}{T_{E,i}} V^{k+1}_{R,i} \right) \\ &+ \frac{\Delta t}{2}\left( -\frac{1}{T_{E,i}} E^{k}_{fd,i}\left[K_{E,i} + S_{E,i}\left(E^{k}_{fd,i}\right)\right] + \frac{1}{T_{E,i}} V^{k}_{R,i} \right) \end{aligned} \quad \forall i = 1, \ldots, N_{sm}\,, \tag{B.9}$$

$$\begin{aligned} V_{R,i}^{k+1} = V_{R,i}^{k} &+ \frac{\Delta t}{2}\left( -\frac{1}{T_{A,i}} V_{R,i}^{k+1} - \frac{K_{A,i}}{T_{A,i}} R_{F,i}^{k+1} + \frac{K_{A,i}}{T_{A,i}}\left( V_{REF,i} - V_{i}^{k+1} \right) \right) \\ &+ \frac{\Delta t}{2}\left( -\frac{1}{T_{A,i}} V_{R,i}^{k} - \frac{K_{A,i}}{T_{A,i}} R_{F,i}^{k} + \frac{K_{A,i}}{T_{A,i}}\left( V_{REF,i} - V_{i}^{k} \right) \right) \quad \forall i = 1, \ldots, N_{sm} \ , \qquad \text{(B.10)} \\ &+ \Delta t \left( \frac{K_{A,i}}{T_{A,i}} \upsilon_{i}^{\min,k+1} - \frac{K_{A,i}}{T_{A,i}} \upsilon_{i}^{\max,k+1} \right) \end{aligned}$$

$$\begin{aligned} R_{F,i}^{k+1} = R_{F,i}^{k} &+ \frac{\Delta t}{2}\left( \begin{array}{c} -\dfrac{1}{T_{F,i}} R_{F,i}^{k+1} + \dfrac{K_{F,i}}{T_{E,i}T_{F,i}} V_{R,i}^{k+1} \\ -\dfrac{K_{F,i}}{T_{E,i}T_{F,i}} E_{fd,i}^{k+1}\left[ K_{E,i} + S_{E,i}\left( E_{fd,i}^{k+1} \right) \right] \end{array} \right) \\ &+ \frac{\Delta t}{2}\left( \begin{array}{c} -\dfrac{1}{T_{F,i}} R_{F,i}^{k} + \dfrac{K_{F,i}}{T_{E,i}T_{F,i}} V_{R,i}^{k} \\ -\dfrac{K_{F,i}}{T_{E,i}T_{F,i}} E_{fd,i}^{k}\left[ K_{E,i} + S_{E,i}\left( E_{fd,i}^{k} \right) \right] \end{array} \right) \end{aligned} \quad \forall i = 1, \ldots, N_{sm} \ . \qquad \text{(B.11)}$$

Lastly, equations associated with the governors and turbines, i.e., (B.12) and (B.13) through (B.15), respectively, were discretized through the trapezoidal rule:

$$\begin{aligned} P_{out,i}^{k+1} = P_{out,i}^{k} &+ \frac{\Delta t}{2}\left( -\frac{1}{T_{gob,i}} P_{out,i}^{k+1} + \frac{1}{T_{gob,i}} P_{REF,i} - \frac{1}{T_{gob,i} R_i \omega_s}\left( \omega_i^{k+1} - \omega_s \right) \right) \\ &+ \frac{\Delta t}{2}\left( -\frac{1}{T_{gob,i}} P_{out,i}^{k} + \frac{1}{T_{gob,i}} P_{REF,i} - \frac{1}{T_{gob,i} R_i \omega_s}\left( \omega_i^{k} - \omega_s \right) \right) \end{aligned} \quad \forall i = 1, \ldots, N_{sm} \ , \text{(B.12)}$$

$$\begin{aligned} P_{hp,i}^{k+1} = P_{hp,i}^{k} &+ \frac{\Delta t}{2}\left( \frac{1}{T_{ch,i}} P_{gob,i}^{k+1} - \frac{1}{T_{ch,i}} P_{hp,i}^{k+1} \right) \\ &+ \frac{\Delta t}{2}\left( \frac{1}{T_{ch,i}} P_{gob,i}^{k} - \frac{1}{T_{ch,i}} P_{hp,i}^{k} \right) \end{aligned} \quad \forall i = 1, \ldots, N_{sm} \ , \qquad \text{(B.13)}$$

$$\begin{aligned} P_{ip,i}^{k+1} = P_{ip,i}^{k} &+ \frac{\Delta t}{2}\left( \frac{1}{T_{rh,i}} P_{hp,i}^{k+1} - \frac{1}{T_{rh,i}} P_{ip,i}^{k+1} \right) \\ &+ \frac{\Delta t}{2}\left( \frac{1}{T_{rh,i}} P_{hp,i}^{k} - \frac{1}{T_{rh,i}} P_{ip,i}^{k} \right) \end{aligned} \quad \forall i = 1, \ldots, N_{sm} \ , \qquad \text{(B.14)}$$

$$P_{lp,i}^{k+1} = P_{lp,i}^{k} + \frac{\Delta t}{2}\left(\frac{1}{T_{co,i}}P_{ip,i}^{k+1} - \frac{1}{T_{co,i}}P_{lp,i}^{k+1}\right) + \frac{\Delta t}{2}\left(\frac{1}{T_{co,i}}P_{ip,i}^{k} - \frac{1}{T_{co,i}}P_{lp,i}^{k}\right) \quad \forall i = 1,\dots,N_{sm}, \tag{B.15}$$

where:

- $k+1$ and $k$ denote the time instants $t_{k+1}$ and $t_k$, respectively, at which variables are evaluated.

# Appendix C Estimated measurement equations

The physical set of measurements provided by the SCADA system and PMUs are mathematically represented by the corresponding set of estimated measurements. All these mathematical representations are reported in this Appendix.

## C.1 SCADA measurements for the static state estimator

The estimated measurements $\hat{\boldsymbol{z}}(\boldsymbol{.})$ associated with physical measurements of active and reactive power flows are given by

$$\begin{aligned}\hat{P}_{pq,i}^{SCADA} &= \left(a_{pq,i}\right)^2 V_{p,i}{}^2 (g_{sepq,i} + g_{shpq,i}) \\ &\quad - a_{pq,i} a_{qp,i} g_{sepq,i} V_{p,i} V_{q,i} \cos(\theta_{p,i} - \theta_{q,i}) \quad \forall i = 1,\ldots, N_{\mathcal{T}_{oe}}\ , \\ &\quad - a_{pq,i} a_{qp,i} b_{sepq,i} V_{p,i} V_{q,i} \sin(\theta_{p,i} - \theta_{q,i})\end{aligned} \tag{C.1}$$

$$\begin{aligned}\hat{Q}_{pq,i}^{SCADA} &= -\left(a_{pq,i}\right)^2 V_{p,i}{}^2 (b_{sepq,i} + b_{shpq,i}) \\ &\quad + a_{pq,i} a_{qp,i} b_{sepq,i} V_{p,i} V_{q,i} \cos(\theta_{p,i} - \theta_{q,i}) \quad \forall i = 1,\ldots, N_{\mathcal{T}_{oe}}\ . \\ &\quad - a_{pq,i} a_{qp,i} g_{sepq,i} V_{p,i} V_{q,i} \sin(\theta_{p,i} - \theta_{q,i})\end{aligned} \tag{C.2}$$

Similarly, the physical measurements associated with nodal active and reactive power injections are represented by

$$\hat{P}_{p,i}^{SCADA} = \sum_{k=1}^{N_{buses}} V_i V_k \left|Y_{ik}\right| \cos\left(\theta_i - \theta_k - \alpha_{ik}\right)\ \forall i = 1,\ldots, N_{oe}\,. \tag{C.3}$$

The nodal reactive power injection equations are represented by:

$$\hat{Q}_{p,i}^{SCADA} = \sum_{k=1}^{N_{buses}} V_i V_k \left|Y_{ik}\right| \sin\left(\theta_i - \theta_k - \alpha_{ik}\right)\ \forall i = 1,\ldots, N_{oe}\,. \tag{C.4}$$

Lastly, the estimated measurements $\boldsymbol{c}(\boldsymbol{.})$ of zero active and reactive power injections at transition buses are given by

$$\hat{P}_{p,i} = \sum_{k=1}^{N_{buses}} V_i V_k \left|Y_{ik}\right| \cos\left(\theta_i - \theta_k - \alpha_{ik}\right) = 0\ \forall i = 1,\ldots, N_{tbe}\,, \tag{C.5}$$

$$\hat{Q}_{p,i} = \sum_{k=1}^{N_{buses}} V_i V_k \left|Y_{ik}\right| \sin\left(\theta_i - \theta_k - \alpha_{ik}\right) = 0 \;\; \forall i = 1,\ldots,N_{tbe} \,, \tag{C.6}$$

where:

- $N_{buses}$ is the total number of buses in the system.
- $V_i$ is the nodal voltage magnitude of the *i*-th node (p.u.).
- $V_k$ is the nodal voltage magnitude of the *k*-th node (p.u.).
- $\theta_i$ is the nodal phase angle of the *i*-th node (p.u.).
- $\theta_k$ is the nodal phase angle of the *k*-th node (p.u.).
- $\left|Y_{ik}\right|$ is the magnitude (p.u.) of the complex component of $Y_{bus}$ in the row *i* and column *k*.
- $\alpha_{ik}$ is the angle (rad) of the complex component of $Y_{bus}$ in the row *i* and column *k*.

## C.2 PMU measurements for the WADSE's

The equations associated with the real and imaginary components of the complex branch currents' measurements provided by PMUs are given by

$$\begin{aligned} \hat{I}_{realpq,i}^{PMU,k+1} = {} & \left(a_{pq,i}\right)^2 g_{sepq,i} V_{p,i}^{k+1} \cos(\theta_{p,i}^{k+1}) \\ & - \left(a_{pq,i}\right)^2 b_{sepq,i} V_{p,i}^{k+1} \sin(\theta_{p,i}^{k+1}) \\ & - a_{pq,i} a_{qp,i} g_{sepq,i} V_{q,i}^{k+1} \cos(\theta_{q,i}^{k+1}) \quad \forall i = 1,\ldots,N_{\mathcal{T}_{oe}} \,, \\ & + a_{pq,i} a_{qp,i} b_{sepq,i} V_{q,i}^{k+1} \sin(\theta_{q,i}^{k+1}) \\ & - \left(a_{pq,i}\right)^2 b_{shpq,i} V_{p,i}^{k+1} \sin(\theta_{p,i}^{k+1}) \end{aligned} \tag{C.7}$$

$$\begin{aligned} \hat{I}_{imagpq,i}^{PMU,k+1} = {} & \left(a_{pq,i}\right)^2 b_{sepq,i} V_{p,i}^{k+1} \cos(\theta_{p,i}^{k+1}) \\ & + \left(a_{pq,i}\right)^2 g_{sepq,i} V_{p,i}^{k+1} \sin(\theta_{p,i}^{k+1}) \\ & - a_{pq,i} a_{qp,i} b_{sepq,i} V_{q,i}^{k+1} \cos(\theta_{q,i}^{k+1}) \quad \forall i = 1,\ldots,N_{\mathcal{T}_{oe}} \,. \\ & - a_{pq,i} a_{qp,i} g_{sepq,i} V_{q,i}^{k+1} \sin(\theta_{q,i}^{k+1}) \\ & + \left(a_{pq,i}\right)^2 b_{shpq,i} V_{p,i}^{k+1} \cos(\theta_{p,i}^{k+1}) \end{aligned} \tag{C.8}$$

Furthermore, the physical measurement of nodal frequency at the *i*-th observable node is mathematically represented as a nodal average angular frequency computed by

$$\hat{f}_i^{k+1} = \left[ \frac{\left( \dfrac{\theta_i^{k+1} - \theta_i^k}{\Delta t} \right) \left( \dfrac{1}{f_{nom}} \right) + 2\pi}{2\pi} \right] \left( f_{nom} \right) \ \forall i = 1, \ldots, N_{oe} . \tag{C.9}$$

where:

- $k+1$ and $k$ denote the time instants $t_{k+1}$ and $t_k$, respectively, at which variables are evaluated.
- $f_{nom}$ is the nominal frequency of the system (Hz).
- $\Delta t$ is the PMU report rate (s).

## C.3 PMU's measurements for the unscented Kalman filter

The equations representing physical measurements of the real and imaginary components of the current injected at terminals of the synchronous generator connected to the *p*-th node are represented by

$$\hat{I}_{realp}^{PMU,k+1} = I_d^{k+1} \cos\left( \delta_p^{k+1} - \frac{\pi}{2} \right) - I_q^{k+1} \sin\left( \delta_p^{k+1} - \frac{\pi}{2} \right), \tag{C.10}$$

$$\hat{I}_{imagp}^{PMU,k+1} = I_q^{k+1} \cos\left( \delta_p^{k+1} - \frac{\pi}{2} \right) + I_d^{k+1} \sin\left( \delta_p^{k+1} - \frac{\pi}{2} \right). \tag{C.11}$$

Similarly, the estimated measurements of the real and imaginary components of the nodal voltage at terminals of the synchronous generator connected to the *p*-th node are given by

$$\begin{aligned} \hat{V}_{realp}^{PMU,k+1} = {} & \left[ E_d'^{k+1} + \left( X_q' - X_d' \right) I_q^{k+1} \right] \cos\left( \delta_p^{k+1} - \frac{\pi}{2} \right) - E_q'^{k+1} \sin\left( \delta_p^{k+1} - \frac{\pi}{2} \right) \\ & - \left( I_d^{k+1} r_s - I_q^{k+1} X_d' \right) \cos\left( \delta_p^{k+1} - \frac{\pi}{2} \right) + \left( X_d' I_d^{k+1} + I_q^{k+1} r_s \right) \sin\left( \delta_p^{k+1} - \frac{\pi}{2} \right), \end{aligned} \tag{C.12}$$

$$\begin{aligned} \hat{V}_{imagp}^{PMU,k+1} = {} & \left[ E_d'^{k+1} + \left( X_q' - X_d' \right) I_q^{k+1} \right] \sin\left( \delta_p^{k+1} - \frac{\pi}{2} \right) + E_q'^{k+1} \cos\left( \delta_p^{k+1} - \frac{\pi}{2} \right) \\ & - \left( I_d^{k+1} r_s - I_q^{k+1} X_d' \right) \sin\left( \delta_p^{k+1} - \frac{\pi}{2} \right) - \left( X_d' I_d^{k+1} + I_q^{k+1} r_s \right) \cos\left( \delta_p^{k+1} - \frac{\pi}{2} \right), \end{aligned} \tag{C.13}$$

where:

- $k+1$ and $k$ denote the time instants $t_{k+1}$ and $t_k$, respectively, at which variables are evaluated.